Contribution to the design and fabrication of an integrated micro-positioning system

Muneeb Ullah Khan

Muneeb Ullah KHAN

Contribution to the design and fabrication of an integrated micro-positioning system.

Dissertation presented
to obtain the grade of
Doctor from UTC, France
and TU Braunschweig, Germany.

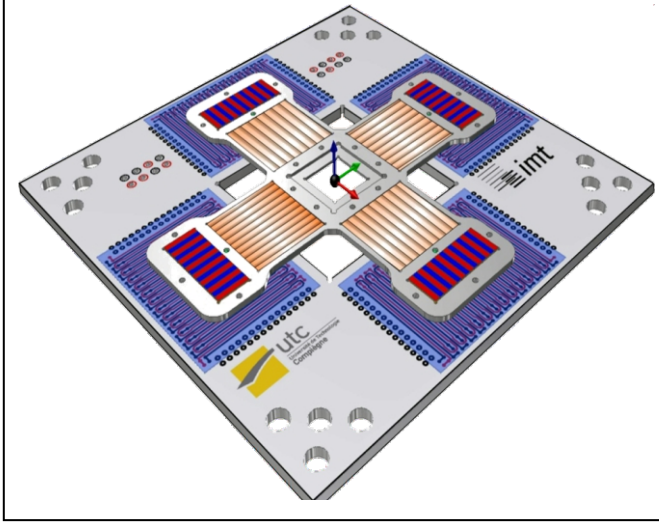

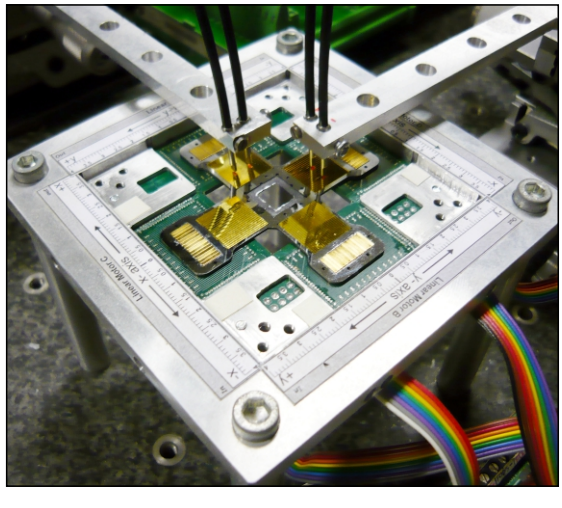

Defended on: March 24, 2014

Discipline : Mechanical Engineering

D1671

Contribution to the design and fabrication of an integrated micro-positioning system

From the faculty of the Mechanical Engineering of the
Université de Technologie de Compiègne at Compiègne, France

and

From the faculty of the Mechanical Engineering of the
Technische Universität Carolo-Wilhelmina at Braunschweig, Germany

Dissertation

written by

Muneeb Ullah Khan

Filed on: 25.10.2013
Oral Exam: 24.03.2014
Defense date: 24.03.2014

Jury members:

PhD directors:	
Prof. Dr. Christine Prelle	Université de Technologie de Compiègne, France
Prof. Dr. rer. nat. Stephanus Büttgenbach	Technische Universität Braunschweig, Germany
Reviewers:	
Prof. Dr. rer. nat. Bertram Schmidt	Universität Magdenburg, Germany
Dr. Michaël Gauthier	FEMTO-ST, Besançon, France
Examiners:	
Prof. Dr.-Ing. Rainer Tutsch	Technische Universität Braunschweig, Germany
Prof. Dr. Vincent Lanfranchi	Université de Technologie de Compiègne, France
Chairman of the oral examination jury:	
Prof. Dr. rer. nat. Andreas Dietzel	Technische Universität Braunschweig, Germany
President of the PhD defence jury:	
Prof. Dr. Vincent Lanfranchi	Université de Technologie de Compiègne, France

Preface

This manuscript represents the summary of my research activities since October, 2008. These activities were performed under a joint PhD degree program between Roberval laboratory (UMR 7337) at Université de Technologie de Compiègne (UTC), France and Institut für Mikrotechnik at Technische Universität (IMT-TU) Braunschweig, Germany.

The work presented deals with the realization of an integrated miniature positioning system. It combines the design and development of a positioning platform and a long range optical displacement sensor. From the perspective to be used either as a stand alone system or a subsystem to pre-existing macro scale positioning machines in macro/micro realm, the design of the positioning platform has been optimized to reach overall small foot print size for whole positioning system.

While taking into account the international aspect of this work and the joint PhD degree program agreement signed by both universities, the writing of this thesis report has been carried out in English language except the abstract which is written in English, German and French languages.

Abstract

Modern positioning systems are significantly applied in many engineering fields dealing with products emerging from different technologies at macro-, micro- and nano scale. These systems are the back-bone systems behind any manipulation task in these areas. Currently, miniaturization trend have led numerous scientific communities to realize down scaled versions of these systems with a footprint size up to few hundreds of millimeters. These miniature positioning systems are cost effective solutions in many micro applications.

This thesis presents the development of a miniature positioning system integrated with a non contact long range displacement sensor. The uniqueness of the presented positioning system lies in its simple design with ability to perform micrometer to millimeter level strokes with pre-embedded auto guidance feature. Its design consists of a mobile part driven with four electromagnetic linear motors. Each motor consists of a fixed two phase current carrying planar electric drive coil and permanent magnet array that is realized with 14 permanent magnets arranged in north-south configuration. In order to achieve smooth motion a four point contact technique with hemispherical glass beads has been adapted to minimize the adherence effect. The overall design of the planar positioning system have been optimized to achieve a footprint size of 80 mm x 80 mm. The device can deliver motion within working range of 10×10 mm^2 in *xy*-plane with sub micrometer level resolution at a speed of 12 mm/s. The device is capable to deliver a rotation motion of $\pm11^{\circ}$about the z axis in the *xy*-plane.

Secondly, in order to measure the displacement performed by the mobile part, a non contact long range linear displacement sensor has been designed. The overall dimensions of the sensor were optimized using a geometrical model. The fabrication of the sensor has been carried out via microfabrication in silicon material to achieve compact dimensions, so that it could be integrated in the mobile part of the positioning system. The sensor is able to provide 30.8 nm resolution with a linear measurement range of 12.5 mm. At the end, a novel cross structure has been designed and fabricated using microfabrication with the perspective to integrate the long range sensor.

***Keywords*:** Permanent magnet array , Electromagnetic actuator, Positioning system, Electric coil design, Optical sensor, Microfabrication, Thin layer coating, Anisotropic etching of silicon, Direct drive technology, Dry etching of silicon

Résumé

Les systèmes modernes de positionnement sont grandement utilisés dans de nombreux domaines de l'ingénierie portant sur des produits issus de différentes technologies aux échelles macro, micro et nano. Ces systèmes sont les pierres angulaire de toutes tâches de manipulation à ces échelles. Actuellement, la tendance à la miniaturisation a entraîné de nombreuses communautés scientifiques à réaliser des versions miniaturisées des ces systèmes d'une taille allant jusqu'à quelques centaines de millimètres. Ces systèmes de positionnement miniature deviennent alors des solutions adaptéess à de nombreuses applications à l'échelle microscopique.

Cette thèse présente la conception et le développement d'un système de positionnement qui intègre un capteur de déplacement sans contact. L'originalité du système de positionnement présenté réside dans sa conception épurée avec la possibilité d'effectuer des déplacements micrométriques sur une étendue millimétrique avec une fonction de guidage intégrée. Le dispositif est constitué d'une partie mobile entraînée par quatre moteurs linéaires électromagnétiques. Chaque moteur est constitué d'un bobine fixe à deux phases et d'une barre d'aimants réalisée avec 14 aimants permanents disposés dans une configuration nord-sud. Afin que le mouvement s'effectue sans heurt la structure repose sur quatre points grâce à des billes de verre hémisphériques dans le but de minimiser l'effet d'adhérence. La conception globale du système de positionnement planaire a été optimisée pour tenir sur une surface 80 mm$\times$80 mm. Le dispositif peut se déplacer sur une course de 10×10 mm^2 dans le plan *xy* avec une résolution submicrométrique et à une vitesse de 12 mm/s. De plus, le dispositif peut se déplacer en rotation ($\pm11^\circ$) autour de l'axe z dans le plan *xy*.

En second lieu, afin de mesurer le déplacement effectué par la partie mobile et dans le but d'asservir le système de positionnement, un capteur optique, sans contact, de longue étendue de déplacement linéaire, a été conçu. Les dimensions globales et les performances du capteur ont été optimisées en utilisant un modèle géométrique. Le réseau a été microfabriqué en silicium dans un but de compacité, afin qu'il puisse être intégré dans la partie mobile du système de positionnement. Le capteur est capable de fournir une résolution de 30,8 nm sur une plage de mesure linéaire de 12.5 mm. Enfin, une structure mobile a été conçue et microfabriquée en silicium avec l'objectif d'arriver à une meilleure intégration du capteur longue étendue.

***Mots-clés*:** Barre d'aimants permanents, Actionneur électromagnétique, Système de positionnement, Bobines électriques, Entraînement direct, Capteur optique, Microfabrication, Gravure anisotrope du silicium, Dépôt de couches minces, Gravure à sec de silicium.

Zusammenfassung

Moderne Positioniersysteme werden in vielen aufstrebenden Bereichen der Technik eingesetzt. Die Produkte stammen hierbei aus unterschiedlichen Technologiebereichen, die den Makro-, Mikro- und Nano- Maßstab abdecken. Diese Systeme bilden die Basis jeder Manipulationsaufgabe, in diesen Bereichen. In jüngster Zeit hat der Miniaturisierungstrend dazu geführt, dass in zahlreichen wissenschaftlichen Bereichen immer kleinere Versionen von Systemen realisiert wurden. Die typischen Abmessungen wurden dabei auf einige hundert Millimeter reduziert. Diese Miniatur Positioniersysteme sind kostengünstige Lösungen in vielen Mikro Anwendungen.

Die vorliegende Arbeit stellt die Entwicklung eines Miniatur-Positioniersystems dar, in welches ein berührungsloser Wegsensor für lange Distanzen integriert wurde. Die Einzigartigkeit dieses Positionierungssystems liegt in der Einfachheit der Konstruktion in Kombination mit der Fähigkeit Bewegungen vom Mikrometer bis zum Millimeter Bereich mittels einer eingebetteten Autopilotfunktion auszuführen. Das Design besteht aus einem beweglichen Teil, welches mit vier elektrischen Linearmotoren angetrieben wird. Jeder Motor besteht aus zwei Teilen: Einem planaren elektrisch angetriebenen Schlitten und einer Anordnung von Permanentmagneten. Die Anordnung ist mit 14 Permanentenmagneten in Nord-Süd Ausrichtung realisiert. Um eine sanfte Bewegung zu erreichen wird eine Vierpunktauflage mit halbkugelförmigen Glasperlen verwendet. Hierdurch werden Adhäsionseffekte minimiert. Das Positionierungssystem kann Bewegungen im Arbeitsbereich von 10×10 mm^2 in der xy-Ebene mit Submikrometer Auflösung und einer Geschwindigkeit von 12 mm/s ausführen. Das Gerät ist in der Lage eine Drehbewegung von $\pm11^\circ$ um die z-Achse in der xy-Ebene auszuführen.

Weiterhin wurde, um die Verschiebung des beweglichen Teils zu messen, ein kontaktloser Langstrecken-Wegsensor entworfen. Die Gesamtabmessungen des Sensors wurden mit einem geometrischen Modell optimiert. Die Herstellung des Sensors wurde mittels Mikrostrukturierung in Silizium ausgeführt um eine kompakte Abmessung zu erreichen, so dass es in den beweglichen Teil des Positionierungssystems integriert werden konnte. Der Sensor erreicht eine Auflösung von 30,8 nm in einem linearen Messbereich von 12.5 mm. Am Ende der Arbeit wurde eine neue Kreuz-Struktur konzipiert und hergestellt, gleichfalls mit Hilfe der Mikrostrukturierungstechnik. Hieraus ergibt sich die Perspektive den Langstrecken Wegsensor problemlos zu integrieren.

***Schlüsselwörter*:** Permanentmagnet Array, Elektromagnetischer Antrieb, Positioniersystem, Elektrospulen, Direkter Antrieb, Optischer Sensor, Mikrotechnik, Anisotropes Ätzen von Silizium, Dünnschichtabscheidung, Trockenätzen von Silizium.

Acknowledgment

This study was conducted in the Roberval laboratory, UMR 7337, UTC/CNRS, Université de Technologie de Compiègne (UTC), directed by Prof. Dr. Jean-Marc Roelandt and Institut für Mikrotecknik (IMT), Technische Universität Braunschweig, directed by Prof. Dr. rer. nat. Andreas Dietzel. I owe particular thanks to both of the directors for having me in their institutes.

I would like to express the deepest appreciation to my PhD supervisors, Prof. Christine Prelle (at UTC) and Prof. Stephanus Büttgenbach (at TU Braunschweig). I sincerely thank them for their advice and support. Without their guidance and persistent help on both professional and personal levels, this dissertation would not have been possible.

I would also like to thank Dr. HDR. Frédéric Lamarque (Directeur Génie systèmes mécanique), Dr. Laurent Petite, Dr. Emmanuel Doré, Mr. Phillipe Pouille, Dr. Monika Leester-Schädel, Dr. Tobias Beutel and all the other staff members of the Roberval laboratory at UTC and IMT at TU Braunschweig to provide me their immense support during this research work.

My time at UTC and TU Brauschwieg was made enjoyable for the most part due to all my friends and colleagues (Ahmad Jawad, Sajid Zaidi, Shahid Umer Khan, Shazia tanveer, Nabil Jouni, Neha Arora, Zeina el Rawashdeh, Pengfei Huyan, Balaji Ragavan, Jan Dittmer, Barbara Matheis, Anke Vierheller, Stefan Schieseck, ...). I thank them for their moral support and also nice and cheerful environment.

Finally, I owe my deepest gratitude to my family and especially my parents for their support and encouragement throughout the years.

Table of contents

List of figures

List of tables

List of abbreviations

CAD	Computer Aided Design
CCD	Charge Coupled Device
CNC	Computer Numerically Control
DAQ	Data Acquisition
DOF	Degree Of Freedom
DRIE	Deep Reactive Ion Etching
EMA	ElectroMagnetic Actuator
FCC	Face Centered Cubic
FEA	Finite Element Analysis
FODS	Fiber Optic Displacement Sensor
IC	Integrated Circuits
ICP	Inductively Coupled Plasma
IMT	Institute für Mikrotechnik
LED	Light Emitting Diode
LIA	Linear Induction actuator
LM	Linear Motor
LRA	Linear Reluctance Actuator
LUT	Look-UP Table
MEMS	Micro Electro Mechanical System
MPS	Minaiture Positioning System
MST	Micro System Technology
NS	North-South
PA	Piezo Actuator
PC	Piezo Ceramics
PCB	Printed Circuit Board
PCI	Peripheral Component Interconnect
PECVD	Plasma Enhanced Chemically Vapor Deposition
PEDC	Planar Electric Drive Coil
PD	Photo Diode

PI	Proportional Integral
PM	Permanent Magnet
PMA	Permanent Magnet Array
PMMA	PolyMethyl MethAcrylate
PV	Peak-Valley
PVD	Physical Vapor Deposition
PZT	Lead Zirconate Titanate
QDR	Quick Dump Rinser
RIE	Reactive Ion Etching
RMS	Root Mean Square
SCS	Single Crystal Silicon
SEM	Scanning Electron Microscope
SMA	Shape Memory Alloy
TU-BS	Technische Universität Braunschweig
UTC	Université de Technologie de Compiègne
UV	Ultra violet
Chemical solutions:	
CH_3COOH	Acetic acid
Br	Bromine
$(NH_4)_2Ce(NO_3)_6$	Ceric ammonium nitrate
AZ 351AB	General purpose developer
HF	Hydrofluoric acid
IPA	Isopropyl alcohol
HNO_3	Nitiric acid
$HClO_4$	Perchloric acid
H_3PO_4	Phosphoric acid
ma-P1215	Positive photoresist
KOH	Potassium hydroxide
SiO_2	Silicon dioxide
Si_3N_4	Silicon nitride
H_2SO_4	Sulfuric acid
TMAH	Tetramethylammonium hydroxide

Introduction

The accelerated research and developments in the field of system miniaturization technology has played an important role over past sixty years after the invention of integrated circuits in 1950s. These developments have introduced innovative products in our society. Personal computers, digital camera, and smart phones are few of the triumphs of these developments. The ever greater diversity, economy and power of integrated electronic components have provided an inspiration to develop miniaturized mechatronic systems in various engineering domains. The evolution of automobile industry is one of the prominent examples in this era. Currently, automobiles are equipped with numerous systems composed of sensors (pressure sensor, temperature sensor, light sensor, fuel sensor, etc.) and actuators (micro valves, control switches, micro motors, etc.) to control the status of an automobile via on-board computer to ensure the safety and comfort of the user.

Apart from this industrial sector, the success behind the increasing demand in mechatronic systems is related to facilitate positioning/manipulation tasks in micro applications such as cell manipulation in biomedicine, surface analysis in meteorology, etc. These applications, demand modern positioning systems that should be able to deliver displacement strokes with sub micrometer level accuracy, high precision and repeatability. Currently, the scale down versions of these modern positioning systems are often developed with embedded functionalities such as multiple-DOF, integrated sensors, etc., by taking into account the current miniaturization trend. Numerous solutions have been introduced over time to economize these systems with compact dimensions. The work presented in this thesis is also based on the development of a compact miniature positioning system for micro applications.

The main objectives of the work presented in this manuscript include:

- Design and development of a miniaturized planar actuation platform that is able to deliver millimeter level strokes with sub micrometer level resolution
- Design and development of a high resolution non contact long range displacement measurement sensor
- Realization of an integrated compact miniature positioning system.

In order to reach these objective, the work presented in this manuscript is divided into six chapters.

Chapter 1 provides the state of the art regarding the different existing miniature multi-DOF positioning systems. The classification of these systems have been carried out on the basis of the actuation technologies. It also provides the state of the art related to the different displacement measurement sensor technologies and their integration approach.

Chapter 2 is dedicated to the working principle and modelling of a planar actuation system. At first, the concept of the actuation system is described along with the general layout of the system. Due to the symmetrical design of the system, the construction and functioning of a single linear electromagnetic actuator is discussed for the purpose of simplification. In addition, analytical models have been realized and verified using Finite Element Analysis (FEA). These models have been implemented to perform static and dynamic simulations in order to evaluate the performance of the whole system in open and closed loop control.

In chapter 3, the development of the Miniature Positioning System (MPS) prototype has been carried out. In the first part, the detail design layout of the MPS and the construction of its components have been discussed. Different design and fabrication solutions have been presented to realize a two part based compact system with optimal foot print dimensions on the basis of the concept introduced in chapter 2. Afterward, experiments have been performed in order to examine the different motion characteristics of the MPS in open and closed loop control.

Chapter 4 presents the design and development of a miniature long range optical displacement sensor. The long range sensor concept and working principle have been discussed and its geometrical optimisation has been carried out. In order to realize the long range sensor, a microfabrication approach was used to fabricate the silicon grating.

Chapter 5 details the sensor integration approach into the MPS. A novel silicon material based cross structure has been developed in order to facilitate the sensor integration and reduce the fabrication/assembly errors. In this chapter, some initial experiments have been conducted with whole system to provide an overview of the functioning of the integrated positioning system.

Chapter 6 provides a general conclusion and perspectives regarding the work presented in this manuscript.

The details regarding the published and presented papers can be found in Appendix-A.

Chapter 1

State of the art

This chapter provides the literature review in the field of the miniature multi-DOF positioning systems. Current design trends and different actuation technologies have been presented to realize these systems. Further, displacement sensors from their interaction and integration aspect have been discussed. At the end, a conclusion has been carried out based on the regarding actuation technique and displacement measurement sensors from their compactness and integration point of view.

1.1 Mechanical positioning system

Mechanical positioning systems are back-bone systems behind every object manipulation task. The functioning of these systems is based on the conversion of some form of input energy (mostly electrical) into the mechanical motion. One whole positioning system consists of single or multiple actuators, feedback sensors, mechanical platform, a central control unit and a power source (see figure 1.1). These components perform their respective functions to achieve positioning tasks in a workspace. Actuators are the components that convert input energy into specific tasks such as motion, force or a combination of both. Sensors are the components that measure a physical quantity (for example position, speed, force, etc.) and convert it into electrical signals that are interpreted by the central control unit. The central control unit analyzes the signal according to the desired inputs and generates respective electric signals to control the actuators. In addition, a power source delivers the input power to these components. The task of a mechanical structure is to provide a movable output platform and integrate the mobile parts of the sensors and actuators to guide their operation during motion.

In general, positioning systems are employed in different applications in order to gain high precision and automation in object handling/positioning tasks. For example, *in the semiconductor industries*, the production of Integrated Circuits (ICs) such as Microprocessors, etc., is carried out on a semiconducting material such as silicon, using a multiple-step

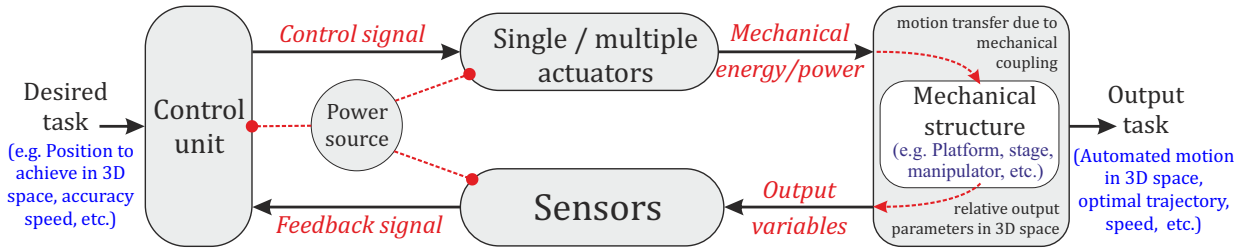

FIGURE 1.1: The schematic diagram of the functioning of a positioning system.

sequence of photolithographic and chemical processes. In photolithographic steps, micro or nano level geometric patterns are transferred from photo mask to silicon substrate (coated with light sensitive chemical "called photo resist"). High precision positioning systems are used to align silicon wafers with photo masks during a photolithographic process to ensure accurate transfer of geometric patterns.

In micromechanics field, micro mechanical parts (e.g. micro gears) are fabricated and assembled. Different fabrication approaches have been realized such as microfabrication (similar to the technology used in semiconductor industry), laser cutting, etc. Due to the small size, human precision is not sufficient to handle these delicate mechanical parts during manufacturing, assembly and inspection stages. In this scenario, positioning systems along with various tools are used to carefully manipulate these parts during manufacturing, assembly and inspection.

In biomedicine, often single or multiple biological cells are cultured and studied in response to certain medicine. These biological cell studies demand high resolution optical and positioning systems for culturing and inspection.

In contact surface metrology, surface parameters (e.g. roughness, flatness, etc.) measurement of micro components is often needed for their qualification. High resolution positioning stages are applied as scanning platform to handle the part under the scanning probe.

In early 90s, the researchers at the Mechanical Laboratory (MEL) in Japan have introduced the micro factory concept by developing a small fabrication unit (overall size $625\times490\times380$ mm^3) which consists of a micro turning machine, micro milling machine, micro drill machine, etc., [Okaz 04]. This concept could be employed as a solution to reduce the unit production cost of the miniature components. In such desktop factories the positioning of the components or raw material for machining can be realized with miniature positioning conveyors [Benc 06].

Apart from the application area, the main task of a positioning system can be recognized as object (e.g. part, raw material, etc.) conveyance, its manipulation or combination of both. In order to realize the above mentioned positioning tasks, conventional

macro application based positioning systems are not cost effective solutions. For example, in automated auto mobile industries, mechanical parts are fabricated on Computer Numerically Controlled (CNC) machines (e.g. milling, turning, drilling, machines, etc.). These machines are equipped with positioning stages to position the raw material in front of the cutting tool during the machining process. The integration of such sized positioning stages are inappropriate in micro applications and can lead to expensive, bulky overall systems. However, the miniaturization trend has introduced numerous technological solutions to realize down scale versions of these machines to make it compatible with the micro world. This chapter discusses these kinds of solutions into positioning systems used in the micro applications.

1.2 Innovation into the positioning systems

In order to realize Miniature Positioning System (MPS) designs, the choice of mechanical structure, drive technology, sensor integration and fabrication technology have been extensively studied. This section discusses the current developments in the positioning systems. The descriptions regarding innovation into the positioning systems are mostly taken from [Ahme 05, Benc 06, Wim 06, Ratc 06, Hell 09, Joub 12].

1.2.1 Mechanical design approach

The mechanical design of the positioning system is realized in either with serial or parallel kinematics (figure 1.2). In serial kinematics, multiple single DOF positioning actuators are assembled into a mechanical structure by stacking one after another. On the contrary, in parallel kinematics they are assembled into a mechanical structure in parallel configuration. [Benc 06].

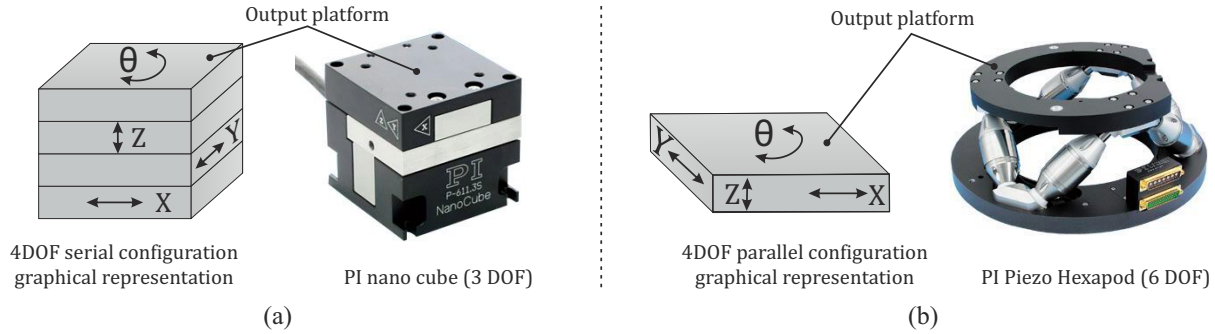

FIGURE 1.2: MPS mechanical design configuration (a) Serial kinematics (b) Parallel kinematics.

In micro applications, positioning systems realized with serial configuration provide large stroke (up to centimeters) as compared to parallel configuration, but they suffer from low stiffness, poor dynamics and large weight [Wim 06]. Moreover the first positioning device takes all the load of the rest of the devices and so on, which makes it

more sensible to uncertainties (e.g. vibrations, assembly errors, etc.) that lead to accumulation of precision errors. Despite having small stroke, parallel configuration based positioning systems does not suffer from the above mentioned problems [Ratc 06]. This makes parallel configuration a suitable candidate for the positioning systems used for micro application as the required maximum stroke size in these applications are up to few millimeters.

1.2.2 Motion drive technology

According to the literature, the motion drives can be classified into *Indirect drive technology* and *direct drive technology*. Indirect drive technology is based on the mechanical conversion of the rotary motion (often generated by the rotary motor) into linear motion [Ahme 05]. The positioning systems based on this technology have the driving part (i.e. actuator, motor) indirectly coupled with the driven part (i.e. stage or platform) via flexible or rigid mechanical coupling elements such as belts, lead screw, gear train, etc. Positioning systems based on indirect drive technology have high load driving capacity and simple control but they suffer from issues like backlash, low efficiency, low accuracy, etc.,[Ratc 06]. The problems like these are unacceptable, especially when the positioning systems are to be used for micro applications where high precision is one of the essential parameters.

The alternate solution is direct drive technology in which the motion generated by motors is directly transmitted to the driven part [Joub 12]. These drives eliminate the need of the mechanical coupling elements thus making them more compact and suitable for micro applications demanding high precision and accuracy [Hell 09]. Moreover, a direct drive solution reduces the number of components, simplifies assembly and thus reduces the overall cost of the positioning system.

1.2.3 Sensor interaction and integration approach

A sensor is a device that when exposed to a physical phenomenon (temperature, displacement, force, etc.) produces an output signal (electrical, mechanical, magnetic, etc.),[Bish 08]. Positioning measurement sensors can be classified into contact sensors and non-contact sensors based on their interaction with a physical system. Contact sensors need physical contact with the object being sensed. A potentiometer is one of the examples of such sensors. This type of the position sensor often proves to be the simplest, low cost solution in applications where contact with the target is acceptable,[Wils 05]. However, in micro manipulation tasks, contact type sensors can deteriorate the functioning of the positioning systems or vice versa. The most effective choice for these systems is non-contact type sensors. These sensors do not need a physical contact to perform their

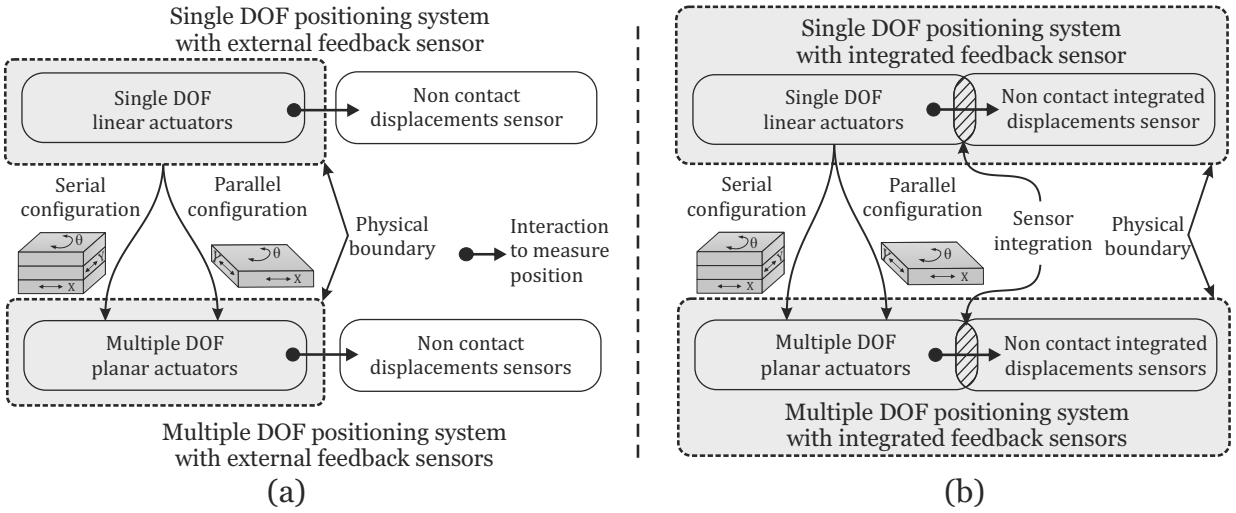

FIGURE 1.3: Construction of (a) non-integrated (b) integrated positioning systems.

respective position sensing task. CCD Cameras, capacitive sensors and light detecting sensors are few of the examples of non-contact sensors.

Modern positioning system designs are either integrated or non-integrated with the non-contact displacement measurement sensors. In non-integrated approach the displacement sensors are outside of the physical boundary of the positioning system (figure 1.3(a)). The main reason is that the dimensions of the sensor are too big to be accommodated into the positioning system. For example, a high resolution camera can be used as a sensor to measure the displacement via image processing technique, but its volumetric size is too big to be integrated in the MPS. On the other hand, in integrated approach the sensors are installed inside the physical boundary of the positioning system (figure 1.3(b)). This approach involves fusion of complete sensor or sensor part directly into the positioning systems. The integrated approach demands miniaturization of sensor dimensions so that it could be easily accommodated within the geometrical dimensions of the MPS. Microfabricated MPS are often integrated with sensors to achieve monolithic and compact designs.

1.3 Miniature positioning system actuation technologies

The most common MPS actuation technologies are based on the use of active material or the field interaction technique. The first trend is to utilize the physical deformation characteristics of an active material (mostly a smart material) for the actuation purpose. The second approach involves the interaction of the electric and/or magnetic field to realize actuation forces. In micro applications, these trends can be classified with respect to different actuation principles. According to the literature review, the most common actuation principles adapted to realize multi-DOF MPSs are:

- Actuation principles based on the smart materials
- Thermal actuation principle
- Pneumatic actuation principle
- Electrostatic actuation principle
- Electromagnetic actuation principle

1.3.1 Actuation principles based on the smart materials

Smart material is a material that has one or more properties that can be significantly changed in a controlled fashion by external stimuli, such as stress, electric or magnetic fields, temperature. PZT (Lead zirconate titanate), Terfenol-D, Nickel-titanium alloys are some of the examples of such materials that results in piezoelectric actuators, magnetostrictive actuators and Shape Memory Alloy (SMA) actuators,respectively. Currently, PZT material is widely used for actuation purpose in MPS designs due to its instant response and high energy conversion efficiency.

1.3.1.1 Mechanically Amplified Piezoelectric Actuators (MAPA)

The principle of piezoelectric actuator is based on piezoelectricity phenomenon. It was first discovered in quartz by Jacques and Pierre Curie in 1880, [Beeb 04]. Piezoelectricity is the ability of some materials (notably crystals, certain ceramics, and biological matter, such as bone, DNA, and various proteins) to generate a difference of electric potential in response to the applied mechanical stress (figure 1.4(a)). The effect is closely related to the appearance of an electric dipole density within the material's volume. An applied stress induces charge surface densities on the electrodes deposited onto the piezoelectric material. The piezoelectric effect is reversible, such as under the applied difference of electric potential, the production of stress and/or strain can be observed. This inverse piezo-effect can be utilized for actuation (figure 1.4(b)).

Piezoelectric actuators are usually formed by stacking multiple piezoceramic materials (figure 1.4 (c)). This formation increases the displacement capacity of the actuator

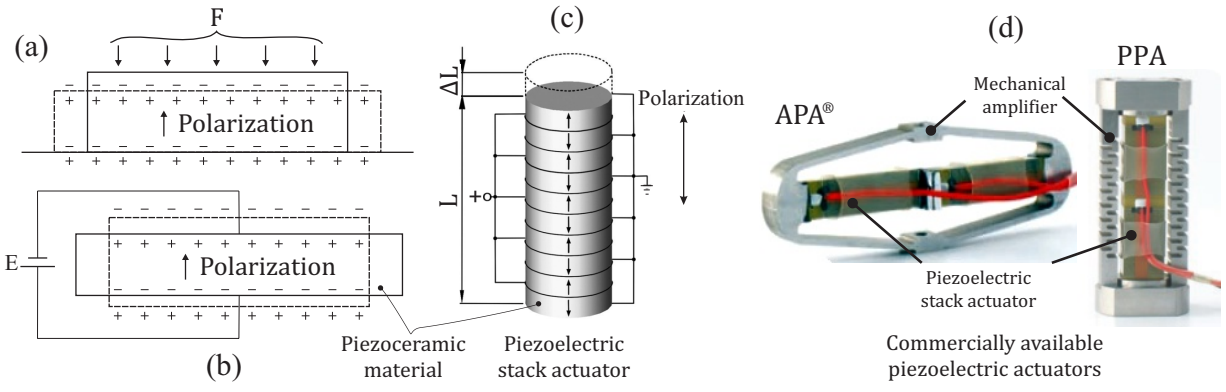

FIGURE 1.4: (a) Direct and (b) Converse piezoelectric effect [Bish 08] (c) Piezoelectric stack actuator [PI 12] (d) APA® and PPA, Courtesy of CEDRAT technologies.

due to the accumulated displacement of all the piezoceramic materials, [PI 12]. These actuators can directly be used to realize multi-DOF MPSs, but they have very small stroke (usually around 100 μm). In order to increase the working stroke, piezoelectric actuators are used with mechanical amplification mechanisms [Cart 11]. Numerous mechanical amplification mechanisms have been developed for positioning stages.

CEDRAT technologies have developed Amplified Piezoelectric Actuators (APA®) and Parallel Pre-stressed Actuators (PPA) (figure 1.4 (d)). They are solid state long-stroke linear actuators that use an external deformable frame to pre-stress the piezo stacked ceramics. The expansion of the active material with amplification mechanism results in 1 mm displacement. Based on this principle, they have developed a compact positioning stage for the fiber positioning and micro scanning applications (figure 1.5(a)). In order to measure the displacement, strain gauge type displacement sensors are integrated in the design. Moreover, the MPS offers a maximum displacement of 25 μm in *xy*-plane with 0.2 nm resolution in closed loop [Cedr 11].

Sabri *et al.*, have developed an integrated Si-PZT hybrid *xy*-stage (figure 1.5(b)). The device consists of two PZT actuators with silicon based moonie amplification mechanism[1] to amplify the work range in *xy*-plane. The micro stage was micro fabricated using Deep Reactive Ion Etching (DRIE) technique and offers a maximum displacement of 80$\times$60 μm^2 in *xy*-plane. An integrated micro fabricated capacitive sensor was used to measure the displacement of the micro stage.

Physik Instrumente[2] has developed a parallel kinematic based PIMars XYZ Piezo Nano MPS with direct PZT stack actuator for nano applications (figure 1.5(c)). The positioning system has a mechanically amplified work range of 300$\times$300$\times$300 μm^3. The device is able to perform motion in *xy*-plane and offers *z*-axis vertical motion with pitch and yaw functions. In addition, the device is integrated with capacitive sensor having a resolution of 1 nm to measure the displacement [PI 12].

1.3.1.2 Stepping mode actuators

Another method to increase the work stroke in MPS is to use the actuators based on step mode operation. The actuation principle of the stepping mode actuators is an inspiration taken from the movement of some earthworms.

Inchworm actuator: The simplest linear inchworm actuator design comprises of three independently driven actuators. Piezoelectric ceramics and magnetostrictive materials are the most common active material used in these actuators. These materials can be configured in different ways, but the most typical one is depicted in figure 1.6(a) using

[1]The authors have measured the change in displacement using moonie angle (θ_{max} = 2°) of the amplification structure [Sabr 09].

[2]http://www.physikinstrumente.com

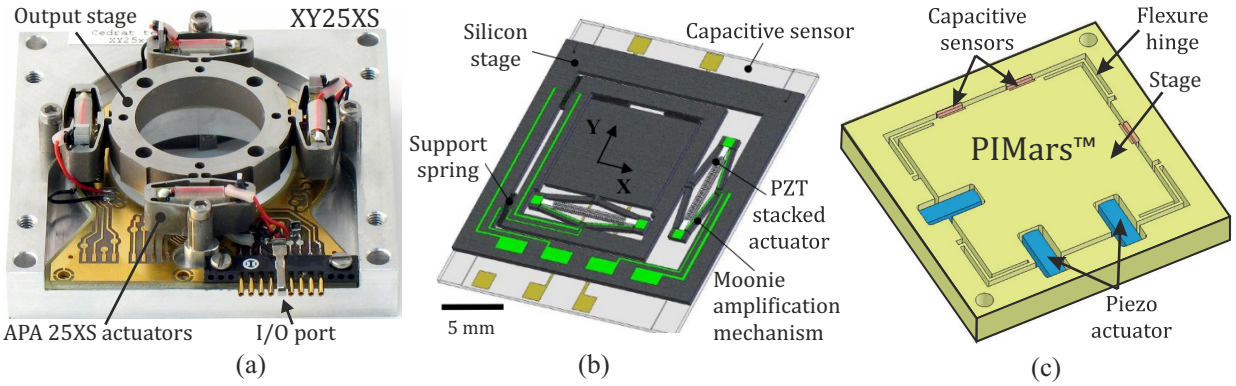

FIGURE 1.5: (a) *xy* stage [Cedr 11] (b) Silicon *xy* micro stage [Sabr 09] (c) PIMars™ [PI 12]

Piezo Ceramics (PC). In this configuration, PC_1 and PC_3 are actuated to achieve fixation during motion and PC_2 is actuated along motion direction to realize "Δx" displacement. The functioning of an inchworm actuator is presented in figure 1.6(a). The repetitive operation of the three piezo ceramics PC_1, PC_2, PC_3 is used to achieve linear displacement.

Inchworm actuators are capable to deliver unlimited strokes which depend on the length of the rotor plane but they are slow in nature and their operating frequency bandwidth is not more than a few tens of hertz [Pons 05]. They are mostly employed in the single DOF positioning devices due to their operation. However, Wu *et al.*, have developed a compact planar micro-robot for micro conveyance (figure 1.6(b)). Their design consist of a novel type of $XY\theta$ mechanism and a single piezo actuator employed with flexures. The overall size of the robot is 20×20×12 mm^3 and it provides an average 14 μm/step along x- and y-axes and 27 arcsec/step of displacement resolution.

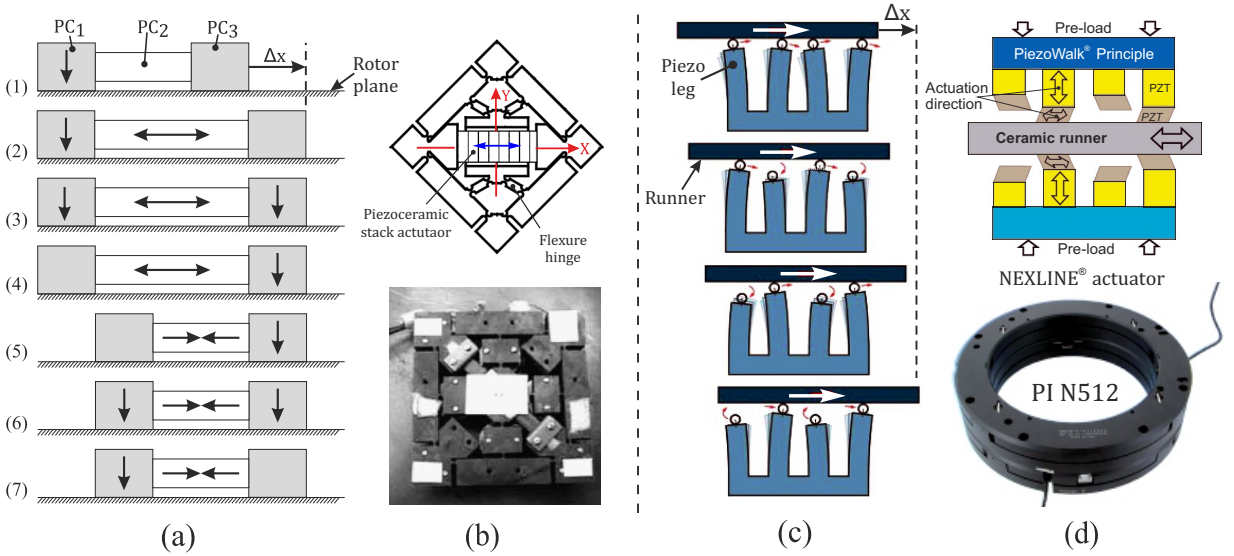

FIGURE 1.6: (a) Inchworm actuator principle [Benc 06] (b) Micro robot developed by Wu *et al.*, [Wu 04] (c) PiezoWalk drive principle [PI 12](d) NEXLINE® actuator and N-512 Positioning stage [PI 12]

PiezoWalk drives: These drives consist of piezo legs, that are actuated in multi-steps. The piezo legs are piezoceramic shear modules that contract to release the rotor, and then deforms to achieve next step. The continuous operation of each piezo leg displace the rotor. The operation of these actuators are presented in figure 1.6 (c).

Physik Instrumente has developed a NEXLINE® actuator. The actuator consists of a runner and two piezoWalk drive modules (see figure 1.6 (d)). The continuous operation of these drive modules displaces the rotor along motion direction. This technology has been used to realize a nano positioning system PI N-512 as shown in figure 1.6(d). The positioning system provides 6×6 mm travel in a plane with 10 nm resolution. The dimensions of the system is not provided.

Stick-slip actuator: The functioning of stick-slip actuator mainly consists of two steps. In first step, a slow expansion of the Piezo Actuator (PA) moves the load along the actuation direction using the driving object that is fixed to the PA (figure 1.7(a)). Due to the static friction between the slider and the driving object a stick effect appears that holds the driving object and load together. In second step, a rapid contraction of the PA slides the driving object towards its initial position. Due to the rapid contraction, the inertial force due to the mass of slider dominates the static friction forces between slider and driving object (slip effect). With the assumption of no friction loss, this effect results in the final displacement "Δx ".

Based on this principle, A. Bergander has developed an *xy*-stage using four hemispheric beads that result in point contact between the mobile part and driving object (figure 1.7(b)). The rapid/slow deformation of the active materials along an axis results in a linear motion. The prototype provides a displacement of 2 mm×2 mm in *xy*-plane. The author has not disclosed further information regarding the prototype.

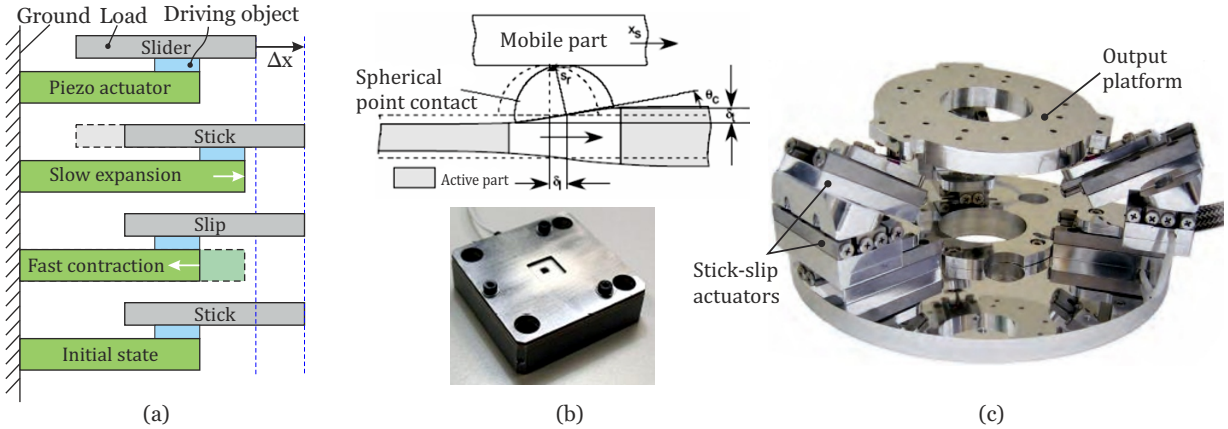

FIGURE 1.7: (a) Stick-slip actuator principle (b) [Berg 03] (c) "SMARPOD" [Smar 11]

SmarAct[3] have developed a long travel range integrated MPS "SMARPOD" for micro

[3]http://www.smaract.de

applications. The MPS has been realized with inclined assembly of stick-slip actuators as shown in figure 1.7(c). In this configuration, the weight of the output platform has been utilized for sticking effect during motion. It is able to perform motion at maximum velocity of 10 mm/s and delivers a maximum linear (rotational) stroke of 20 mm (35°) with a resolution of 1 nm (1 μrad), respectively. Moreover the MPS has been integrated with micro encoders for displacement measurement.

Friction-inertia drives: The operating principle of these drives are based on the reaction caused when a mass is accelerated. The functioning of these actuators is similar in concept as of stick-slip actuators. However, these actuators use the inertial force for the actuation purpose. A slow expansion of active material, such as piezoceramic, drags the inertial mass to be moved relative to the ground, while ensures the adhesion of the load with the ground. The rapid contractions accelerate the inertial load towards each other. In this scenario, the inertial force dominates the adhesion forces thus allowing the load to move "Δx" as shown in figure 1.8(a). The movement can be realized in both directions by reversing the rate of deformation phase (expansion/contraction) of the active material. The design of inertial actuators is limited by the use of active materials with low response time to generate rapid acceleration in deformations [Breg 98].

Zesch *et al.*, have developed a 3DOF motion system called "Abalone" (figure 1.8(b)). It has been realized with three friction-inertia drives to perform motion with unlimited strokes within a theoretically infinite horizontal workspace. In the stepping mode, the maximum speed of 1 mm/s in translation and 7 deg/s in rotation was achieved. In the local range of the 6 mm travel the authors have reported a displacement resolution better than 10 nm.

In another study, Nomura *et al.*, developed an $XY\theta$ inertial driven micro robot based on the principle described early in this section (see figure 1.8(c)). It integrates four PAs connected with the main object and the counter object. When two parallel sets of PAs are activated in the opposite manner, such as, one expanding but the other contracting, the

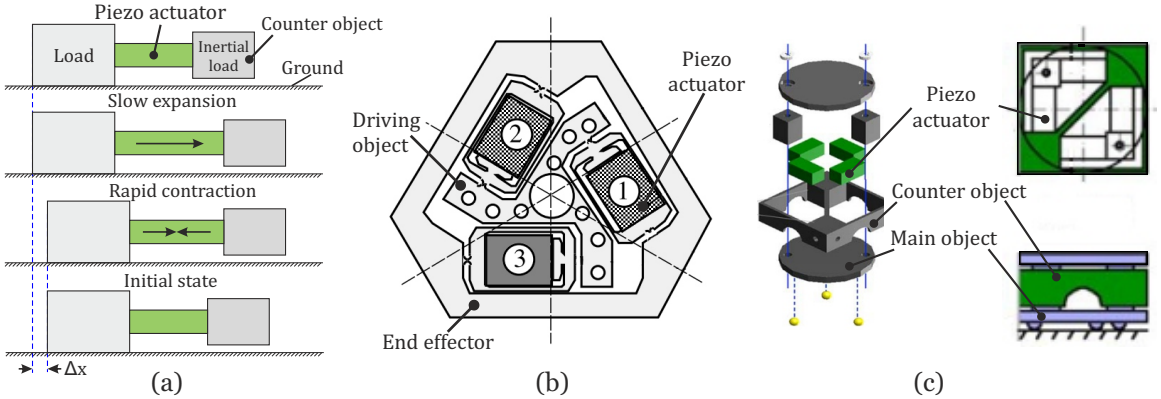

FIGURE 1.8: (a) Friction-inertia drive principle (b) “Abalone” [Zesc 95] (c) [Nomu 07]

inertial drive actuator will travel along one direction. When the other two are activated in an opposite manner, the inertial drive actuator will travel towards another direction. If either pair of PAs in a parallel position is activated in the same manner, the inertial drive actuator will rotate. The robot is compact in design and provides a displacement resolution of 17 nm with a maximum travel speed of 1 mm/s.

1.3.1.3 Ultrasonic linear motors

Ultrasonic motors utilize the vibration of the elastic body (stator) in the ultrasonic frequency band and the reverse piezoelectric effect of the piezoceramic materials [Zhao 11]. These motors have two energy conversion processes. The first process converts electrical energy into mechanical energy using reverse piezoelectric effect. The second process changes vibration of the stator into macro one direction movement of the slider due to the friction between the elastic body and slider (figure 1.9(a)). For optimal operation, the slider and elastic body must be maintained in contact at all times. The most common technique is to use the weight of the slider to ensure permanent contact.

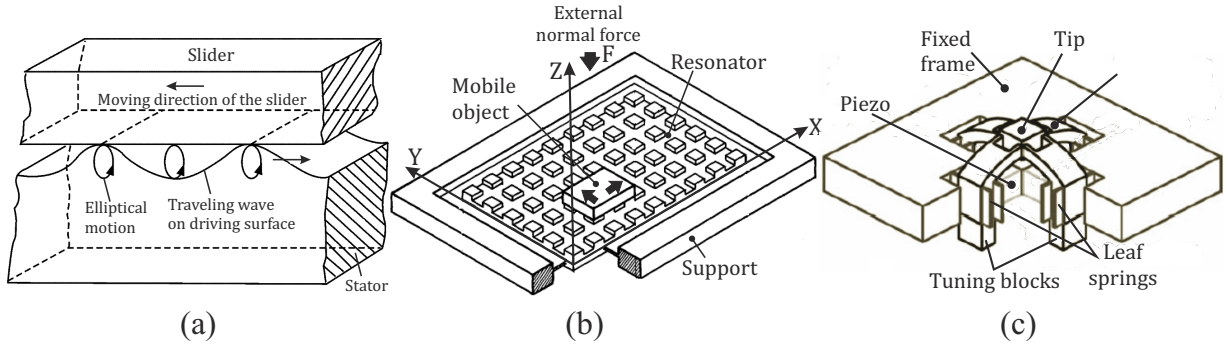

FIGURE 1.9: (a) Ultrasonic linear motor principle (b) [Mino 96] (c) [Devo 04]

In general, these motors have been adapted for planar applications in two different manners. The first approach is to use a deformable membrane excited by reverse piezoelectric effect. Minotti *et al.*, have used this solution as shown in figure 1.9(b). Their design consists of a piezoceramic material based membrane (*Resonator*) which is polarized perpendicular to the motion plane (i.e. along z-axis). The motion forces in xy-plane are achieved by generating stationary standing waves by polarizing the resonator with out-of-phase voltage. The pads situated directly on the resonator create a frictional contact between mobile object and the pad surface which transmit the force to move the mobile object. The weight of the mobile object is used to maintain the contact with the resonator [Mino 96].

The second approach is to assemble multiple ultrasonic linear motors to realize a multi-DOF positioning system. Devos *et al.*, have developed a xy-planar drive based on this approach that combines the fast positioning capability of the resonant motors for

fine positioning in the nanometer range [Devo 04]. A pair of piezoelectric actuators is assembled to a pair of tuning blocks along each axis (figure 1.9(d)). These tuning blocks are in contact with the cube and acts as deformable legs. Upon excitation, each pair of legs describe an elliptical trajectory in the plane corresponding to the excited pair, thus realizing a planar motion of the cube in *xy*-plane. A maximum speed of 60 mm/s speed under no load conditions was reported by the authors.

1.3.2 Thermal actuation principle

Thermal actuators are based on the thermal expansion of materials (mostly solids) when subjected to a heating source. In MPS designs, thermal expansion/contraction of the material are carried out based on resistive heating technique. It involves the utilization of the current carrying coil wrapped around or embedded in the material to generate heat based on joule heating effect. Bimetal and bimorph type configurations are more commonly adapted to realize linear actuation. In bimetal, two same sized metals but having different coefficient of thermal expansion are assembled together (figure 1.10(a)). Upon resistive heating, the material with higher value of coefficient of thermal expansion will expand more with respect to other which results in motion.

Similarly, a bimorph consists of two metallic arms (referred as hot and cold arms) fabricated in the same material (figure 1.10 (b)). In this configuration the cross section of the hot arm is smaller than the cold arm. when current is injected in the bimorph, the hot arm will expand more due to smaller cross section relative to the cold arm. Due to the difference in volumetric expansion an actuation can be realized. Figure 1.10(c) represents another approach to realize linear motion by means of applying fixed constraints. In this approach the expansion legs have same cross section and material. When heated, the expansion legs will experience change in dimensions. In order to compensate the change in length due to temperature rise, an in-plane deformation will be realized by the expansion legs which will move the translating shuttle.

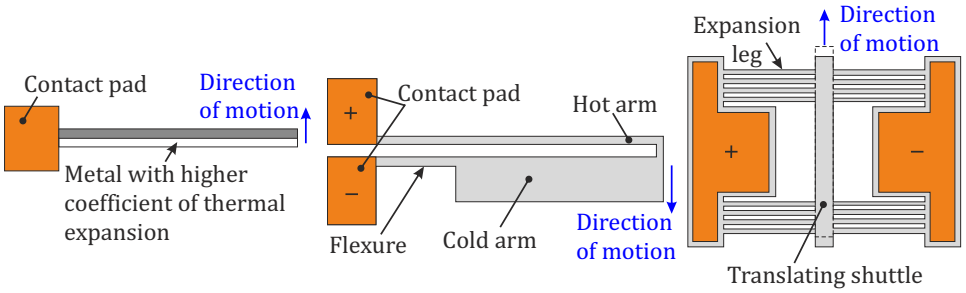

FIGURE 1.10: Thermal actuator principle (a) bimetal (b) bimorphe (c) Geometrically constrained single metal based actuator

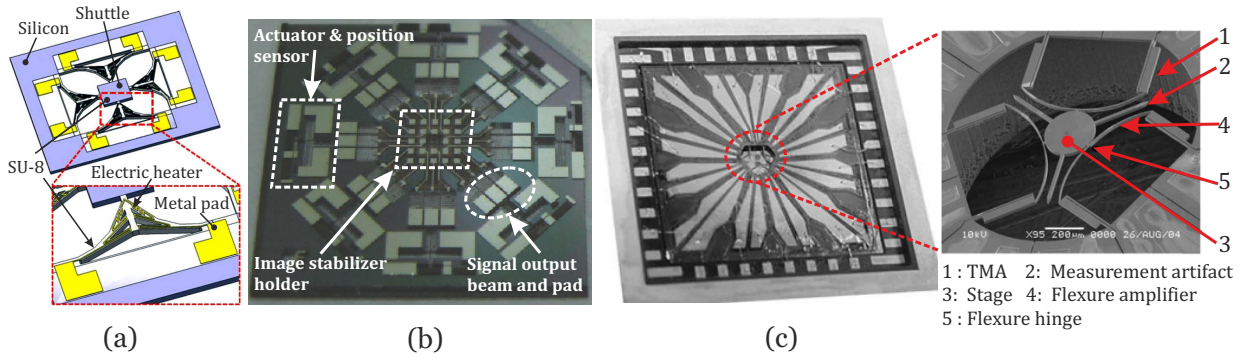

FIGURE 1.11: MEMS based *xy*-stages (a) [Lee 09] (b) [Lin 11] (c) μHexFlex [Culp 06]

Thermal actuators exhibit strong forces but the main drawbacks include their temperature dependency and control difficulties which limits their application to MEMS based MPS in order to optimize required input energy for actuation. Lee *et al.*, have developed a novel micro *xy*-stage with SU-8 based polymer actuator based on thermal actuation principle. The stage can deliver a maximum 41 μm displacement stroke at 250°C. The monolithic design consists of a sandwich structure integrated with the metal heating coils in between two layers of SU-8 material (figure 1.11(a)). The device carries a 0.5×0.5 mm^2 shuttle [Lee 09]. In another study, Lin *et al.*, have used constrained type (see figure 1.10(c)) design approach to realize a 4-axis *xy*-micro stage to resolve anti-shaking problem of an image sensor. The stage was micro fabricated using Inductively Coupled Plasma (ICP) etching process (figure 1.11(b)).

Based on bimorph , C.S.Chen and M.L.Culpepper have developed a small-scale nano-positioner (μHexFlex, see figure 1.12). It consists of six-axis compliant mechanism and three pairs of two-axis thermo-mechanical micro-actuators. A Φ3 mm diameter prototype provides a maximum range of 8.4×12.8×8.8 μm^3 and 19.2 ×17.5 ×33.2 mrad^3. The displacement resolution of the device has been measured at 1Å. The device was created using Deep Reactive Ion Etching (DRIE) technique [Culp 06].

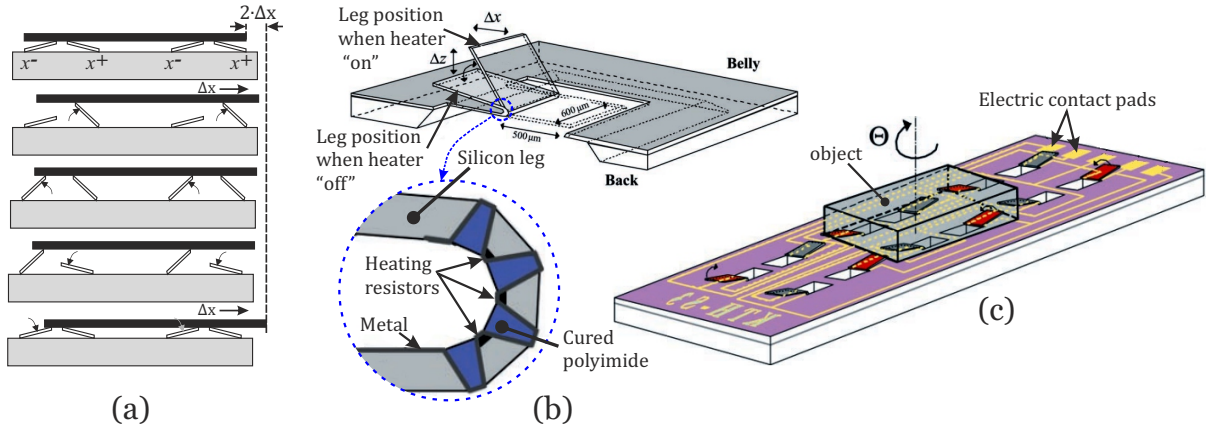

FIGURE 1.12: (a) Actuation principle (b) Single silicon leg (c) Micro conveyor [Ebef 00]

Ebefors *et al.*, have constructed a micro conveyance system based on arrays of movable robust silicon legs. Figure 1.12(a) represents the step by step actuation technique proposed by authors for moving a flat abject in the horizontal plane. The conveyance system is realized with curved polyimide joint (figure 1.12(b)). These joints deform when electrically heated, which create "Δz" and "Δx" displacement. When the heating is turned off the polyamide joint returns to its original position. Based on this actuation concept, the authors developed a platform composed of several polyamide actuators using heating resistors [Ebef 00]. The fabricated conveyor (see figure 1.12(c)) consists of a 15×15 mm^2 chip having 12 silicon legs to move a flat object at millimeter range. It can perform translational and rotational motion in horizontal plane. The maximum conveyance velocity of 12 mm/sec has been reported by the authors.

1.3.3 Pneumatic actuation principle

Positioning systems based on pneumatic actuation method utilize the pressure of the compressed gas (i.e. air, nitrogen, etc.) injected via small inlets (called *nozzles*, see figure 1.13(a)) to move and levitate the object at the same time. One of the methods to generate an air-flow is by using several nozzles fabricated into a flat mechanical structure. The inlets of the nozzles are controlled using pneumatic valves. The direction of motion can be achieved by systematic operation of these pneumatic valves. Pneumatic actuation technique is commonly adapted for small size and lightweight object conveyance. This technology results in cleaner, non flammable and low cost object conveyance systems.

Based on this principle, Chapuis *et al.*, have developed a distributed conveyance system to move light objects. The system is constructed with 560 MEMS actuators in a 35 mm$\times$35 mm conveyance area. The functioning of a single nozzle to levitate and move the object is shown in figure 1.13(a). The inlet of the nozzle is controlled by using beam electrode. When right side beam electrode is turned "ON", the float moves toward right

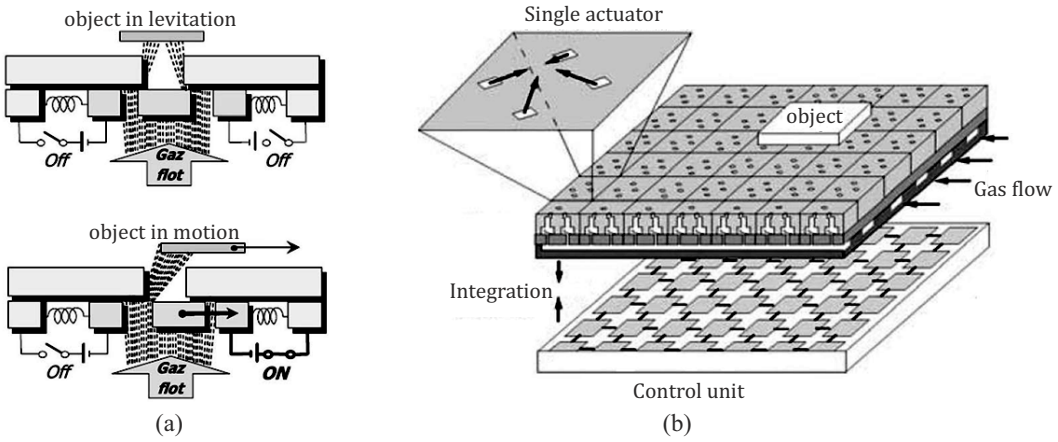

FIGURE 1.13: Distributed conveyance system [Chap 04] (a) Object in levitation and motion states (b) MEMS actuators assembly

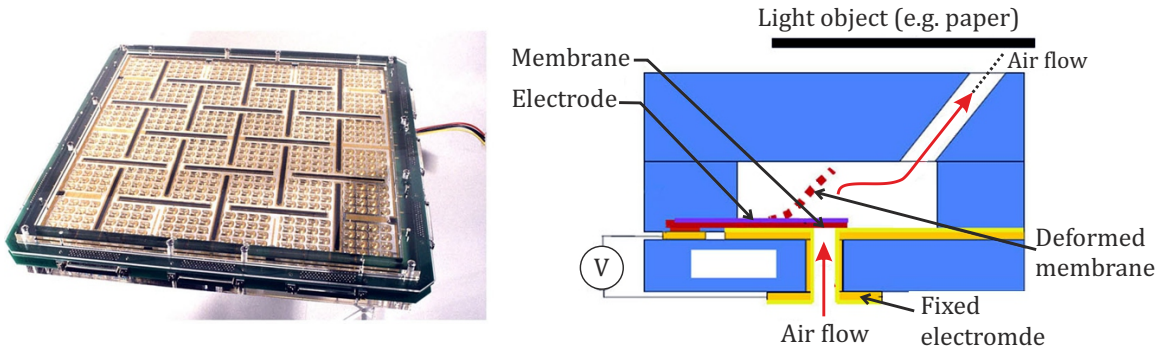

FIGURE 1.14: Light weight object handling table [Berl 00] (a) Experimental prototype (b) Schematic of a single pneumatic actuator

which allows the gas to flow from left side of the float through nozzle creating a right ward thrust on the object. The various parts of the conveyer are shown in figure 1.13(b). The basic cell size in the micro fabricated conveyance system is 1×1 mm^2 and the size of the nozzle is 165×590 μm^2. The system utilizes nitrogen gas at 17 kPa and can carry up to 4 mg weight. The conveyance system developed by Chapuis *et al.*, is based on digital actuation concept however the levitation position and motion speed can be set by controlling the pressure of the inlet gas.

Berlin *et al.*, have developed an active surface based flexible object integrated handling system (figure 1.14(a)). 1152 MEMS based arrays of air valves and sensors located in 30.5 cm$\times$30.5 cm overall dimensions are used to levitate and control the motion of a flexible planar object, such as a sheet of paper without any contact. Each air valve is a tilted air jet module that acts as a pneumatic actuator (figure 1.14(b)). The airflow is controlled by a membrane that is deformed electrostatically. An experimental device has been manufactured and tested to validate the principle of this movement.

Delettre *et al.*, have developed a new contactless conveyor system for handling clean and delicate products using induced air flows (figure 1.15). The object is moved indirectly

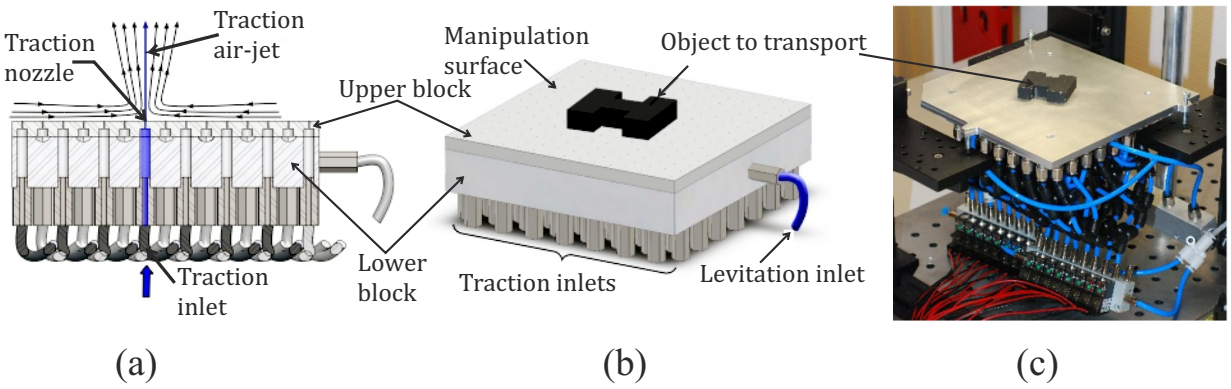

FIGURE 1.15: Conveyor system developed by A.Delettre *et al.*, [Dele 11] (a) Sectioned view (b) Global view (c) Experimental prototype

by an air flow which is induced by strong vertical air jets. The induced air flow square surface is of 120 mm×120 mm in dimensions. The system consists of an upper block having an array of 15×15, 0.4 mm drilled holes (nozzles) and a lower block with 112 drilled holes in staggered rows. These holes are connected to two independent air inlets. The network of holes creates the air cushion under the object to levitate and move in a plane.

1.3.4 Electrostatic actuation principle

Electrostatic actuators are based on the well known Coulomb law, which was reported in 1780. In these actuators, electrostatic charge arises from a build up or deficit of free electrons in a material, which can exert an attractive or repulsive force on oppositely or similarly charged objects respectively [Beeb 04]. The simplest design of these actuator consists of two facing surfaces called electrodes (figure 1.16(a)). The force is derived from the gradient of the electrostatic potential between the two electrodes.

Electrostatic actuators provide contact less actuation but the main drawback of these actuators is their dependency on the electrode facing surface area and the air gap in-between. This deeply effects the work range of these actuators which restrict their application in micromechanical positioning system designs [Benc 06].

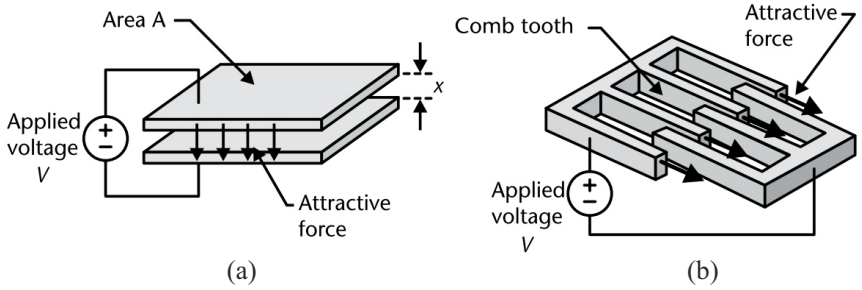

FIGURE 1.16: Principle (a) Parallel-plate electrostatic actuator (b) An electrostatic comb actuator, [Malu 04]

Comb drive actuator is one of the most adapted actuator in positioning systems based on electrostatic actuation principle (see figure 1.16(b)). It consists of a comb shaped mobile and fixed part. When an electric potential is applied, an opposite charge appears along the comb teethes of the fixed and the mobile part facing each other. This generate attractive force which results in a linear motion of the mobile part. Comb drive actuators are compact and provide controllable precise positioning [Sun 08]. In multi-DOF positioning systems, two or more comb drive actuators are generally fabricated or assembled together to achieve compact designs.

Liu *et al.* [Liu 07], have developed a 3DOF based nanopositioing stage (figure 1.17(a)). It was micro fabricated using DRIE technology in a 500 μm thick Pyrex substrate. Four orthogonally arranged comb drive actuators have been used to actuate a 1×1 mm^2 center

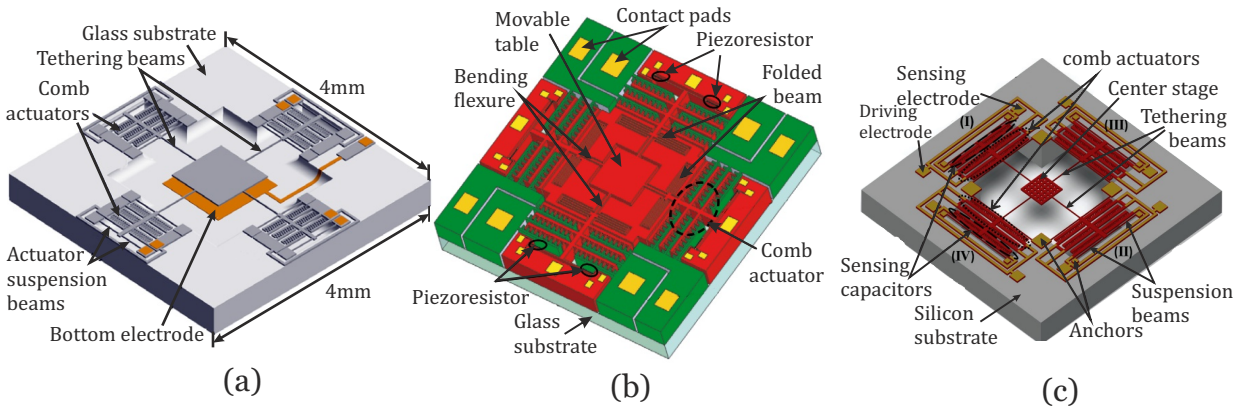

FIGURE 1.17: MEMS micro stages (a) Liu *et al.*, [Liu 07] (b) Sun *et al.*, [Sun 08] (c) Ji *et al.*, [Ji 10]

stage in *xy*-plane. A displacement of ± 12.5 μm was reported by the authors. In addition, a bottom electrode of 1 mm^2 was fabricated under the center stage. The bottom electrode and center stage acts as parallel-plate actuator. By this means Liu *et al.*, have realized a 3.5 μm displacement in z-axis. The open loop repeatability of the stage was reported to be 17.3 nm along all three axes. External optical microscope with a digital camera (resolution: 2.58 nm) and an optical interferometer (resolution: 7.1 nm) was used to measure planar and vertical displacement, respectively. The device is compact in nature but due to its small size it does not integrate the positioning measurement sensors.

Similar kind of design has been proposed by Sun *et al.*, [Sun 08]. They have developed an integrated micro *xy*-stage with a 2×2 mm^2 movable table (figure 1.17(b)). The stage is integrated with displacement measurement sensors. They have used double-sided bulk-micromachining technology to fabricate their stage. The micro device is composed of four comb actuators and piezoresistors with a full Wheatstone bridge circuit that is used for displacement measurement. The integrated micro stage is able to deliver a ± 10 μm displacement along a single a axis.

Ji *et al.*[Ji 10], have developed a micro positioner (figure 1.17(c)) for nano applications. The device is integrated with four orthogonally arranged comb-drive actuators and capacitive sensors to measure in-plane displacement. The actuation force from comb actuators is transmitted to the 520×520 μm^2 center stage through 700 μm long tethering beams. The positioner has a average range from ± 6.64 μm.

Takahashi *et al.*[Taka 07], have developed an *xy*-stage mechanism for the 2D lens scanner based on electrostatic actuation principle (figure 1.18(a)). The stage has a small footprint (2×2 mm^2) compared with an integrated silicon lens (dia 1 mm). The overall device is dual layer design utilizing comb actuators with a double-gimbal structure to perform 2D motion. It was fabricated in silicon-on-insulator (SOI) and offers a maximum lateral displacement of 19 μm in the x-directions and 23 μm in the y-directions.

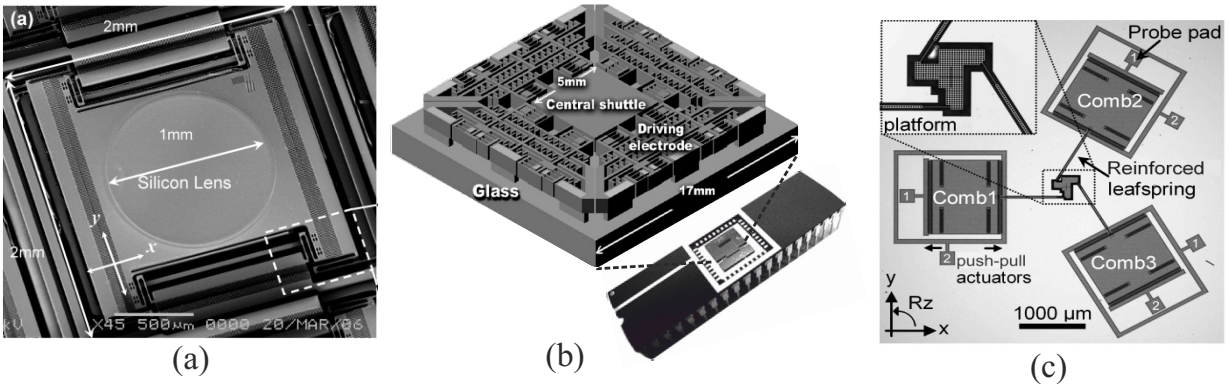

FIGURE 1.18: (a) Takahashi *et al.*, [Taka 07](b) Kim *et al.*, [Kim 03] (c) Ultra small 3DOF manipulator developed by Boudewijn de Jong [Jong 06]

For data storage applications, Kim *et al.*[Kim 03], have developed a small device that consists of a 5×5 mm^2 shuttle area (figure 1.18(b)). A 3×3 mm^2 mirror plate was integrated in order to measure in-plane static displacement by non contact laser displacement sensor. The positioning range of the stage at 0.1 Hz was measured to be 36×36 μm^2. However, at 140 Hz the micro stage could deliver a maximum stroke of 50 μm in *xy*-plane. The overall dimension of the micro stage is 17×17 mm^2. A packaged Integrated Circuit (IC) was made for installation purposes in data storage devices.

Boudewijn de Jong [Jong 06], has developed an ultra small planar 3DOF based parallel kinematic manipulator micro fabricated in single-crystalline silicon wafer (figure 1.18(c)). The purpose of this manipulator is to provide accurate and stable positioning of a small sample (10×20×0.2 μm^3) in nano applications. Three comb actuators (arranged at 120°) are used to actuate a triangular platform over ±10 μm stroke in the *x*- and *y*-directions with a maximum rotation of ±2 μm. The displacement measurement was carried out using image-processing technique by taking a set of pictures and counting the pixel resolutions.

1.3.5 Electromagnetic actuation principle

Electromagnetic actuation principle is based on the appearance of the electromagnetic force exerted on an electrically charged particle moving in the presence of a magnetic field. The main advantages of actuators based on this principle include, hight speed, fast response, simple design and low cost. In multi-DOF MPS designs, one of the major problems is the appearance of frictional forces due to the mechanical contact between mobile and fixed part of the MPS. One of the ways to reduce/eliminate this problem is by levitating the mobile part using pneumatic drives (see section 1.3.3). However, electromagnetic actuators can offer both translation and levitation in a single module, thus making them a fruitful choice. The actuators realized with electromagnetic principle

can be classified into three types based on the generation of the electromagnetic forces. The description regarding these forces is mostly taken from [Mole 00, Furl 01, Benc 06].

1.3.5.1 Linear Induction Actuator (LIA)

The working principle of the LIA is based on the generation of the induction force. When a conductive plane is exposed to a magnetic field, currents are induced in it according to the Faraday's law. The interaction between the induced currents (which lead to secondary magnetic field according to Lenz's law) and the magnetic field leads to induction forces. A typical configuration of a LIA consists of a movable slider with conductor windings, a fixed stator and a conducting material as shown in figure 1.19(a).

LIAs possess high temperature bearing capability and deliver extremely high speeds. However, they are mostly applied in application-specific drives such as compressors, pumps, etc., due some drawbacks. These include force-ripple effect, acoustic noise, high power consumption due to absence of permanent magnets [Mole 00].

In mechatronics field, LIAs are often used to construct multi-DOF planar motors for small object conveyance. For example, Dittrich *et al.*, have developed an integrated planar motor for heavy miniature component conveyance (figure 1.19(b)). Four orthogonally arranged LIAs were used to realize 3DOF motion on a copper sheet. In order to compensate the weight of the planar motor (2.5 kg), air bearings have been used (details not provided). The planar actuator is able to carry 21.5 N load at maximum speed of 0.36 mm/s and is integrated with two optical sensors (resolution 63.5 μm). Similar approach have led Kumagai *et al.*, to develop their 3DOF based planar actuator (figure 1.19(c)). They have used three LIAs in delta (Δ) configuration. The core of the planar actuator was realized with 100 magnetic steel sheets resulting in a 4.8 kg total mass. The planar actuator travels over a 1.5 mm copper sheet and offers a payload capacity of 60 N with a maximum 12 m/s^2 acceleration. Three laser sensors were integrated in the planar actuator to provide displacement parameters (details not provided).

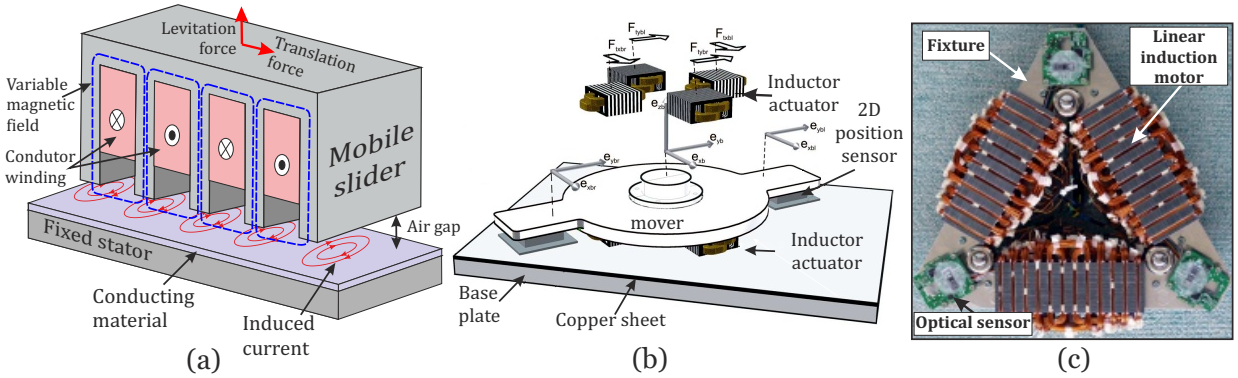

FIGURE 1.19: (a) LIA principle (b) Dittrich *et al.*, [Ditt 06] (c) Kumagai *et al.*, [Kuma 12]

In order to achieve levitation of the heavy mobile part in compact MPS designs LIA's based levitation solution is often preferred over pneumatic leviation technique due to their compactness. One of such solution was adapted by Jung *et al.*, in their MPS design as shown in figure 1.20(a). The 3DOF MPS proposed by authors was designed for a maximum travel range of ± 15 mm in xy-plane and ± 1 mm in z-axis. The translation (based on EMAs (see section 1.3.5.3)) and levitation (based on LIAs) motion are carried out with independent solutions but the decoupling between the motion axes and the levitation axes was not obtained. Later in 2010, Jung *et al.*, have developed a contact-free planar stage based on LIAs (figure 1.20(b)). In this design, the authors have employed air bearings to levitate the mobile platform of the planar stage. The system was integrated with capacitive sensor and it offers a working range of 10 mm$\times$10 mm in a plane.

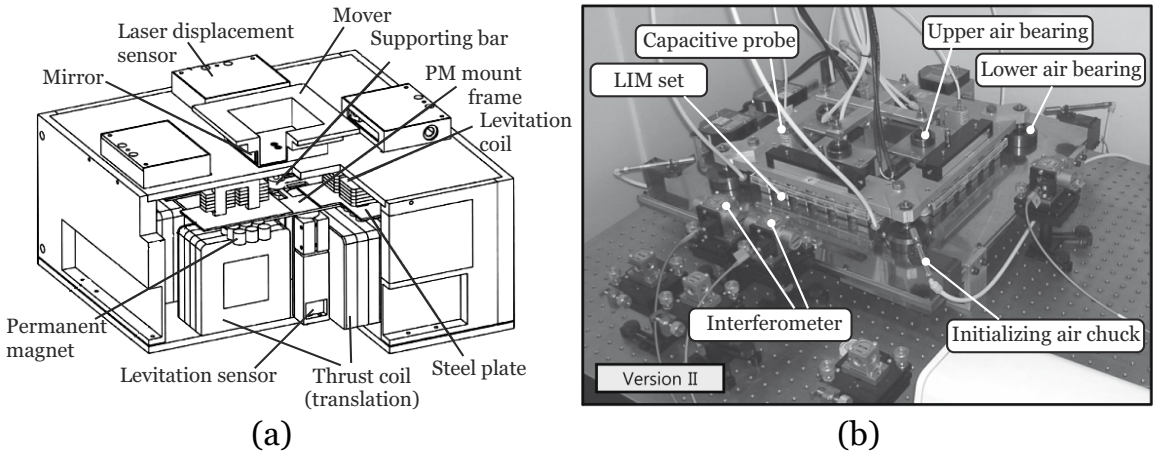

FIGURE 1.20: LIAs based MPS proposed by Jung *et al.* (a) [Jung 05] (b) [Jung 10]

1.3.5.2 Linear Reluctance Actuator (LRA)

The principle of LRA is analogous to the flow of the electric energy in an electrical circuit. In electric circuit, the electric field causes an electric current to follow the path of least resistance. Similarly, in a magnetic circuit the magnetic field causes magnetic flux to follow the path of least magnetic reluctance/resistance. In a magnetic circuit the magnetic energy is stored rather than dissipating it like in electrical circuit. So, when the coil in the magnetic circuit is energized, the reluctance force appears in order to minimize the overall reluctance of the magnetic circuit.

LRAs are strong, compact and power economic actuators. The maximum force density of the reluctance force depends on the saturation level of the yoke material, geometrical parameters, material's relative permeability and air gap. The construction of an LRA is similar to LIA, but it requires one less element, since a coil and an iron target is enough to generate reluctance forces (figure 1.21(a)). However, in micro applications, LRAs

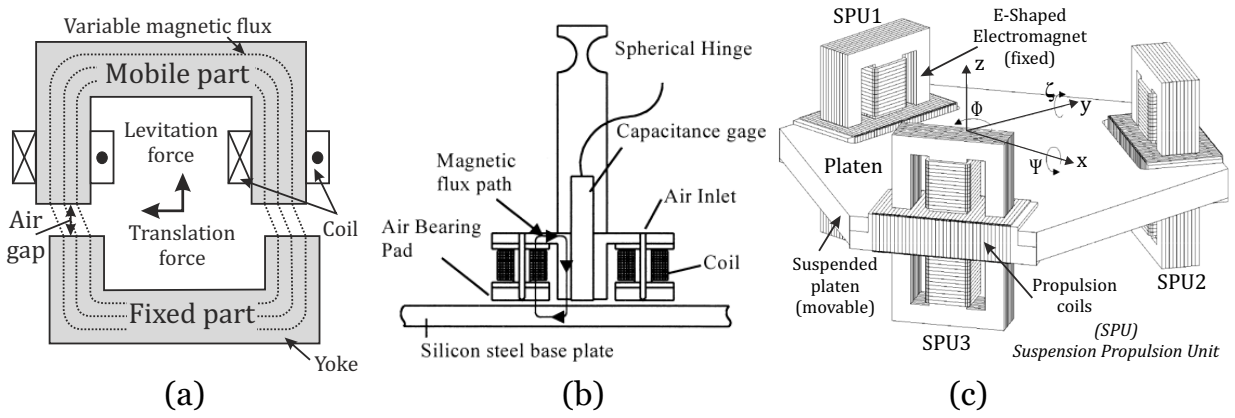

FIGURE 1.21: (a) LRA principle (b) Solution proposed by Lee *et al.*, to control the pneumatic actuator [Lee 00] (c) Molanaar *et al.*, [Mole 96]

suffers from complex yoke design and due to their non-linear behavior of current-to-force relationship, the controller design is often very difficult [Mole 00]. Due to these complications LRAs are mostly used in single-DOF motion applications. For example, Lee *et al.*[Lee 00], have proposed a solution to control the z-axis motion using air bearings with LRAs (figure 1.21(b)). The air bearing provide levitation and guidance along z-axis whereas LRAs are implemented to produce an attraction force between the air bearing and the base plate. A displacement resolution of 25 nm was obtained over 40 μm travel range along z-axis.

Molanaar *et al.*[Mole 96], have proposed a design based on a Suspension and Propulsion Unit (SPU). It combines the active magnetic suspension (reluctance force) with direct propulsion (Lorentz force). The design was proposed with three SPUs offering a 10 mm^2 travel planar range (figure 1.21(c)). No further details can be found regarding the realization of the prototype.

Based on the reluctance actuation principle, Pan *et al.*[Pan 11], have developed a novel 2DOF planar motor for position control applications (figure 1.22). The guide rail based planar actuator design provides a work stroke of 100 mm $\times$180 mm and has the

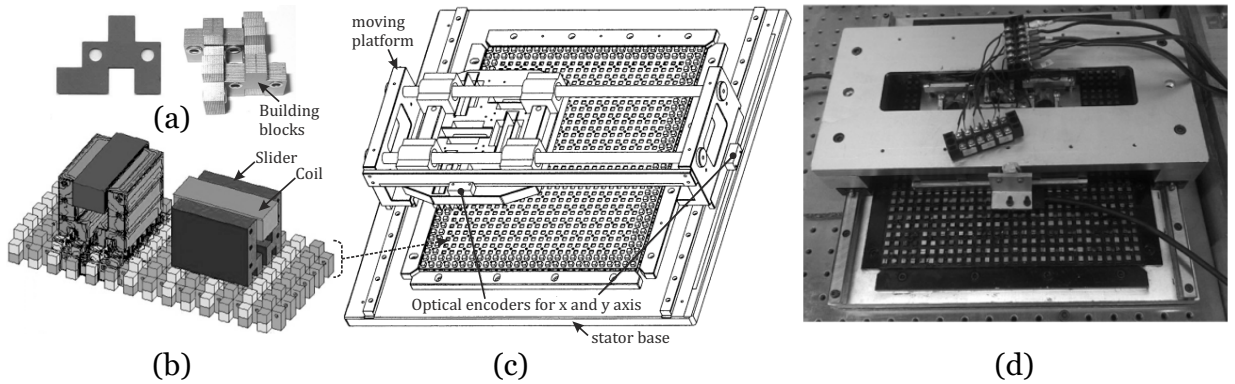

FIGURE 1.22: (a) Building blocks of the stator (b) Interaction principle (c) Schematics of the planar motor (d) Developed prototype Pan *et al.*, [Pan 11]

ability to withstand hostile operating conditions in industries. The stator of the planar motor was realized with small sheets assembled together to form building blocks. These building blocks are put together to realize the stator part of the planar motor. The motor was integrated with optical encoders (resolution=1 μm) to measure the planar displacement.

1.3.5.3 Electro-Magnetic Actuator (EMA)

Another approach to realize actuation for positioning systems based on electromagnetic principle is to use EMAs. The principle of EMA is based on the generation of Lorentz force. It originates due to the direct interaction between a current carrying electrical conductor and a magnetic flux density prevailing around the conductor (figure 1.23(a)). In comparison with LIAs and LRAs, EMAs are simple in design and are simple to control due their linear current-to-force relationship [Mole 00]. The construction of EMA consists of a movable slider and a fixed stator. According to the literature, two design solutions are mostly used to realize MPS based on EMAs. The first approach is "*moving coil and fixed PMs technique*" (figure 1.23(b)) and the second one is "*moving PMs and fixed coil technique*" (figure 1.23(c)).

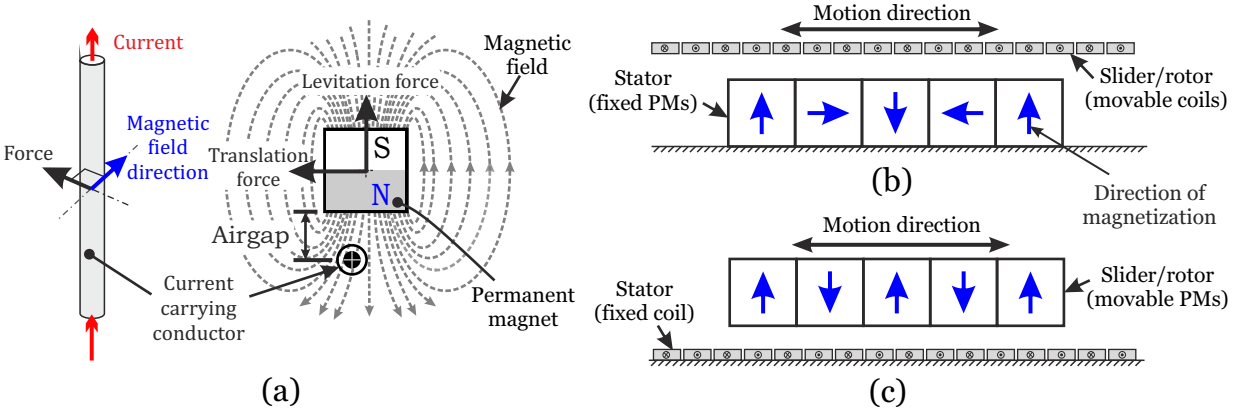

FIGURE 1.23: (a) EMA principle (b) Moving coil and fixed PMs construction (c) Moving PMs and fixed coil construction [Benc 06]

a) MPS realized with moving coil and fixed PMs technique

This construction technique is the inspiration taken from conventional rotary motors. In these motors the permanent magnets are located at the stator part of the motor and the rotor include the conductor windings. DC motors is one of the example of such motors that are mostly found in the appliances. The same construction approach is being followed in multi-DOF planar MPS based on EMAs. The electric coils are placed in the slider part and PMs are fixed on the stator side (figure 1.23(b)). The main advantage of this technique is the ability to extend the travel range of the MPS by adding more number of PMs to the fixed stator. Due to this reason it is mostly applied for MPSs dedicated for object conveyance purposes. In addition, the stator part for these MPSs are often

constructed with PMs assembled in specific magnetic orientation to enhance the magnetic field strength (see figure 1.23(b) for Halbach configuration of the PMs). This is because the both sides of the PMs can not be exposed to current carrying coils which limits the per unit area electromagnetic forces generation for the levitation and translation of the mobile part.

Based on this technique, Hu *et al.*, Yu *et al.*, and Nguyen *et al.*, have developed their planar MPSs for conveyance application [Hu 06, Yu 10, Nguy 12]. The MPS developed by Hu *et al.*, provides six degrees of freedom and is driven by three EMAs (figure 1.24(a)). The coils of these EMAs are embedded inside the Δ-shape platen that resulted in a 5.91 kg total weight. Moreover, the stator part is realized with PMs matrix to form a concentrated magnetic field. The positioner provides a travel range of 160 mm in a plane with a displacement resolution of 20 nm. The displacement measurement was carried out using three external laser interferometer sensors (resolution = 0.6 nm each). In similar fashion, Yu *et al.*, and Nguyen *et al.*, have developed their compact MPSs with two and six coils, respectively (figure 1.24 (b) and (c)). The overall weight of their platen resulted in 1.5 kg and 0.64 kg, respectively. The travel range of both MPSs is around 20 cm in a plane with the positioning resolution of 8 μm. These positioners are compact in design but in order to compensate the overall weight of the platen they are equipped with aerostatic bearings (details not provided).

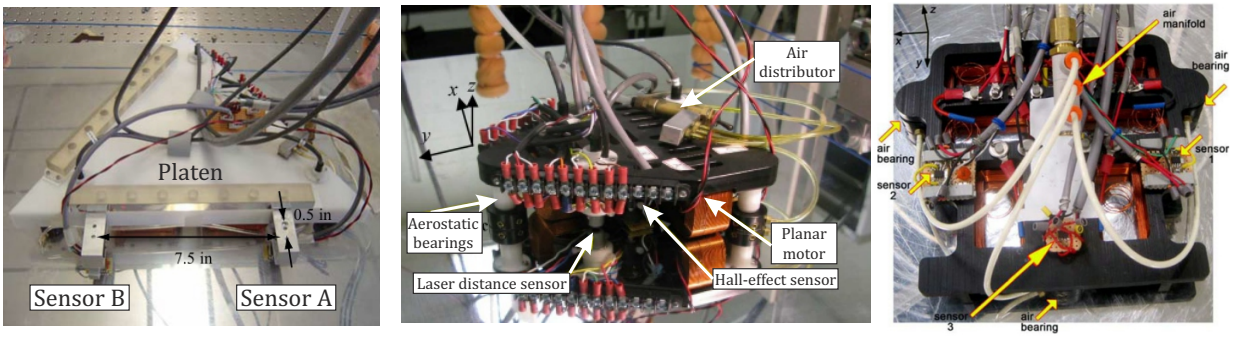

(a) (b) (c)

FIGURE 1.24: Positioning systems developed by (a) Hu *et al.*, [Hu 06] (b) Yu *et al.*, [Yu 10] (c) Nguyen *et al.*, [Nguy 12]

The application of the aerostatic bearings in the MPSs based on the moving coil and fixed permanent magnet technique is often needed to first, levitate the heavy mobile part and second, to remove the joule heat generated during their functioning. However, this solution often reduces the availability of the potential space on the mobile part due to the extensive wires or air manifold tubes that are connected to it (see figure 1.24). This problem often leads to positioning limitation in a plane as the length of the mentioned elements restricts the movement of mobile part to a certain range.

b) MPS realized with fixed coil and moving PMs technique

In this technique, the permanent magnets are directly assembled to the slider (or mobile part) and coils are fixed at the stator (figure 1.23(c)). The main advantages of this technique includes, easy removal of joule heating without disturbing the functionality of the MPS and possibility to realize wireless movable part which often provides a huge margin to directly integrate external components (e.g. sensors, etc.). In literature, most of the modern MPSs based on EMAs are realized with this technique. These systems are often referred to Maglev (Magnetically levitated) systems as the mobile part in these systems can be electromagnetically levitated.

Based on this technique, Trumper *et al.* [Trum 98], have developed their maglev micro stage (figure 1.25(a)). The stage consists of four independent driving units to generate levitation and translation forces. The authors have used PMs in Halbach configuration to construct a Permanent Magnet Array (PMA). The stator of the stage was constructed by wrapping the conductor around a non-ferromagnetic material block which helps in to remove the joule heat generated due to the current flow. In order to measure the translation displacement external interferometers were used with mirrors that were fixed to the mobile part. Moreover, the stage was integrated with capacitive sensors to measure the vertical motion. The maximum translational stroke is $50\times50\times0.4$ mm^3 with 5 nm accuracy and rotation stroke is 600 μrad.

Similar approach has led Holmes *et al.* [Holm 00], from the same research team to develop a MPS for scanned-probe microscopy application (figure 1.25(b)). The stage utilizes four levitation linear motors to suspend and move the moving part (platen). Position measurement was carried out using three interferometers and three capacitance probes integrated inside the MPS volume. The MPS offers a resolution of 10 nm with a maximum travel range of 25 mm$\times$25 mm$\times$0.1 mm along three axis. The overall weight of the mobile part resulted in 12 kg. The mobile part was floated in the oil to reduce disturbances such as heat and micro vibration during functioning.

In another study, two of the maglev systems were proposed by Kim *et al.* [Kim 07], as shown in the figure 1.26. The Δ-maglev stage and Y-maglev stage have been developed for multi-axes nano scale positioning tasks [Kim 07]. The Δ-maglev stage is constructed with a pair of three horizontal and vertical electrical coils. Each pair shares a single cylindrical permanent magnet that is attracted or repelled due to the generation of electromagnetic forces (figure 1.26(a)). The maximum planar travel range is 300 μm and rotational range is 3.5 mrad with a resolution of 5 nm along all three axes.

The second generation stage (refers to Y-maglev stage) is based on same construction approach as of Δ-maglev stage. However, it offers 15 times more travel range (5 mm$\times$5 mm$\times$7 mm) as compared to Δ-maglev stage. The maximum rotational range about z-axis of Y-maglev stage is 5°. These two types of MPS only integrate the capacitive sensors only

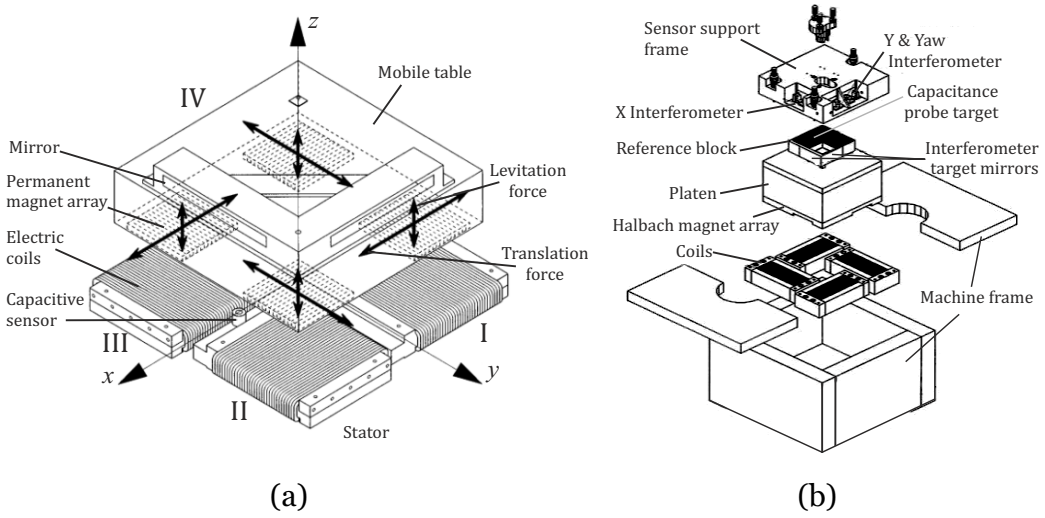

FIGURE 1.25: Maglev positioning systems developed by (a) Trumper *et al.*, [Trum 98] (b) Holmes *et al.*, [Holm 00]

to measure the displacement in levitation. In order to measure long range displacement external laser interferometers were used.

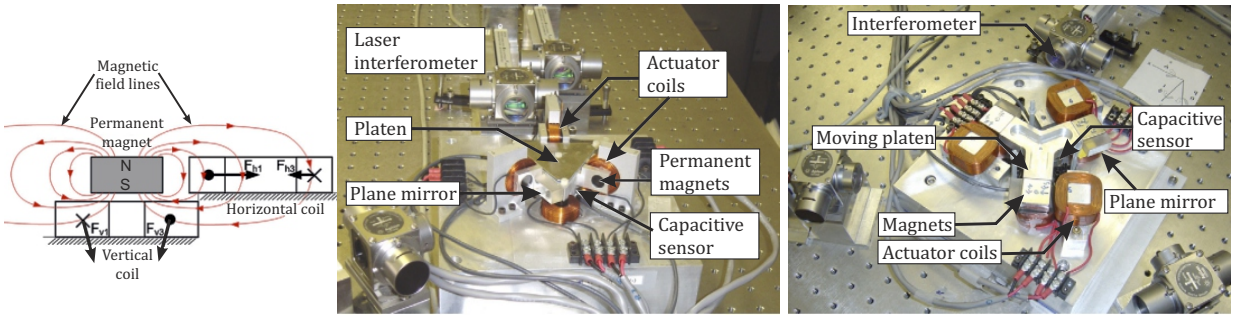

FIGURE 1.26: MPSs developed by Kim *et al.*, [Kim 07] (a) Actuation principle and EMA structure (b) Δ-maglev stage (c) Y-maglev stage

Chen *et al.*, have developed two MPSs based on flexure and EMAs to achieve smooth motion. The positioning stage presented in figure 1.27(a) utilizes six EMAs (three actuators along each axis) to deliver the translation force to the flexures that are connected to the mobile part (sample holder). The prototype delivers a ± 50 μm displacement range with a resolution of 50 nm measured via three integrated capacitive sensors. Later, the same research group have used this concept to develop a compact 3DOF submicro positioner (figure 1.27(b)). It consists of a monolithic parallel flexure mechanism actuated with four EMAs. Three optical and three fiber interferometer sensors were used to measure the displacement. The maximum travel range is limited to ± 0.5 mm (due to fiber interferometer sensor) in *xy*-plane. The resolution of the device was reported 5 μm.

Culpepper *et al.* [Culp 04], have developed a low cost nano-manipulator which utilizes a monolithic spatial compliant mechanism (figure 1.27(c)). The manipulator delivers a

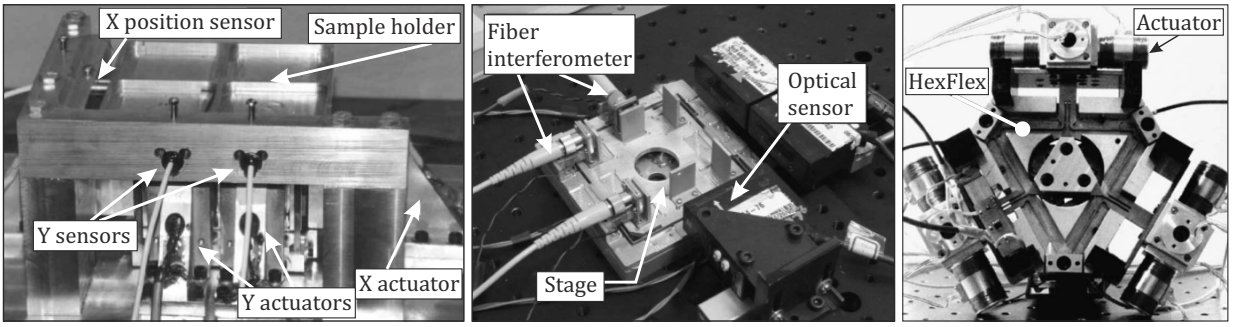

(a) (b) (c)

FIGURE 1.27: MPSs constructed with EMAs and compliant mechanism (a) Chen *et al.*, [Chen 04] (b) Chen *et al.*, [Chen 10] (b) Culpepper *et al.*, [Culp 04]

100 μm stroke along six-axis with a 23 nm resolution. The motion forces are generated using three EMAs directly attached to spatial compliant mechanism. This manipulator concept has led Culpepper *et al.*, to build a thermally actuated planar stage (see figure 1.11(c)).

Gao *et al.*, have developed a surface driven planar motion stage (figure 1.28(a)). The stage delivers 3DOF motion and integrates a surface encoder (displacement sensors) to measure the positing of a grid on the platen. Four orthogonally arranged coils and PMs were used to actuate the platen. The overall dimensions (platen + stage base) of the stage are 260×260×23 mm^3 which resulted in a 10.2 kg total mass. The thrust force of the stage along single axis was reported 1.6 N/A. However, this force is not enough to move the heavy platen. To solve this problem, the authors have used four air bearings at the extremities to compensate the weight of the platen. The stage offers a displacement resolution of 20 nm in translation and 0.2" in rotation with a maximum travel range of 40 mm in *xy*-plane. The device is compact and the integrated surface encoder permits to measure the displacement without any contact.

Dejima *et al.*[Deji 05], from the same research group have developed a positioning

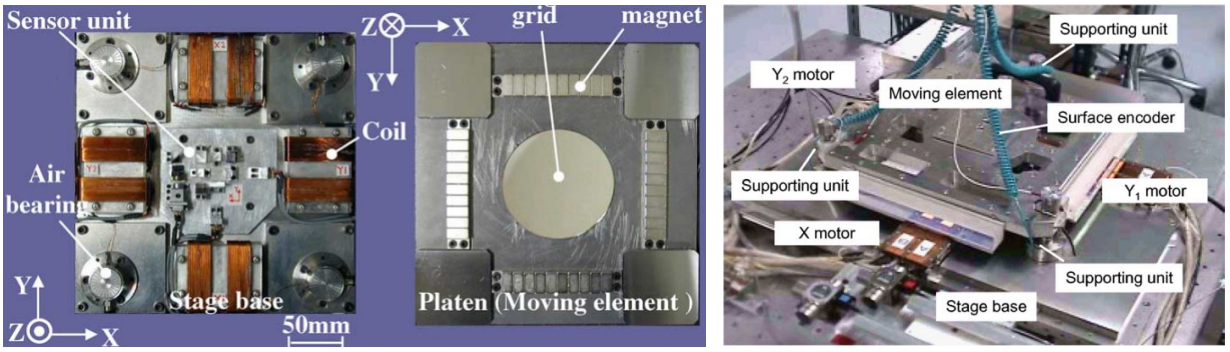

(a) (b)

FIGURE 1.28: MPS developed by (a) Gao *et al.*, [Gao 04] (b) Dejima *et al.*, [Deji 05]

system with integrated surface encoders proposed by Gao *et al.*, [Gao 04]. The translation and levitation characteristics of the heavy platen (24.9 kg) was achieved with EMAs and air bearings, respectively. Moreover, in order to control and achieve multi-DOF motion of the heavy platen, piezo actuators were vertically employed which resulted in a complex design as shown in figure 1.28(b). The system is capable to deliver a displacement and levitation stroke of 200 mm and 10 μm, respectively.

In micro component manufacturing industries, positioning systems capable to deliver millimeter level strokes are often applied to transport the components during manufacturing. Electromagnetically actuated MPSs are mostly preferred due to their high speed and ability to provide wireless designs. Lu *et al.*, have developed one such positioning system for long range motion applications (figure 1.29(a)). The authors have realized the fixed part of the MPS with 3-phase planar coils fabricated in a 16 layer printed circuit board and the mobile part consists of four magnet arrays fixed to a mobile platen (overall weight 2.3 kg). To generate sufficient electromagnetic forces for translation and levitation of the heavy platen the magnetic arrays are constructed with PMs arranged in Halbach configuration and the thickness of the copper coils have been selected 210 μm to inject high current values. The authors have reported an average planar motion resolution of 0.5 μm measured via an external stereo vision sensor (details not provided).

In another study, Gloess *et al.*, have developed a novel positioning system with three EMAs (figure 1.29(b)). Each EMA consists of two planar coils and a set of permanent magnets arranged in Halbach configuration. The mobile platform of the system is wire free and delivers a planar motion of 100 mm^2 with 5 nm resolution in closed loop control. In order to get high stability in all 6-DOF the authors have developed a new 6D sensor measurement system (optical+capacitive) installed beneath the mobile platform. The sensing system utilizes a structured grid plate to measure the displacement. The maximum speed of 100 mm/s (limited due to the controller) with a maximum carrying load of 500 grams was reported by the authors.

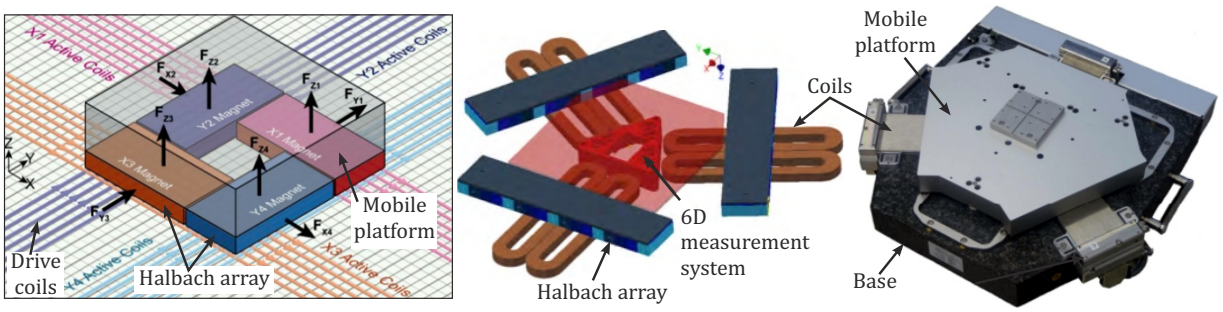

FIGURE 1.29: MPSs proposed by (a) Lu *et al.*[Lu 12] (b) Gloess *et al.*[Gloe 12]

Based on moving PMs and fixed current coils technique, N.Bencheikh at Roberval laboratory of the Université de Technologié de Compiègne (UTC), developed a long range

linear EMA to realize compact miniature conveyance device for desktop factories. In order to achieve planar motion, the miniature conveyor was realized with four orthogonally arranged EMAs assembled to a Zerodur cross structure (figure 1.30). The prototype is able to perform *xy*motion in a plane and a rotation about z-axis. Each EMA is driven using a two phase planar electric drive coils that are injected with 1.6 A (peak to peak) currents. In order to measure the displacement, two non contact external fibre optic sensors (resolution $\approx$ 2 nm). The conveyor prototype was designed for 5 mm$\times$5 mm travel in *xy*-plane but was tested for only 2 mm due to the limited range of the fiber optic sensors. In addition, the resolution of the device was reported around 20 μm due to the friction between the mobile and fixed part of the system. Further, a maximum rotation of $\pm 8°$about z-axis was reported [Benc 06].

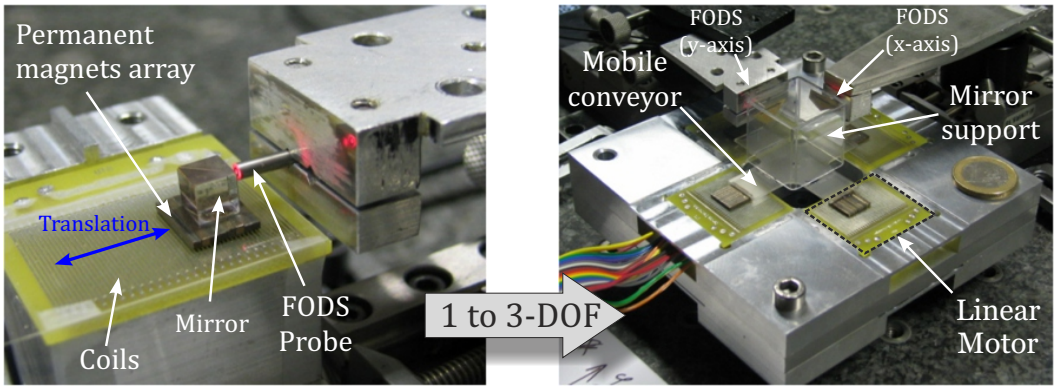

FIGURE 1.30: Long range linear EMA and proposed solution to realize a 3DOF miniature conveyor [Benc 06]

1.4 Miniature displacement measurement sensors

In modern positioning systems, non contact sensors are mostly preferred over contact type sensors due to their ability to measure the motion characteristics such as displacement, speed, acceleration, etc., of the mobile part (or rotor) without any interruption during functioning of the positioning systems. These sensors provide higher dynamic response with high measurement resolution, low or no hysteresis and can measure delicate structures as compared to contact type sensors such as potentiometer, etc. [Lai 05]. A wide variety of displacement sensors have been developed based on the principles of capacitive, inductive, magnetic and optical sensing. However, where the overall dimensions of the positioning system reduce in to micro realm, the selection of appropriate sensor becomes a challenging task from their operation and integration aspect.

In practice, optical sensors are probably the most popular for measuring position and displacement. Their main advantages are simplicity, the absence of the loading effect, and relatively long operating distances [Frad2004]. In addition, optical sensors are insensitive to stray magnetic fields and electrostatic interferences as compared to non contact sensors

based on capacitive, inductive and magnetic measurement principles. This makes optical sensors a suitable choice for many MPSs used in sensitive applications. Concerning optical displacement sensors, numerous designs have been reported in past, employing principle of triangulation , interferometry , diffraction and speckle [Khia 07]. In most of these designs the construction of the sensors mainly consists of a light source, a photodetector and light guidance device that may include lenses, mirrors, optical fibers, etc. The light emitted by the light source guides through the guidance device and hits the movable object such as the mobile part of the MPS. The reflected and/or diffracted light is collected by the photodetector which converts into electrical signals. These signals are manipulated by the electronics behind these sensors which determines the displacement change at nano meter level after interpolation. These components can easily be configured for desired measuring tasks in systems but their large volume due to the light guidance devices do not guarantee their integration into the MPSs as presented in [Kim 07, Jung 10]. In addition, multi-DOF positioning systems often demand multiple sensors to control the motion behaviour in real time. In such scenario, the application of multiple optical sensors such as laser interferometers along each motion axis increases the overall cost of the system.

Optical encoders are one of another solution that is adapted in several studies presented in previous section [Gao 04, Ditt 06, Smar 11, Pal 11, Kuma 12]. Their working principle is mainly based on the measurement of the relative movement of a scale and scanning reticle [Heid]. As compared to interferometers or sensors based on triangulation principle, they are compact in volume and offer nano meter level resolution after interpolation. The main advantages include their ability to measure at long range but they are often one dimensional due to their design constraint. So, in order to measure the motion characteristics in MPSs, numerous sensors are needed. In addition, in angular optical encoders the scanning reticle has fixed axis which often leads to incompatibility with MPS offering in-plane angular motion without fixed axis such as the case of planar conveyors [Lu 12, Benc 06].

Fiber optic displacement sensors are one of most compact and cost effective solution available in optical sensors [Kiss 74]. The light emitting and receiving probe in these sensors is made of a bundle that consists of at least one emission and one receiving fiber. In reflective principle based fiber optic displacement senors, the light injected by the LED into the emission fiber exits from the probe and is reflected by a flat mirror. The reflected light feeds through the reception fiber bundle that is connected to a photodiode on the other end as shown in figure 1.31(a). When the facing mirror moves perpendicular to the probe axis, the angle of incident light changes. This results in variation in the intensity of the reflected light collected by the reception fiber which is interpreted by the photo diode. The typical output response curve of this type of sensor is presented in figure 1.31(b).

Due to the small dimensions of the probe, their integration in compact MPS designs

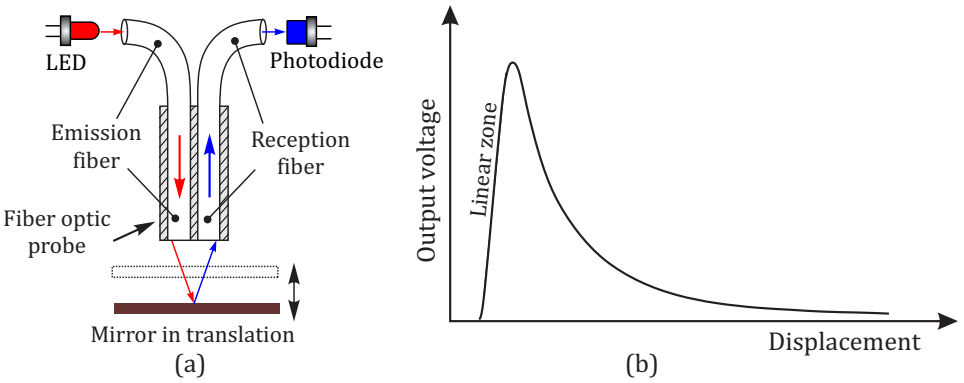

FIGURE 1.31: (a) Fiber optic displacement sensor principle (b) Sensor response

is easy as compared to other optical sensors, as they can reach in congest places without consuming too much space. Further, in order to measure the motion characteristics along multiple axes the integration of multiple fiber optic probes does not affect the cost and volume of the overall system. In addition, the arrangement of the fibers in the probe can be used to measure two dimensional and angular displacement with nano meter level resolution. However, their application in MPSs is not common as they exhibit small working range (up to few hundred microns) in their high sensitivity region.

Prelle *et al.*, at Roberval laboratory (UTC) have proposed a solution to extend the linear working range of the fiber optic sensor up to several millimeters (figure 1.32(a)). According to the literature [Prel 06], fiber optic sensors were used with small step like structure "*called grating*" in their high sensitivity zone. In order to avoid discontinuity during the displacement measurement two fiber optic probes (each Ø2 mm, L=10 mm) were employed in the setup and a signal switching has been performed.

Later, Khiat *et al.*, have developed an initial prototype of the sensor with the collaboration of Institut für Mikrotechnik, TU Braunschweig, Germany (figure 1.32(b)). The optimal design of the prototype consists of two fiber optic probes (each, Ø1 mm, L=10 mm) and a flat gold coated grating (13×13×0.5 mm^3). The grating was micro fabricated in silicon material using wet etching technique [Khia 08]. The novel 2D sensor offers a

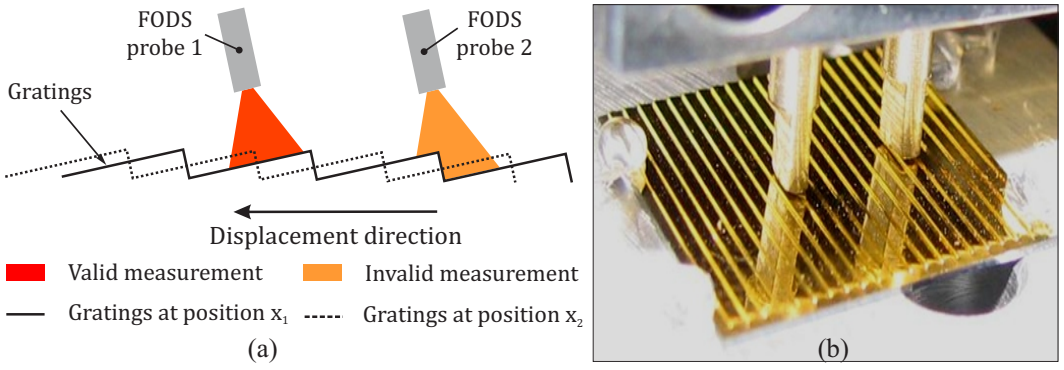

FIGURE 1.32: Long range sensor (a) working principle [Prel 06] (b) Prototype [Khia 08]

resolution of 27.4 nm over a linear working range of 9 mm in a plane. Further details regarding this sensor will be discussed later in this thesis.

1.5 Overview of the presented positioning systems

The presented actuation technologies have been analyzed on the basis of the physical characteristics (e.g. maximum work stroke, overall size, etc.) of the developed positioning systems for micro applications. Table 1.1 represents some of these characteristics for the MPSs discussed in the previous section.

Piezoelectric based actuation principle offers great variety of linear actuators from its application point of view. The MPS realized with piezoelectric actuators have a very fast response time and provide a nano metric displacement resolution. However, their direct application restricts their work strokes up to few hundreds of micrometers due to the very small relative deformation (0.1%) of the piezoceramic material [Cart 11]. Their application in step-mode operation (see section 1.3.1.2) offers MPSs with large displacement strokes but they are slow in nature. From integrated design perspective, the integration of feedback sensors is often difficult in MPS based on step-mode operation due to their design [Wu 04, Zesc 95].

Thermal and electrostatic actuation technology is often adapted for MPS used in MEMS modules due to their small foot print size. MPS realized with thermal actuators have high power density but at macro/meso scale these actuators deliver slower response time. On the other hand, electrostatic actuators have very high frequency bandwidth but the generated force are relatively low as compared to other actuation principles [Karp 08]. However, the low current consumption characteristics of the electrostatic actuators makes them highly efficient. The main drawback of these actuators is their small working strokes in a single module due to their optimal design and functional limitations.

Pneumatically actuated MPSs are clean and deliver strong output forces but due to the digital control of the air flow control unit their accuracy is limited as compared to other actuation technologies. Further, their scale down version is difficult to fabricate due to the complex design of the nozzles. However, their strong output force characteristics are often applied in electromagnetically actuated MPSs to achieve levitation and remove heat generated due to the current flow in conductor at the same time.

Electromagnetic actuators are simple in design, easy to control and cost effective solution in most of the positioning systems [Gilb 96]. Further, their application at macro, meso and micro level scale have been well established as compared to other actuation technologies. These actuators demonstrate very high operation speeds as reported by

TABLE 1.1: Characteristics of the presented positioning systems

Ref.	A.T	DOF	Dimensions	Max. Stroke	Res.	Sensor
MPS based on smart material actuation principle						
[Cedr 11]	MAPA	2	50×50×20 mm^3	25×25 μm^2	2 nm	*Capacitive
[Sabr 09]	MAPA	2	45×40×1.4 mm^3	80×60 μm^2	-	*Capacitive
[PI 12]	MAPA	3	150×150×25 mm^3	300× 300× 300 μm^3	-	Capacitive
[Wu 04]	PIWA	3	20×20×12 mm^3	Theoretically infinite	14 μm	none
[PI N512]	PWD	2	-	6×6 mm^2	15 nm	none
[Zesc 95]	FID	3	38×38×9 mm^3	6×6×6 mm^3	10 nm	none
[Smar 11]	SSA	6	Ø110×45 mm^2	20×20×10 mm^3	1 nm	*Encoder
[Nomu 07]	FID	3	28×28×1.65 mm^3	-	17 nm	none
MPS based on thermal actuation principle						
[Lee 09]	EHR	2	2×2 mm^2	41×41 μm^2	-	Camera
[Lin 11]	EHR	2	8.8×8.8×0.2 mm^3	25×25 μm^2	-	Camera
[Culp 06]	EHR	6	Ø3 mm	8.4×12.8×8.8 μm^3	0.1 nm	Camera
[Ebef 00]	EHR	3	15×15 mm^2	-	-	Camera
MPS based on Pneumatic actuation principle						
[Chap 04]	-	3	35×35 mm^2	Same as dimensions	-	-
[Berl 00]	-	3	30.5×30.5 mm^2	Same as dimensions	-	-
[Dele 11]	-	3	120×120 mm^2	Same as dimensions	-	-
MPS based on electrostatic actuation principle						
[Liu 07]	CD	3	4×4×0.5 mm^3	±12.5, 3.5 μm	-	Camera
[Sun 08]	CD	2	-	±10 μm	-	*Piezoresistor
[Ji 10]	CD	2	3.75×3.75 mm^2	±6.64 μm	-	*Capacitive
[Taka 07]	CD	2	2×2 mm^2	19×23 μm^2	-	Camera
[Kim 03]	CD	2	17×17 mm^2	36×36 μm^2	-	Laser
[Boud 10]	CD	3	-	±10 μm, θ=2 μm	-	Camera
MPS based on electromagnetic actuation principle						
[Ditt 06]	LIA	3	4.6×4×2 cm^3	≈ facing surface area	31.75 μm	*Optical
[Kuma 12]	LIA	3	Ø180 mm	≈ facing surface area	-	*Optical
[Jung 05]	LIA	3	30×30×20 mm^3	-	-	*Laser
[Jung 10]	LIA	3	-	10×10 mm^2	-	Interferometer
[Pan 11]	LRA	2	340×350 mm^2	100×180 mm^2	-	*Optical encoder
[Hu 06]	EMA	6	95.25×190.5 mm^2	160×160 mm^2	20 nm	Interferometer
[Yu 10]	EMA	6	170×152×53 mm^3	220×200 mm^2	10 μm	*Hall sensor
[Nguy 12]	EMA	3	185.4×157.9 mm^2	15.2×20.32 cm^2	8 μm	*Hall sensor
[Trum 98]	EMA	3	-	80×69×17.5 mm^3	5 nm	Interferometer
[Holm 00]	EMA	2	-	25×25×0.1 mm^3	10 nm	*Interferometer
[Kim 07]	EMA	6	80×69×17.5 mm^3	0.3×0.3×0.5 mm^3	5 nm	Interferometer
[Kim 07]	EMA	6	115×127×112.7 mm^3	5×5×0.5 mm^3	4 nm	Interferometer
[Chen 04]	EMA	2	-	100×100 μm^2	20 nm	*Capacitive
[Chen 10]	EMA	3	100×100×100 mm^3	1×1 mm^2	5 μm	*Optical
[Culp 04]	EMA	6	-	100×100×100 μm^3	23 nm	Camera
[Gao 04]	EMA	3	260×260×23 mm^3	40×40 mm^2	20 nm	*Encoder
[Deji 05]	EMA	5	720×720×60 mm^3	200×200×0.01 mm^3	-	*Multiple
[Lu 12]	EMA	6	559×320×5.7 mm^3	260×60×2.5 mm^3	0.5 μm	Interferometer
[Gloe 12]	EMA	3	-	100×100×0.1 mm^3	5 nm	*Capacitive+optical
[Benc 06]	EMA	3	100×100×20 mm^3	5×5 mm^2, ±8°	200 nm	Fiber optics
Acronym used in the table						

Mechanically Amplified Piezoelectric Actuator (**MAPA**), Piezo InchWorm Actuator (**PIWA**), Friction Inertia Drive (**FID**), PiezoWalk Drive (**PWD**), Comb Drives (**CD**), Stick-slip actuator (**SSA**), ElectroMagnetic Actuator (**EMA**), Linear Induction Actuator (**LIA**), Linear Reluctance Actuator (**LRA**), Electric Heat Resistor (**EHR**), Diameter (**Ø**) Integrated inside the MPS (*), Displacement resolution (**Res.**), Actuator Type (**A.T**)

several research groups [Gloe 12, Lu 12, Kim 07]. In order to realize contact less actuation, their ability to generate levitation and translation forces in a single module makes them more compact from their design aspect as compared to other actuation technologies. In addition, this technology results in high actuation forces, long strokes (displacement), low voltage control and bidirectional motion characteristics in MPSs [Voll 10, Mole 00]. From miniaturization point of view, MPSs realized with EMAs based actuation solution is mostly preferred by several researchers due to their flexible design, fabrication (see table 1.1). Further, the input energy required to realize the magnetic field in the case of LIAs and LRAs is no more needed in EMAs due to the PMs which reduces the energy consumption. In addition, these systems offers wire free mobile platforms which further enhance their ability to integrate external components such as sensors, etc.

However, the miniaturization of this technology into the micro domain often lead to two kinds of problems. First, the difficulty of fabricating small electric coils and PMs and second reduction in output power due to the miniaturization. In order to solve the first problem related to fabrication of the miniature components for MPSs realized with EMAs, Micro System Technology (MST) have played an important role over the past few years. Currently, PMs and electric coils can easily be realized with small dimensions using micro fabrication technology. Concerning the reduction of output power due to the miniaturization of PMs and electric coils there exist alternate solutions to compensate the force losses due to the miniaturization of EMAs. One of the commonly adapted solution is to levitate the mobile part of the MPS via aerostatic bearings during motion such as in the cases [Deji 05, Gloe 12].

For precise positioning, feedback sensors play a vital role in controlling the motion behaviour of these systems. Their selection is mostly carried out on the basis of their compatibility with the MPS environment that include, actuation technology, overall volume, work stroke, etc. For example, in electromagnetically actuated MPSs, the application of sensors based on capacitive, magnetic or inductive measurement principle are in common as the electromagnetic field from the PMs can disturb their functionality. On the other hand, optical sensors are the ones which can work in almost every environment. The only constraint that limit their functionality is the quality of the reflecting surface. In most of the MPSs presented in table 1.1, the displacement measurement has been carried out using optical sensors, e.g. camera, interferometers, etc. However, due to their large volume their integration is difficult. Fiber optic displacement sensors are easy to integrate due to their small dimensions and offer nano meter level resolution. The only limitation concerning these sensors is their ability to measure at long range. The research carried out at our Roberval Laboratory, has led our team to realize a compact version of these sensors to enhance their ability to measure at long range in two dimensions.

Taking into the account the presented actuation technologies, an analysis have been

carried out in the following section to select a drive technology in order to realize a multi-DOF MPS in this work.

1.6 Conclusion

In this section, based on the start of the art regarding the miniature positioning system technologies presented in this chapter and summarized in table 1.1, different actuation technologies have been evaluated in table 1.2 for different design parameters such as working stroke, resolution, compactness, sensor integration, etc. From table 1.2, it can be seen that smart material, thermal and electrostatic actuation based MPSs mostly suffer from their small work stroke size. Different engineering solutions may be employed in order to maximize their work stroke but it results in complex design of the whole MPS. Pneumatic, induction and reluctance actuators based MPSs offer larger work strokes but their poor resolution often limit their applications to conveyance systems. On the other hand, Lorentz force actuator based MPS provide millimeter level strokes with possibility to achieve nanometer level resolution. The only drawback in these MPSs is their smaller output force. However, different solution can be employed to solve this problem. In this work, Lorentz force actuator has been selected as a drive choice to realize the MPS.

TABLE 1.2: Drive choice in the multi-DOF miniature positioning systems

Principle →	Smart material				Thermal	Electrostatic	Pneumatic	Electromagnetic		
Actuator types →	Piezo-stack actuator	Mechanically amplified actuator	Stepping mode actuator	Ultrasonic motor	Bimorph actuator	Comb drive	-	Induction actuator	Reluctance actuator	Lorentz force actuator
Stroke size (>1 mm)	≈ 100 µm	≈ 300 µm	> 1 mm	>1 mm	≈ 41 µm	≈ 36 µm	>> 1 mm	>>1 mm	>>1 mm	>1 mm
Resolution (< 1 µm)	≈ 2 nm	≈ 2 nm	≈ 10 nm	≈ 20 nm	≈ 1 nm	≈ 1 nm	≈ 10 µm	≈ 10 µm	≈ 10 µm	≈ 5 nm
Response time(< 1ms)	Very fast	Very fast	Moderate	Very fast	Slow	Fast	Slow	Fast	Fast	Fast
Output force	Moderate	Large	Moderate	Moderate	Very large	Very low	Large	Very large	Moderate	Low
Design complexity	Moderate	Moderate	High	High	Moderate	Very high	High	High	High	Low
Sensor integration	Easy	Easy	Difficult	Difficult	Difficult	Moderate	Moderate	Easy	Easy	Moderate
Speed (> 1 mm/s)	Very fast	Very fast	Slow	Fast	Slow	Fast	Slow	Very fast	Very fast	Very fast
Miniaturization	Very easy	Easy	Moderate	Moderate	Difficult	Moderate	Moderate	Very hard	Moderate	Moderate

Strong advantage | Weak drawback | Strong drawback

1.7 Thesis objectives

After selecting the actuation technology to realize a compact integrated MPS, the research realized in this manuscript has been divided into three main tasks as shown in the figure 1.33. The description of these tasks are provided in the following text:

Task 1: The initial task is based on the improvement of the previous prototype developed by the Dr. Nabil Bencheikh [Benc 06]. In this task, redesigning of the prototype will be carried out in order to increase its planar working stroke while selecting a minimum foot print size for the new miniature positioning system prototype. In addition, the new design should be adaptable to integrate top and bottom side planar electric drive coils to optimize its output characteristics such as load carrying capacity, current input, etc.

Task 2: The second task deals with the improvement of the long range optical sensor. For this task, the fabrication of the silicon gratings using microfabrication technology will be carried out using the fabrication process proposed by Dr. Ali Khiat [Khia 07]. However, the main objectives behind this fabrication are to obtain improved surface parameters for the silicon gratings and to achieve a micro machining process that must deliver homogenous silicon gratings with better roughness and flatness parameters. In addition, taking into the design parameters of the new MPS design in task 1, the geometrical parameters of the long range sensor will be optimized for integration purpose.

Task 3: Finally, an integrated MPS capable to deliver 3DOF motion will be realized. For this task, the silicon gratings will be integrated in the mobile part of the miniature positioning system.

During each task, analytical models will be developed and experimentations will be performed in order to validate the MPS design.

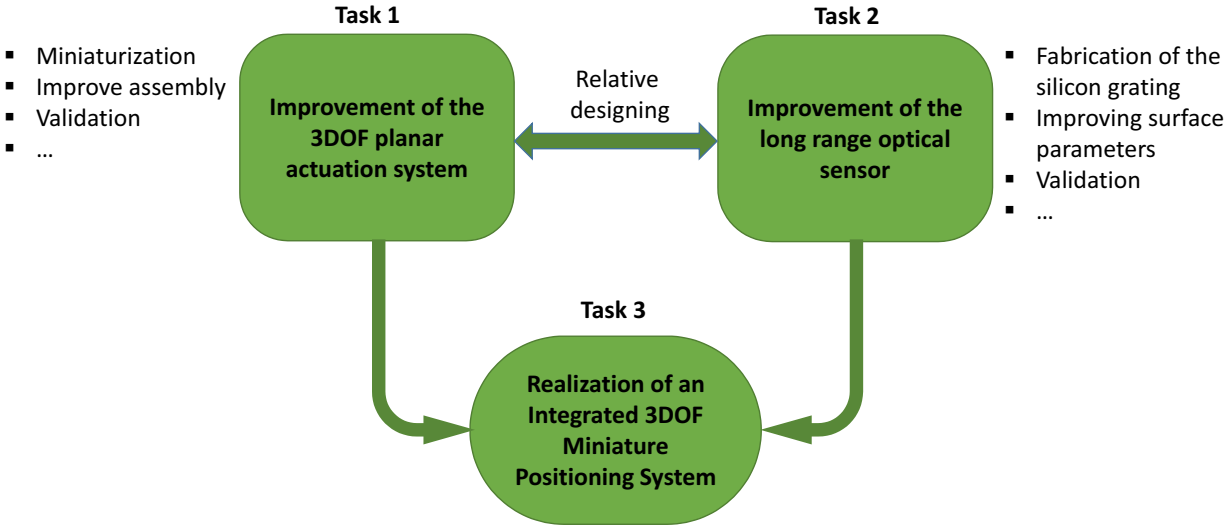

FIGURE 1.33: Research objectives

Chapter 2

Principle and modeling of a miniature planar actuation system

In this chapter the working principle and modeling of the planar actuator system has been carried out. At first, the concept of the actuation system is described along with the general layout of the system. Due to the symmetrical design of the system, the construction and functioning of a single linear electromagnetic actuator is discussed for the purpose of simplification. Then, analytical models have been realized and dynamic simulation results are shown to evaluate the performance of the whole system in open and closed loop control.

2.1 Miniature positioning system concept

The Miniature Positioning System (MPS) presented in this work is based on in-plane symmetrical assembly of four direct drive Linear[1] Motors (LMs) as shown in the figure 2.1. Each LM is an electromagnetic actuator based on the "*moving magnets and fixed coils*" technique. The MPS consists of a mobile part and a fixed part. The mobile part consists of four orthogonally arranged Permanent Magnet Arrays (PMAs) that are fixed to the edges of a thin cross shaped platform, here called "*cross structure*". The fixed part consists of orthogonally arranged four Planar Electric Drive Coils (PEDC) in *xy*-plane. The combination of a single PMA and facing PEDC acts as an LM. By this way four LMs such as LM_A, LM_B, LM_C and LM_D, can be distinguished (see figure 2.1).

The functioning of the positioning system is tied up to the electromagnetic force generated by each LM. In order to perform displacement in *xy*-plane between any two positions P_1 and P_2, all four LMs can be used simultaneously to generate motion forces (see figure 2.1(b)). If we assume no assembly errors between LMs situated along an axis, the generated electromagnetic force is the sum of the forces generated by each LM along

[1]The term "*Linear*" represents single degrees-of-freedom of motion i.e. translation

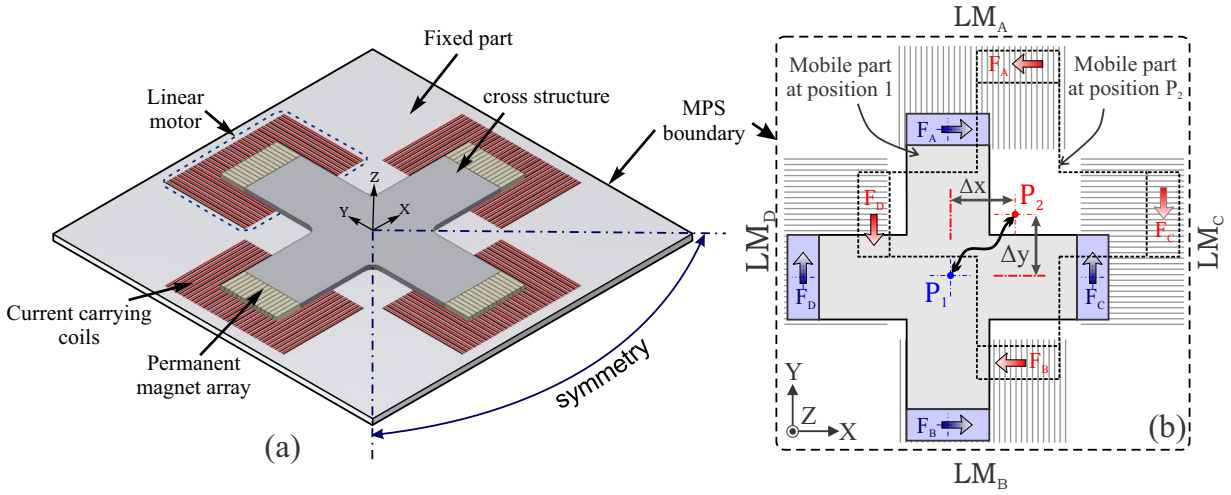

FIGURE 2.1: (a) General layout of the positioning system (b) planar motion concept

an axis. Moreover, in order to realize linear displacement along a single axis the device only requires two active LMs. For example, to achieve linear displacement "Δx" along x-axis, LM_A and LM_B can be used, similarly for "Δy" displacement along y-axis, LM_C and LM_D can be used. The direction of the generated motion force depends on the direction of injected current into each LM. So, by inverting the current in the PEDCs, the motion direction can be reversed. In addition, if the direction of the current in the LMs situated along an axis is reversed with respect to each other, a torque can be produced about the center of the mobile part of the MPS. Hence, by this means a rotation of the mobile part can be realized.

2.2 Actuation principle

The actuation principle of a single linear motor is based on generation of the Lorentz forces. When a PM is placed near a current carrying conductor, an electromagnetic force appears due to the magnetic field from the PM and magnetic field generated from the electric current in the conductor. The relative interaction between two fields results in a force $\vec{F}$ which appears over the PM (figure 2.2(a)). Taking into account the case that the current carrying conductor is fixed and PM is free, the generated electromagnetic force will move the PM in xz-plane in order to align the magnetic field relative to the magnetic field of the conductor. The amount of this generated electromagnetic force (or Lorentz force) can be computed using equation (2.1) [Furl 01].

$$F = I \int_{wire} dl \times B_{ext} \tag{2.1}$$

Where, F is the generated electromagnetic force, l is the length of the current carrying conductor facing PM, I is the current in the conductor and B_{ext} is the external magnetic

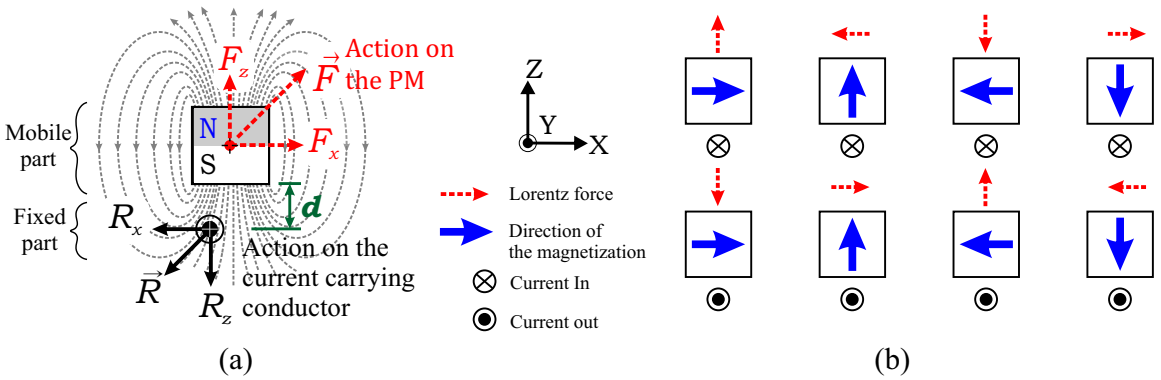

FIGURE 2.2: (a) Electromagnetic actuation principle (b) Directions of the Lorentz force with different configurations of PM and conductor

flux density on the conductor, created by the PM.

The direction of the generated electromagnetic force on the permanent magnet depends on the relative orientation of the PM magnetization and direction of the current carrying conductor. Figure (2.2(b)), represents the different directions of the electromagnetic force generated with respect to the orientation of the magnetization and direction of the current. Depending on the relative position between the conductor and the PM, the electromagnetic force F can be decomposed into its three components. For the purpose of simplification, the 3D problem has been reduced to 2D by assuming that the conductor is perfectly aligned along the length of the PM such as, in y-axis direction (see figure 2.2(a)). The components of the electromagnetic force can be written as,

$$F = \begin{Bmatrix} F_x \\ F_y \\ F_z \end{Bmatrix} = \begin{Bmatrix} +I_y \cdot B_z \cdot l \\ 0 \\ -I_y \cdot B_x \cdot l \end{Bmatrix} \tag{2.2}$$

The components F_x and F_z represents the translational and levitation forces in xz-plane. The magnitude of these forces depends on the intensity of the magnetic flux density, magnitude of the current and length of the current carrying conductor facing the PM. In order to increase the magnitude of the electromagnetic force, these parameters can be altered toward maximum. However, their maximum value is often limited due to the design constraints. For example, the magnitude of the current depends on the cross sectional area of the conductor. So, for a fixed cross sectional area of the conductor the increase in the current could lead to Joule heating effect, which may either destroy or degrade the remanent magnetization of the PM or the conductor itself. Similarly, the intensity of the magnetic flux density from the PM depends on the volumetric shape, its material and its relative distance from the current carrying conductor. For the same material, the intensity of the magnetization is proportional to the increase in the geometrical dimensions, however, increasing the geometrical dimensions means more weight, which may lead to

reduction of usable net motion forces. Another way to increase the electromagnetic force is to reduce the relative distance (known as air gap, "*d*" in the figure 2.2(a)) between the conductor and PM. In MPSs, the above mentioned parameters are carefully dealt with as they can change the overall performance the system.

2.2.1 Linear motor layout and its working principle

The actuation principle presented in the previous section is extended to realize long range linear motion by adding a larger number of PMs and conductors in the mobile part and the fixed part, respectively, as shown in figure 2.3. The combination of these parts results in an LM that is able to perform continuous motion along $\pm x$-axis . In order to illustrate the functioning of the LM, the solutions regarding the construction of the mobile and fixed part is first presented.

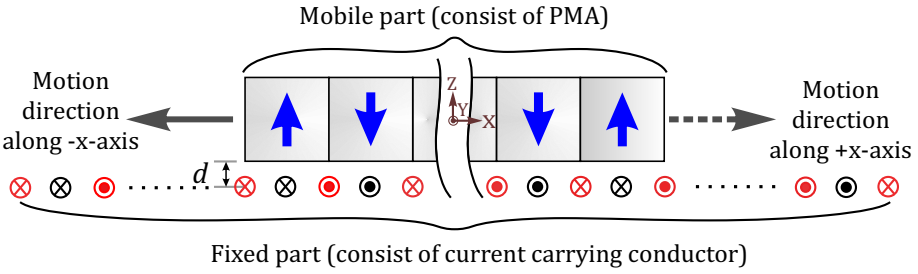

FIGURE 2.3: General layout of the long range LM

2.2.1.1 Permanent Magnets Array (PMA)

In order to realize the PMA, two types of PMs layouts are in practice as shown in figure 2.4. The first approach is to assemble the PMs in "Halbach array configuration". In this configuration PMs are combined with a spatially rotating pattern of the magnetization which augments the magnetic field on the one side of the PMA while decrease the magnetic field to near zero on the other side [Nguy 12]. This feature is very beneficial

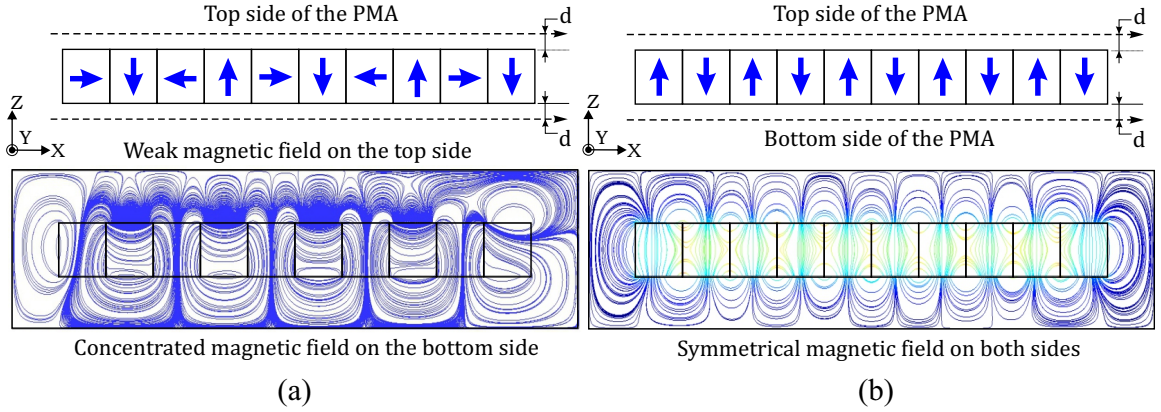

FIGURE 2.4: (a) Halbach array configuration (b) North-South array configuration.

in electromagnetic actuators designed for the MPS used in micro applications. However, where this configuration results in the increase in the magnetic field is increased along the one side of the PMA, the other side cannot be exposed to current carrying conductors due to the unsymmetrical magnetic field (see [Benc 06]). Due to this reason the application of this configuration is mostly limited in the designs where the availability of the potential space for placing current carrying conductors on the both sides of the PMA is difficult [Hu 06]. For example, in MPS based on the moving PMs and fixed current coils technique, the current carrying conductors cannot be placed on the both sides due to the design constraints. So, in such case the Halbach array configuration is suitable to increase the magnetic field to the side which is exposed to conductor to gain more power.

The second approach is to assemble the PMs in "North-South (NS) array configuration". It consists of the assembly of the PMs with opposite magnetic orientation as shown in figure 2.4(b). The NS array configuration is simple and offers several advantages in MPS designs over Halbach array configuration. For example, the NS configuration offers symmetrical magnetic field on top and bottom sides of the PMA as shown in figure 2.5. So, in order to increase the magnitude of the electromagnetic forces, another set of conductors can easily be applied with same characteristics.

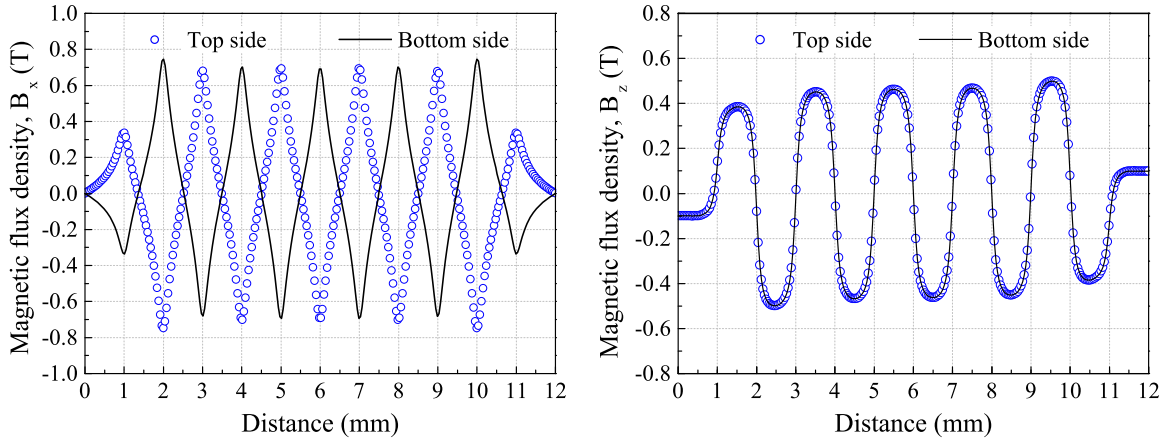

FIGURE 2.5: Magnetic flux density on both sides of the NS array at an air gap d=170 μm

Furthermore, NS array requires a smaller number of phase current coils as compared to Halbach array to generate continuous motion [Lu 12]. This feature of the NS array configuration is very beneficial from miniaturization and control point of view. In addition, from the PMs assembly perspective, Halbach arrays are difficult to realize and demand positioning and bonding equipments to apply pressure to align and bond PMs in this configuration with specific magnetic orientation [Kim 97]. On the other hand, the assembly of the PMs in NS array configuration is very easy and does not need any equipment for bonding and alignment due to the opposite orientation of the PMs magnetization. On the basis of these conclusions, we have adapted NS configuration for the PMA in this thesis.

2.2.1.2 Drive coil construction

In order to be in accordance with the magnetic pole orientation in PMA, the electrical conductors can be arranged in various configurations to form multi-phase coils. These coil formations that are mainly classified as “core based coil formation” and “planar coil formation”, reduce the input current source lines.

The core based coil formation is realized by winding the electric conductor around a ferromagnetic material such as soft iron (see figure 2.6(a)). The presence of the core in this formation enhances the magnetic field strength which can be used to increase the electromagnetic forces as in [Trum 98, Kim 07]. However, this coil formation demands excessive length of the conductor and despite having more number of turns in the coil, the interaction between the PMA and the coil itself remains in the area where the coil is exposed to the magnetic field. This reduces the full usage ($> 50\%$) of the coils with respect to its volume. Furthermore, this coil formation is mostly realized with automated machines to attain compactness and avoid improper shape due to manual winding.

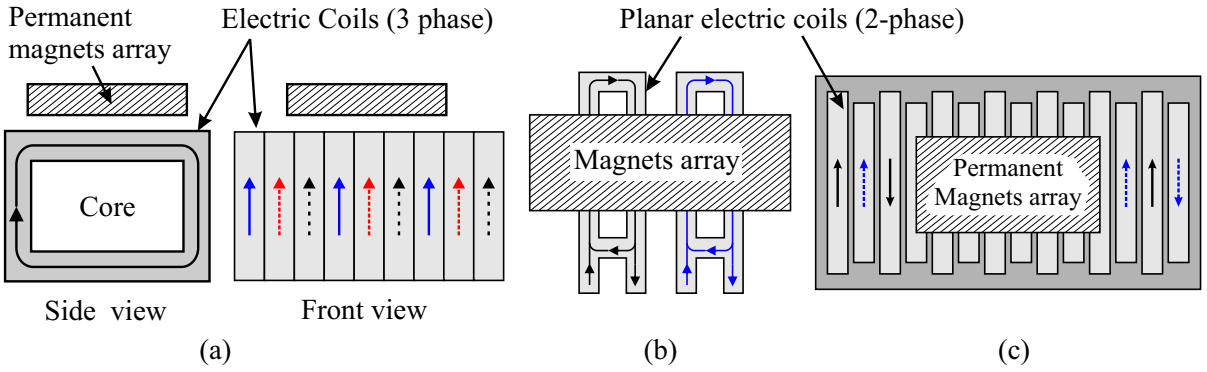

FIGURE 2.6: Different coil construction (a) Core based formation (b) Separated planar formation (c) Overlapped planar formation [Benc 06]

The planar coil formation offers an economical solution in miniature systems due to the absence of the core. It is realized by arranging the multi phase coils in a single plane as shown in figure 2.6(a) and (b). The main advantage of the planar coils is their reduced overall geometrical dimensions which increase their usability in terms of exposed coil surface area. So, the need of excessive length is no more required due to the absence of the core. In addition, this coil formation can easily be fabricated in to Printed Circuit Board (PCB) which leads to uniform coil dimensions. However, this coil formation often leads to reduction of electromagnetic forces due to the absence of core and fabrication limitation to reach compact layouts for placing more number of conductors. In this scenario, aerostatic bearing [Deji 05] or application of another set of planar coils on both sides of the PMA can be employed to compensate the electromagnetic force loss [Benc 06].

One of the common issues related to the coils is the Joule heating due to the current flow. The amount of this heat is a function of the geometrical and physical properties

of the coils such as cross section, material, length, etc. So, to gain more power in LMs these parameters are optimized based on application area. In addition, forced or natural cooling (e.g. via gas or liquid) can be used to remove Joule heat. In core based coils this is done by cooling the core and in planar coils an air cooling technique is commonly adapted [Holm 00].

In this work, an overlapped planar coils formation approach has been adapted to reach compact volume ($32\times20\times0.035$ mm^3) of the Planar Electric Drive Coils (PEDC) of the LM. In order to be in accordance with the magnetic pole orientation of the PMs in the PMA and minimize the number of input currents source lines, the PEDC consists of two phase coils as shown in figure 2.7(a). In addition, the coils have been been fabricated onto a double sided 1.4 mm thick PCB to attain optimal geometric parameters such as conductor length "l=20 mm", height "h_c=35 μm" and width "w_c=250 μm", etc. The value of these parameters and the number of conductors in the PEDC depends on the design (e.g. motion range, maximum input current, etc.) and PCB fabrication constraints. The overlapped connections between the conductors in a single phase coil (on the top side) have been carried out from the bottom side of the PCB using through holes called "*vias*" as shown in the PCB model of the PEDC in figure 2.7(b).

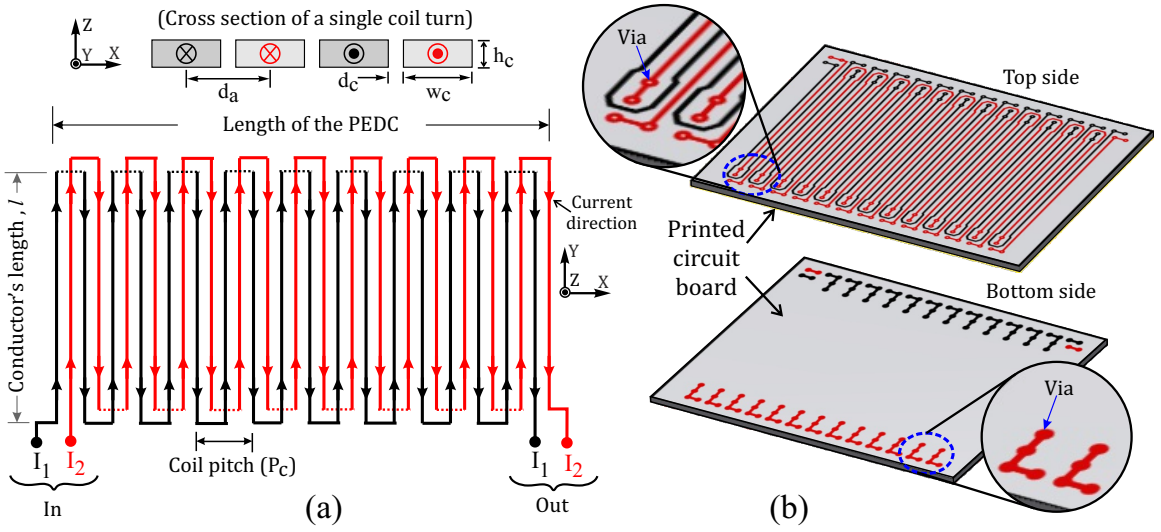

FIGURE 2.7: (a) Two phase coil and cross sectional view (b) PCB model of a PEDC

2.2.1.3 Working principle of the linear motor

The working principle of the LM to perform long range continuous motion is presented in figure 2.8. To provide a better view of the concept, the PMA (i.e. mobile part) of the LM is constructed with four PMs arranged in NS array configuration and the PEDC (i.e. fixed part) is constructed with eight conductors representing two coils with currents "I_1"

and "I_2" with a relative phase shift of "$\pi/2$" and are expressed as in equation (2.3).

$$\begin{aligned} I_1 &= I_{max}\sin(\omega t + \varphi_i) \\ I_2 &= I_{max}\sin(\omega t + (\varphi_i + \pi/2)) \end{aligned} \tag{2.3}$$

Where, I_{max} is the maximum amplitude, ω is the frequency and φ_i is the initial phase of the current injected into the conductors of the PEDC.

In order to realize, long range continuous motion in *xz*-plane, the coil pitch "P_c" of a single coil should be equal to the period of the PMA "P_m" (see figure 2.8(a)). This condition ensures the alignment of the peak current amplitude with respect to the peak magnetic flux density generated by the periodic magnetic poles of the PMA. As a result, the current to magnetic field interaction leads to generation of Lorentz forces along same direction.

To illustrate the working principle of the LM, the generation of the Lorentz forces are presented in four steps at 8 discrete locations which indicates the position of the conductors having currents "I_1" and "I_2". During these steps, it can be seen that when

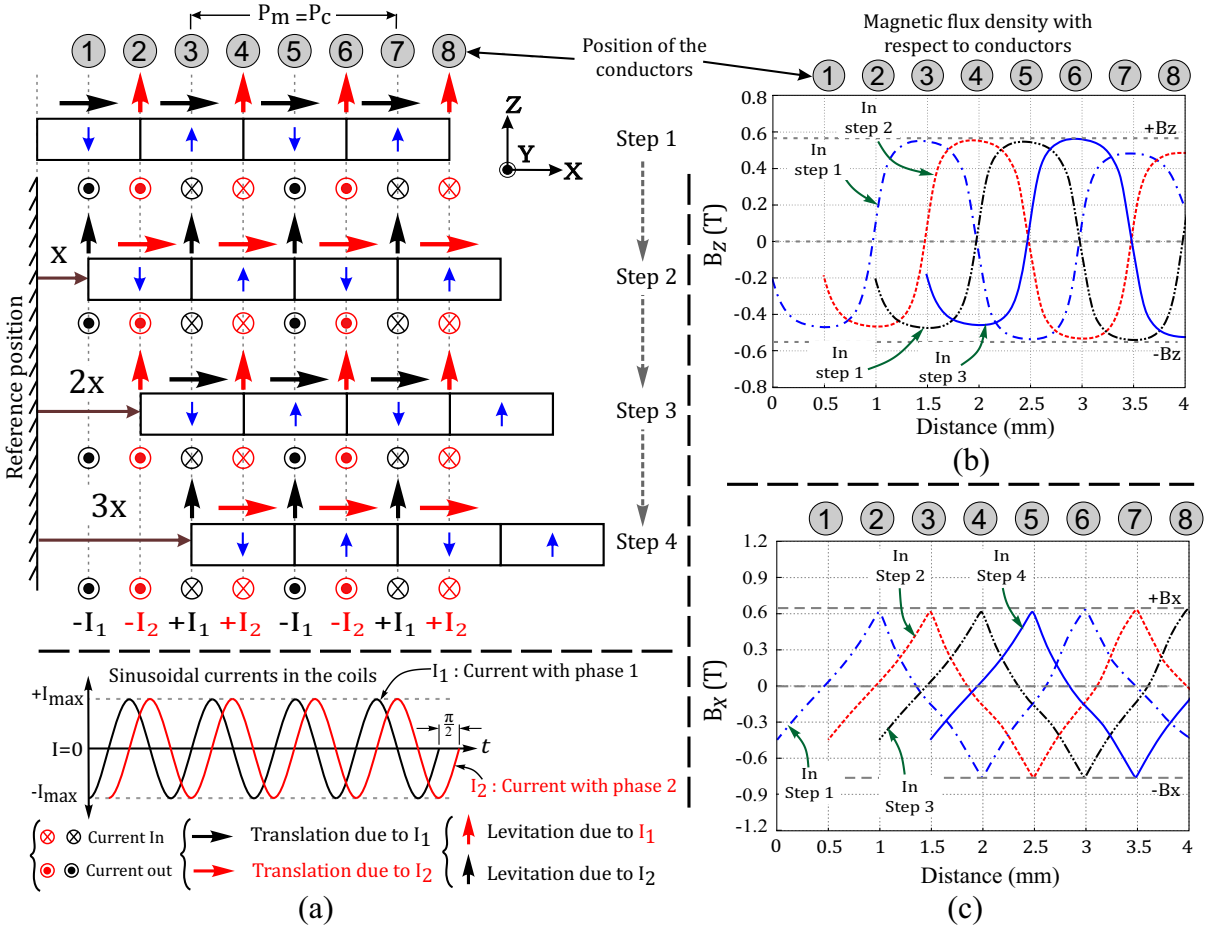

FIGURE 2.8: Working principle of the LM in four steps (a) PMA with respect to the conductors with currents "I_1" and "I_2" (b) Magnetic flux density "B_z" relative to the position of the conductors (c) Magnetic flux density "B_x" relative to the position of the conductors

PMA offers peak value of "B_z" the value of "B_x" is near zero and vice versa (figure 2.8 (b) and (c)). This is due to the orientation of the PMs in the PMA.

When the currents are injected in the conductors, electromagnetic forces will appear over each PM due to the interaction of the current I_1 and magnetic flux density component $\pm B_z$ at the positions 1, 3, 5 and 7. These forces will move the PMA to distance "x" along *x*-axis. At the same instant, the interaction of the current I_2 in the conductors and $\pm B_x$ at position 2, 4, 6 and 8 will generate levitation forces along *z*-axis.

In step 2, the translation forces will appear at positions 2, 4, 6 and 8 due to the interaction of the currents I_2 and the peak magnetic flux density component "$\pm B_z$". Similarly, the levitation forces will appear at positions 1, 3, 5 and 7 due to the interaction of currents I_1 and peak magnetic flux density component "$\pm B_x$". The current shifting (i.e. from I_1 to I_2 and vice versa) is because of the relative phase difference ($\pi/2$) to compensate the periodic poles of the PMA (see figure 2.8 (a)). Further, in step 3 and 4, the translation and levitation forces are generated in similar fashion which moves the PMA at "2x" and "3x" distances from reference position. For the conductors length "*l*" along *y*-axis, the total translation and levitation force is the sum of the individual forces appeared at each conductor locations which are presented in the table 2.1.

TABLE 2.1: Generated electromagnetic force at different position during four steps

Position	**1**	**2**	**3**	**4**	**5**	**6**	**7**	**8**	**Total force**	
Currents	**-I_1**	**-I_2**	**+I_1**	**+I_2**	**-I_1**	**-I_2**	**+I_1**	**+I_2**	**translation**	**levitation**
Step 1	$+I_1B_z$	$+I_2B_x$	$+I_1B_z$	$+I_2B_x$	$+I_1B_z$	$+I_2B_x$	$+I_1B_z$	$+I_2B_x$	$4I_1B_zl$	$4I_2B_xl$
Step 2		$+I_2B_z$	$+I_1B_x$	$+I_2B_z$	$+I_1B_x$	$+I_2B_z$	$+I_1B_x$	$+I_2B_z$	$4I_2B_zl$	$4I_1B_xl$
Step 3		$+I_2B_x$	$+I_1B_z$	$+I_2B_x$	$+I_1B_z$	$+I_2B_x$	$+I_1B_z$	$+I_2B_x$	$3I_1B_zl$	$4I_2B_xl$
Step 4			$+I_1B_x$	$+I_2B_z$	$+I_1B_x$	$+I_2B_z$	$+I_1B_x$	$+I_2B_z$	$3I_2B_zl$	$3I_1B_xl$

From the above table it can be seen that during all steps the generated translation force at each conductor location is in the same direction due to which the PMA will translate along $+x$-axis with respect to the PEDC. So, in similar way if the number of conductors is increased in the PEDC, the travel range of the PMA can be increased. Moreover, in order to increase the magnitude of the translation and levitation forces, the number of PMs can be increased. In this scenario, the equation (2.4) represents the generalized form of the total electromagnetic force due to currents I_1 and I_2 in the conductors.

$$F_{total} = \begin{Bmatrix} F_x \\ F_y \\ F_z \end{Bmatrix} = \begin{Bmatrix} l \cdot \sum_{i=1}^{n} (I_1 B_z(x,y,z))_{2i-1} + l \cdot \sum_{j=1}^{m} (I_2 B_z(x,y,z))_{2j} \\ 0 \\ l \cdot \sum_{i=1}^{n} (I_1 B_x(x,y,z))_{2i-1} + l \cdot \sum_{j=1}^{m} (I_2 B_x(x,y,z))_{2j} \end{Bmatrix} \tag{2.4}$$

Where, i and j are the position index of the conductors, n and m are number of the conductor with currents I_1 and I_2, respectively, B_x and B_z are the horizontal and vertical magnetic flux density components, F_x and F_z are the total translation and levitation forces.

In practice the distance between the adjacent conductors (in our case d_a=0.5mm, see figure 2.7(a)) in the PEDC may be limited due to the fabrication constraints. In this case, the force contribution due to current carrying conductors may lead to small fluctuations during translation of the PMA. This is due to the insufficient overlap of the generated translation force between two adjacent conductors during motion as shown in figure 2.9(a)). In order to reduce this effect, W. J Kim [Kim 97] proposed to increase the number of phase currents facing Halbach array. This ensures the generated electromagnetic force overlap between the adjacent conductors and reduces the fluctuations during motion. A Similar solution can also be applied to NS array by introducing another set of current carrying coils (I_3, I_4) with relative phase shift of $\pi/4$ on the top side of the PMA as shown in the figure 2.9(b) for a single period of the PMA. The value of the phase shift depends on the number of input phase currents and the relative position of the coils. However, in real case scenario the relative position of these conductors may vary due to the fabrication or assembly errors. So, a corrective phase term "$\Delta\varphi_i$" can be added to adapt these variations in the phase currents as presented in equation (2.5). Due to this conductor arrangement, the total translation force generated over a period of the PMA is the sum of the force contributed by each conductor.

$$\begin{aligned} I_1 &= I_{max}\sin(\omega t) & I_3 &= I_{max}\sin(\omega t + (\pi/4 + \Delta\varphi_3)) \\ I_2 &= I_{max}\sin(\omega t + (\pi/2 + \Delta\varphi_2)) & I_4 &= I_{max}\sin(\omega t + (3\pi/4 + \Delta\varphi_4)) \end{aligned} \tag{2.5}$$

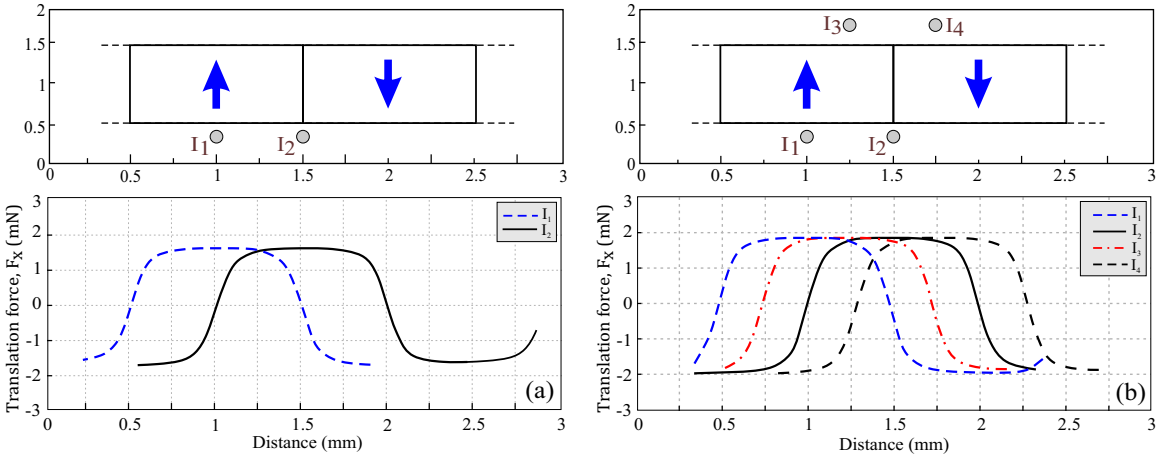

FIGURE 2.9: Contribution of currents in generation of translation force (a) two conductors (b) four conductors

In order to change the direction of the motion, the current phase lead-lag technique is used. The relative phase difference of the injected currents is changed from $+\pi/2$ to

-$\pi/2$ as shown in figure 2.10. Further, if a constant current is injected into the coils. The mobile part (i.e. PMA) will lock its position with respect to the conductors. This effect is due to the appearance of electromagnetic forces in opposite direction because of the NS arrangement of the PMs in the PMA.

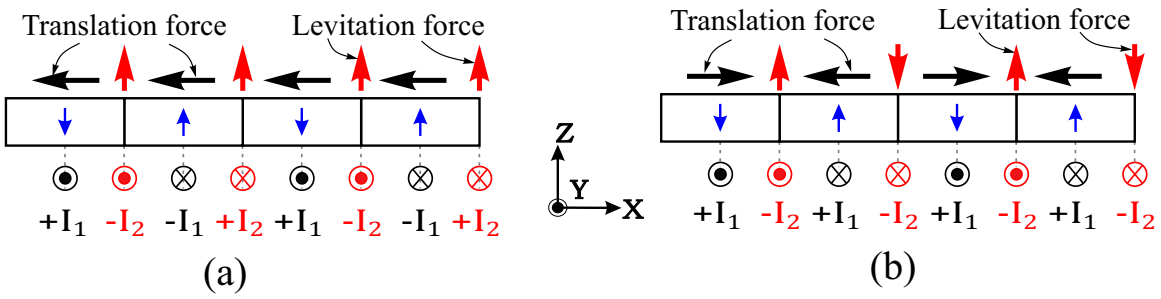

FIGURE 2.10: (a) Direction of motion by changing the phase of the current I_1 to -$\pi/2$ (b) Influence of the steady state currents

In the following section, the single DOF based LMs solution has been used to realize a planar motion system.

2.3 Long range planar motion

In order to realize long range planar motion system, multiple LMs based on the working principle described in the previous section can be assembled to a mechanical structure. The PMAs of the LMs are fixed to a mechanical structure which results in the mobile part of the MPS. Similarly, the PEDCs of the LMs can be assembled accordingly to realize the fixed part of the MPS. In order to assemble multiple LMs, two assembly approaches can be proposed based on the orientation of the translation axes of the LMs as shown in figure 2.11. In the first assembly approach, the translation axes of the LMs merge at a single point and in the second approach the translation axes of the LMs results in multiple merging points. Both methods are equally employed in miniature MPS designs, however the second assembly approach offers an additional rotation motion about the origin of the mobile part of the MPS as compared to the assembly approach presented in figure 2.11(a).

In practice, LMs can be arranged in either “triangle” or “square” formation, e.g. [Gloe 12, Lu 12]. The “triangle” formation demands three LMs arranged at 120° and “square” formations are realized with four LMs arranged at 90°. In “triangle” formation, the linear motion is realized with three translation force components generated by each LM but in the case of the “square” formation , two LMs are sufficient to generate the same linear motion. In addition, during the planar motion, the additional LM in the “square” formation increases the translation force capacity as compared to “triangle” formation in which it remain the same [Mole 00]. Further, a simpler control can be employed with

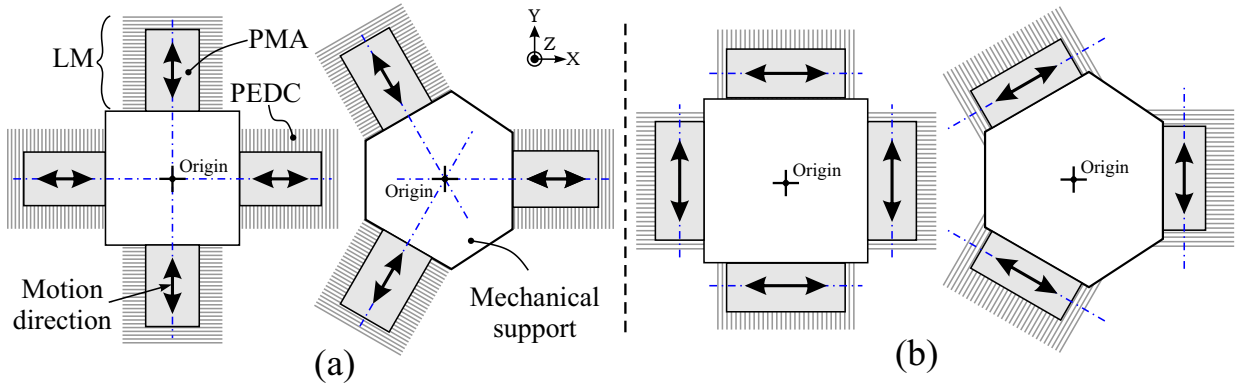

FIGURE 2.11: Architecture with motion axes of the LMs coincides at (a) single point (b) multiple points

"square" formation and LMs situated along single axes can be controlled separately to attain guidance during motion along single axis .

The MPS presented in this work is based on the orthogonal arrangement of four LMs. However, instead of using a square plate like mechanical structure, a cross shaped mechanical structure was adapted to achieve light weight of the mobile part [Benc 06]. The main goal behind selecting a cross shaped structure is to attain light weight for the mobile part as the generated electromagnetic forces becomes smaller due to the reduction in the dimensions of the PMs and limited magnitude of the injected current in the PEDC.

Based on the functioning of the LMs presented in the previous section, the motion of the mobile part of the MPS can be generalized into four different ways as presented in figure 2.12.

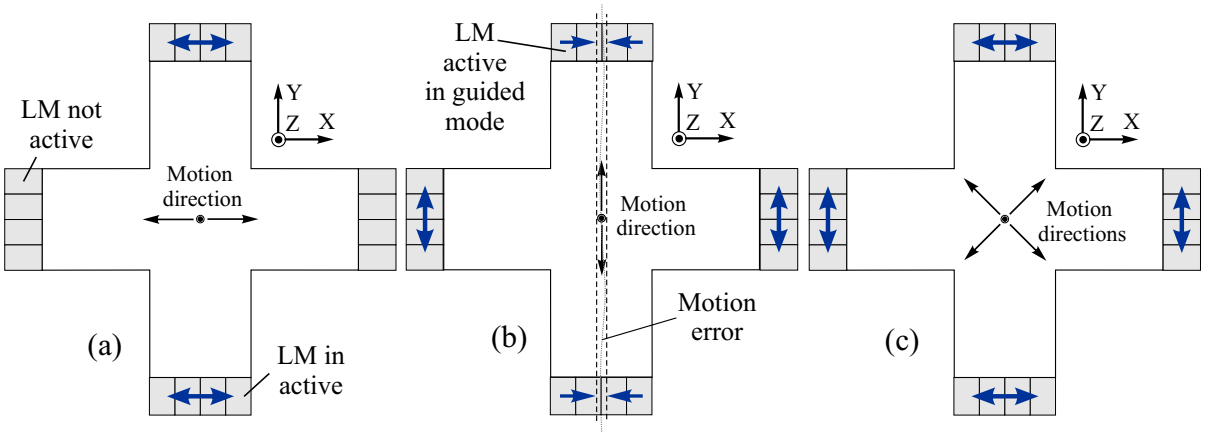

FIGURE 2.12: (a) Unidirectional motion (b) Unidirectional motion with guidance (c) planar motion

In the case of linear motion, two LMs are sufficient to drive the mobile part of the MPS as shown in figure 2.12 (a). In this case the characteristics of the injected currents are kept identical in the LMs located along motion axis. Further, the total generated translation force will be the sum of the forces generated by individual LMs that are active. However,

in real case scenario, these forces are not always identical. For example, the variation in the magnetic field due to the dimension tolerances of the PMs or due to the PMA assembly errors can lead to generation of different magnitude of the forces along an axis. This variation may introduce a drift effect of the mobile part during linear motion. To solve this problem, constant currents can be injected into the LMs situated perpendicular to the motion axis (see figure 2.12 (b)). These constant currents will guide the mobile part during linear motion and minimize the motion error due to the locking principle presented in figure 2.10 (b).

To realize planar motion, all four LMs are injected with sinusoidal currents. In this case the guidance along a single axis could not be achieved as shown in figure 2.12 (c). As a result, due to the generation of non-identical forces along single axis a small rotation may occur. However, because of this rotation a restoring torque (t_z) appears over each PMA during motion, which tends to align the mobile part with respect to PEDCs (see figure 2.13(a)). This phenomenon occurs due to the variation in the magnetic flux distribution over the length of the conductors in the PEDC during small rotation [Benc 06]. The magnitude of the restoring torque depends on several parameters such the magnitude of the injected current, the rotation angle, the air gap between the PMA and PEDC, etc. In order to identify the amount of the restoring torque, an analysis has been performed in a semi-analytical software RADIA® by rotating the PMA at a small angle ($\alpha = \pm 5°$) in the *xy*-plane with respect to the PEDC. For an injected current of 1A in the PEDC of a single LM, the amount of the restoring torque (t_z) on the PMA at different air gap values is shown in figure 2.13(b).

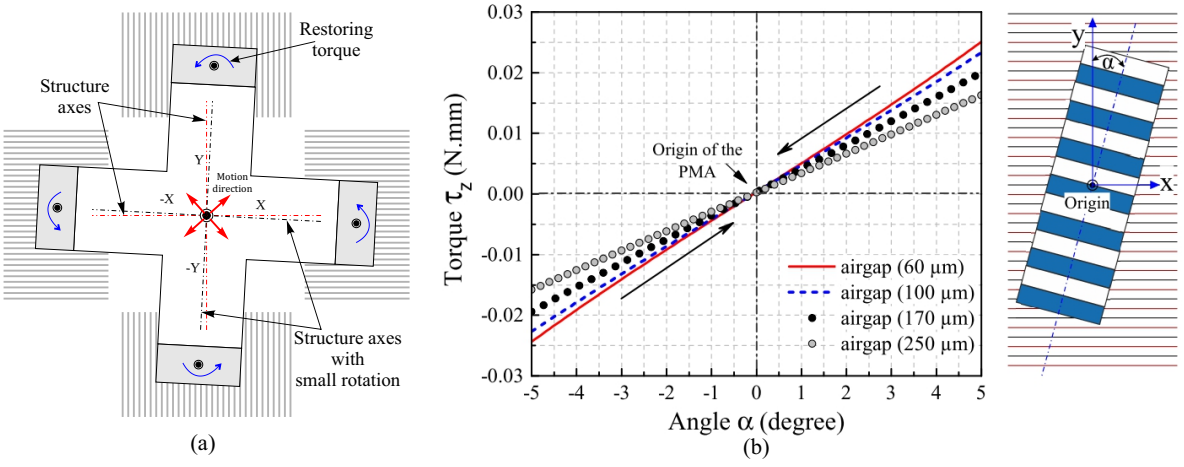

FIGURE 2.13: (a) Small rotation (b) Restoring torque

2.4 Modeling

In this section analytical modeling of the MPS has been carried out. For the purpose of simplification, the modeling has been performed for a single LM due to the symmetrical

design of the MPS. At first, the magnetic flux density distribution model have been realized. Then, the electromagnetic force computation model is presented. At the end, the mechanical model has been realized in this section. These models have been implemented with MATLAB® to study the dynamic behaviour of the system.

2.4.1 Magnetic flux density distribution model

The PMs used in our application are parallelepiped in shape with each having cross section 1×1 mm^2 and length 6 mm. Due to the finite length of the PMs, a three dimensional analytical model based on surface charge model was realized to compute the external magnetic flux density components B_{ext} at any point P(x, y, z) located outside the PMA. However, some assumptions have been carried out. These assumptions include, identical physical characteristics of all PMs in the PMA, perfect alignment of magnetic polarization of each PM along z-axis in free space and no variation in magnetization along the length of the PMs. Based on these assumptions, a single PM with is reduced to a distribution of equivalent magnetic charge as shown in figure 2.14 [Furl 01].

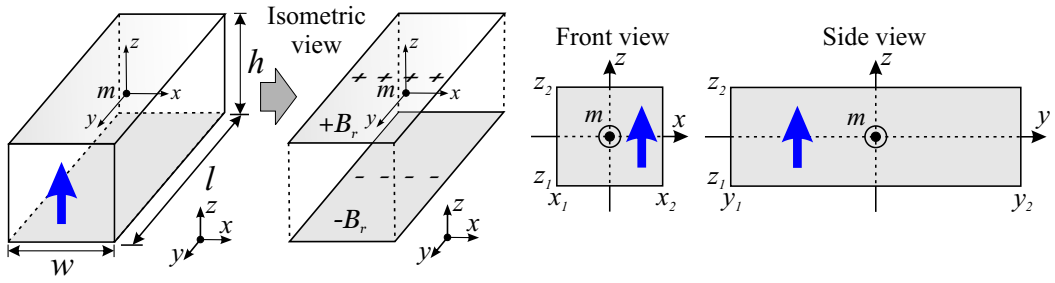

FIGURE 2.14: Reduction of a single PM to equivalent magnetic charge distribution and its 2D representation in reference frame

For a PM with the center located at "m" and dimensions $(x_2 - x_1), (y_2 - y_1), (z_2 - z_1)$ along three axes the analytical expression for magnetic flux density components B_x, B_z at any point located outside a single PM is provided in equation (2.6) [Furl 01].

$$B_x(x,y,z) = \frac{\mu_0 M_s}{4\pi} \sum_{k=1}^{2} \sum_{m=1}^{2} (-1)^{k+m} \ln \left(\frac{(y-y_1)+\left((x-x_m)^2+(y-y_1)^2+(z-z_k)^2\right)^{1/2}}{(y-y_2)+\left((x-x_m)^2+(y-y_2)^2+(z-z_k)^2\right)^{1/2}} \right)$$

$$B_y(x,y,z) = \frac{\mu_0 M_s}{4\pi} \sum_{k=1}^{2} \sum_{m=1}^{2} (-1)^{k+m} \ln \left(\frac{(x-x_1)+\left((x-x_1)^2+(y-y_m)^2+(z-z_k)^2\right)^{1/2}}{(x-x_2)+\left((x-x_2)^2+(y-y_m)^2+(z-z_k)^2\right)^{1/2}} \right) \tag{2.6}$$

$$B_z(x,y,z) = \frac{\mu_0 M_s}{4\pi} \sum_{k=1}^{2} \sum_{n=1}^{2} \sum_{m=1}^{2} (-1)^{k+n+m} \times \tan^{-1} \left(\frac{(x-x_n)(y-y_m)(z-z_k)^{-1}}{\left((x-x_n)^2+(y-y_m)^2+(z-z_k)^2\right)^{1/2}} \right)$$

where, B_x, B_y and B_z are the magnetic flux density components (T) along x-, y- and z-axis, respectively. μ_0 is the magnetic permeability of air ($4\pi \times 10^{-7}$ N·A^{-2}) and M_s is the magnetization of the permanent magnet (A/m).

In similar fashion, the solution presented in (2.6) is used to construct the magnetic flux density distribution model for "R" PMs assembled with NS configuration in a PMA. All PMs are reduced to the distribution of equivalent magnetic charge as shown in the figure 2.15.

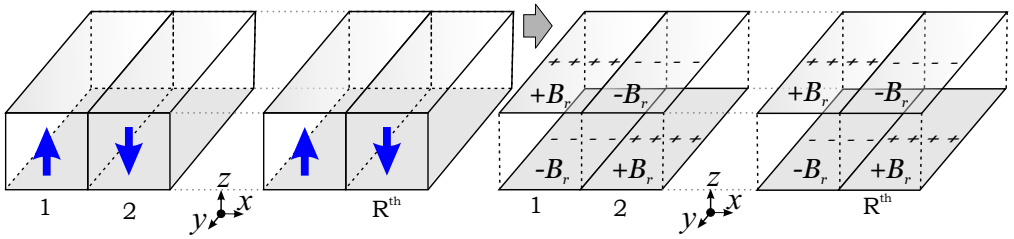

FIGURE 2.15: Reduction of the PMs in a PMA to equivalent magnetic charge distribution

The total magnetic field solution at any point in three dimensional space outside the PMA is the sum of the contribution of each PM assembled in the PMA at that point and is calculated using equation (2.7) [Furl 01].

$$B_{ext}\left(x,y,z\right)=\sum_{i=1}^{R}\left(-1\right)^{i}\times B_{ext}^{(i)}\left(x,y,z\right) \tag{2.7}$$

Where B_{ext} represents the external magnetic flux density component B_x, B_y and B_z that is computed using (2.6) and "*i*" is the index of the PM in the PMA.

The analytical model presented in (2.7) was implemented with MATLAB for a PMA with four PMs to illustrate the magnetic flux distribution in *xy*-plane. Moreover for simulation the vertical distance "*z*", which represents the air gap between PMA and conductors, was kept constant at 100 μm. Figure 2.16 represents the three magnetic flux density components of the PMA in free space.

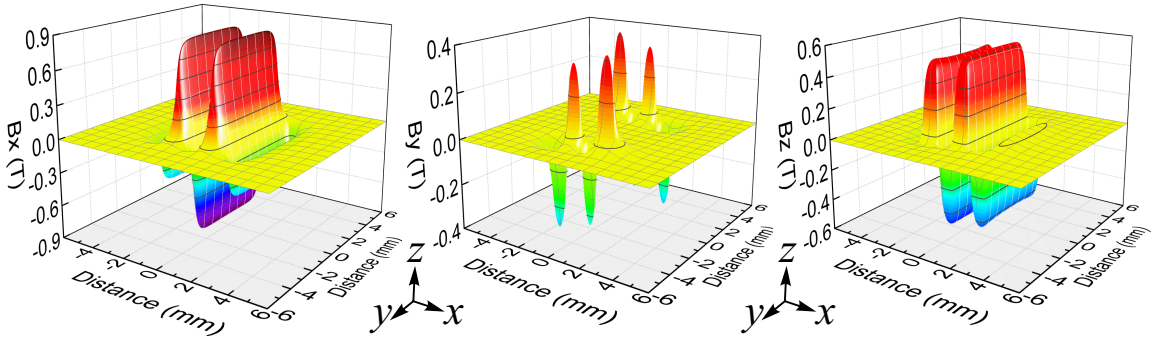

FIGURE 2.16: Reduction of single PM into equivalent current distribution

It can be concluded that over the PMA length (along *y*-axis), the B_y component of the magnetic field remains constant except at the edges of the PMA where its value is around 0.3 T. This effect is due to the concentrated magnetic field near the ends of PMs.

However, in our studies we have neglected this component in order to reduce the magnetic flux density computation time during our simulations. The main reason behind this assumption is that the contribution of this magnetic flux density component in the generation of the electromagnetic force is very small (see table 2.2). In addition, during motion the B_x and B_z magnetics field components are the ones responsible to generate translation and levitation forces. So, in this scenario the assumption for neglecting the B_y component can be justified.

Validation of the analytical model

In order to validate the magnetic flux density computation model for a PMA that consists of 14 PMs each having a cross section 1×1 mm^2, length 6 mm and remanent magnetization B_r=1.43 T was carried out using MATLAB©. The B_x and B_z magnetic field components generated by the PMA at an air gap of 100 μm were compared to Finite Element Analysis (FEA) result that was realized in COMSOL® with 8×10^5 mesh elements. The comparison of both components is shown in figure 2.17. The result reveals a good agreement with relative error in the order of 10^{-5} T.

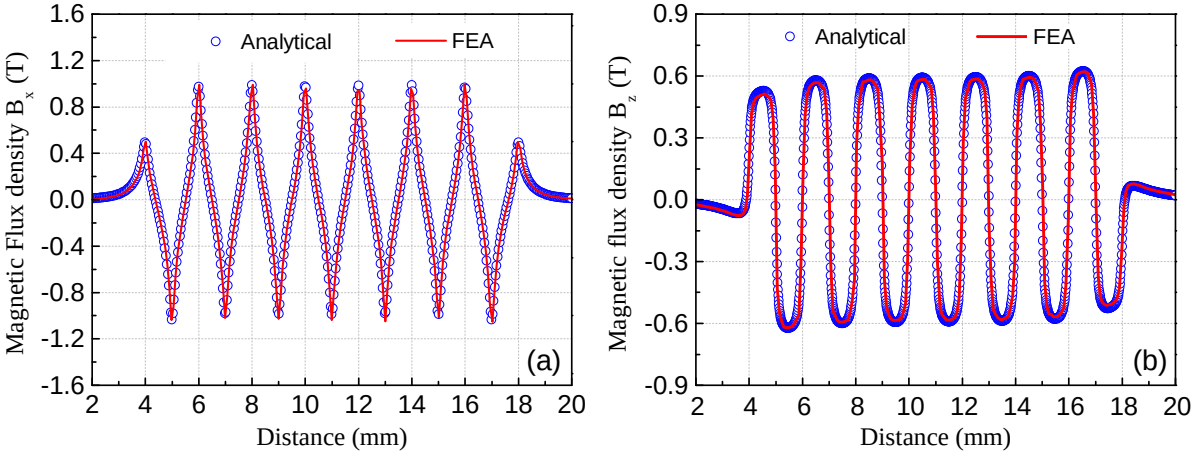

FIGURE 2.17: Comparison of the magnetic flux density components

In addition, another study has been performed to validate the analytical model (2.7) in the case of the small rotation of the mobile part about z-axis. In this case the B_x and B_z magnetic flux density components over the length of the conductor will vary due to the relative angle between the PMA and PEDC. So, a simulation has been performed in MATLAB© by rotating the PMA (consists of 4 PMs) at an angle "θ" as shown in figure 2.18. In order to implement the model in rotation case, the magnetic field computations have been carried out by meshing the PEDC along the length of the conductors. For a conductor length of 20 mm, the B_x and B_z were computed with 20000 mesh elements where each mesh element represents an increment of d_x =1 μm along the length of the conductor in x-axis.

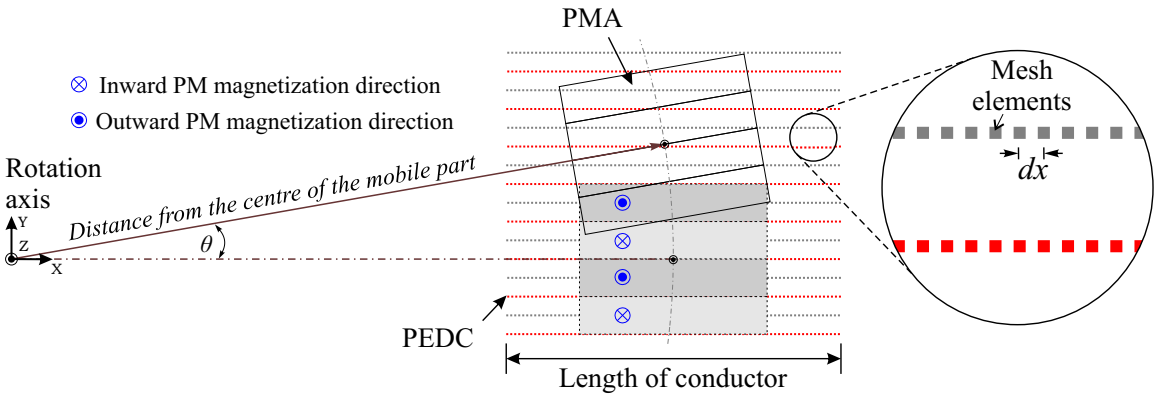

FIGURE 2.18: Magnetic flux density measurement in rotation

Figure 2.19 represents the comparison of magnetic field components (B_x and B_z) computed via analytical model (2.7) and FEA at θ=0°, 2.5°,5° rotation angles. From the comparison, a good agreement was found between the FEA and analytical model, thus this model can be used to represent the magnetic field variation over the length of PEDC.

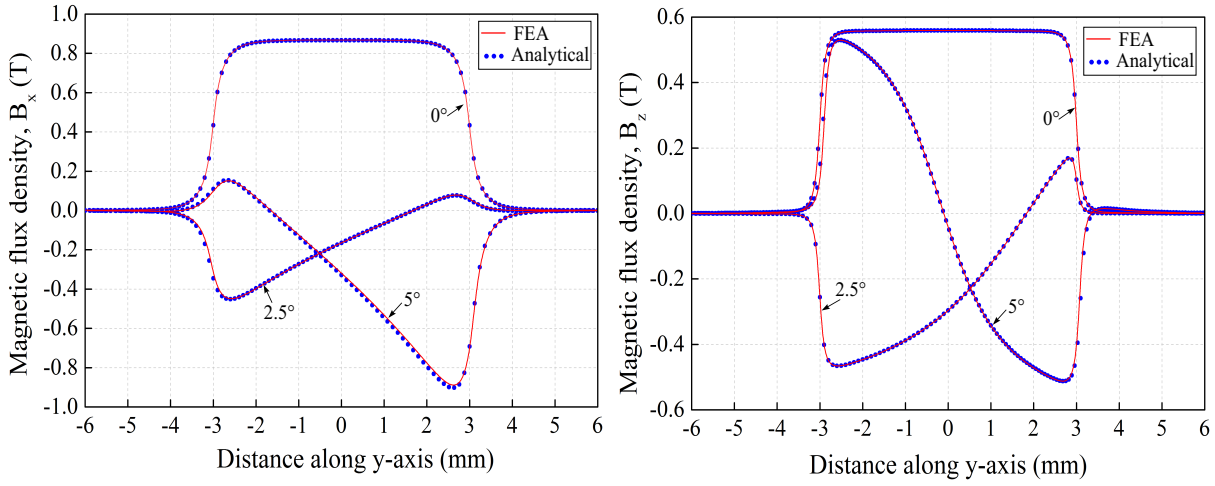

FIGURE 2.19: Comparison of the magnetic flux density components

Conclusion: The described analytical model is able to compute magnetic field components during translation and rotation motion. However, in rotation case the magnetic field computation time was found to be around 9.7 seconds as compared to translation case which is around 0.83 s. The reason of large computation time in rotation case is total number of mesh elements required to precisely compute the B_x and B_z over the conductors. Whereas, in translation case the number of these mesh elements can be significantly reduced with the assumption that the coils remain parallel to the PMAs. In addition, It can also be noted that the simulation is performed for a PMA realized with four PMs and in our case the PMA of single LM is realized with 14 PMs which further increases the magnetic flux density computation time. Numerous solutions can be adapted to minimize

the computation time such as with the help of Look Up Tables (LUT) the magnetic calculations can be done off line during dynamic simulations. However, due to the motion characteristics of the MPS proposed in this thesis, the translation and rotation cases are dealt separately because the rotation of the mobile can only be achieved by changing the direction of the injected currents in the PEDC.

2.4.2 Electromagnetic force and torque computation

The total force generated by a single LM is the sum of the individual forces that appear over each PM in the PMA and are computed using equation (2.8). Where, the B_{ext} is the external magnetic flux density component in *xz*-plane. Its computation has been carried out using (2.7). The superscript (k) denotes the relative position index for the magnetic flux density computation with respect to I_1 and I_2 current carrying coils in a PEDC. The *N* denotes the total number of the current carrying conductors in a single coil. In addition, the total force about the center of the MPS is the vector sum of the electromagnetic forces generated by each LM of the MPS. Further, due to the generated electromagnetic force along an axis, a torque will appear about the center of the stage. The amount of this torque for single LM was computed using equation (2.9). Where, *r* is the distance from the center of the PMA to the center of the mobile part (see figure 2.18).

$$F_{electromagnetic} = N \sum_{k=1}^{2} I_k \int_{wire} dl \times B_{ext}^{(k)} \tag{2.8}$$

$$\vec{\tau}_z = r \times \vec{F}_{electromagnetic} \tag{2.9}$$

In order to identify the magnitude of the generated electromagnetic force and torque, a static analysis has been performed for a single LM that consists of a PMA having 14 PMs and a PEDC having 60 conductors representing two phase coil currents. For a 0.8 A amplitude of injected currents in the PEDC at air gap of 100 μm the results are presented in table 2.2. It can be seen that the analytic computation provides a very good agreement with the relatively very small error in comparison with the results obtained with RADIA®. In addition, it can be seen that the magnitude of the F_y is very small as compared to F_x and F_z. This is due to reason that the currents in PEDC are parallel to the length of PMA, so the effect of this force is neglected in our dynamic simulations.

	Units	Radia®	Analytical model	Error
Translation force (F_x)	mN	36.61	36.91	2.98×10^{-1}
Levitation force (F_z)	mN	55.36	55.32	3.45×10^{-2}
Force (F_y)	mN	3.55×10^{-10}	8.17×10^{-12}	3.63×10^{-10}
Torque (τ_z)	N.mm	1.025	1.026	2.40×10^{-4}

TABLE 2.2: Static analysis of the electromagnetic force and torque for a single LM

2.4.3 Mechanical model

The fixed part of the MPS is insulated using a thin glass layer (thickness 130 μm) to provide a smooth motion surface for the mobile part due to the copper height (35 μm). Further, due to the assembly constraints the mobile part of the MPS is supported with the help of four hemispherical glass beads (see figure 2.20(a)). The detailed discussion regarding these assembly constraints has been carried out in the next chapter. The integration of the glass beads and thickness of the glass layer impose an air gap constraint as shown in the figure 2.20 (b). This air gap reduces the magnetic field intensity near to the coils which as a result reduces the magnitude of the generated electromagnetic force. Numerous solutions can be applied in order to increase the amount of generated electromagnetic forces. For example, increasing the number of PMs in the PMA can further increase the magnitude of the electromagnetic forces to compensate the reduction force loss due to the air gap. In addition, the smaller value of insulation layer can also improve the motion performance of the LM.

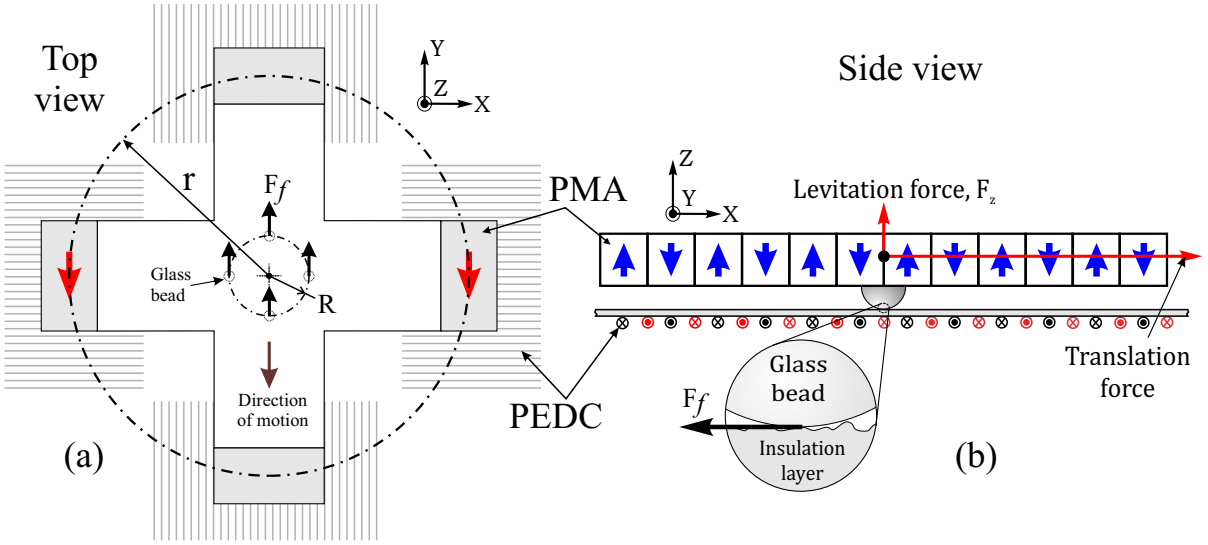

FIGURE 2.20: (a) Layout of the MPS with mechanical support (b) Detail view of a single LM with glass bead support

Due to the mechanical contact between the mobile part and the fixed part a friction force will appear as shown in figure 2.20(b). This friction force is defined as static and dynamic friction forces during the translation of the mobile part. In addition due to the generation of the levitation force during motion, the net weight ($W_{net} = W - F_z$) has been used to compute these forces using equation (2.10).

$$\begin{aligned} F_{static} &= W_{net} \times \mu_{static} \\ F_{dynamic} &= W_{net} \times \mu_{dynamic} \times sign(\nu) \end{aligned} \tag{2.10}$$

where, μ_{static} and $\mu_{dynamic}$ are the static and dynamic friction coefficients. ν is the velocity of the mobile part. In our study the static friction coefficient was experimentally measured (μ_{static} = 0.47) using an inclined plane technique, however, the dynamic friction coefficient ($\mu_{dynamic}$ = 0.43) was approximated due to the difficulty to distinguish between the two coefficients during experimentation. In addition, no data regarding dynamic friction was found for the material that is used as an insulation layer. In order to implement the friction force during dynamic simulations, the condition presented in equation 2.11 was adapted. According to this condition, if the generated electromagnetic forces enters in the range of [-F_{static}, +F_{static}] its value is set to zero. Otherwise, translation force (F_{net}) is computed using dynamic friction.

$$\begin{cases} if\ F_{net} < F_{static} \Rightarrow F_{net} = 0 \\ if\ F_{net} > F_{static} \Rightarrow F_{net} = F_{total} - F_{dynamic} \end{cases} \tag{2.11}$$

While neglecting the thermal and hysteresis effect as disturbances, Newton's second law is used to develop the general solution for translation as given in equation (2.12). The total displacement is computed with double integration of the acceleration $\ddot{x}$ (m·s^{-2}) of the mobile part.

$$\begin{aligned} F_{net} - F_f &= M\ddot{x} \\ \Rightarrow\ x &= \frac{1}{M} \iint_{t_0-t_1} (F_{total} - F_f)\, dt^2 \end{aligned} \tag{2.12}$$

where M represents the total mass of the mobile part in kg, t represent the time in seconds and x is the total displacement realized by the mobile part in meters.

Similarly due to small rotation about the center of the mobile part, the friction force will exert a resistive torque about the center of the stage. The amount of this torque is computed using $\vec{\tau}_f = R \times \vec{F}_f$, where R is the radial distance of the glass bead from the center of the mobile part (see figure 2.20 (b)). In addition, the torque generated by a single LM is computed via equation (2.9). The rotation angle realized by a single LM about the z-axis is computed using equation (2.13) by double integration of the angular acceleration $\ddot{\theta}_z$ (rad·s^{-2}).

$$\begin{aligned} \tau_{net} - \tau_f &= J\ddot{\theta}_z \\ \Rightarrow\ \theta_z &= \frac{1}{J} \iint_{t_0-t_1} (\tau_{net} - \tau_f)\, dt^2 \end{aligned} \tag{2.13}$$

where $\tau_{net} = R \times \vec{F}_{net}$ is the net torque in N.m, J is moment of inertia of the mobile part in kg.m^2, t represent the time in seconds and θ_z is the rotation angle about z-axis in radians.

2.5 Dynamic simulation of the MPS

In this section, the dynamic simulations have been carried out in order to study the motion behaviour of the MPS. Due to the symmetrical MPS design the control model will be discussed for a single LM. The analytical models developed in the previous section concerning a single LM has been implemented with MATLAB Simulink©. Further, the total weight (5.8×10^{-3}kg) of the mobile part (i.e. weight of the four PMA and the cross structure) was used during dynamic simulations.

For simplification purpose, the air gap (d) between the mobile part and the fixed part of the MPS was set to a constant value of 130 μm. This air gap represents the distance between the four PMA and their respective PEDCs. This constant value was adapted due to the reason that the residual levitation force ($F_z - W$) during motion is small ($\approx$ 10 mN per LM) for a maximum current value of 0.8 A. So, it was assumed that the levitation forces generated by each LM only helps to overcome the adhesion forces between the mobile part and fixed part due to the mechanical contact by compensating the weight of the mobile part during motion. In addition, due to the identical characteristics of each LM it was assumed that the small rotations do not occur to reduce simulation time. This is because, the similar characteristics of each LM lead to the generation of the same amount of translation forces, so the torque generated by each LM located along a single axis about the center of the mobile part will theoretically cancel each other.

2.5.1 Description of the simulation parameters for a single LM

On the basis of the assumptions presented above, a single LM was modeled with 14 PMs in a PMA with each PM having dimensions $1\times1\times6$ mm^3 and remanent magnetization B_r=1.43 T as shown in figure 2.21. The PEDC was modeled with an array of 50 conductors separated by a distance (d_a) of 500 μm and with each having length (L_c) of 20 mm. These conductors represent the two phase coils with currents I_1 and I_2 flowing through them with a relative phase difference of $\pi/2$. The pitch of a single coil turn is 2 mm which is equivalent to the period of the PMA (2π).

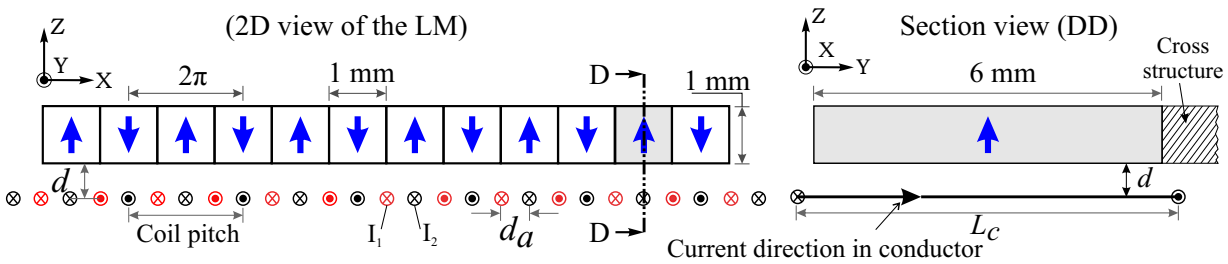

FIGURE 2.21: Detail description of a single LM attached to the cross structure

2.5.2 Open loop control

The open loop control of a single LM is presented in figure 2.22. The currents I_1 and I_2 are generated and injected to the force computation model to compute the Lorentz forces. This model takes into account the magnetic model (see equation (2.7)) to compute the magnetic flux density distribution of the PMA at the relative position (x, z) of the mobile part. The initial position of the PMA in order to compute the magnetic flux density was selected as (x_0=0, z_0=air gap). Further, the generated Lorentz force was inserted in to the mechanical model which calculates the displacement realized by the mobile part via equation (2.12). To realize these calculations, a 10^{-3} s simulation step size was selected in MATLAB Simulink© which corresponds to 1 kHz frequency of sinusoidal currents injected into the PEDC.

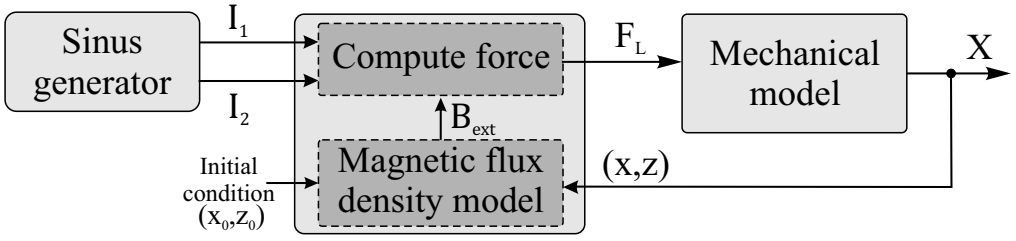

FIGURE 2.22: Schematic layout of the open loop control of a single LM

To perform a periodic backward and forward translation motion, the phase lead and phase lag concept was used by changing the phase of the current I_1 from $+\pi/2$ to $-\pi/2$ with respect to current I_2 as shown in figure 2.23.

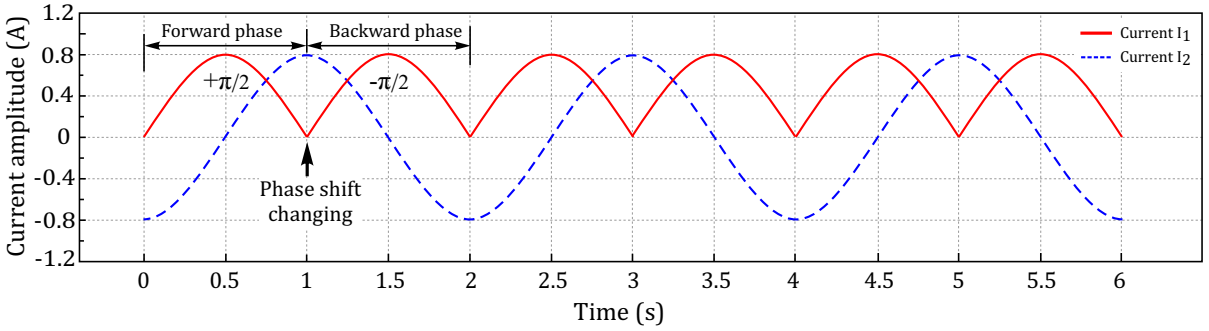

FIGURE 2.23: Currents I_1 and I_2 to realize forward and backward linear motion

To realize linear motion, a half period of sinusoidal currents are injected into the two LMs situated along a single axis. Figure 2.24 represents the three cycles of the forward and backward displacement realized by the mobile part along x-axis. The total displacement realized by the mobile part between the position A and position B was found to be 889.13 μm. The displacement loss can be explained by the dynamic friction effect during motion. Further, as only two motors are used to realize the linear motion, the total

weight of the mobile part is supported by the levitation forces generated by only two LMs. In addition, it can be seen that an adherence effect appears at positions A and B. At these positions the magnitude of the currents becomes very small which leads to generation of small levitation forces. These forces are not high enough to overcome static friction (see equation (2.11)) and as a result the mobile part does not perform any motion.

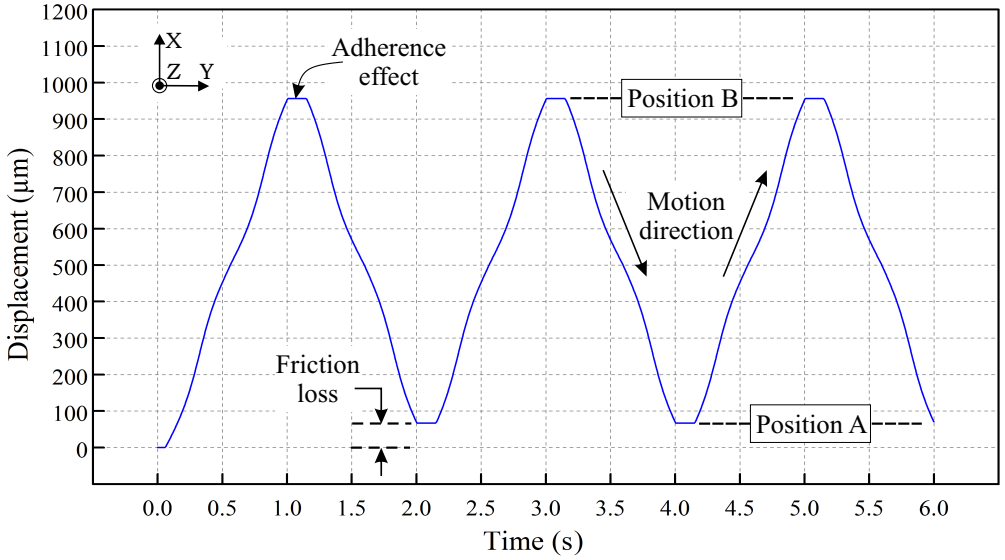

FIGURE 2.24: Open loop model of single LM

The displacement loss due to the dynamic friction during motion depends on the amplitude of the inject currents. For example, by employing a smaller amplitude of the currents, the displacement loss increases and vice versa. However, due to the open loop control, this loss is expected as the current value can not be adjusted during motion. In addition, during planar motion all four motors lead to the generation of much larger levitation forces which results in a total displacement of 961.73 μm along single axis. In our studies, this open loop control have been used to evaluate the experimental results.

2.5.3 Closed loop control

For precise positioning, a Proportional-Integral (PI) controller was adapted to the open loop control of a single LM as shown in figure 2.25. This control was selected due to its simple application and its ability to exhibit no steady state error due to the integrator [Benc 06]. In our application, this controller was used to control the sinusoidal currents (see equation (2.14)) that have been injected to the PEDC in order to generate electromagnetic forces for translation.

$$\begin{aligned} I_1 &= I_{max}\sin(\omega t + \varphi_i) \\ I_2 &= I_{max}\sin(\omega t + (\varphi_i + \pi/2)) \end{aligned} \tag{2.14}$$

Where I_{max} (A) is maximum current amplitude, ω (rad/s) is the frequency of the current, φ_i (radians) is the initial current phase and t is the time in seconds.

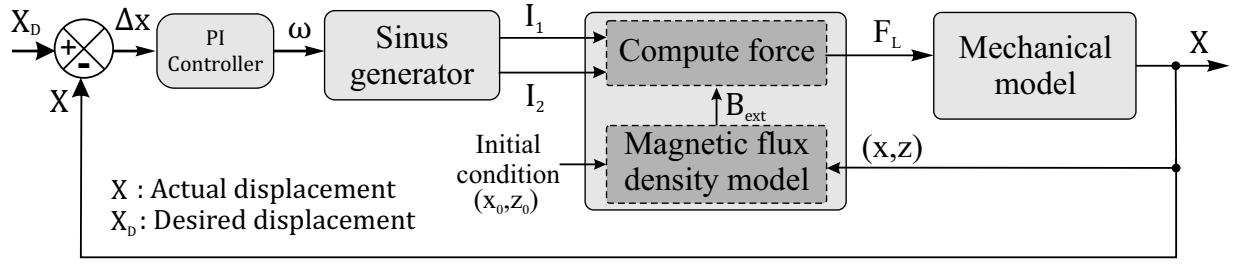

FIGURE 2.25: Schematic layout of the closed loop control of a single LM

The PI control algorithm presented in equation 2.15 has been adapted in order to reduce the displacement error ($\Delta x = X_D - X$) by changing the frequency ω of injected currents during motion of the mobile part. Where X_D (m) is the desired displacement, X (m) is the actual displacement realized by the mobile part, K_P (Hz/m) is proportional gain and K_I (Hz/m) is the integral gain. From this control it can be concluded that the frequency of the currents I_1 and I_2 tends toward zero when the displacement error reduces.

$$\omega = 2\pi \cdot \left| K_P \cdot \Delta x + K_I \int_{t_0 \to t_1} \Delta x \, dt \right| \tag{2.15}$$

Figure 2.26 represents the desired and actual displacement for different displacement steps such as 1 mm, 2 mm and 100 μm realized by the mobile part with 0.8 A sinusoidal currents. The $K_P = 7.5 \times 10^{-3}$ and $K_I = 5.5 \times 10^{-3}$ was selected for the simulations to avoid any overshoot with respect to the desired displacement. The settling time within

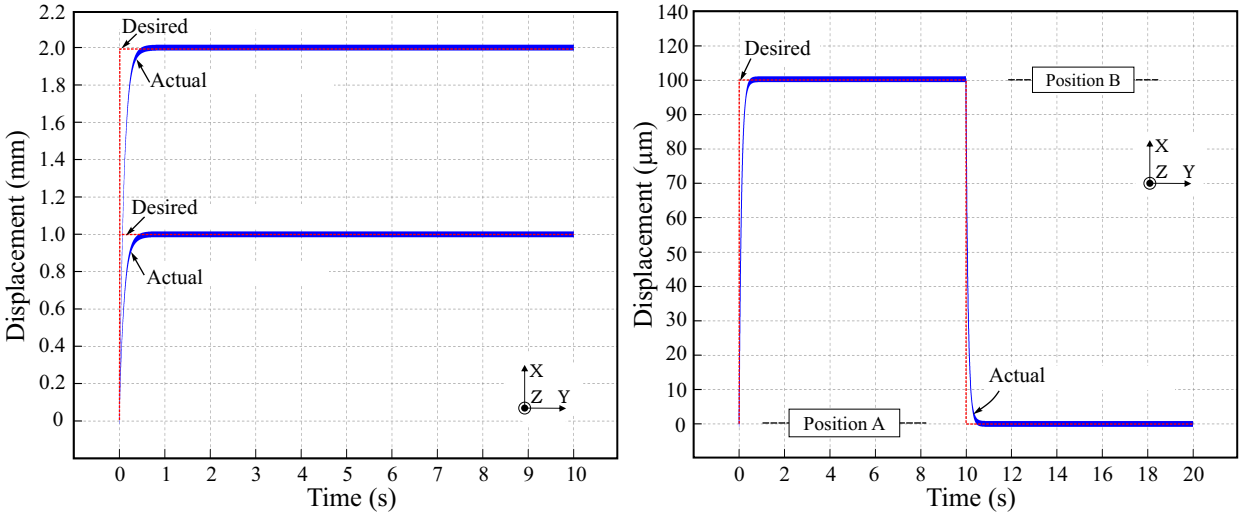

FIGURE 2.26: Step response along *x*-axis

the range of 2% value of the desired displacement value was found to be around 0.4 s in 1 mm and 2 mm case and 0.37 s in 100 μm.

Furthermore, a sinusoidal displacement with an amplitude of 100 μm (peak to peak) has been carried out to evaluate the motion tracking of the mobile part along single axis. The simulated result is presented in figure 2.27(a). In order to compare the result with the desired displacement values, a tracking error plot was realized by subtracting the desired displacement from simulated displacement response as shown in figure 2.27(b). It can be evaluated from the results that the PI control tends to retain the error with in $\pm$0.5 μm range. The displacement error peaks in the tracking error plot indicate the adherence effect.

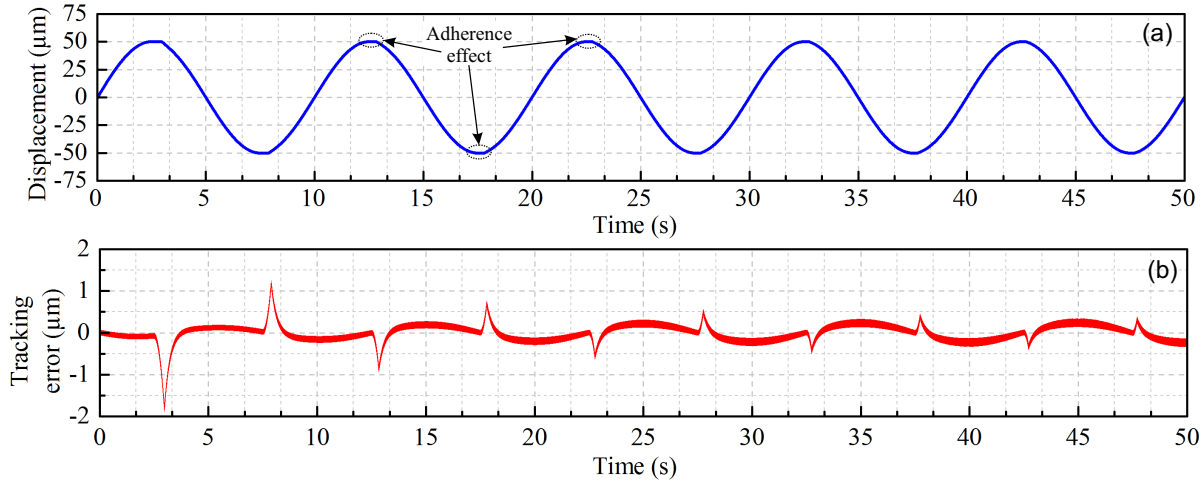

FIGURE 2.27: (a) Sinusoidal displacement response (b) Displacement error along *x*-axis

Regarding the planar motion behaviour, all four LMs are simultaneously used to generate translation and levitation forces. A 100 μm displacement in *xy*-plane has been realized by injecting 0.8 A currents into all four LMs. A ramp function with a slope of 10 μm/s was selected as a desired profile to gradually increase the displacement change.

The results presented in figure 2.28 illustrate that the mobile part experiences a time delay, (T_d=0.35 s) in order to realize the desired displacement trajectory. This is due to the adherence effect as for a very small displacement change, the magnitude of the generated electromagnetic forces are less than the static friction force. As a result, the mobile part does not perform motion. However, after this zone the controller adjusts the injected currents to achieve the desired displacement trajectory.

In addition, a 100 μm circular motion has been realized by using the same controller gain parameters adapted as in sinusoidal displacement case along single axis. The results presented in figure 2.29 show the response of four cycles of the circular motion profile realized by the mobile part in the *xy*-plane. From the results it can be concluded that

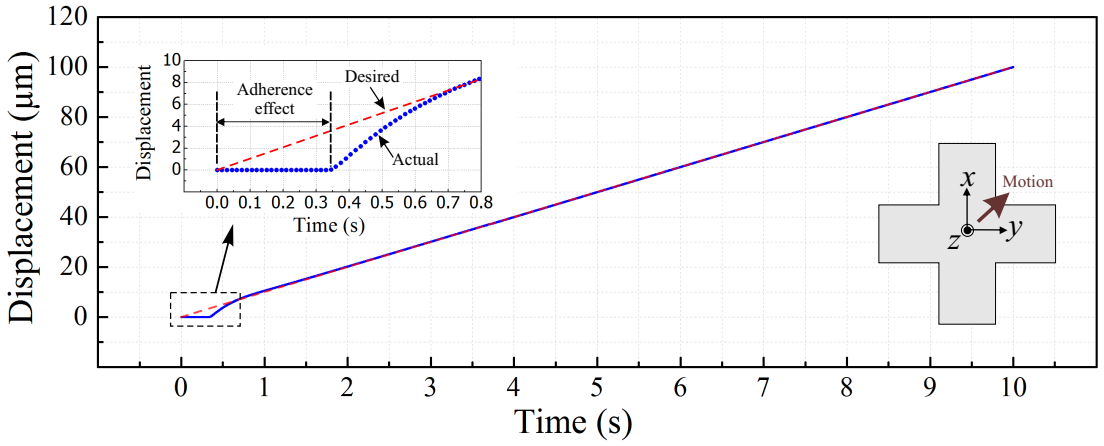

FIGURE 2.28: Linear motion realized by the mobile part in *xy*-plane

the controller successfully adapts the desired displacement profile however at angles 0, 90, 180 and 270° the response becomes linear due to the adherence effect as explained previously.

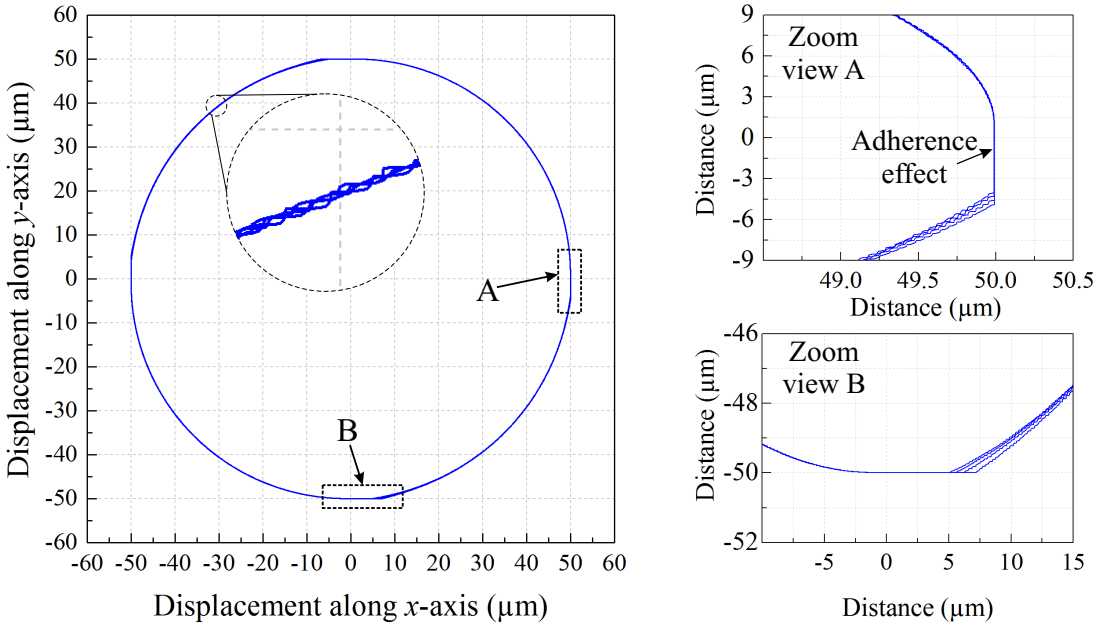

FIGURE 2.29: Simulated results of circular motion realized by the mobile part in *xy*-plane

The open and closed loop model developed in this section have been used to compare the experimental results in this thesis. In addition, due to the difficulty to adapt the real case scenario regarding the small variations in the forces generated by all four LMs, the small rotation effects are not simulated here in this work. However, the error generated by these small rotations during motion is very small due to the auto alignment feature of the mobile part with respect to the fixed part. In future studies, these errors may be included in order to investigate their influence during motion.

2.6 Conclusion

In this chapter, a Lorentz force based compact positioning system with a stack of four LMs in parallel configuration is presented. The overall design of the system consists of a mobile and a fixed part. The uniqueness of the proposed MPS lies in its simple design and ability to perform millimeter level strokes with pre-embedded auto guidance feature.

At first, the long range motion concept of the MPS has been explained with a functioning of a single LM due to the symmetrical design of the MPS proposed in this work. Further, taking into account the earlier research that has been carried out at our Roberval laboratory [Benc 06], the solutions adapted in order to realize the miniature drive components such as planar coils and permanent magnet array have been presented. In addition, a cross structure based orthogonal assembly of the four LMs has been selected to attain a symmetrical design. This assembly approach enhances the magnitude of the electromagnetic forces along single motion axis and reduces the number of input source lines. After description regarding the planar assembly and planar motion concept, modeling have been carried out in order to simulate the motion behaviour of the MPS. A three dimensional magnetic flux distribution model has been presented along with Lorentz force computation model. In addition, the mechanical modeling has been carried out which integrates both electromagnetic force computation model and friction forces computation model due to the mechanical support.

At the end, the developed analytical models have been used to evaluate the dynamic performances of the MPS in open loop control. For precise positioning, a PI control was adapted to realize a closed loop control model. From the simulation, the developed models have been evaluated by subjecting the MPS to different motion scenarios in open loop and closed loop control.

Chapter 3

Realization of the prototype and experimentation

In this chapter, the development of the MPS prototype and it's assessment to realize planar motion have been carried out. In the first part of this chapter, the detail design layout of the MPS and construction of it's components will be discussed. In addition, different design and fabrication solutions adapted to realize two parts based compact MPS will be presented. In the second part of this chapter, experimentations have been carried out in order to examine the different motion characteristics of the MPS in open and closed loop control. Different linear and planar motion trajectories have been realized to examine the dynamic behaviour of the complete system.

3.1 Design layout of the prototype and component description

The detail layout of the electromagnetically actuated MPS prototype is presented in figure 3.1 (a). As described in the previous chapter, it consists of two main parts that is a mobile part and a fixed part. The mobile part has been realized by assembling a mechanical cross structure with four PMAs. In order to support the mobile part over the fixed part, point contact technique was selected by fixing four glass beads from the bottom side of the mobile part as shown in figure 3.1 (b). The fixed part consists of four orthogonally arranged PEDCs fabricated into a single PCB to avoid assembly errors. In addition, a square through cavity was realized to fix a set of glass layers to support the mobile part (see figure 3.1 (b)). In order to illustrate the design parameters of the MPS in detail, the development of each component will be first presented in this section.

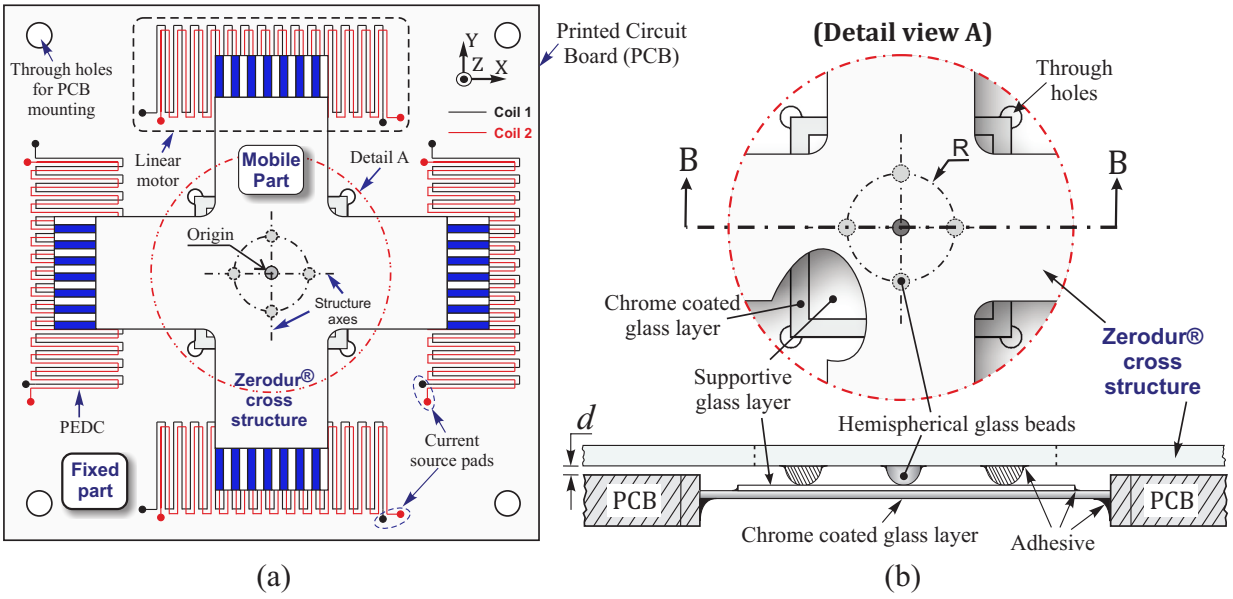

FIGURE 3.1: (a) Design layout of the MPS prototype (b) Detail view of the center

3.1.1 Mechanical cross structure

The mechanical structure of the mobile part is presented in figure 3.2. The design parameters of this structure was earlier proposed in the study [Benc 06]. According to this study, the cross structure design offers a 50% lighter weight as compared to square plate design for the same outer dimensions and material. The overall dimensions of the cross structure was selected in order to reduce/eliminate the generation of the parasitic magnetic field at the center area of the cross structure due to the PMAs. This magnetic field can disturb the functioning of the mobile part or any current carrying miniature component installed at the center area, e.g. displacement sensors, etc.

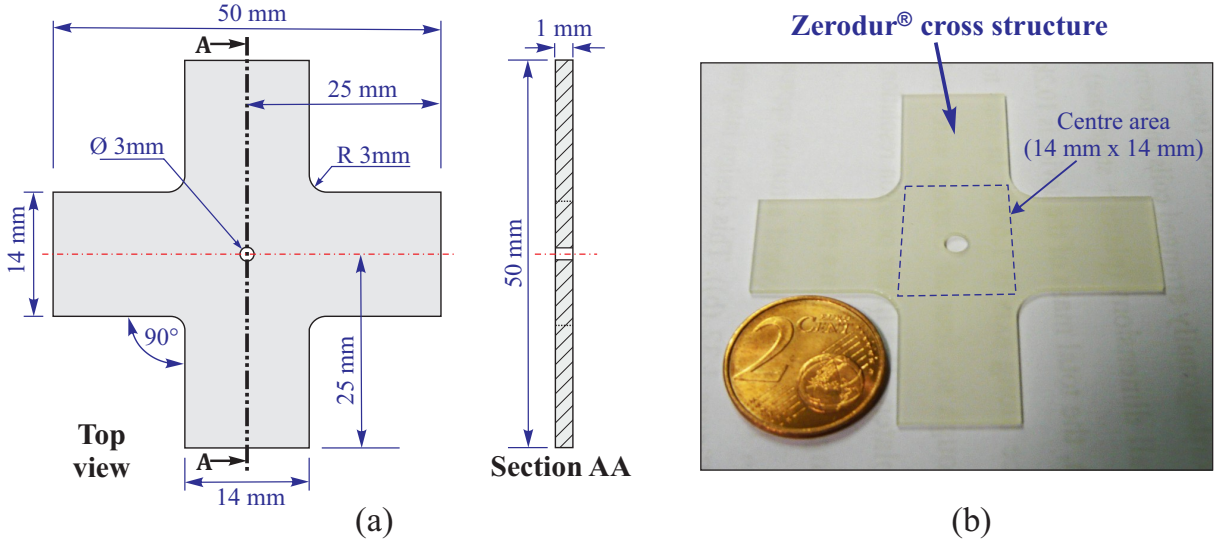

FIGURE 3.2: Geometrical design and fabricated mechanical cross structure

In addition, the cross structure design was realized in a 1 mm thick Zerodur® glass material via conventional machining (see figure 3.2(b)). This material was selected because of its low density (2530 kg·m^{-3}), high strength (90.3 GPa) and low thermal deformation coefficient (0.02$\times$10^{-10} K^{-1}) [Scho 10]. In our MPS prototype, we have used the same mechanical cross structure to build the mobile part due to the above mentioned characteristics. The weight of the fabricated cross structure presented in figure 3.2(b), is 2.3$\times$10^{-3} Kg. This small weight is due to the selected design dimensions and low density of the Zerodur® material, which is an additional advantage as it results in the construction of a light weight mobile part after assembling the four PMAs and sensory components.

3.1.2 Permanent Magnet Array (PMA)

The translation forces can be generated with even a single period of PMs arranged with NS arrangement in a PMA as described in previous chapter. However, in order to compensate the total weight (8.41 g) of the mobile part with generated levitation force during motion, the PMA of a single LM has been realized with 14 PMs. The total weight of the mobile mainly includes the weight of the mechanical structure (2.3 g), weight of all four PMAs (2.4 g) and the weight of the mirror cube used for displacement measurement ($\approx$ 3.7 g).

In the mobile part, the number of PMs assembled in a set of PMA are limited due to the edge dimension of the Zerodur® cross structure. Moreover, each PM is parallelepiped in shape with the cross section 1$\times$1 mm^2 and length 6 mm. These dimensions for a single PM were selected in manner to align the magnetization poles with respect to the pitch of the coil in the PEDC (see section 2.2.1.3) and reduce the Joule heating effect by minimizing the overall resistance of the PEDC designed for 10 mm displacement stroke. To realize the PMA with these specifications, the PMs were purchased from supermagnete[1] GmbH in Neodymium Iron Boron (NdFeB) material with gold coating to protect it from corrosion. This material was selected because of its high remanent magnetization (1.41-1.47 T) and high coercive force (1138-1043 kA/m) [Benc 06]. These characteristics of this material lead to the generation of high electromagnetic forces in miniature design.

3.1.2.1 Mobile part assembly

In practice, the PMA was realized by first finding the orientation of a single PM with the help of a reference PM[2] with marked South pole. Then, by fixing the first PM on a flat surface to avoid its orientation due to earth magnetic field, the rest of the PMs are placed near to it one by one to form a set of 14 PMs. Due to the opposite magnetic pole orientation, the PMs orient and attach automatically to the set of the PMA. This self

[1] http://www.supermagnete.de
[2] Honeywell, 101MG7, http://www.radiospares-fr.rs/

assembly is fairly easy as it does not require any precise alignment tools or bonding agent. Figure 3.3 (a) represents the real view of a PMA.

After realizing the four sets of PMAs, each one is fixed to the side edges of the Zerodur® cross structure as shown in figure 3.3 (b). A thin layer of cyanoacrylate glue was applied to the assembly area (1×14 mm^2) and the PMA with pre-assembled PMs in NS configuration was manually pressed against the assembly area for a short period of time. This assembly approach was selected from the perspective to use both sides of the PMA with the help of two PCBs placing on top side and bottom side of the PMA due to the magnetic field symmetry. In addition, the separation distances (d_1 and d_2) between the top and bottom PEDCs with respect to PMA surfaces can manually be adjusted to achieve desired electromagnetic forces (see figure 3.3 (c)).

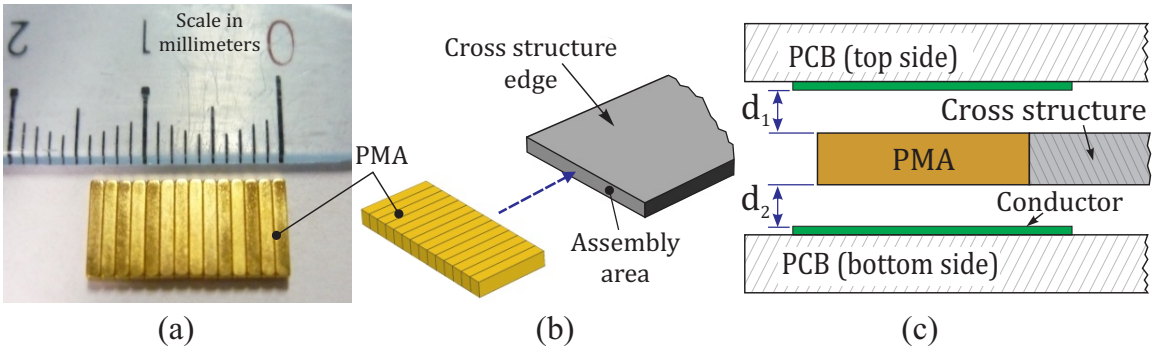

FIGURE 3.3: (a) Real view of a single PMA (b) Assembly approach (c) Implementation of top and bottom PEDCs over PMA

The separation distance is one of the most important parameters in the generation of the levitation forces to compensate the overall weight of the mobile part. Moreover, as described in the previous chapter, the friction force value depends on the residual levitation forces (F_{net}=F_z-W) generated during motion. So, in order to identify the maximum limit of the separation distance "d" between the mobile part and fixed part, a static analysis has been performed in RADIA® to compute the levitation force (F_z) with 0.8 A currents in the PEDC for different air gap values. The total levitation force is the sum of the levitation forces generated by each active LM during motion.

Figure 3.4(a), represents the generated levitation force in two motion scenarios of the mobile part, i.e. linear motion along single axis and planar motion in *xy*-plane. For both cases, the residual levitation forces (F_{net}=F_z-W) have been computed using the total weight of the mobile part (W = 82.50 mN) as shown in figure 3.4(b). From analysis, it has been concluded that for worst motion case scenario when only two LMs are used to compensate the total weight of the mobile part, the separation distance between the PMA and PEDC must be less then 140 μm to avoid the adherence effect during motion. In planar motion case scenario, all four LMs are used so at separation distance of 140 μm between

the mobile part and the fixed part the magnitude of the residual levitation force becomes very large. Due to this effect, the load carrying capacity can be increased accordingly.

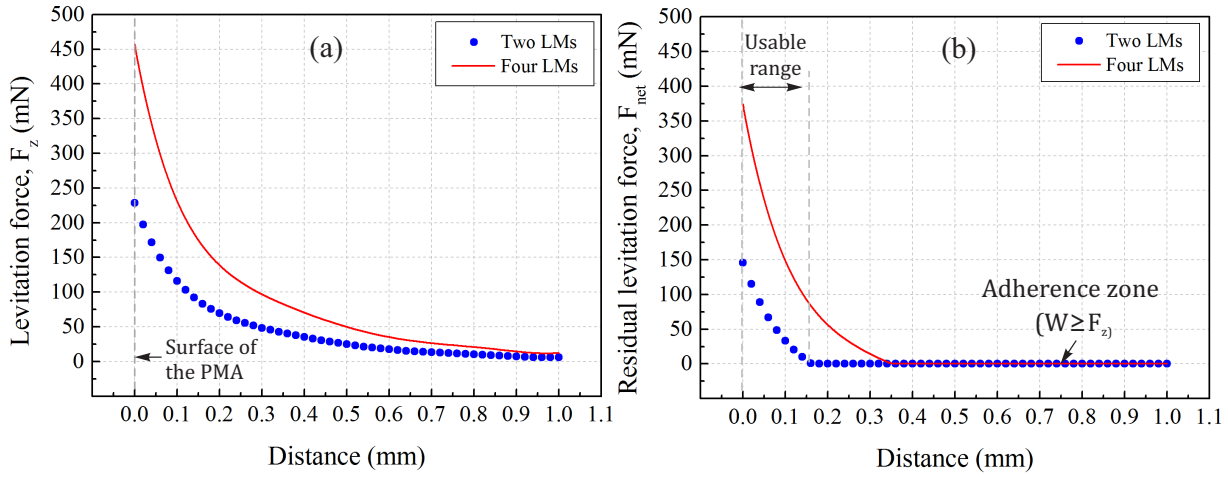

FIGURE 3.4: (a) Levitation force generated in linear and planar motion cases at different air gaps (b) Residual levitation force

Several solutions may be adapted to realize the separation distance between the mobile part and the fixed part. For example, the solution proposed in [Benc 06] was to use a flat glass layer (thickness≈ 130 μm) as shown in figure 3.5(a). However, this solution demands a small assembly offset to avoid any contact between the mobile part and the glass layer due to mechanical deformation of the cross structure when subjected to small load. The main drawback of this approach is that the separation distance can not be minimized due to the thickness of the glass layer. In our design an alternate solution has been adapted by fixing four 0.5 mm diameter hemispherical glass beads to the cross structure to achieve a much smaller separation distance ($d = z_2 - z_1$) as shown in figure 3.5(b). Further, to support the mobile part, the glass layer has been fixed at z_1 distance in a through cavity realized in the fixed part (see figure 3.1(b)). These glass beads have been glued to the bottom side of the cross structure as shown in figure 3.5(c).

3.1.3 Fixed part

In order to construct the fixed part of the MPS, first, the designing of a single PEDC that consists of two phase coils with currents I_1 and I_2 has been carried out. For a PMA with a foot print area ($w_c \times l_c$) of 6×14 mm^2, the PEDC was designed with an array of 52 conductors, each having length l=20 mm and separated by a distance 500 μm. This separation distance (a) was selected to attain a coil pitch (P_c) of 2 mm in order to align the magnetic poles of the PMs in the PMA with respect to conductors. Further, due to the PCB fabrication constraints, a conductor width (w) of 250 μm was adapted which results in an air gap (m) of 250 μm between adjacent conductors as shown in the cross section view in figure 3.6(a). Moreover, the number of the conductors and their length

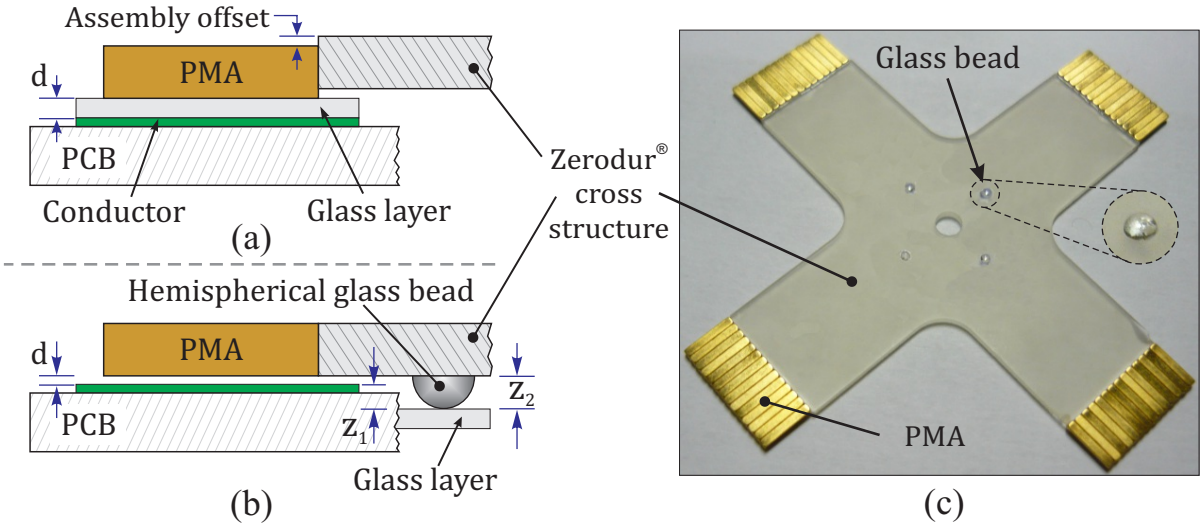

FIGURE 3.5: (a) Use of glass layer (b) Variable separation distance via point contact approach (c) Complete mobile part

parameter in a single coil of the PEDC have been optimized to achieve minimum coil resistance (0.86 Ω) to reduce Joule heating. The selected design parameters of the PEDC led to an foot print area of 384 mm^2 for a single LM.

After defining the design parameters of a single PEDC, the fixed part of the MPS was constructed with a circular array of the orthogonally separated four PEDCs in *xy*-plane. The center to center distance (D= 56 mm) between the PEDCs situated along single axis was selected due to the dimensions of the mobile part as shown in figure 3.6(a). While taking in to account the PCB fabrication edge tolerances (f_1, f_2) of 2 mm, the minimum foot print size ($L \times W$) of the fixed part was set to 80×80 mm^2. In addition, at the center of the fixed part, a through cavity of 30×30 mm^2 dimensions was defined in order to fix the glass layers to support the mobile part. These dimensions were selected in order to avoid complexity during assembly of the mirrors into the PCB.

3.1.3.1 Motion range

The planar motion range of the mobile part with above mentioned fixed part dimensions are found to be 10×10 mm^2 about the center of the fixed part in *xy*-plane. This range is limited due to the length (w_p) of the PEDC which can be increased by adding more number of conductors in the PEDC. However, the addition of conductors may lead to problems like conductor overlap (see figure 3.6(a)) and increase in the overall resistance of the coil. In our MPS design, we have avoided these constraints in order to reduce the fabrication complexity of the PCB.

For the selected design parameters of the fixed part, the rotation range of the mobile part about *z*-axis can be geometrically defined. A geometrical limit for which all the PMAs remain in the boundary of their respective PEDC (see figure 3.6(b)) has been selected

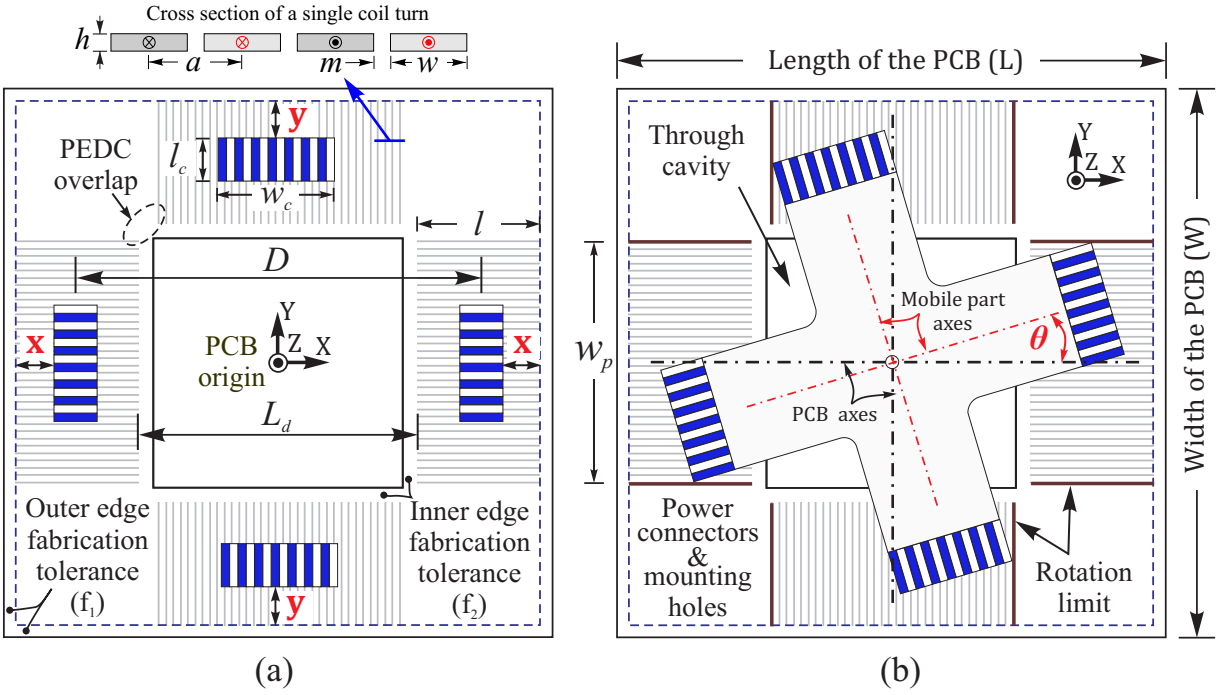

FIGURE 3.6: (a) Fixed part dimensions along with partial view of the PMAs aligned to each PEDC (b) Rotation of the mobile part

in our case. This choice has been made in order to continuously expose the current carrying conductors to the full width (w_c) of the PMA which is necessary to realize a symmetrical torque along both axes of the mobile part. On the contrary, if the PMA exits the PEDC area, a sudden reduction in translation force over the PMA may appear which can lead to unsymmetrical torques along both axes, thus making it more difficult to control. In addition, this geometrical limit also eliminates the possibility of any contact between the PMAs and the power connectors that are located at the corners as shown in figure 3.6(b). Based on this geometrical limit, the maximum rotation of the mobile part can be geometrically calculated using equation (3.1).

$$\tan\theta \leqslant \left[\frac{w_p - 2w_c}{(D - l_c) - 2l}\right] \tag{3.1}$$

This equation takes into account the geometrical parameters of the fixed part and the mobile part (see figure 3.6) to determine the maximum rotation limit of the mobile part. However, apart from the geometrical calculation, the magnetic field distribution of the PMAs over PEDC is one of the main criteria that limits the rotation capacity. As presented in the previous chapter, the increase in the relative angle between PMA and PEDC in *xy*-plane, results in the reduction of the torque about the center of the mobile part due to the magnetic field variation over PEDC. In this scenario, the injected currents will not be able to rotate the mobile part for large (i.e., >10°) rotation angles.

3.1.3.2 Printed Circuit Board (PCB) fabrication

In order to realize the fixed part, the PCB layouts was designed in CadSoft EAGLE PCB Design Software[3] to meet commercial PCB fabrication standards. The approach for fabricating the PEDCs on a single PCB was selected to eliminate assembly errors and achieve uniform dimensions i.e. copper width, height, air gap, etc.

After developing the PCB design, it was fabricated from Multi Circuit Boards Ltd[4] into a 1.5 thick double sided PCB as shown in figure 3.7. The connection between the coil turns of a single coil have been carried out from the bottom side using through vias as shown in the enhanced view of the bottom side. In order to facilitate the mounting and alignment process of the PCB during experimentation, some alignment and mounting holes have been fabricated.

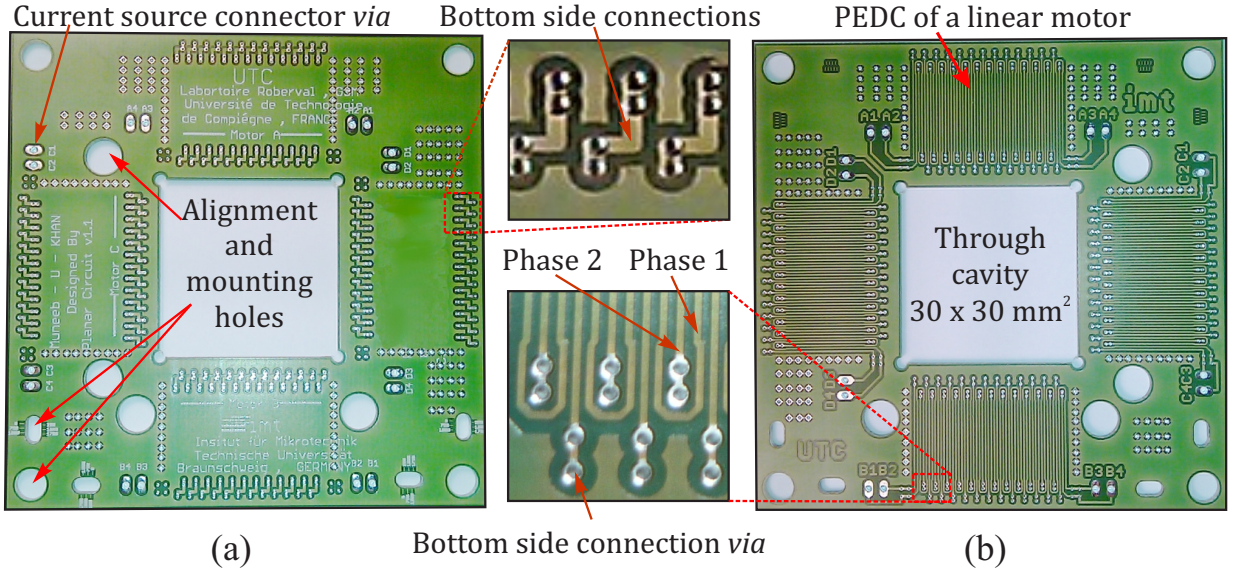

FIGURE 3.7: Fabricated PCB (a) Bottom view (b) Top view

Furthermore, to support the mobile part (via glass beads) over the fixed part, a set of glass layer were installed at the center cavity of the PCB. This set of glass layers consists of a 130 μm thick fine glass layer and a 0.7 mm thick supportive glass layer. The highly polished surface of the fine glass layer was used to achieve the smaller value of friction coefficient between the glass beads and glass layer it self. However, the direct installation of this layer in the PCB cavity was avoided in order to eliminate the possibility of any deflection due to the weight of the mobile part. In addition, the handling of this glass layer was difficult due to its less thickness. So, to solve these problems, an additional chrome coated glass layer with dimensions $30\times30\times0.7$ mm ^{3} was used. Another purpose, for using this coated thick glass layer was to achieve a reflective surface so that the fixed part can be leveled using a laser during experimentations.

[3]http://www.cadsoftusa.com/
[4]http://www.multi-circuit-boards.eu/

In order to assemble the set of glass layers in the PCB through cavity, the process presented in figure 3.8 has been adapted to realize a 100 μm air gap between the mobile and the fixed part of the MPS. The assembly has been carried out from the bottom side of the PCB. A combination of different set of glass layers (e.g. glass layer A, B and glass wafer, see figure 3.8) having different thickness was used to achieve the desired height in the through cavity of the PCB to assemble the chrome coated supportive glass layer. In addition, the copper track height (35 μm) along with the height of the glass beads that are assembled to the mobile part (see figure 3.5) have been taken into account to compute the required assembly height to generate 100 μm air gap. After acquiring the assembly height, the supportive glass layer was fixed to the PCB along its edges from the bottom side using cyanoacrylate glue. Upon successive bonding, the PCB with assembled supportive glass layer was released and the fine glass layer was glued on the supportive glass layer from the top side as shown in the figure 3.8.

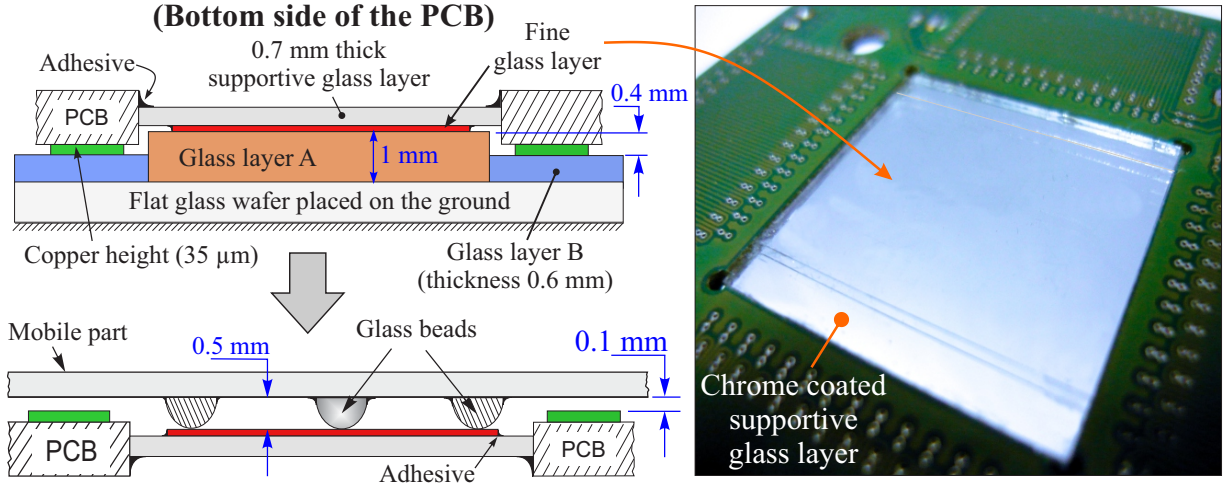

FIGURE 3.8: Assembly of the set of glass layer into the PCB through cavity

3.1.4 Analysis of the MPS prototype components

The proposed MPS is designed for conveyance purpose and precise positioning in micro applications. This implies that in practice, the center of the mobile part will be installed with a small load. However, due to the electromagnetic actuation principle and design parameters adapted for the MPS, the influence of the LMs on that load need to be assessed in order to qualify the design for experimentation. So, in this section, some analyses have been performed in order to examine different influential parameters at the center of the mobile part.

3.1.4.1 Influence of magnetic field generated by PMAs

In the mobile part, the PMs assembled to the cross structure will generate some parasitic magnetic field. This can disturb the characteristics of any object susceptible to magnetic field placed at the center area of the cross structure (14×14 mm^2) as shown in figure 3.9(a). For example, in biomedicine applications, this parasitic magnetic field can alter the characteristics of micro cells in the specimen. So, a study has been conducted in order to identify the magnitude of this parasitic magnetic field. This study indicates that the magnetic induction due to the PMAs is 1.28×10^{-5} T. From the results presented in figure 3.9(b) it was concluded that the magnetic induction generated by the PMAs is very small. So, its influence on any object placed at the center area can be neglected.

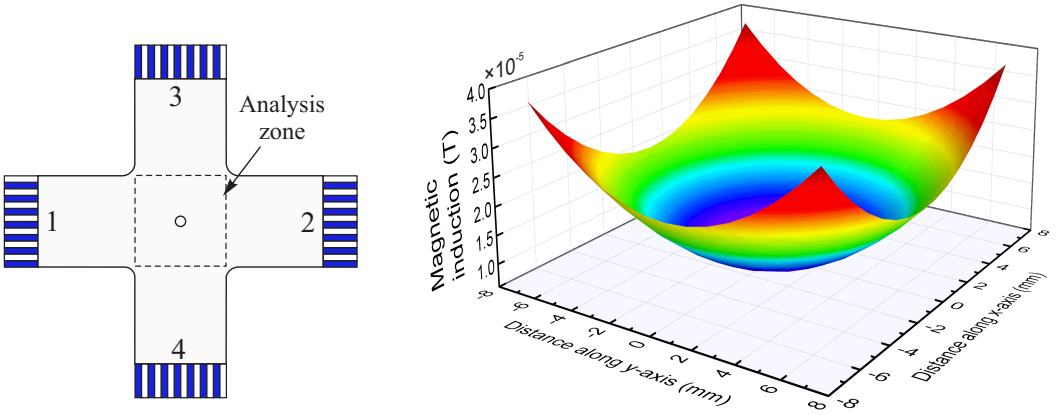

FIGURE 3.9: Magnetic induction at the center of the mobile part

In addition, a single PMA (e.g. PMA at position 1) will also be subjected to a static magnetic force due to the rest of the PMAs (i.e. PMAs located at position 2,3,4) in the assembly. An analysis has been performed in RADIA® which revealed that for the selected design dimensions of the mobile part, the magnitude of the static magnetic forces is 3.83 μN. This force is very small and its influence is negligible as compared to the electromagnetic forces generated by a single LM (i.e. 35 mN).

3.1.4.2 Influence of the vibrations

During functioning of the MPS, the horizontal component of the electromagnetic force (F_x) is responsible to drive the mobile part, whereas, the vertical component (F_z) tends to levitate the mobile part. However, the magnitude of this force does not remain constant and as result a small variation in the form of vibrations occurs. The influence of these vibrations generated by each LM can lead to a resonance condition in which the Zerodur® cross structure can fail. In order to examine the influence of these vibrations, first, an analysis has been carried out in order to determine the natural frequency of the structure.

Modes	**1**	**2**	**3**	**4**	**5**	**6**
Structure without load (Hz)	3320	7340	7340	12400	12700	15700
Structure with load (100 g) (Hz)	665	4152	4507	6711	7027	7304

TABLE 3.1: Natural frequencies of the Zerodur® cross structure, [Benc 06]

Table 3.1 represents the corresponding natural frequencies for the first six modes of the cross structure. These frequencies limit the MPS to be used at certain speeds. For example, the displacement at speed 33 mm/s corresponds to the injected current frequency of 3300 Hz, which represents the first mode of the cross structure. During our experiments, the maximum frequency that has been employed is 1 kHz which corresponds to a speed of 10 mm/s. Due to this constraint, the MPS cannot be used at the frequencies presented in table 3.1. However, the interval between the two natural frequencies can be used.

In order to examine the structure under vibrations, an analysis has been carried out (in the Abaqus software) by employing a sinusoidal displacement of 10 μm at the extremities (the faces where PMAs have been attached). The displacement of the center of the cross structure is plotted as a function of excitation frequencies at the extremities of the cross structure.

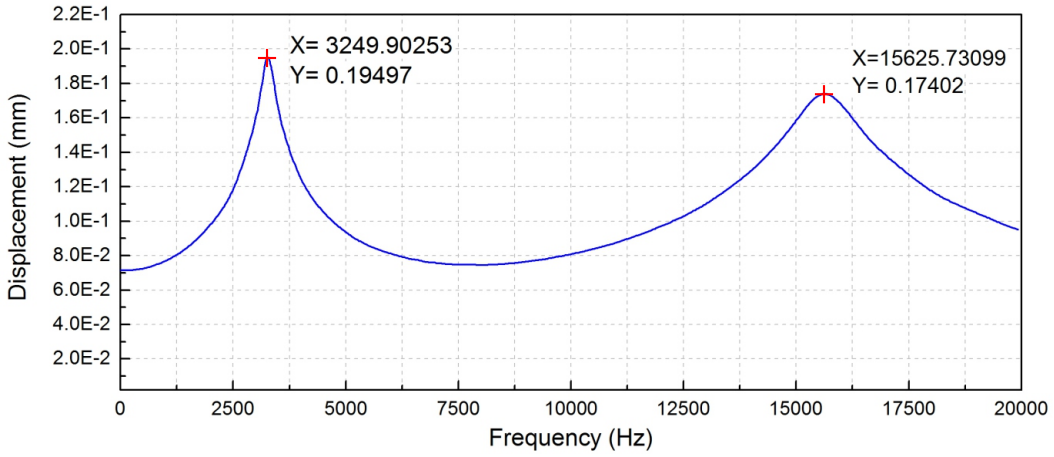

FIGURE 3.10: Response of the cross structure with excitation frequency

The analysis reveals two resonance frequencies for which the amplitude (195 and 174 μm) is 10 times more then the source amplitude (10 μm). These resonance frequencies correspond to the 1^{st} and 6^{th} modes. From the results it can be concluded that the cross structure cannot be used at higher frequencies. However, in our experimentation, the zerodur® cross structure has been used at lower frequencies ($<$ 1kHz) which is three times less excitation frequency then to reach the first mode of vibration.

3.1.4.3 Assembly errors and their correction

In practice, the manual assembly of the mobile part can results in some relative assembly errors between the PMAs located along a single axis of the mobile part as shown in figure 3.11. These errors can lead to misalignment of the generated electromagnetic force along an axis during motion. For example, in the case presented in figure 3.11(a), the forces generated about the center of the each PMA located along an axis (e.g. *x*-axis) are offset by a relative distance of Δx (mm). Due to this offset a small rotation about the center of the mobile part may appear. In order to solve this problem, the relative phase of the injected currents (I_1, I_2 and I_3, I_4) between the LMs situated along single axis has been modified by adding a corrective term ($\Delta\psi_x$) as presented in equation 3.2. In addition, this solution is valid for any misalignment between the LMs along *y*-axis or the PEDCs along both axes.

$$\underbrace{\begin{aligned} I_1 &= I_{max}\sin(\omega t + \Delta\psi_x) \\ I_2 &= I_{max}\sin(\omega t + (\tfrac{\pi}{2} + \Delta\psi_x)) \end{aligned}}_{Currents\ in\ the\ PEDC_1\ of\ the\ LM_1} \qquad \underbrace{\begin{aligned} I_3 &= I_{max}\sin(\omega t) \\ I_4 &= I_{max}\sin(\omega t + \tfrac{\pi}{2}) \end{aligned}}_{Currents\ in\ the\ PEDC_2\ of\ the\ LM_2} \tag{3.2}$$

with,

$$\Delta\psi_x = \frac{2\pi\,\Delta x}{P_m} \tag{3.3}$$

where, P_m is the period of the PMA (in our case, P_m = 2 mm), ω and I_{max} is the frequency and amplitude of the injected currents, respectively.

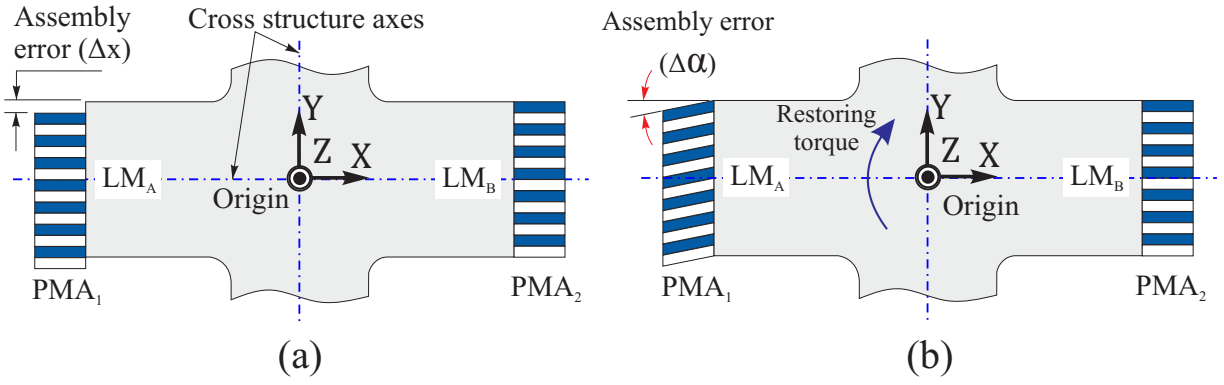

FIGURE 3.11: Assembly errors in the mobile part

Figure 3.11(b) represents angular misalignment error $\Delta\alpha$ (degrees) of a single PMA along an axis. The appearance of this error is linked to several parameters such as fabrication tolerances of the PMs, improper machining of the cross structure edge, uneven thickness of the bonding resin between the PMA and the cross structure, etc. The presence of this error results in non uniform distribution of the magnetic field over the conductors in the PEDC. As a result, during motion the auto alignment feature of the LMs will tend to

align the PMA with respect to conductors in the PEDC by generating a small torque. However, due to the parallel architecture of the MPS, the auto alignment feature will leads to misalignment of other PMAs with respect to their facing PEDCs. As a result, a repetitive torque will appear during motion along a single axis thus resulting in displacement loss. Unfortunately this kind of error cannot be resolved by adjusting the parameters of the injected current such as amplitude, current phase, etc. In our case, to eliminate this error, the defective PMAs were disassembled and then again re-assembled to the cross structure using some alignment tools.

The assembly errors presented in this section are mainly tied up to the assembly procedure and small assembly area on the cross structure. So, in order to solve this assembly problem a new cross structure has been proposed and developed. The detail description of this cross structure is presented in chapter 5. In our initial prototype, the motion loss due to a small rotation error ($\Delta\alpha \approx 0.75^{\circ}$) was carefully reduced by injecting constant currents in the PEDCs parallel to the motion axis.

3.2 Experimentation

In this section, the motion characteristics of the initial MPS prototype have been evaluated. However, before realizing the experimental setup of the whole MPS, first an experiment was performed in order to measure the real magnetic field generated by the PMAs. This is necessary firstly, to verify the orientation of the PMs in each set of the PMA and secondly to examine the real value of the magnetic field generated by the PMAs. In the following section, the detail description of this experiment is presented.

3.2.1 Measurement of the real magnetic induction

The real magnetic induction was measured using a Hall sensor (A1301) fabricated by Allegro Microsystems Inc[5] and its characteristics are mentioned in table 3.2. This sensor was selected due to its small size and simple application. Further, it provides a corresponding output voltage when exposed to an external magnetic field, which can be acquired though data acquisition modules in real time. The magnitude of the sensor output voltage depends on the intensity and direction of the applied magnetic field. So, in our case, the only limitation of this sensor is that it only interprets the vertical component (i.e. B_z component) of the magnetic field. However, this is sufficient in order to verify the magnetic induction strength, the orientation of PMAs and the magnetic model developed in the previous chapter.

To realize the magnetic induction measurement task, the schematic layout presented in figure 3.12 has been adapted. A motorized linear stage (Newport, M-MFC25CC) was

[5]http://www.allegromicro.com/

Characteristics	Value
Source voltage	5V (4.5-6V)
Induction	without limit
Sensitivity	2.5 (2.0-3.0) mV/Gauss
Source current	9 mA
Utilization temperature	-20°C to +85 °C

TABLE 3.2: Characteristics of the Hall sensor A1301

used to translate the PMA (attached to the cross structure) beneath the Hall sensor. In order to drive/control the linear stage, the command signals were generated using LabView® software. These signals are sent to the dedicated Newport controller which generates corresponding driving voltage for the linear stage.

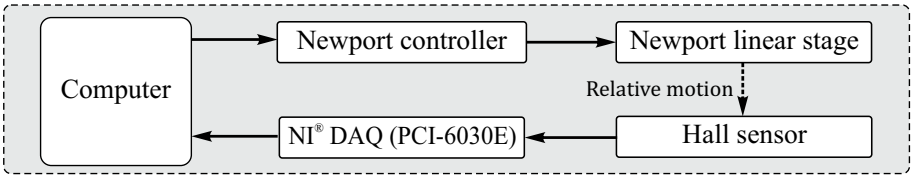

FIGURE 3.12: Magnetic induction measurement principle

Similarly, the output voltage generated by the Hall sensor is acquired using the analog channels of the National Instrument data acquisition modules (NI® PCI-6030E) in real time. These voltage data were processed and stored using Labview®software.

In practice, the described components have been assembled together to realize the experimental setup. Both, Hall sensor and the PMA have been insulated from the metallic components using non-magnetic supports (1) and (2) as shown in figure 3.13(a). This insulation is necessary in order to avoid any kind of disturbances during experimentation such as magnet-metal attraction, thermal variation, etc. Further, the Hall sensor was fixed to a manual linear stage (Newport, UMR 5.16) using a mechanical support to adjust the air gap "d" between the PMA surface and Hall sensor along z-axis (see figure 3.13(b)). An additional glass wafer was fixed on top of the non-magnetic support (2) in order to avoid any free suspension of PMAs due to the small surface area of the non-magnetic support (2). This is done in order to avoid the scenario in which, small vibration (generated by the mobile part of the motorized linear stage during motion) can propagate into the PMAs and can break them from the cross structure edge.

a) ***Calibration of the Hall sensor:*** After realizing the experimental setup, first, the calibration of the Hall sensor has been preformed. This task has been carried out with the help of a reference PM by placing it beneath the Hall sensor instead of the PMAs in the mobile part of the MPS. The fabricator of this PM has provided reference magnetic

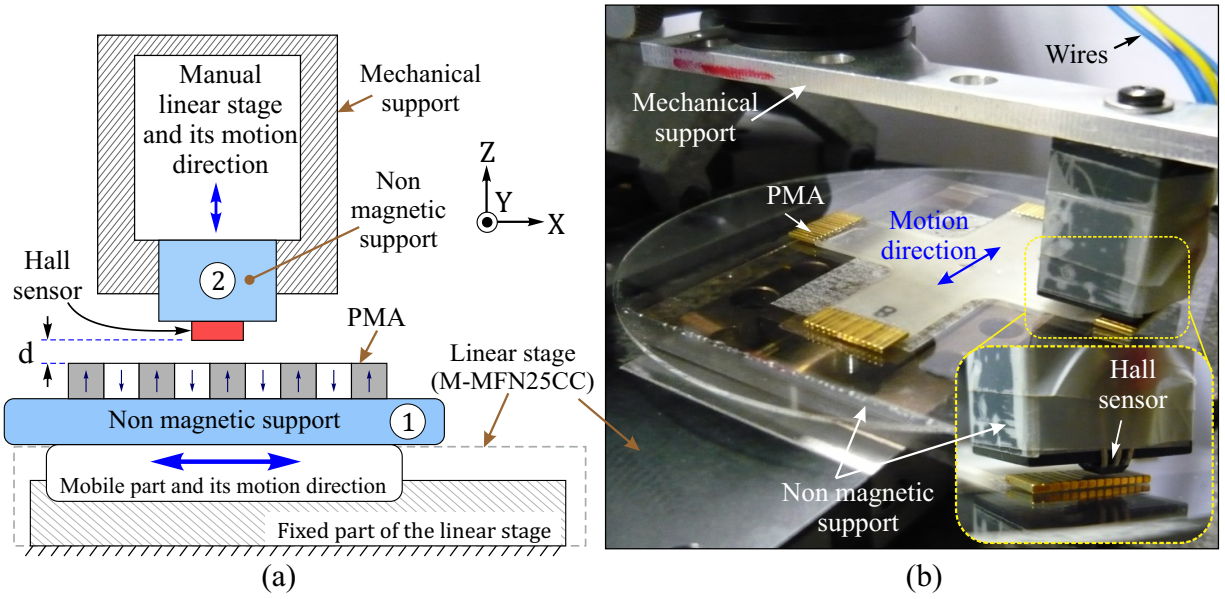

FIGURE 3.13: Magnetic induction measurement (a) Schematic layout (b) Experimental setup with enhanced view of the Hall sensor and a single PMA

induction values at different air gaps (see table 3.3). After leveling the Hall senor with respect to the reference PM, it was vertically moved (i.e., along z-axis, see figure 3.13(a)) with the help of the manual linear stage. The output voltage from the Hall sensor and the reference PM magnetic induction values (provided by the fabricator) are plotted against the displacement as shown in figure 3.14(a). Moreover, polynomial fits have been applied to the data to acquire a relationship with respect to displacement. Further, the expressions obtained have been used to construct the relationship between output voltages in terms of the applied magnetic field as shown in figure 3.14(b). A linear fit is then applied in order to determine the sensitivity of the Hall sensor which was found to be 25.13 V/T (2.513 mV/Gauss). The value of the sensitivity is in good agreement with the Hall sensor manufacturer value (see table 3.2).

The precision error of the Hall sensor measurement was carried out by measuring the magnetic induction of the reference PM at the air gaps provided by the fabricator. However, the measurement for the first air gap value (i.e., d = 0.25 mm) could not be carried out as the Hall element in the sensor is located 0.5 mm inside the sensor package (see data sheet of A1301). For the rest, the measured values of the magnetic induction are presented in the table 3.3. The results show a very good agreement between the measured and reference magnetic induction values with a very small precision error of $\approx$ 1.1 mT. The influence of this error can easily be neglected.

b) ***Magnetic induction measurement of the PMAs:*** After calibration of the sensor, the PMAs in the mobile part of the MPS have been analyzed. A 200 μm air gap (d) between Hall sensor and PMA surface was selected to avoid any physical contact during measurement. After adjusting these parameters, the mobile part of the MPS is translated for 18

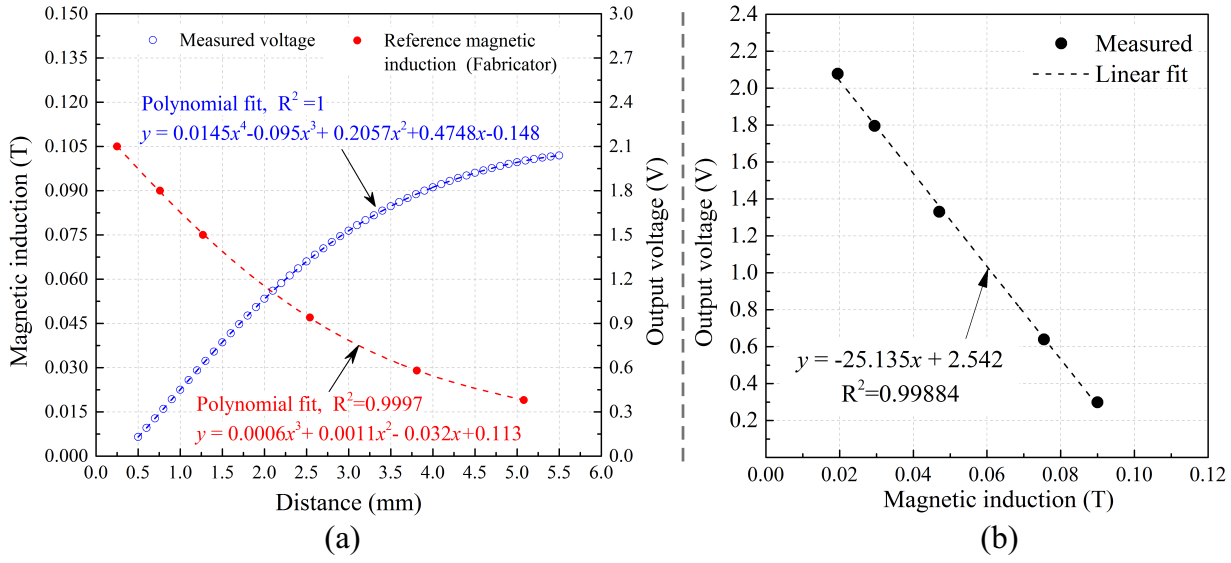

FIGURE 3.14: Hall sensor calibration curves

Air gap (mm)	0.25	0.76	1.27	2.54	3.81	5.08
Reference magnetic induction (T)	0.105	0.090	0.075	0.047	0.029	0.019
Measured magnetic induction (T)	-	0.091	0.076	0.046	0.028	0.018

TABLE 3.3: Comparison of the magnetic induction values at different air gaps

mm beneath the Hall sensor with a speed of 20 μm step/s using the motorized linear stage. At each step, the output voltage of the Hall sensor is stored using Labview® software. After doing so, the comparison between the result obtained for a single PMA and FEA results have been performed. A good agreement was found between both results as presented in figure 3.15(a). In addition, the small variation in the experimental results is due to the non uniform dimensions of the PMs assembled in a PMA. This problem is mainly linked to fabrication tolerances ($\pm$100 μm) which can not be controlled in commercially purchased PMs.

Furthermore, an analysis has been performed to measure the magnetic flux density variation between the PMAs along both axis (see figure 3.15(b)). This analysis is necessary to avoid large variation in the magnetic field which can deteriorate the performance of the MPS. From the analysis the mean value of these variations was found to be 0.006 T with a standard deviation of $\pm$0.015 T. So, the influence of these small variations on the generation of the electromagnetic forces has been neglected as compared to the electromagnetic forces generated by the real magnetic flux density generated by each PMA.

After analyzing the PMAs, the experiments have been carried out in order to evaluate different motion characteristics of the MPS. The description of these experiments is presented in the following section.

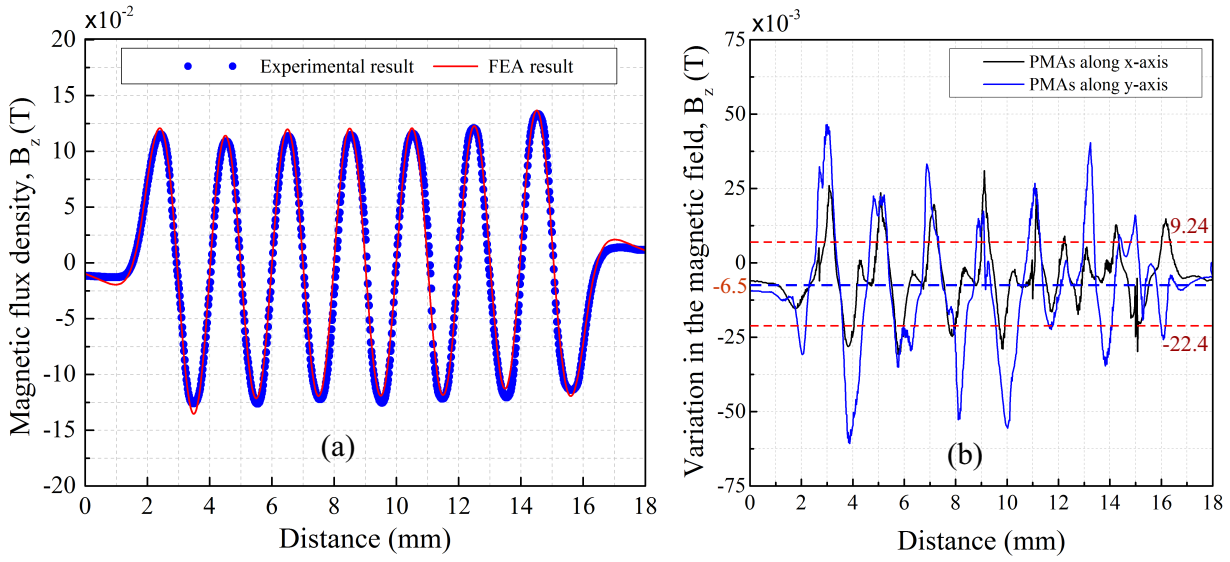

FIGURE 3.15: (a) Comparison of magnetic flux density (b) Magnetic flux density variation along both axes

3.2.2 Performance assessment of initial MPS prototype

To demonstrate the motion characteristics of the initial MPS prototype, first the description of the experimental setup and the details regarding the experimental components that had been employed in order to control the prototype will be presented in this section. Afterward, the different motion performances such as speed, displacement range, etc., in open and closed loop control will be presented.

3.2.2.1 Realization of the experimental setup

To demonstrate the actual motion characteristics of the MPS prototype, first the experimental setup has been realized. This mechanical setup consists of two types of mechanical mountings as shown in the pictorial view along a single axis as shown in the figure 3.16. Initially, the MPS prototype mounting has been carried out by installing the fixed part (see figure 3.8) onto the tilt stage (A). In addition, due to small height of the tilt stage, a mechanical support (1) was used to acquire the proper height of the fixed part relative to the feedback sensor. The whole mechanical setup of the MPS was fixed on the experimental platform. Afterward, the fixed part of the MPS was leveled with the help of a flat mirror and a laser as depicted in the figure 3.16. Furthermore, a gold coated mirror cube was fixed on the mobile part to facilitates the measurement via non contact technique along both axes in *xy*-plane. At the end, the complete mobile part was placed on top of the fixed part.

After realizing the MPS prototype mounting, the feedback sensor mounting has been realized. To examine the planar motion characteristics during experimentation, two Fiber

Optic Displacement Sensor (FODS) probes have been installed to measure the displacement realized by the mobile part along both axes in *xy*-plane (see figure 3.17(a)). In order to position/calibrate these sensors in front of the mirror cube, different components (e.g. Lab jack, tilt stage, manual and motorized linear stages, mechanical supports, etc.) have been assembled together to realize a set of the feed back sensor mounting as shown in the figure 3.16.

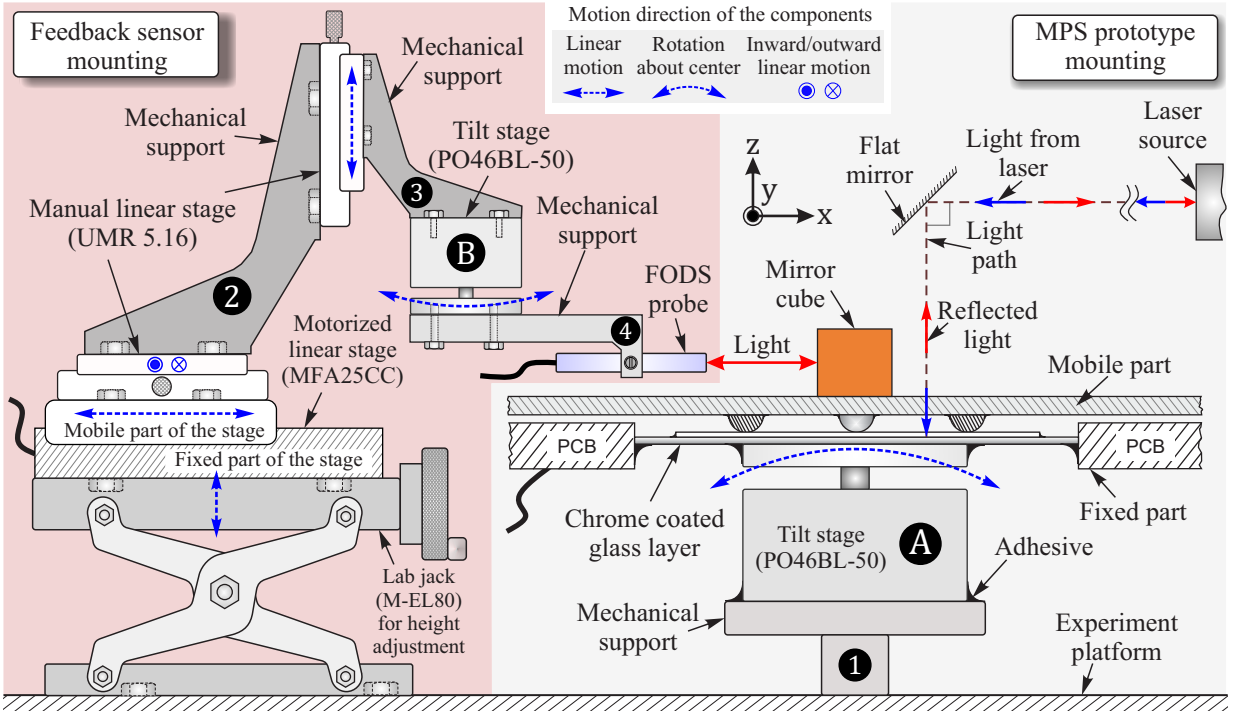

FIGURE 3.16: Pictorial view of the mechanical setup along single axis

Figure 3.17(a) represents the real view of the MPS with two FODSs. During experimentation, the role of each sensor employed in the setup is provided in figure 3.17(b) and (c). For example, in linear motion case presented in figure 3.17(b), the FODS$_y$ that is installed along the motion axis (i.e. *y*-axis) has been used to measure the change in the displacement Δy between two positions (1) and (2) of the mirror cube. At the same time, the FODS$_x$ which is installed perpendicular to the motion axis (i.e. *x*-axis) is used to measure the motion straightness and drift effect of the mobile part during experimentation.

Similarly, in the case of planar motion, both FODSs have been used to measure the change in the displacements (Δx and Δy) in the *xy*-plane as shown in the figure 3.17(c).

3.2.2.2 Realization of the motion control unit

After realizing the complete experimental setup, the schematic layout presented in figure 3.18 has been adapted to drive and control the MPS prototype. The control signals were generated via LabView® software and fed to the Voltage to Current convertors using

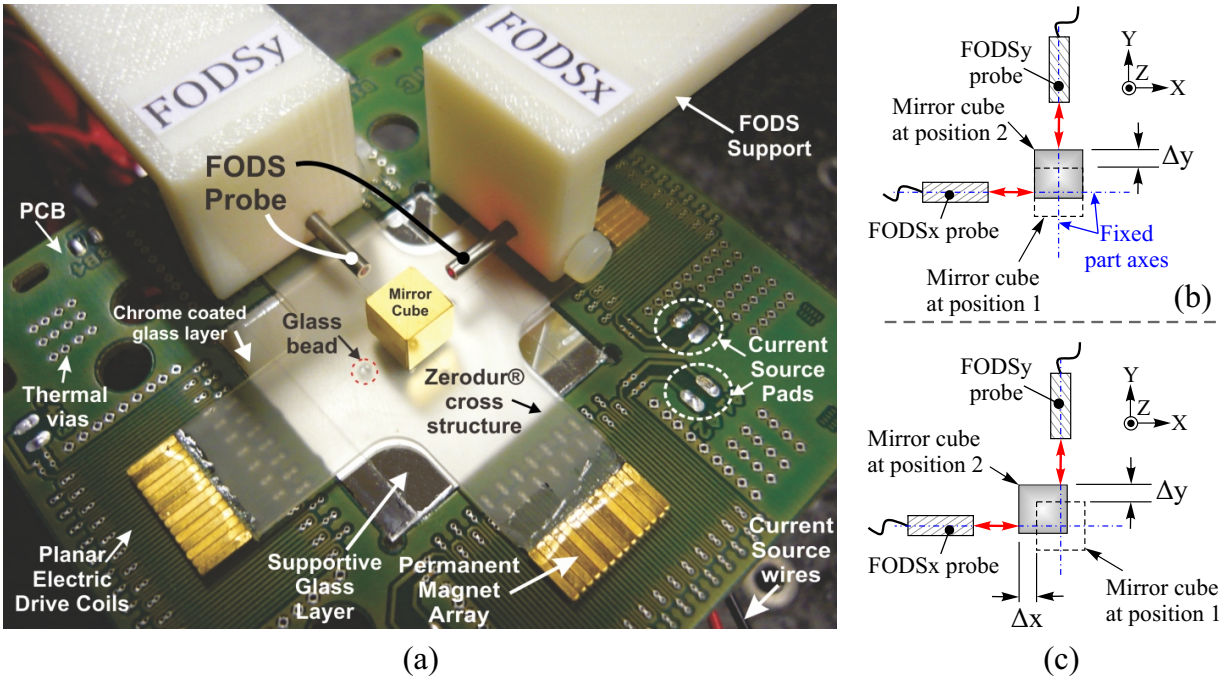

FIGURE 3.17: (a) Real view of the experimental setup (b) Top view, displacement measurement in linear motion case (c) Top view, displacement measurement in planar motion case

NI® DAQ output module to generate controlling currents for the LMs of the MPS. Furthermore, the motion realized by the mobile part has been measured using two FODSs installed in the experimental setup. Each sensor consists of a FODS probe and a signal processing unit. The output of the FODS is acquired using NI® DAQ input module via LabView® in real time.

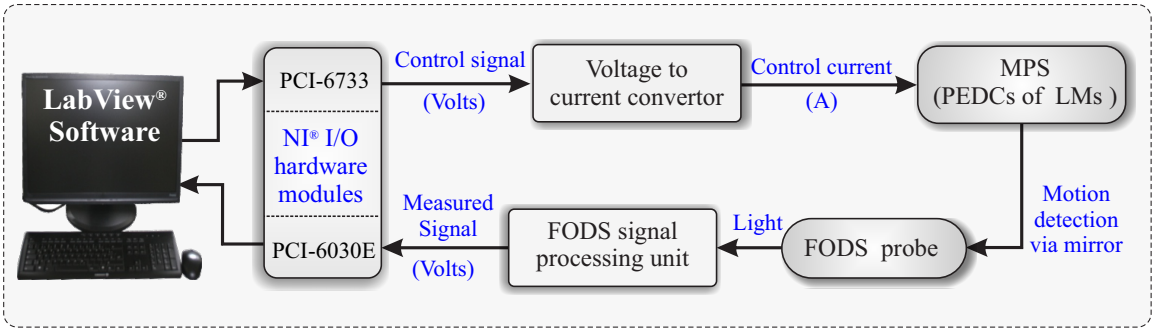

FIGURE 3.18: Schematic layout of the experiment

In the following text, the details description of each component employed in order to realize the motion control unit have been discussed.

Data Acquisition Boards (DAQ)

In our experiment setup, two types of the DAQs (purchased from National instrument) have been used. The typical characteristics of these cards are presented in table 3.4.

The input and output of these cards have been managed via an interface developed in LabView® software.

NI® DAQ card	Analog input ports	Analog output ports	Resolution	Sampling frequency	Application
PCI-6733	0	8	16 bit	1 MHz	Output
PCI-6030E	16	2	16 bit	200 kHz	Input

TABLE 3.4: Specification of the NI® DAQs used in the experiment

The PCI-6733 card is used as an output device to feed the voltage signals (generated via Labview® interface) to the voltage-to-current convertors. Whereas, PCI-6036E card has been used as an input device to treat the input voltage signals attained by the FODS. Both cards have 16 bits resolution and can be calibrated to a maximum voltage range of $\pm$10 V. The voltage resolution of these cards have been computed via equation 3.4

$$\text{Voltage resolution} = \frac{\Delta V}{2^n} = \frac{V_{\max} - V_{\min}}{2^n} \tag{3.4}$$

Where, ΔV is the voltage range and *n* is the number of bits of the NI® DAQ. According to the equation 3.4, for a voltage range of 10 V, the smallest voltage increment that have been realized with PCI-6733 card is 0.15 mV at its 8 analog output channels. Similarly, for the same voltage range, the input PCI-6030E device is able to measure the smallest voltage value of 0.15 mV.

Voltage-to-Current converter (V-C)

In order to drive the LMs of in the MPS prototype, the driving currents have been generated using V-C converters. According to the literature presented previously in this chapter it has been concluded that 0.8 A current per coils of the PEDC is sufficient to drive the MPS prototype. So, by taking into account different parameters such as resistance of the each coil in the PEDCs, maximum output of the PCI-6733 DAQ, etc., the converters used in our experiment are able to generate $\pm$3 A for a voltage range $\pm$10 V with a frequency bandwidth of 50 kHz (see figure 3.19(a)). These converters have two input voltage channels (to feed PCI-6733 DAQ output voltage) and two output current channels to inject currents into each coils in a single PEDC. Two pairs of such converters were used in order to drive all four LMs individually.

In addition, to examine the output current generated over a single channel, a ramp of input voltage signal with an increment of 0.25 V was applied for a load of 2Ω. Figure 3.19(b) represents the output current generated over each channel which indicates that the voltage to current conversion is linear with a linearity error less then 1%.

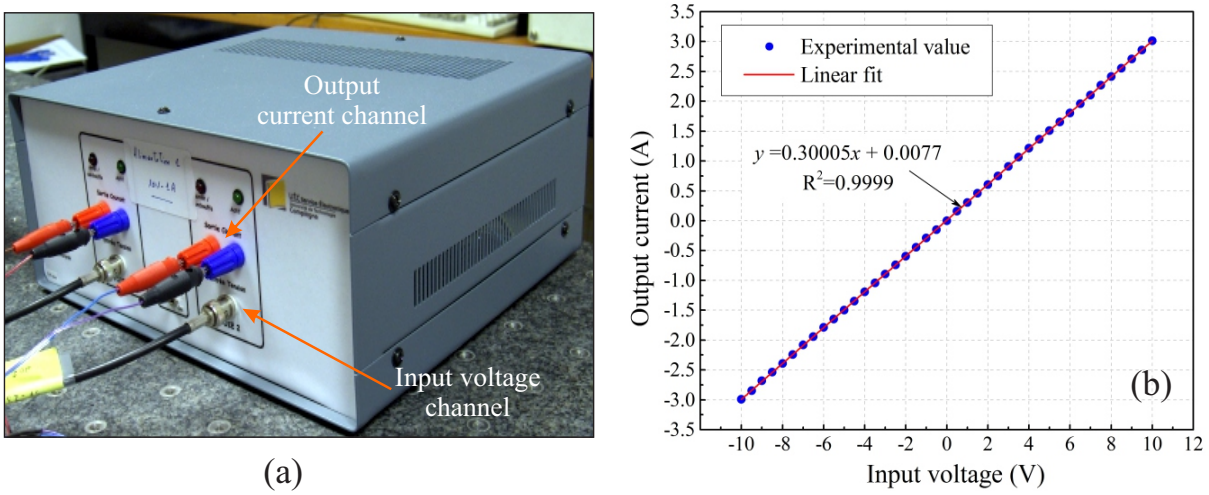

FIGURE 3.19: Voltage to current converter unit and its characteristic curve

Fiber Optic Displacement Sensor (FODS)

During the experimentation, the displacement measurement of the mobile part has been carried out via non contact technique in order to avoid any disturbances due to the functioning of the feedback sensor or vice versa. In addition, due to the compact size of the MPS prototype the application of conventional sensors in this configuration was difficult. In our experiments, two FODS have been employed to measure the position of the mobile part (see figure 3.17(a)). This type of sensor has been developed in an earlier research that was carried out by Dr. Damping Wang at our Roberval laboratory (UTC) [Wang 99]. It consists of a sensor probe and a signal processing unit as shown in the figure 3.20. The FODS probe transmit and collect light whereas, the signal processing unit which consists of the electronic circuitry that interprets the light into voltage and vice versa.

Some of the main advantages of using this sensor include, the small dimensions of the probe (Ø2 mm, Length = 10 mm) due to which it can be used in the congest places, non-magnetic FODS probe which eliminates its susceptibility to electromagnetic effects and its nano-meter level resolution [Prel 06].

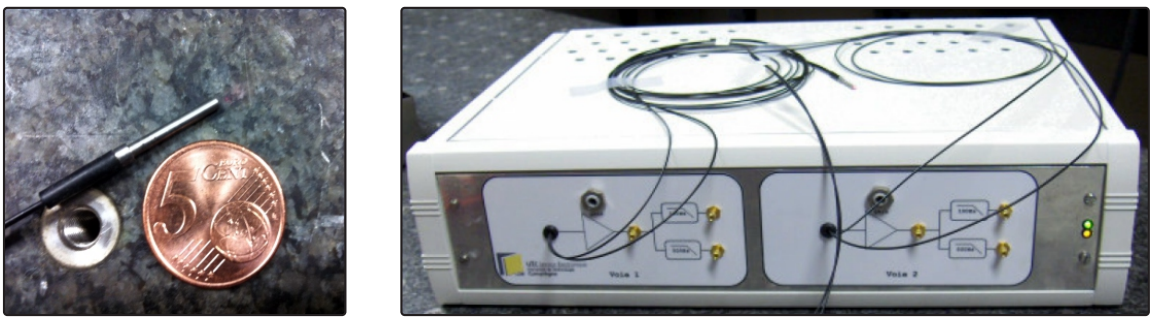

FIGURE 3.20: (a) FODS probe (b) FODS signal processing unit

a) *Working principle of the FODS:*

The FODS probe consists of a bundle of five fibers (one emission fiber and four reception fibers) combined together in a steel cladding as shown in figure 3.21(a). The centrally located emission fiber emits light that is generated via a Light Emitting Diode (LED) in the FODS signal processing unit. Upon placing a flat mirror target in front of the probe, the light is reflected and is collected by the reception fibers situated around the emission fiber. The received light is translated into voltage with the help of a Photo Diode (PhD) in the FODS signal processing unit. The amount of reflected light is a function of the linear displacement between the sensor probe and the flat mirror placed perpendicular to the FODS probe. So, by this means, if the flat mirror is displaced in front of the FODS probe, the variation in the amount of light received by the reception fibers leads to the variation in the output voltage.

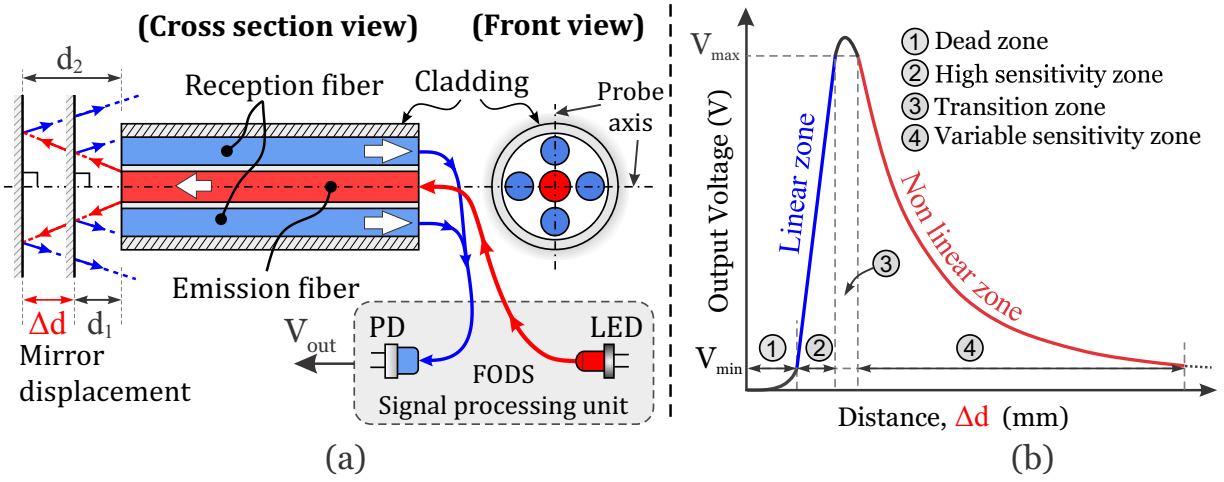

FIGURE 3.21: FODS (a) Working principle (b) Characteristic curve, $V_{out} = f(\Delta d)$

The typical output voltage characteristic curve of the FODS used in our studies, as a function of the change in the distance ($\Delta d = d_2 - d_1$) of the flat mirror from the FODS probe, consists of four zones (see figure 3.21(b)). The zone (1) is termed as "Dead zone" because the sensor exhibits very low (<1 V) output voltage as no light is collected by the reception fibers in this zone. In addition, the range of this zone is few microns and the sensor exhibits non linear characteristics. In the zone (2), the FODS response is linear and exhibits maximum sensitivity with respect to other zones. The span of this zone is around 200 μm which depends on the linearity criterion (usually <1%) and reflectivity of the mirror [Benc 06]. Upon further increasing the distance between the FODS probe and the flat mirror, the output response of the FODS enters in the zone (3) which is termed as "transition zone" in figure 3.21(b). In this zone, the output of the FODS reaches to its peak voltage value ($\approx$ 13 V) and start to decrease with respect to increase in the distance. Moreover, in zone (4) the sensor response is non linear. As compared to other zones, the span of this zone for displacement measurement is large ($\approx$4 mm). However, the

sensitivity of the FODS decreases with respect to increase in the displacement and the usable range for displacement measurement is around 2.75 mm. In our experiment, the FODSs have been used in zone (2) for high resolution measurement and in zone (4) for long range measurement.

b) *Calibration of the FODS in the experiment*

The FODSs installed in our experiment have been calibrated using the mechanical setup presented in figure 3.16. At first, a constant current is injected along a single axis to align the mobile part with respect to the PEDCs. Then, the FODS$_x$ and FODS$_y$ situated along *x*- and *y*-axis, respectively, were sequentially calibrated by moving it away from the mirror cube with the help of motorized linear stage (see figure 3.16). In addition, a Labview® software has been used for data acquisition and drive the motorized linear stage at 20 μm/s speed. The data acquisition frequency was 100 Hz which represents the band width of the FODS sensor. Furthermore, due to the maximum input voltage limit of the NI® DAQ 6036E, the calibration of the FODS was carried out in the range of 0-10 V. Due to this limitation, the complete range of the linear zone was reduced to 140 μm as the NI® DAQ saturates at 10V.

Figure 3.22 represents the sensitivity curves for the linear and and non linear zones of the FODS$_x$ and FODS$_y$. For a linearity criterion $<1\%$, the functional range for displacement measurement with high resolution was found to be 80 μm for both sensors in linear zone and 2.5 mm in the non linear zone. The variation in the sensitivity curves of the FODS$_x$ and the FODS$_y$ is mostly due to the electronics of the sensors. In linear zone, the displacement measurement resolution of the FODS$_x$ and FODS$_y$ was found to be 8 nm and 11 nm, respectively.

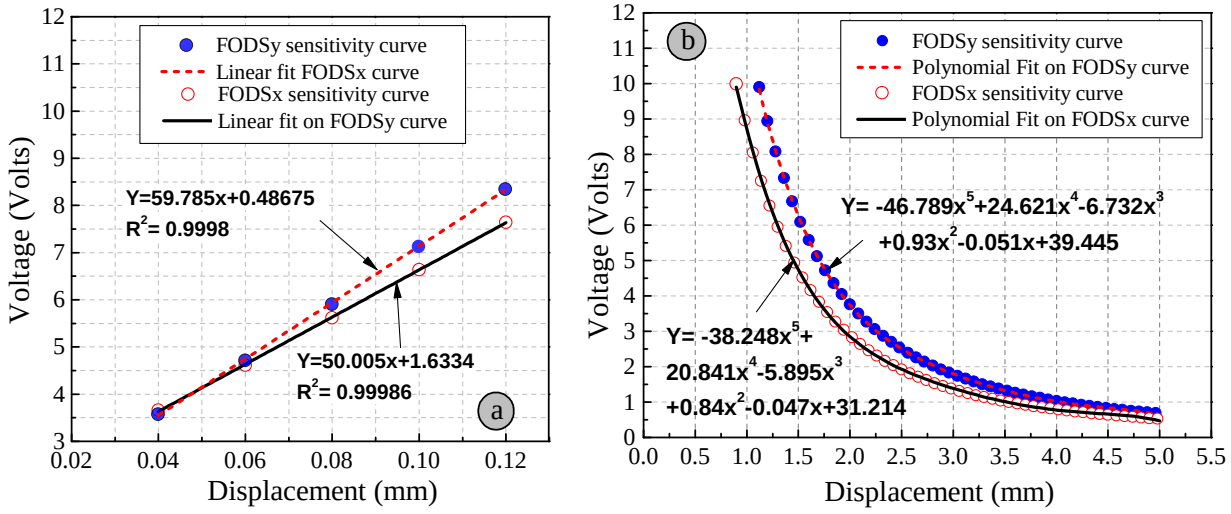

FIGURE 3.22: Sensitivity curves both FODSs in (a) Linear zone (b) Non linear zone

After calibrating the FODSs along both axes, experiments have been carried out in open and closed loop control by injecting the currents in the PEDCs to drive the mobile part of the MPS. In the following section, the experiment results are presented and discussed. However, in order to elaborate these results, the LMs have been named as LM_A, LM_B, LM_C and LM_D according to the convention adapted in the figure 2.1 (b) for the purpose of simplification. The LM_A, LM_B are situated along *y*-axis and when injected with sinusoidal currents they drive the mobile part along *x*-axis. Similarly, LM_C and LM_D are situated along *x*-axis and are responsible to drive the mobile part along *y*-axis.

3.2.2.3 Performance of the MPS in open loop control

a) *Linear displacement:* At first, linear displacement characteristics of the MPS prototype have been evaluated. In order to do so, a half period of 2 Hz sinusoidal currents (I_1, I_2) with 0.8 A (peak) amplitude was injected into the PEDCs of LM_A, LM_B to realize motion along *x*-axis. The sampling frequency of the injected currents was 100 Hz and FODS was used in the nonlinear zone to measure the long range displacement carried out by the mobile part. In addition, a constant current of 0.8 A was also injected into the PEDCs of the LM_C and LM_D to avoid any drift effect during linear motion.

Figure 3.23 represents three cycles of repeated motion of the mobile part along *x*-axis between position A and B. In addition, the experimental result has been compared with the simulation results. The mean value of the simulated and experimental positions A (B) were found to be 66.67 μm (955.85 μm) and 65.01 μm (928.59 μm), respectively. The large difference between experimental and simulated results at position B is because of the low sensitivity of the FODS in zone (2) of the sensor.

Theoretically, for a half period of the sinusoidal signal the mobile part should perform a displacement of 1000 μm. However, the net displacement realized by the mobile part was found to be 863.58 μm via experiment and 889.18 μm via simulation. The loss between theoretical displacement and the real/simulation results is mainly due to the friction effect. However, despite this friction loss, the experimental results provide a good correlation with the simulated results thus validates the analytical model.

b) *Position repeatability:* In order to measure the position repeatability of the MPS prototype, a 10 cycles test was performed in similar fashion as discussed in the linear displacement section. For a mean displacement of 854.54 μm between position A and position B along *x*-axis, the position repeatability error was calculated to be 4.41 μm. The relative error was computed to be 3.03$\%$. This result shows that the MPS exhibits a small repeatability error which can be further reduced with a closed loop control.

c) *Straightness:* Another test has been carried out to measure the motion straightness during motion of the mobile part. For this test, the injected current characteristics were

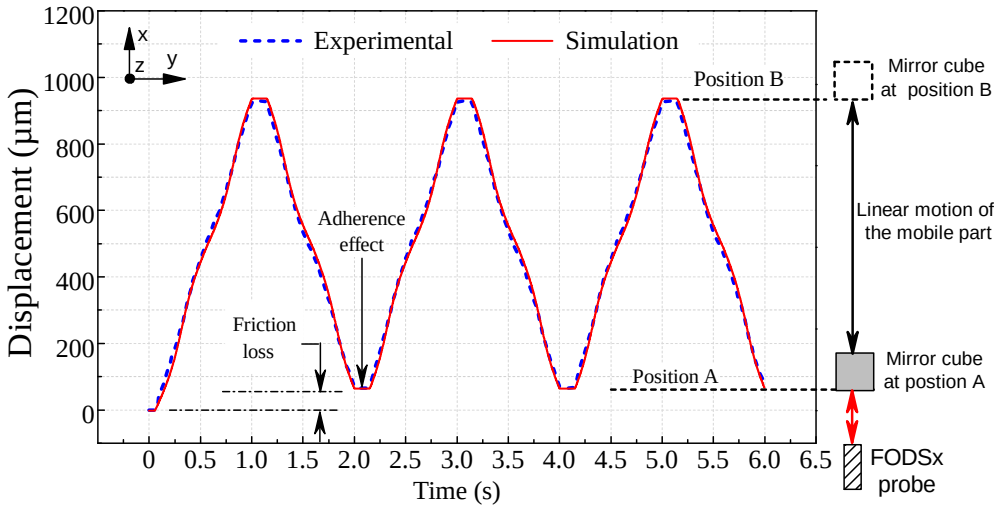

FIGURE 3.23: Linear displacement along *x*-axis

kept same as described in the linear displacement section. However, both FODS$_x$ and FODS$_y$ have been used simultaneously to measure the axial displacement (along the *x*-axis) and lateral displacements (along the *y*-axis) as depicted in the figure 3.13(b). The FODS$_y$ was used in its nonlinear zone and FODS$_x$ was used in its linear zone. The experimental results are presented in figure 3.24(a). For the ease of observation, the lateral displacement result has been magnified by 100.

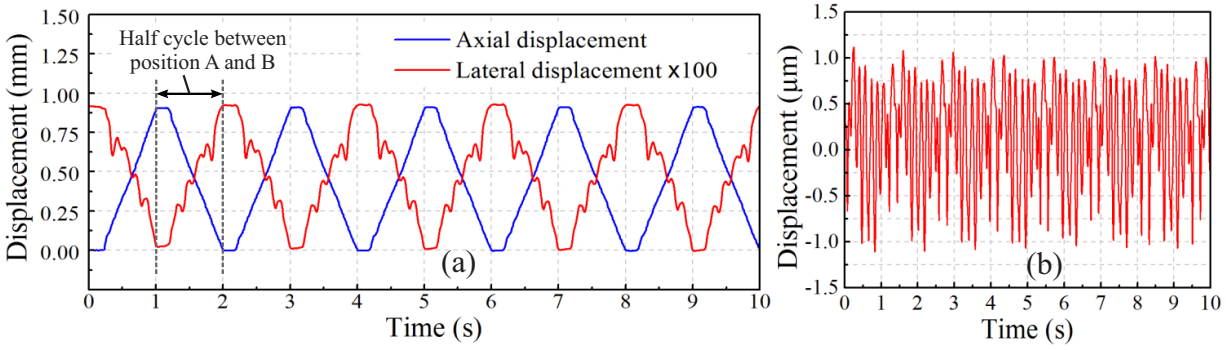

FIGURE 3.24: Rectitude of the MPS in linear motion (a) Axial and lateral displacement (b) Real lateral displacement

During motion, the straightness error is not only because of the lateral displacement, but also due to the assembly error of the mirror cube. Due to the manual assembly of the mirror cube, the mirror cube surface is not parallel to the FODS$_x$. The angle between the displacement axis and the mirror cube surface facing FODS$_x$ was measured to be 0.92°. However, since the FODS$_x$ was used in its linear zone so the real straightness was computed by subtracting this error due to the mirror cube. From figure 3.24(b), the straightness for 1000 μm displacement was calculated to be 2.353 μm with a standard deviation of 0.568 μm. Similarly, for the 500 μm displacement, the straightness error was

found to be 1.991 μm with a standard deviation of 0.460 μm. These results reveal the auto alignment characteristics of the LMs as discussed in chapter 2.

d) XY *Linear profile:* In order to study the *xy* displacement, all four LMs were used simultaneously. Both $FODS_x$ and $FODS_y$ were used in their nonlinear zone to measure the long stroke *xy* linear displacement as shown in figure 3.17(c). A 30 cycle test of linear trajectory in the *xy*-plane was performed by injecting one period of 1 Hz sinusoidal currents with 0.8 A per coil (peak-to-peak) amplitude.

From the result shown in figure 3.25(a), it can be seen that the trajectory is repeatable from position A to B and vice versa. However, the mobile part deviates in backward trajectory (from position B to position A). This hysteresis is due to the appearance of different torques along an axis which is caused by the assembly error. Taking into account the drift effect during motion and variable sensitivity of the FODSs in non linear zone the amount of linear profile hysteresis in *xy*-plane was found to be 57 μm. In order to minimize this error, one solution is to reduce the assembly errors at design level by realizing a cross structure with geometrically pre-defined through cavities. In addition, this error can be reduced by adapting a feedback control to minimize the trajectory deviation in real time.

e) *Velocity response:* The velocity response was measured along *x*-axis using $FODS_x$ and presented in figure 3.25(b). This test has been realized by injecting the sinusoidal currents I_1 and I_2 in the LM_A and LM_B at different control signal frequencies.

The experimentally measured velocities along with theoretical values for 10 cycles of linear travel along single axis, are provided in table 3.5. The variation in the experimental results are due to several phenomenons that occur during translation (e.g. micro rotations, drift effect, etc.). In addition, it can be seen in figure 3.25(b) that as the velocity increases the displacement loss also increases. However, from table 3.5, it can be seen that the real velocities are in good agreement with the theoretical values. Furthermore, the maximum speed is around 12 mm/s which is limited due to the inertia of the mobile part of the MPS.

Control signal frequency (Hz)	**0.5**	**1**	**2**	**4**	**5**	**6**
Theoretical velocity (mm/s)	1	2	4	8	10	12
Measured velocity (mm/s)	1.013 $\pm$0.002	2.016 $\pm$0.017	4.007 $\pm$0.011	8.006 $\pm$0.041	9.954 $\pm$0.086	11.088 $\pm$0.149
Relative error (%)	1.3	0.8	0.175	0.075	0.46	7.6

TABLE 3.5: Velocity response of the MPS prototype in open loop control

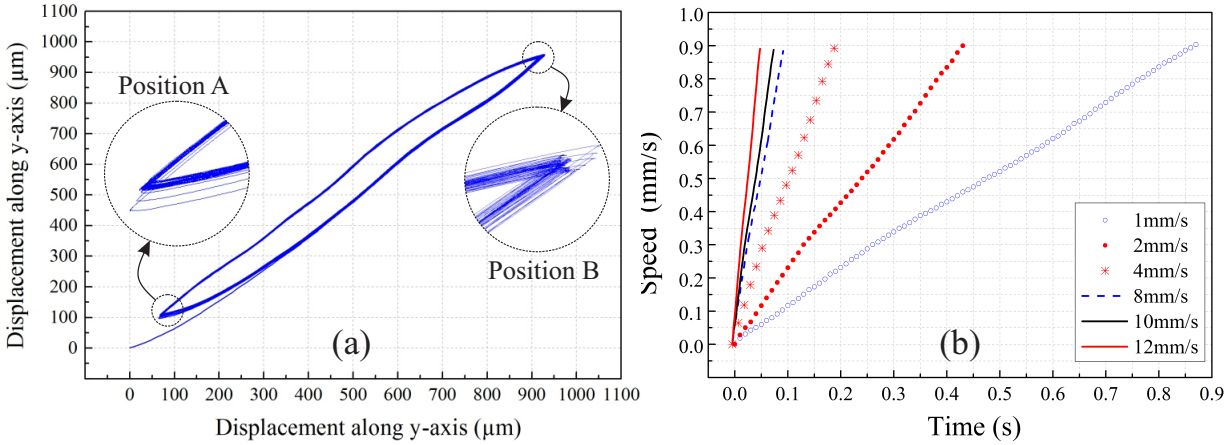

FIGURE 3.25: (a) *xy*-profile (b) Velocity response of the MPS

After realizing the open loop tests, MPS prototype motion characteristics have been analyzed in closed loop control. The description of these experiments are presented in the following text.

3.2.2.4 Performance of the MPS in closed loop control

In this section, the motion of the MPS prototype has been controlled via a PI controller. The desired displacement was achieved by changing the frequency (ω) of the controlling currents with respect to the error computed between desired and real displacement. The selection of PI controller gains depends on several parameters such as dynamics of the prototype, sensitivity of the FODS, etc. To identify the controller gains (K_P and K_I) the linear zone of the FODS has been used as the sensitivity remains constant in this zone.

In practice, there are several uncertainties that change the output of the MPS. For example, micro rotations during linear travel and real system motion error can change the sensitivity of the FODSs, impurities (such as dust) can change the sticking and friction force, etc. These uncertainties require complex multi-physics analyses and significant computational time, programming and experimentation. So, instead of using the global gain values for the PI controller, an approximation was carried out by selecting different gain values such as ($K_P = 0.077$, $K_I = 0.010$) for *x*-axis and ($K_P = 0.085$, $K_I = 0.012$) for *y*-axis in a manner to avoid any overshoot.

a) *Square step response:* At first, the step response of the MPS has been realized for two cycles at short stroke within the range of the linear zone of the FODS$_x$. The results obtained have been compared with the simulation results and a good agreement was found (see figure 3.26(a)). Afterward, for the same gain values, the step responses of the MPS in long strokes (i.e. 0.5, 1, 1.5 and 2 mm) were carried out by using the FODS$_x$ in its non linear zone (see figure 3.26(b)). The average settling time was computed to be 0.921 s (5%) for long strokes and 0.256 s (5%) for short stroke.

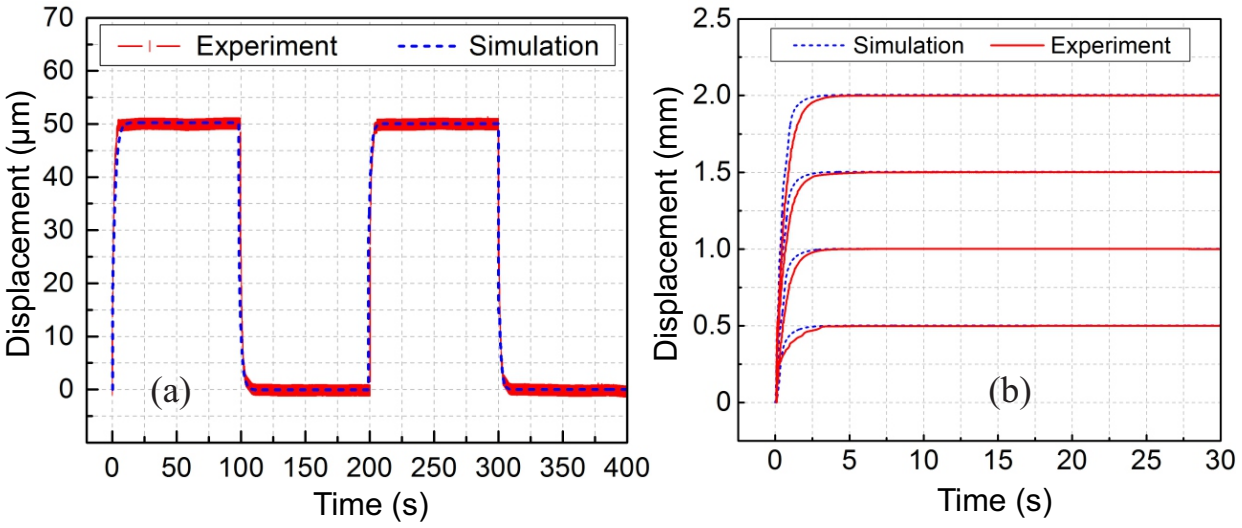

FIGURE 3.26: Step response of the MPS (a) Short stroke (b) Long stroke

The variation between the simulated results and experimental results in long stroke is mainly due to the application of the FODS$_x$ in its non linear zone where the sensitivity varies with respect to the displacement. Furthermore, to measure the position repeatability and precision of the MPS, 10 cycles of square steps have been conducted along x-axis in similar fashion as described previously. The experimental and simulated results are provided in table 3.6. From the experimental results it can be seen that, in short stroke, precision of the MPS reaches 31 nm with a repeatability error of 25 nm. Where as in long strokes this error is less then 1 μm. In addition, the variation in the simulated and experimental results is mainly due to the adhesion effect and FODS characteristics.

Desired displacement (μm)	**50**	**500**	**1000**	**1500**	**2000**
Simulation results (μm)	50.265	500.93	1000.302	1499.325	1999.855
Measured displacement (μm)	49.975	499.793	999.815	1500.387	2000.174
	$\pm$0.031	$\pm$0.268	$\pm$0.309	$\pm$0.451	$\pm$0.36

TABLE 3.6: Position repeatability in 10 cycles square steps test

c) *Step train response:* A step train motion is one of the most common operations for the MPSs applied in micro applications. For example, in the semiconductor industry this type of motion is used to achieve high quality processing in products such as ICs. Therefore in order to validate this characteristic an experiment along x-axis, with each step equal to 100 μm and moving toward $\pm$ 0.5 mm has been conducted. The gain parameters have been kept same as in the case of step response. A very good agreement was observed among the experimental and desired results as shown in figure 3.27. The average settling time (5%) for 100 μm in continuous step was measured to be 306.2 ms.

From this result it can be evaluated that the MPS prototype is able to perform repeatable desired displacement tasks.

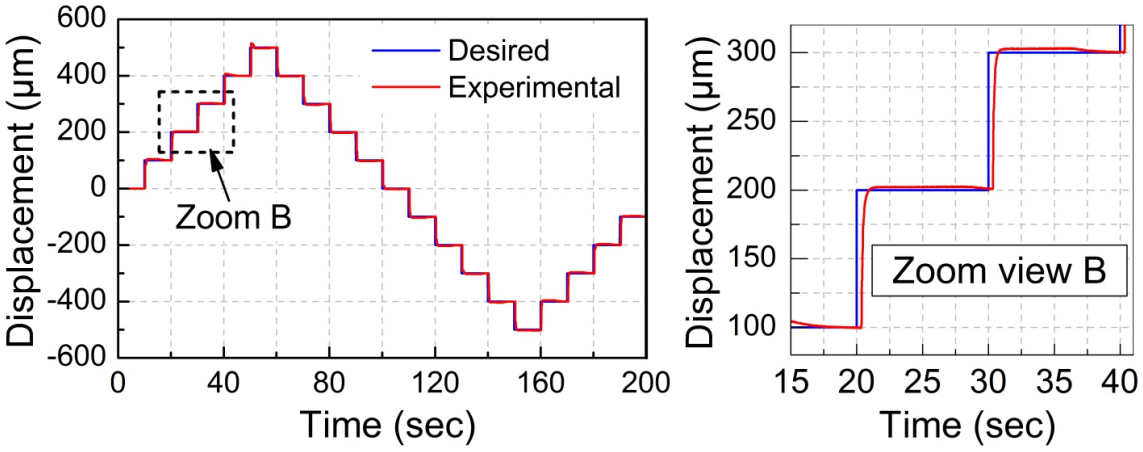

FIGURE 3.27: Step train profile response along x-axis

d) ***Triangular response:*** To illustrate the tracking ability of the MPS, a triangular profile test has been performed. The mobile part of the MPS was guided along the x-axis with the desired triangular profile of 0.5 mm amplitude. The experimental results show a very good agreement (see figure 3.28). However the friction effect can be observed as shown in the zoom view of the figure 3.28. From tracking error plot the magnitude of this friction effect was computed to be 28.38 μm. In the time interval [1 s, 5 s] the positioning stage starts moving and the sticking effect value falls to 5.63 μm due to the dynamics of the MPS. Moreover, the Root Mean Square (RMS) tracking error in zone [1 s, 5 s] remains in the range of 5.134 μm with a standard deviation of $\pm$ 0.929 μm. These performances can be improved with the help of more appropriate controller.

e) ***Planar motion:*** To achieve planar motion performances of the MPS all four LMs are operated simultaneously. For the same controller gain values adapted in the case of the step response, figure 3.29 (a) represents a 5 cycle test for 1 mm linear displacement realized by the mobile part of the MPS in xy-plane. The average linear displacement was found to be 1.039 mm with a standard deviation of $\pm$ 0.937 μm. The chaotic behavior in zone 1 (see figure 3.29 (a)) is due to the friction effect. As the displacement error falls towards zero, the magnitude of the currents that are injected in the PEDCs along motion direction also reduces, thus the relative value of adhesion forces increases with respect to the generated electromagnetic force. This problem can be solved by using adaptive PI controller. However, it can be seen that the open loop hysteresis effect (see figure 3.25(a)) has been eliminated.

In similar fashion, another test was carried out in order to realize a circular motion in xy-plane. Sinusoidal signals with an amplitude of 100 μm (peak-to-peak) with a sampling

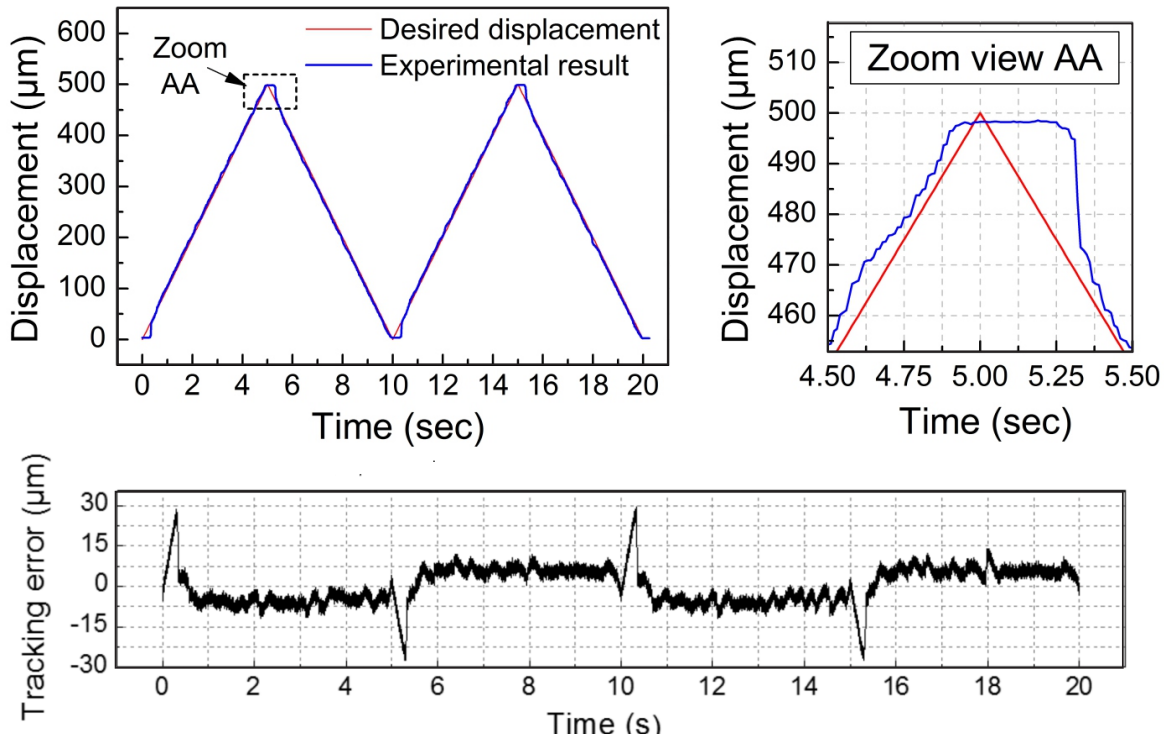

FIGURE 3.28: Motion behaviour of the MPS with triangular profile along single axis

rate of 100 Hz were used as desired displacements along both axes to realize a 100 μm in diameter circular profile at 0.1 Hz. Furthermore, the amplitude of the injected currents were kept 0.8 A in all four LMs. Figure 3.25(b) represents three circular trajectories. In order to measure the tracking error, the real displacement measured along both axes via FODS_x and FODS_y were analyzed separately. This analysis revealed a means value of the tracking error of 2.459 μm with a standard deviation of $\pm$ 0.831 μm along both axes.

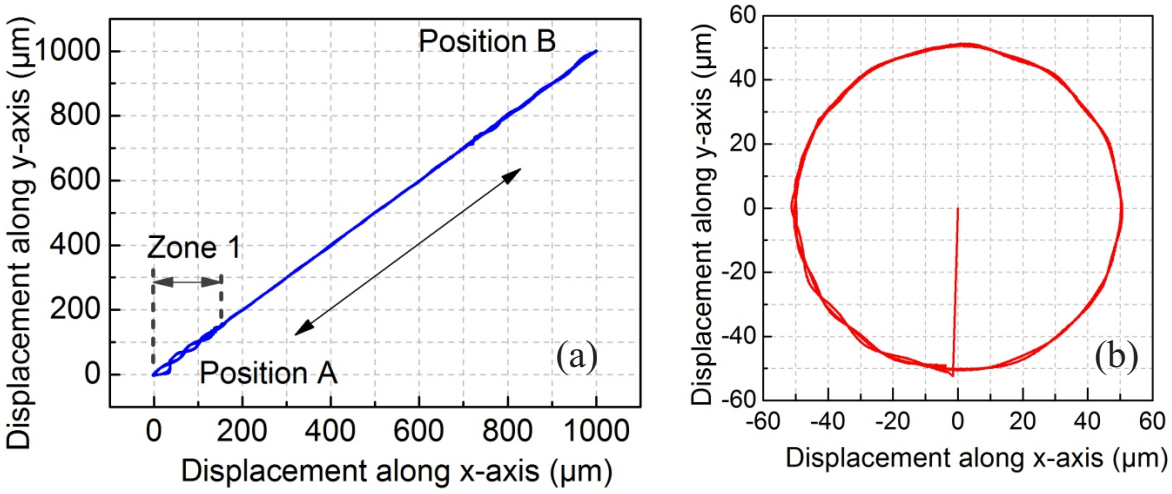

FIGURE 3.29: (a) Linear motion in *xy*-plane (b) $\pm$ 50 μm circular planar trajectory

3.3 Conclusion

A long range MPS design has been realized in this chapter. In the first part, the design layout and the description regarding the components used to realize the prototype have been presented. Different solutions regarding the selection overall design parameters of the fixed and mobile part of the MPS have been discussed. It was concluded that with an overall foot print size of 80×80 mm^2 of the fixed part, the MPS is able to deliver a theoretical motion range of 10×10 mm^2 in *xy*-plane. In addition, some analyses have been performed in order to qualify the MPS design for long range motion application by taking into account the influence of the magnetic field, vibration and the assembly errors generated over each LM.

In the second part, experimentation has been carried out in order to examine the motion characteristics of the MPS prototype in open and closed loop control. It has been concluded that the MPS is able to deliver variable stroke ranging from few micrometers to 2 mm (limited due to the sensors) with sub micrometer level accuracy. Furthermore, by adapting separate controls for LMs along each axis the MPS is able to perform planar motions in *xy*-plane.

Chapter 4

Development of a long range linear displacement sensor

This chapter provides the developments regarding the realization of a long range displacement measurement optical sensor. At first, the architecture and working principle of the fiber optic sensor in its common configuration along with its different performance parameters such as resolution, measurement range, etc., will be discussed. Afterward, the long range sensor principle and its fabrication approach will be presented. At the end, experimentation have been carried out in order to validate the functioning of the long range displacement measurement sensor.

4.1 Description of the fiber optic displacement sensor

The architecture of the Fiber Optic Displacement Sensor (FODS) used in our study consists of three main components such as a Signal Processing Unit (SPU), a fibre optic cable (consists of a bundle of one emission fiber and four reception fibers combined into an FODS probe) and a reflective target surface as shown in figure 4.1. The SPU consists of the electronic circuitry which controls a Light Emitting Diode (LED) to generate a light at 670 nm wavelength and a Photo Diode (PD) with a detection zone of 1 mm^2 to convert the collected light via reception fibers into the electrical signals.

The fiber optic cable consists of five multimodes PolyMethyl MethAcrylate (PMMA) fibers (purchased from OMRON[1] manufacturers) which are combined in a Ø 2 mm steel probe. In the FODS probe, the emission fiber (Ø 486 $\pm$10 μm) is located in the center whereas, the reception fibers (each having Ø 240 $\pm$10 μm) are symmetrically located around the emission fiber (figure 4.1). The numerical aperture of both types of fibers in the FODS probe is 0.46 [Khia 08].

[1] http://www.ia.omron.com/

In addition, a reflective target surface (e.g., flat mirror) is needed in order to realize the complete displacement sensor.

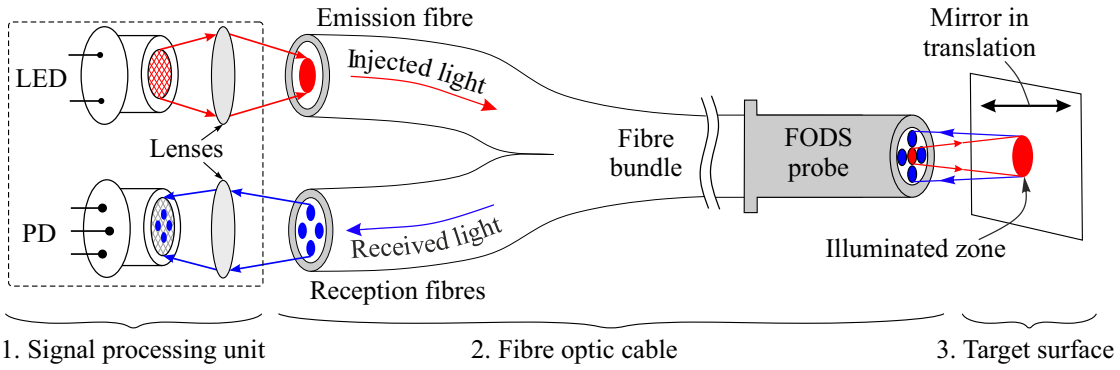

FIGURE 4.1: Schematic layout of the architecture of the fiber optic displacement sensor

The working principle of the sensor is based on injecting light into the emission fiber which illuminates the flat mirror upon leaving the FODS probe. Due to the light reflection principle, the flat mirror reflects the incident light inside the illuminated zone which is received by the reception fibers located around the emission fiber in the probe (see figure 4.1). This received light travels via reception fibers toward the PD installed in the SPU which converts it into output voltage. The amount of collected light by the reception fibers depends on the position of the flat mirror from the sensor probe. So, by moving the flat mirror perpendicularly with respect to the FODS probe surface (see sub figure 4.2), the amount of the collected light changes which results in the output voltage variation. This change in output voltage can be plotted with respect to the distance between the FODS probe and flat mirror as shown in the figure 4.2.

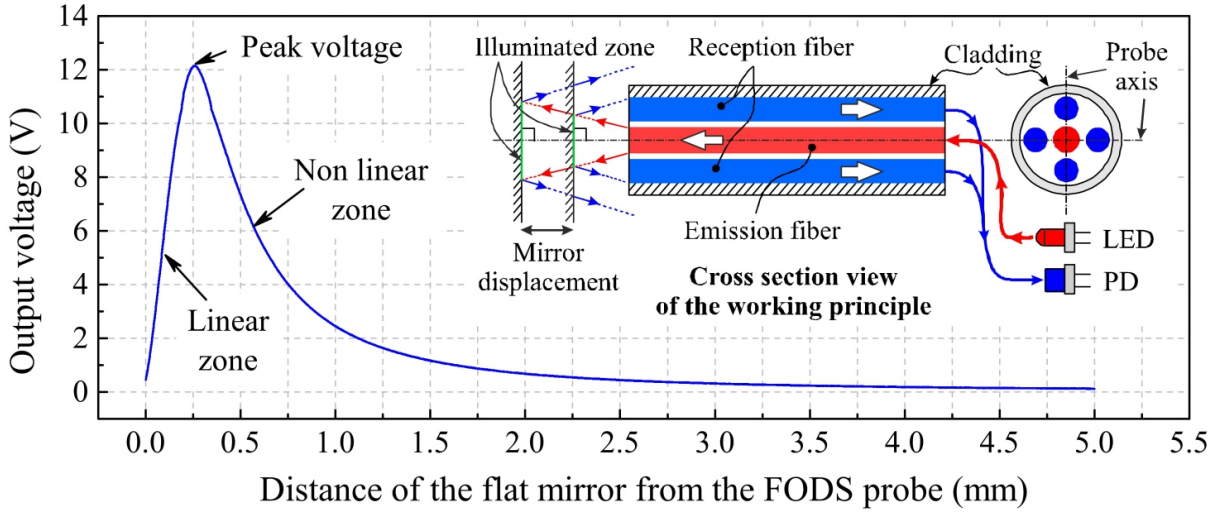

FIGURE 4.2: FODS working principle and its experimentally measured output voltage curve with respect to the position of the flat mirror

4.1.1 Characteristics of the sensor in its common configuration

In this section, the typical characteristics of the FODS, when used in its common configuration[2] will be discussed. From figure 4.2 it can be seen that the output voltage of the sensor delivers a linear and non linear relation with respect to the distance between FODS probe and flat mirror. Despite the ability of the sensor to measure the displacement up to few millimeters when used in its non linear zone, the resolution of the sensor remains very poor [Benc 06]. On the other hand, in linear zone the FODS can reach to a very high displacement measurement resolution (up to few nano meters). In this work, our main objective is to realize a long range displacement sensor while utilizing the linear zone of the FODS due to its high sensitivity in this zone. For this task, first, the different characteristics of the sensor such as sensitivity, resolution, range, etc., of the FODS in the linear zone will be presented.

4.1.1.1 Sensitivity, measurement range and resolution of the sensor

In the linear zone, the sensitivity of the FODS can be determined by applying a linear fit. In order to achieve a best linear fit, the range of the linear zone (i.e., 200 μm, see figure 4.3(a)) is often reduced to minimize the linearity error. The slope of the best linear fit (i.e., change in the output voltage (ΔV) with respect to the change in the distance (Δd) between the flat mirror and the sensor probe) represents the sensitivity of the sensor. Furthermore, the sensitivity of the sensor can be mathematically written as in equation (4.1). The FODS used in our study delivers a 60 mV/μm sensitivity over the range of 130 μm with 0.67% linearity error.

$$S_{axial} = \frac{\Delta V}{\Delta d} \tag{4.1}$$

Where, S_{axial} (V·mm^{-1}) represents the axial sensitivity of the FODS.

The axial resolution (R_{axial}) of the sensor can be determined using the sensitivity (S_{axial}) and Root Mean Square (RMS) noise (N_{rms}) of the output voltage of the sensor. It can be mathematically written as in equation (4.2).

$$R_{axial} = \frac{N_{rms}}{S_{axial}} \tag{4.2}$$

Obviously, the greater is the value of the sensitivity the better is the resolution. In addition, if the RMS noise of the output voltage is low, the sensor can reach nanometer level resolution. Figure 4.3(b) represents the 2 nm resolution of the FODS that is achieved by displacing a flat mirror perpendicularly away from the sensor probe.

[2]Common configuration represents when the flat mirror is displaced perpendicularly from the FODS probe surface, see sub figure 4.2

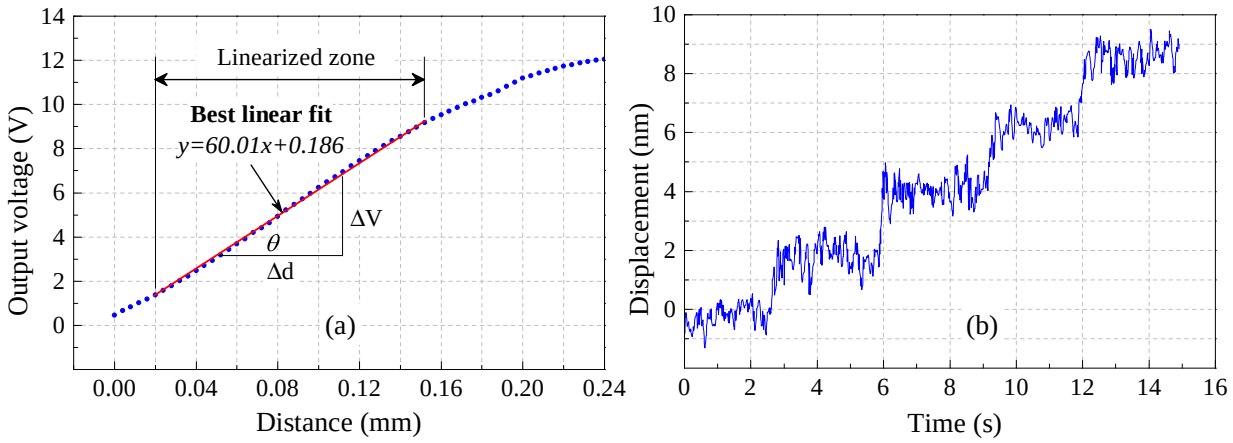

FIGURE 4.3: FODS (a) sensitivity its linear zone (b) resolution [Prel 06]

In practice, there are several factors that influence the output characteristics of the FODS which limits its functionality during experimentation. For example, in order to obtain higher sensitivity the quality of the target surface plays an important role. Its characteristics can be defined using parameters such as its roughness, flatness and the reflectivity factor. Higher values of the roughness and the flatness of the surface can lead to high value of the RMS noise and linearity error of the FODS during its application [Khia 07]. According to the earlier studies conducted in [Wang 99], it has been concluded that in order to obtain nanometer level resolution of the FODS, the roughness and flatness values of the reflective surface be less then 10 nm and $\lambda/10$ (where, $\lambda \in$ [400 nm : 700 nm]), respectively. In addition to these surface parameters, gold coated surfaces lead better sensitivity for a light with a wavelength higher 650 nm due to its higher coefficient of the reflectivity (≈ 0.98), [Khia 07].

The main limitation of the FODS while using it in linear zone is its displacement measurement range. This means that its application in its common configuration into the MPS developed in the previous chapter will eventually limit the motion range of the MPS to a maximum value of 200 μm. For this reason, in the following section a solution has been proposed in order to realize a compact miniature long range displacement sensor.

4.2 Long range displacement sensor principle

In order to extend the displacement measurement range of the FODS while using it in its linear zone, Prelle *et al.*, [Prel 06] proposed a solution in an earlier study conducted at Roberval laboratory. This solution is based on moving the flat mirror at angle (α) with respect to the FODS probe surface as shown in figure 4.4(b). This change in displacement direction increases the measurement range of the sensor by the $(\sin\alpha)^{-1}$ ratio. Figure 4.4 represents a comparative study between two motion direction cases of the flat mirror (see figure 4.4(a) and (b)). From the results it can be seen that in common configuration (i.e.,

α=90°) the measured displacement range is 200 μm. On the other hand, if the mirror is moved with an angle (α=45°) with respect to the probe axis, the measured range of the sensor rises up to 283 μm which represents a 40% increase in the range with respect to the common configuration case.

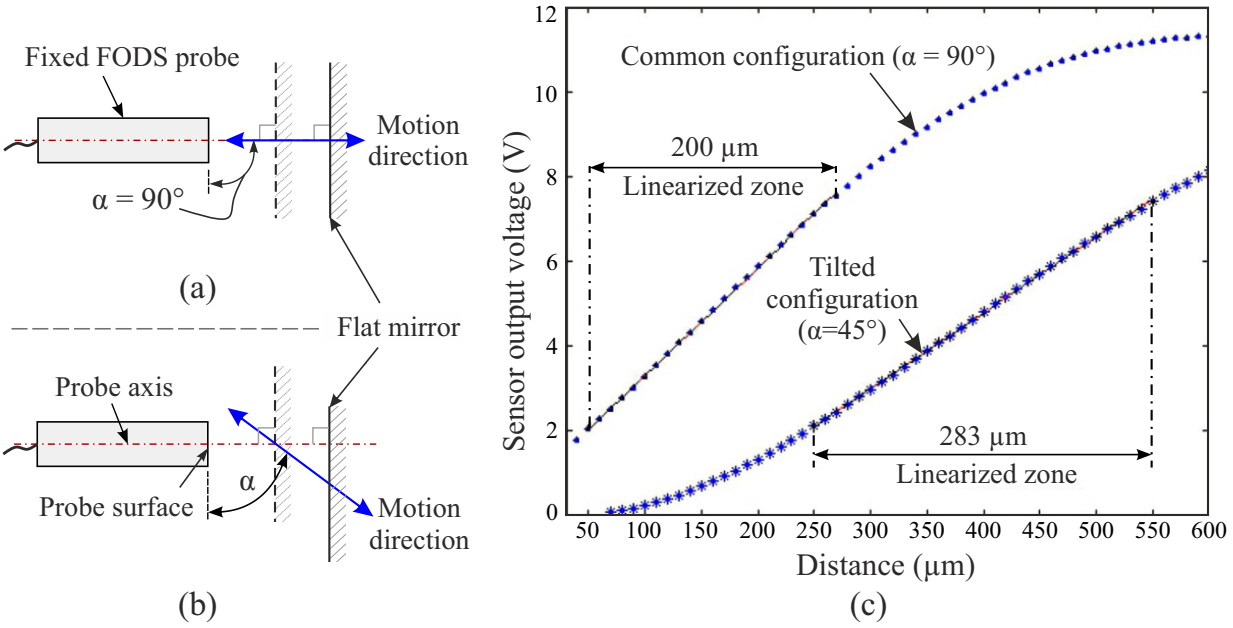

FIGURE 4.4: (a) Common configuration of the mirror and FODS probe (b) Tilted mirror configuration (c) Increase in the sensor range [Prel 06]

A consequence of the proposed solution is that the sensitivity and resolution of the FODS becomes the function of the displacement angle (α). The new sensitivity (S_α) and resolution (R_α) of the sensor with respect to the axial sensitivity and resolution (i.e., when α=90°) can be mathematically written as in equation (4.3).

$$\begin{aligned} S_\alpha &= S_{axial} \sin\alpha \\ R_\alpha &= \frac{R_{axial}}{\sin\alpha} \end{aligned} \tag{4.3}$$

From the above equation it can be seen that the sensitivity of the sensor will decrease with decrease in mirror displacement angle (α). This effect can be seen in the figure 4.4(c) as the slope of the linearized zone in the case of α=45° is reduced as compared to the case, α=90°. This indicates that the resolution of the sensor will deteriorate. However, it will remain in the range of few nanometers. For example, if the axial resolution of the sensor is 2 nm, the lateral resolution (R_α) will be around 2.828 nm for α=45°. Indeed, the value of the lateral resolution is the function of R_{axial} and α, but the sensor operates in the linear zone.

4.2.1 Extending the solution to realize long range measurement

Even with the 40% increase in the measurement range by moving a single mirror at angle (α=45°) with respect to FODS probe surface, it still cannot be employed to measure the long range (millimeter level) displacement. So, to solve this problem, the proposed method has been further extended to implement the FODS with a set of tilted mirrors configuration here called "grating" as shown in figure 4.5. A grating consists of a series of repeated tilted mirror (termed as "grating step"), each inclined at angle α as shown in figure 4.5.

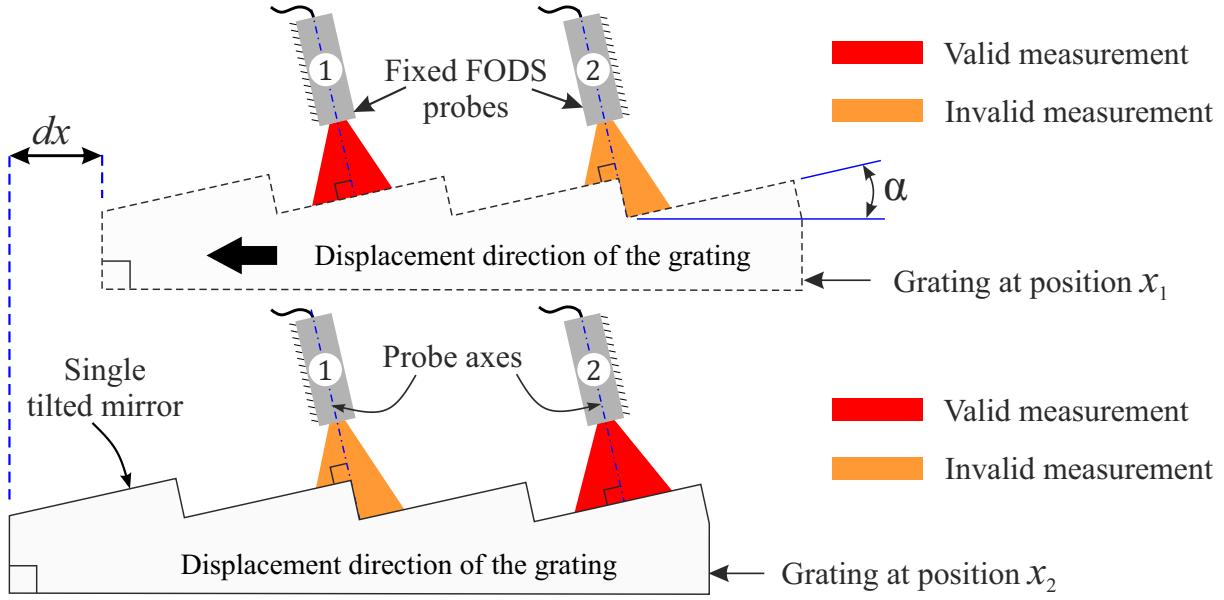

FIGURE 4.5: Long range sensor concept

The main advantage of this approach is that the measurement range of the sensor becomes a function of the number of the grating steps. So, in order to measure the displacement over millimeter level range, more grating steps can be added. In addition, since the sensor is used in its linear zone it will exhibit high sensitivity over each grating step. However, this solution leads to displacement measurement continuity issue during the transition between two adjacent grating steps because a single FODS probe will provide invalid measurement when it illuminates two adjacent grating steps, simultaneously (see figure 4.5). In order to solve this problem, two FODSs are needed to avoid the crossing edge difficulty by means of switching the measurement in between the FODS probes [Prel 06]. For example, in figure 4.5, it can be seen that when grating is at position x_1, FODS probe (1) is in front of the grating step and provides a valid measurement while FODS (2) illuminates two grating steps at the same time, thus providing an invalid measurement. Similarly, if the grating are moved laterally to a distance "*dx*", the FODS probes (1) and (2) will provide invalid and valid measurement respectively, at position x_2.

The proposed design of the long range sensor depends on different geometric parameters such as height and length of the grating steps, FODS probe dimensions, etc. In order to determine these parameters a geometric modelling has been carried out in the following section.

4.3 Geometrical optimisation of the long range sensor

In this section, the geometrical modeling has been realized in order to compute the optimal design parameters of the gratings to achieve smallest possible limit of the resolution (few nanometers). From equation (4.3), it can be seen that the lateral resolution (R_α) is inversely proportional to the sin (α). So, in order to decrease the lateral resolution (R_α), the angle (α) should be as large as possible. However, the value of this angle depends on several geometric parameters as shown in the figure 4.6. The description of these parameters are provided in table 4.1.

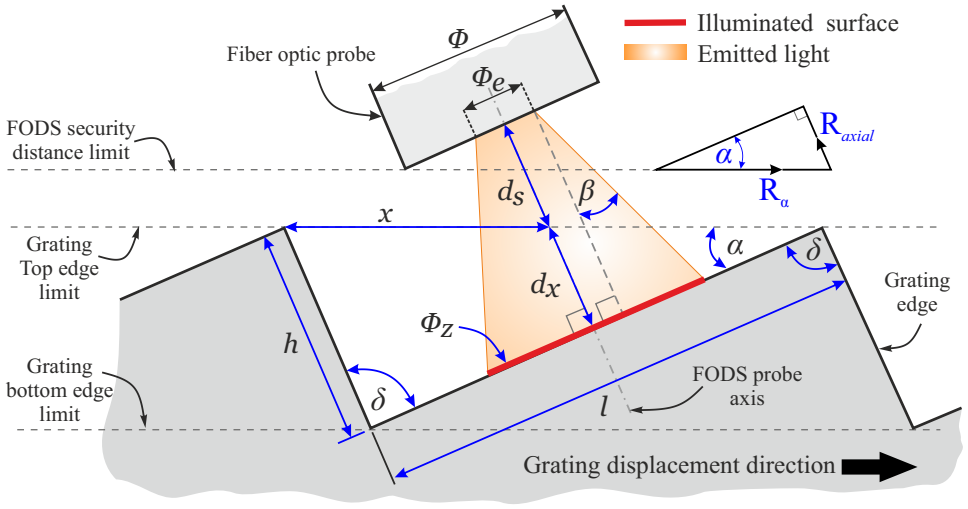

FIGURE 4.6: Enhanced two dimensional view of a single grating step with FODS probe

Symbol	Definition	Symbol	Definition
Φ_e	Emission fiber diameter	h	Height of the grating step
Φ	FODS probe diameter	l	Length of the grating step
β	Half angle of the numerical aperture	d_s	Security distance
α	Angle of the grating step	d_x	Distance: probe/ step = x·sin α
Φ_z	Diameter of the illuminated zone	δ	Bottom angle of the grating step

TABLE 4.1: Definition of the FODS probe and grating step parameters

The diameter of the illuminated zone (Φ_z) as a function of the emission fiber diameter (Φ_e) can be mathematically defined as in equation (4.4).

$$\Phi_z = \Phi_e + 2d \tan \beta \tag{4.4}$$

The relation represents that (Φ_z) is a function of the numerical aperture of the emission fiber and the distance between the FODS probe and grating surface (d=d_s+d_x). Since the numerical aperture is constant once the fibers have been selected, the illuminated surface becomes a function of the distance between the probe and gratings (d). However, this distance consists of a constant value of the security distance (d_s) and the distance (d_x) that varies with respect to the change in the axial displacement (x) between the FODS probe and gratings. If the diameter of the illuminated surface (Φ_z) is less than the grating step length (l) the displacement measurement will be valid for a single probe.

As explained earlier, the FODS will be employed in its linear zone because of its high sensitivity and resolution. Due to the sensor characteristics in this zone the sensor probe will be placed very near to the gratings. However, in order to avoid any collision between the sensor probe and the gratings during experimentation, the security distance (d_s) need to be fixed. Taking in account the diameter of the FODS probe, equation (4.5) provides the basic criterion in order to select the security distance with respect to the inclination of the grating step (α) [Prel 06].

$$d_s > \frac{\Phi}{2} \tan \alpha \tag{4.5}$$

4.3.1 Influence of the FODS probe dimensions

The selection of the FODS probe dimensions is one of the important task in the geometric optimisation of the gratings. From equation (4.5), it can been seen that, for a fixed value of the security distance (d_s) between the sensor probe and the grating step, the diameter of the FODS probe is inversely proportional to the $\tan(\alpha)$. So, by increasing the grating step angle (α), the diameter of the FODS probe needs to be reduced accordingly. However, in reality the selection of the FODS probe diameter (Φ) is not a free choice as it depends on several design/fabrication parameters (e.g., numbers, diameter, arrangement, metallic protection of the fibres, etc.,) in commercially purchased fibers.

In order to realize a long range displacement sensor, the FODS probe used in this work consists of Ø2 mm. With these sensor probe diameter, it was concluded in an earlier study conducted at Roberval laboratory, that for a minimum security distance (d_s=30 μm), a maximum grating step angle (α) of 3.81° can be achieved. For this grating step angle, a 15 nm lateral resolution (R_α) was reported for 1 nm axial resolution (R_{axial}) of the FODS in [Prel 06]. Indeed, in order to improve the lateral resolution of the sensor, the grating step angle (α) needs to be increased. However, for a fixed value of the security distance (i.e., 30 μm) the increase in the grating step angle (α) imposes limitation on the distance (d) between the FODS probe and the grating step.

Figure 4.7 represents the comparison between the sensor probe employed with two types of the gratings having parameters (α_1, l_1) and (α_2, l_2) where ($\alpha_1 < \alpha_2$) and ($l_1 > l_2$).

Assuming that the grating with length (l_1) provides a maximum grating step angle of (α_1) with FODS probe ($\varnothing_1$=2 mm) as presented in case (a), the maximum perpendicular distance (d_1) between the sensor probe and the grating step will be limited to a value of 130 μm due to the working range of the FODS in linear zone (see sub section 4.1.1.1). Now, if the FODS probe is used with the grating having length l_2, the grating step angle (α_2) will lead to a distance (d_2) for the same security distance (d_s) to avoid any collision between the FODS probe and grating (see case (b), figure 4.7). However, the value of this distance (d_2) will be greater than distance (d_1) and as a result the diameter of the illuminated zone (Φ_z) will become larger due to the increase in the distance (i.e., $d_1 \rightarrow d_2$). This will lead to a smaller or invalid measurement length over grating step length (l_2) due to the grating step angle (α_2).

In order to solve this problem, Khiat *et al.* [Khia 07], proposed to reduce the diameter of the commercially purchased FODS probe. By this way, the sensor probe can easily be placed at the same distance (d_1) in front of the grating step with parameters (α_2, l_2) as shown in the case (c) of the figure 4.7.

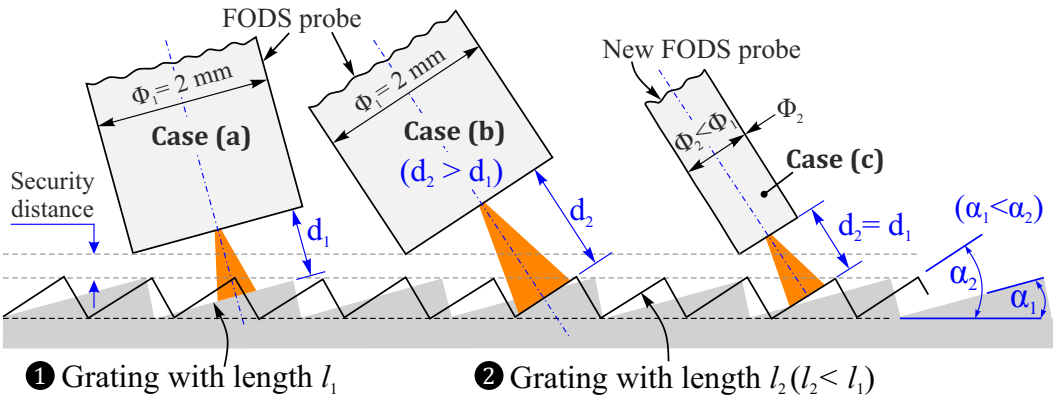

FIGURE 4.7: Selection of the FODS probe for geometric modeling

4.3.1.1 Reduction of the FODS probe diameter

In order to reduce the diameter of the FODS probe, conventional machining approach was selected to reduce the thickness of the steel cladding material that encapsulates the fiber bundle [Khia 07]. However, the machining of the FODS probe described in section 4.1 was not possible as the thickness of the metallic part of the FODS probe was very small (see figure 4.8(a)). So, a new FODS probe has been purchased from OMRON manufacturers. This new sensor consists of seven PMMA fibers each having 175$\pm$10 μm diameter and numerical aperture 0.46. Furthermore, the thickness of the metallic part of this new probe allowed us to remove 500 μm from both sides of the probe as depicted in the figure 4.8(b). The new width dimension of the sensor probe was obtained as 1 mm. A

further reduction of the metallic part was avoided in order to leave some metallic protection to hold the fiber bundle intact after machining as shown in the figure 4.8 (c).

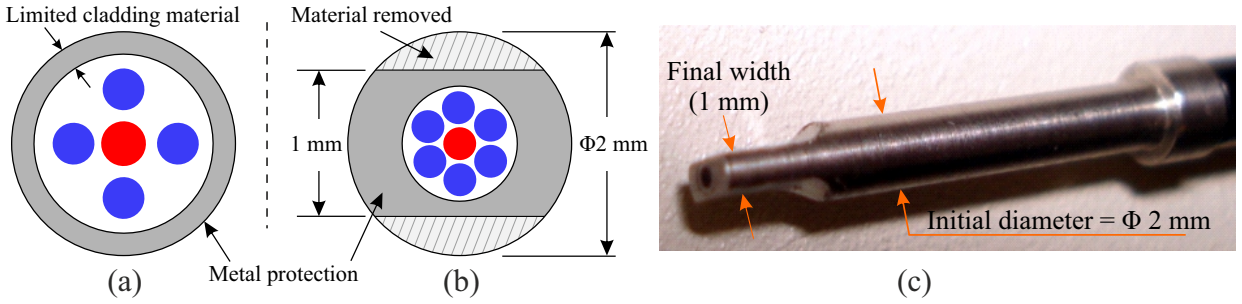

FIGURE 4.8: (a) Old FODS probe with limited cladding material (b) New FODS probe with six reception fibers (c) Real view of the machined new FODS probe

With this new FODS probe, the functioning of the sensor remains the same as described in the section 4.1. The fiber located at the center of the probe acts as an emission fiber and the other six fibers situated around the emission fiber are the reception fibers. However, due to the larger number of the reception fibers in the sensor probe and change in the diameter of the fibers in the bundle, an experiment was carried out to determine the range of the linear zone by moving away a flat mirror in front of the new FODS probe (similar to the case presented in figure 4.2). The range of the linear zone of the new FODS was found to be 170 μm. However, after applying a linear fit it has been concluded that for a linearized zone of 130 μm the sensor delivers a maximum sensitivity of 88 mV/μm with a linearity error less than 1%. Based on this information, during geometric model simulation the maximum value of the distance (d) between the FODS probe and grating step has been fixed to 130 μm.

4.3.2 FODS signal overlap criteria

According to the working principle of the long range sensor, a single FODS probe will lead to signal discontinuation (see figure 4.9(a)). A set of two FODS probes are needed in this case. However, it is not necessary that the application of two FODS probes will provide continuous signal measurement. For example, in the figure 4.9(b) it can been seen that, even with two FODS probes, there is a signal interruption which leads to the discontinuity in the displacement measurement. This is due to the relative distance between the two probes with respect to the grating step. To achieve continuity, a signal overlap (x_o) is needed to properly switch between the two sensors as shown in the figure 4.9(c). In addition, it is necessary that in the overlap zone both sensor should provide valid measurement. So in this scenario, the relative distance (δ_E) between the two sensor probes

(see figure 4.9(d)) has been selected using equation (4.6).

$$\delta_E = (n + \frac{1}{2})\, l \tag{4.6}$$

where, the term n represents a number of the grating step. This parameter is added to avoid the placement complication of the two FODS probe on adjacent grating steps due to their diameters. Moreover, it can been seen in the figure 4.9(d), that the relative distance between the FODS probes (δ_E) has been defined with respect to the centre of the grating step length to obtain a symmetrical overlap zone at the start and end of the FODS signals (see figure 4.9(c)).

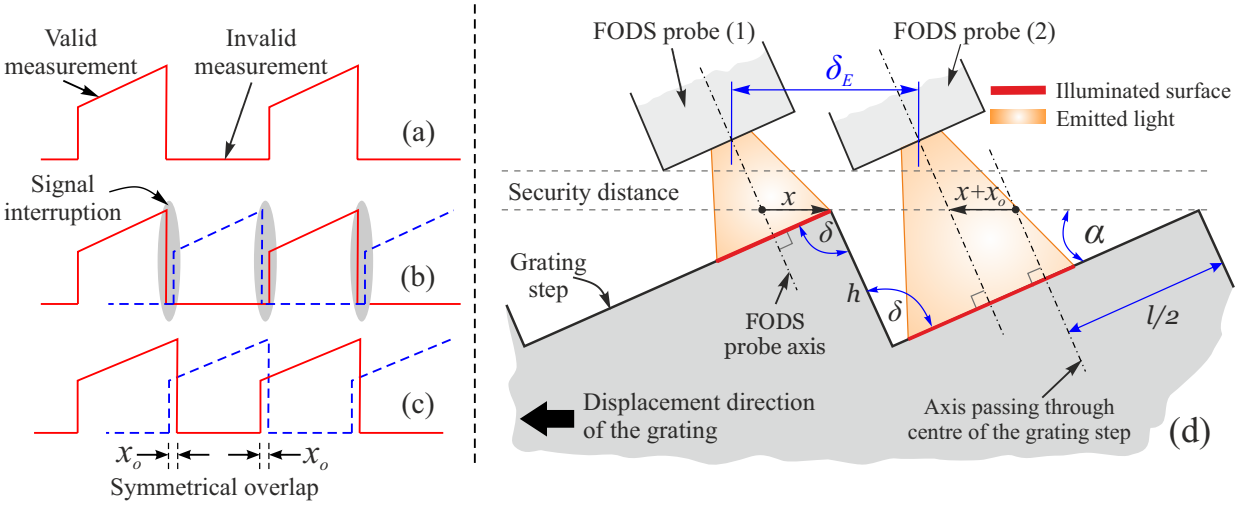

FIGURE 4.9: FODS signal(a) with single probe (b) with two probes without overlap (c) with two probes with overlap [Prel 06] (d) overlap distance setting

4.3.3 Selection of the bottom grating angle

The value of the bottom angle (δ) of the grating depends on the fabrication procedure adapted to realize the gratings. In practice, this angle can be selected in two different ways for the same grating step angle (α) as shown in the figure 4.10. However, in the second case (when $\delta > 90°$, see figure 4.10(b)) the real length of the grating (l_r) becomes smaller as compared to the first case (when $\delta < 90°$, see figure 4.10(a)). This reduction in real length (l_r) is due to increase in the transition zone length, $\Delta l = h_r \cos(\delta\text{-}90°)$, where a single FODS probe illuminates two adjacent grating steps at the same time. In addition, this increase in the transition zone length (Δl) can not be neglected and as a result, in order to achieve valid signal overlap, the distance between two FODS probes (δ_{E2}) needs to be increased by a factor $\Delta l \cos(\alpha)$ as compared to the case where $\delta < 90°$.

Taking into account the fabrication constraints (e.g., machining tolerance, residual radii at the bottom of the grating due to the tool tip, etc.), in our study, the selection of the bottom angle of the grating has been carried out using criteria, $\delta \leq 90°$, as shown

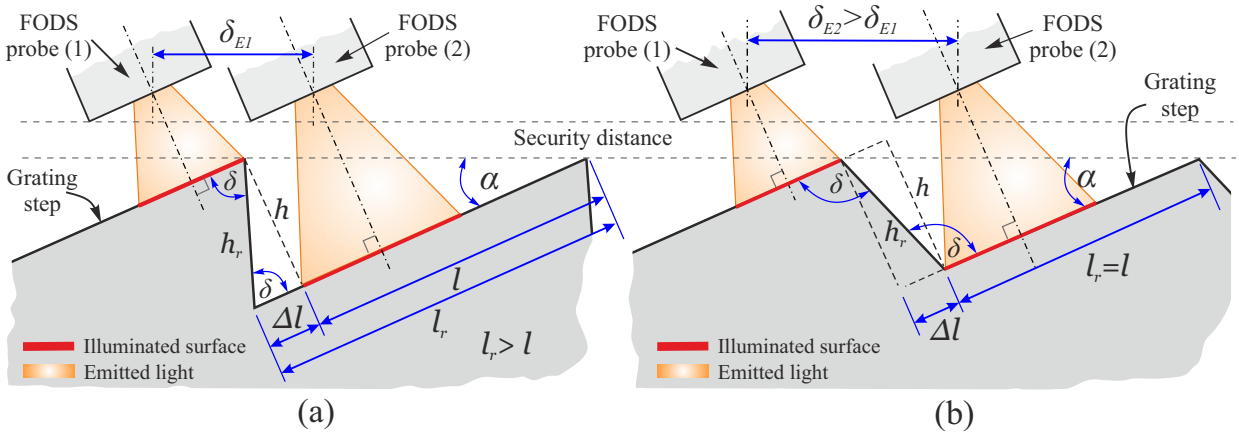

FIGURE 4.10: Bottom angle grating choices (a) $0° < \delta \leq 90°$ (b) $180° > \delta > 90°$

in the figure 4.10(a). The main advantage of this approach is that the useful length (l) depends on the height (h) and angle (α) of the grating even if $l_r > l$. So, the residual length of the grating (Δl) can easily be discarded with respect to the case presented in figure 4.10(b). As a result, to achieve valid signal overlap, the distance between two FODS probes (δ_E) remains the same. For our simulations, the value of the bottom angle of the grating (δ) was kept 70.53°. This value corresponds to the crystallographic orientation of the slow etching planes (i.e., {111} plane) of the silicon when planar grating is realized via microfabrication in single crystal silicon substrate. The choice regarding the selection of this angle (δ) is discussed in the section 4.4.1.4.

4.3.4 Simulation results

By taking into account all these geometrical constraints, a simulation in MATLAB® has been carried out for the FODS probe having 1 mm diameter. A 30 μm security distance (d_s) along with 30 μm signal overlap criteria have been selected on the basis of earlier studies in [Prel 06, Khia 07]. Furthermore, during simulation a condition has been employed that if the overlap zone x_o is less than 30 μm or the distance (d) between the sensor probes and grating step increases beyond 130 μm (i.e., outside the linear zone of the FODS), the output solution for the theoretical resolution result is set to zero. This condition was adapted for the purpose of simplification in order to facilitates the analysis of the output solutions.

Figure 4.11 represents, the theoretical lateral resolution (R_α) of sensor with respect to the length (l) and height (h) of the grating step. From the results it has been concluded that, for the optimal real length (l_r = 653 μm) and height (h_r = 96 μm) of a grating step, the maximum grating step angle (α) was found to be 8.29°. In addition, the useful length (l) over a single grating step was computed to be 621 μm for the selected value of the bottom grating angle (δ=70.53°). Using equation 4.3, the theoretical limit of the resolution of the long range displacement sensor with these optimal geometrical parameters

was computed to be 7 nm for a theoretical axial resolution of 1 nm.

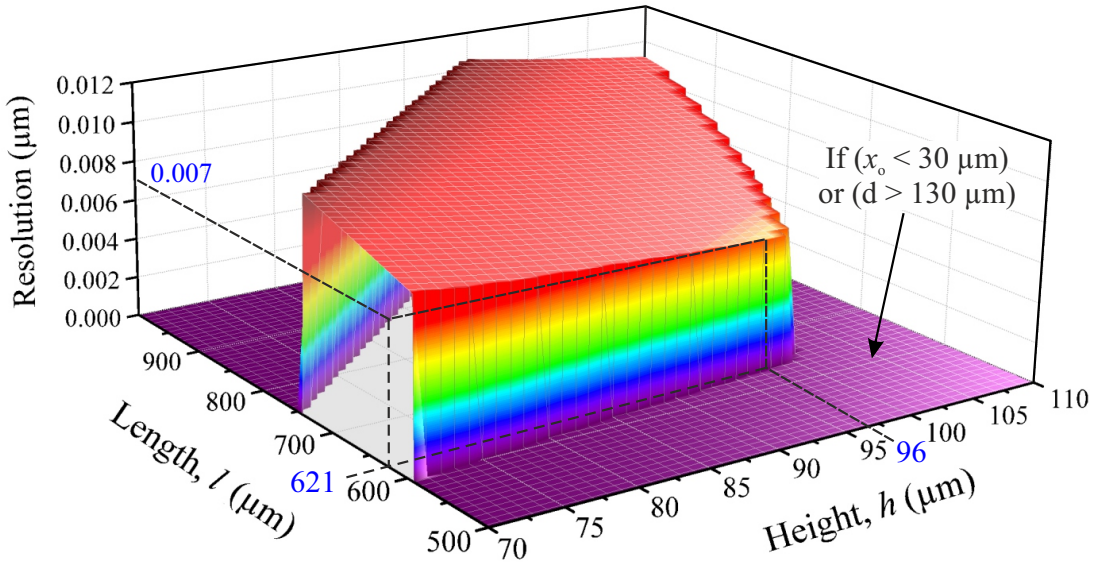

FIGURE 4.11: Limit of the sensor resolution as a function of the grating length and height

Moreover, to validate the signal overlap criteria, the theoretical axial displacement (dx=x· sin α) obtained via simulation has been plotted with respect to the theoretical lateral displacement (x) of the grating as shown in the figure 4.12. An overlap of 30 μm was found which satisfy the requirement for the continuous displacement measurement by switching the signal between two FODSs.

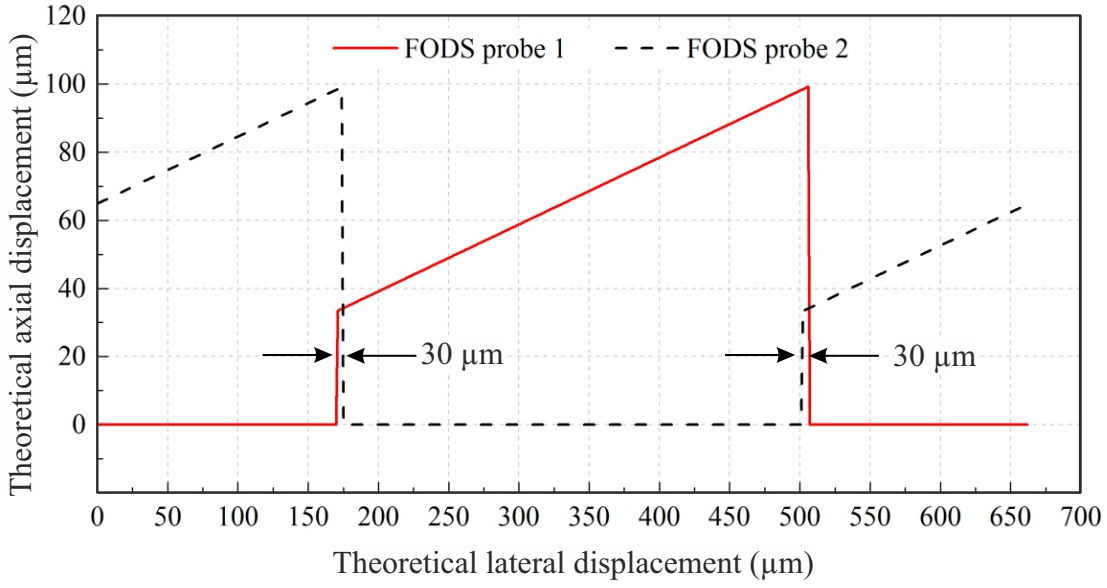

FIGURE 4.12: Theoretical results to represent the overlap between two FODS probe measurement based on the optimal dimensions computed via simulation

4.4 Microfabrication of the planar grating

After determining the optimal geometric parameters of the grating, its fabrication has been carried out. According to the previous studies conducted in [Khia 07] at Roberval laboratory (UTC), it was decided to fabricate this grating via microfabrication. This fabrication technology was selected in order to achieve overall small dimensions of the planar grating with high surface quality (i.e., roughness and flatness parameters in the range of few nanometers) of the grating steps. These characteristics are very difficult to acquire via conventional machining techniques (e.g., shaping, milling, etc.) due to the fabrication constraints such as machine/tool tolerance, material handling, etc. In addition, microfabrication technology leads to the production of miniature components with dimensions from the scale of few micrometer to several millimeter with high accuracy and micrometer level fabrication tolerances. Furthermore, the parallel fabrication (also known as "batch processing") vastly reduce the fabrication cost thus making it more economical solution as compared to conventional fabrication techniques with mechanical tools.

Microfabrication technology is based on collection of different technologies such as lithography, etching, polishing, etc., to fabricate micro components. It has been widely used in the microelectronics industry to realize micro components such as Integrated Circuits (ICs) over the past sixty years. However, this technology demands precise positioning/machining tools for pattern processing, etching solutions for realizing three dimensional structures and most importantly the dust free fabrication environment (known as "clean rooms") in order to avoid any contamination during microfabrication process. In order to meet these standards, in this work the microfabrication of the planar grating has been carried out at the Institute für Mikrotechnik[3], Technische Universität (IMT-TU) Braunschweig, Germany which specializes in this technology.

In general, to realize 3D microstructure, the whole microfabrication process can be described as shown in figure 4.13. Initially, the material selection (in the form of wafers) is usually carried out as the machining of different materials demands different fabrication techniques. For example, materials such as glass, aluminum, copper, etc., cannot be machined with respect to their atomic structure whereas, silicon can be machined with respect to its crystallographic orientation. In addition, the choice of the microfabrication techniques is usually carried out with respect to the need of the three dimensional shapes in the selected material.

Once the microfabrication technique and the material are defined, a mask with desired patterns is designed and fabricated. Afterwards, the wafers are prepared for machining by adding different inorganic layers (e.g., silicon dioxide (SiO_2), silicon nitride (Si_3N_4), etc.,) that serves as masking layers. In addition, the desired pattern is transferred

[3] http://www.imt.tu-bs.de/

via photolithography using the developed mask. The transferred pattern is developed and sacrificial layers are removed to expose the desired areas for machining. Next, the wafers are etched using chemical solutions to form 3D shape in the wafers, once the desired structures are achieved, a post processing of the wafers are carried out which includes verification of the desired 3D structure, removal of sacrificial layers, etc. In the end, the specimens (refers to three dimensional structures) are coated if needed and cut from the wafer with the help of precise cutting tools.

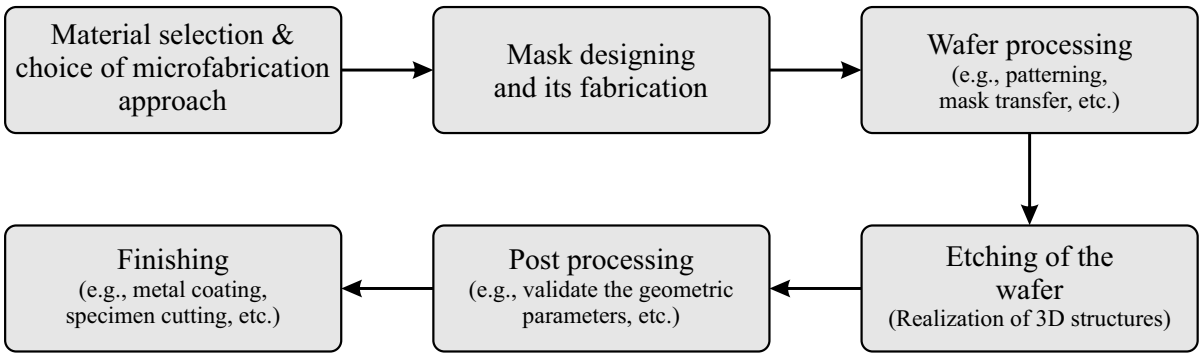

FIGURE 4.13: Schematic layout of the overall microfabrication process

In the following text, the presented micro fabrication steps are discussed in detail in order to realize planar gratings at IMT- TU Braunschweig.

4.4.1 Selection of the material and micromachining approach

In our study, a grating has been machined into silicon material. This material is selected due to its low sensitivity to temperature change (2.6×10^{-6} °C) and high melting point temperature (1413.85 °C) which makes this material more interesting as most of the microfabrication process (e.g., deposition of sacrificial layers, etc.) is often performed at high temperature (between 80°C and 180°C). Due to these listed or non listed characteristics, silicon material is used in many electronic devices such as diodes, transistors, etc., for their important electrical properties.

4.4.1.1 Classification of silicon material

Silicon material is classified into three different types depending upon its crystalline form as depicted in figure 4.14. The simplest form of the silicon is known as the *amorphous* form in which the atoms are randomly oriented. The *polycrystalline* form consists of randomly oriented grains. However, in each grain the orientation of the atoms are along single direction (see figure 4.14(b)). The third form of the silicon which is mostly used in microfabrication is known as *monocrystalline* form. In this form, the atoms of the silicon material are perfectly oriented along single direction which allows it to be machined

along specific crystallographic orientation via microfabrication. Commercially, monocrystalline silicon are fabricated in the form of a circular wafer/substrate as shown in the figure 4.14(b) with marker (a flat or a notch) to identify the crystallographic orientation of the silicon crystal.

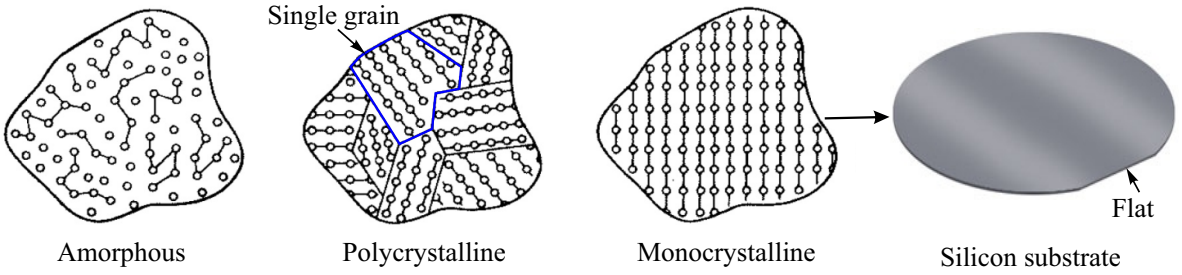

FIGURE 4.14: Different forms of the silicon material [Dech 06]

The silicon crystal has a Face Centered Cubic (FCC) structure in which each silicon atom forms the covalent bonds with four adjacent atoms (see figure 4.15(a)). It is also known as diamond structure [Butt 94]. In a Single Crystal Silicon (SCS)[4] wafer, the crystallographic orientation of the silicon crystal is determined using Miller indices. As an example, figure 4.15(b) represents, three crystallographic planes (i.e., {100}, {110}, {111}) formed in cubic-crystal unit cell of silicon. According to literature, along these planes silicon exhibits different physical properties such as piezoresistivity and Young's modulus values which lies between that of steel and aluminum. However, it is much lighter than these two materials which increases its significance in the MEMS applications to fabricated light weight components. In addition, all planes parallel to each other exhibit the same physical characteristics [Khia 07]

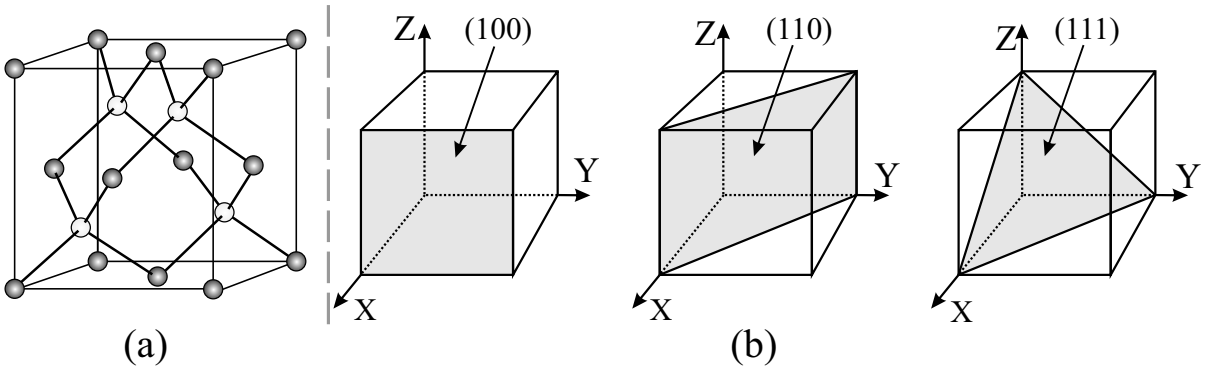

FIGURE 4.15: (a) FCC structure of the silicon (b) Different crystallographic planes in silicon crystal [Rive 04]

[4]Single Crystal Silicon (SCS) is referred to Monocrystalline silicon

4.4.1.2 Micromachining of silicon material

Micromachining of the SCS material is usually carried out by removing the silicon material from the substrate via chemical process known as “etching”. In this process, the etching agent such as a corrosive liquid (e.g., Potassium Hydroxide (KOH), etc.) or a chemically active ionized gas (known as *plasma*) is used to chemically react with the unprotected parts of the silicon substrate (see figure 4.16(a)). In literature, the etching with liquid and plasma are also referred as “wet etching" and “dry etching" technologies, respectively. In microfabrication field, both techniques are significantly employed. However, wet etching approach is mostly preferred due to its low cost, simplicity and high degree of selectivity of silicon material over dry etching [Mado 02]. In this study, to realize three dimensional planar grating in SCS material, we have selected wet etching approach due to the above mentioned characteristics.

4.4.1.3 Wet isotropic/anisotropic etching

Based on the selected etching approach (i.e., wet etching) in the previous sub section, the removal of the silicon material can be carried out in two different manners. First approach consists of non-directional removal of material from the silicon substrate which is also known as “Isotropic etching”. In this approach, the etching agent (usually aqueous acidic solutions containing HydroFloric acid (HF) with Nitric acid (HNO_3) reacts with the unprotected parts of the substrate in all directions with the same etching rate. Moreover, the wet isotropic etching is a diffusion limited process, so the only restriction in this etching approach is that the final structure will always be rounded (see figure 4.16(b)).

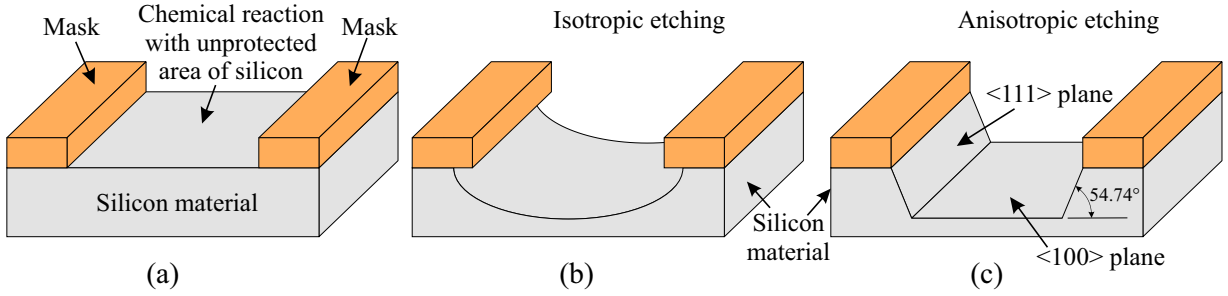

FIGURE 4.16: (a) Silicon substrate with mask (b) Isotropic etching (c) Anisotropic etching

Another approach to machine silicon is known as “Anisotropic etching”. In this approach, basic solutions (e.g., KOH in water) are mostly used to remove the material in order to realize three dimensional structures in SCS substrate. In this approach, the etch rate of different crystallographic planes (see figure 4.15(b)) varies with respect to different etching parameters such as temperature and concentration of the etching solution. The study of J.March *et al.*, highlights these variations in the etching rate of different crystallographic planes with respect to the variation of etching temperature and solution

concentration (see figure 4.17). From this study, it can be observed that the etching rate of the {111} plane is very slow as compared to {110} and {100} planes. In wet anisotropic etching, {111} planes are referred as etch stops and the final shape of the etched structures in SCS substrate is determined with the help of these slow-etching planes as shown in the figure 4.16(c).

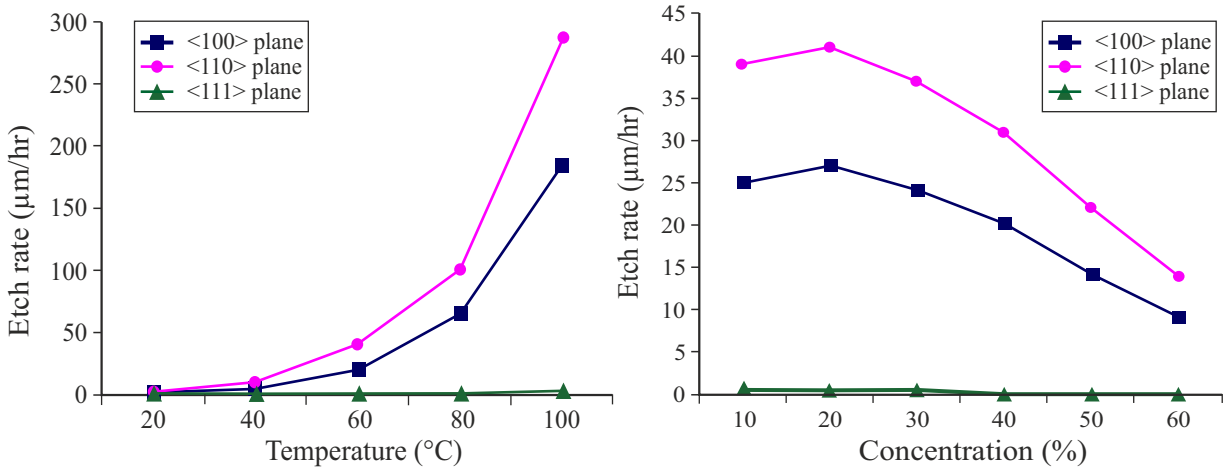

FIGURE 4.17: Etch rate as a function of etching solution (a) Temperature (b) Concentration [Marc 98]

4.4.1.4 Selection of the SCS substrate to realize gratings

In order to achieve a particular geometry for the grating (see figure 4.6), we have selected wet anisotropic etching technique. However, since the functional structure of the grating after wet anisotropic etching of the silicon is determined by {111} plane, a specific orientation of the silicon crystal in SCS substrate was needed to obtain a grating step angle α=8.29°. In practice, the silicon wafers are cut from silicon ingot and the anisotropic etching of silicon wafer with (100) plane as wafer surface, delivers (111) planes as side walls of the etched structures. The opening angle of these side walls with respect to the normal of the (100) wafer surface has a value of 70.53° [Klum 95].

For our application, the selection of the silicon substrate has been carried out on the basis of the study conducted in [Khia 07]. In this study, two possible configurations have been reported to achieve (111) plane of the silicon crystal at 8.29°. These two configurations have been identified by cutting the silicon ingot along either the direction of {110} or {100} planes of the silicon crystal. The first configuration leads to a bottom grating angle, δ=109.47°, between the intersection of the {111} planes as shown in the planar special case (1) in the figure 4.18(a). On the other hand, if the cutting of the silicon ingot (at α=8.29°) is carried out along the direction of the {100} plane, the intersection of the {111} planes yield a bottom grating angle of δ=70.53° (see planar special case (2), figure 4.18(a)). Both types of the configurations can be used to realize planar grating. However, the grating realized with first configuration (see figure 4.18(b))

will lead to higher value of the transition zone length (Δl, see section 4.3.3) as compared to the second configuration (see figure 4.18(c)).

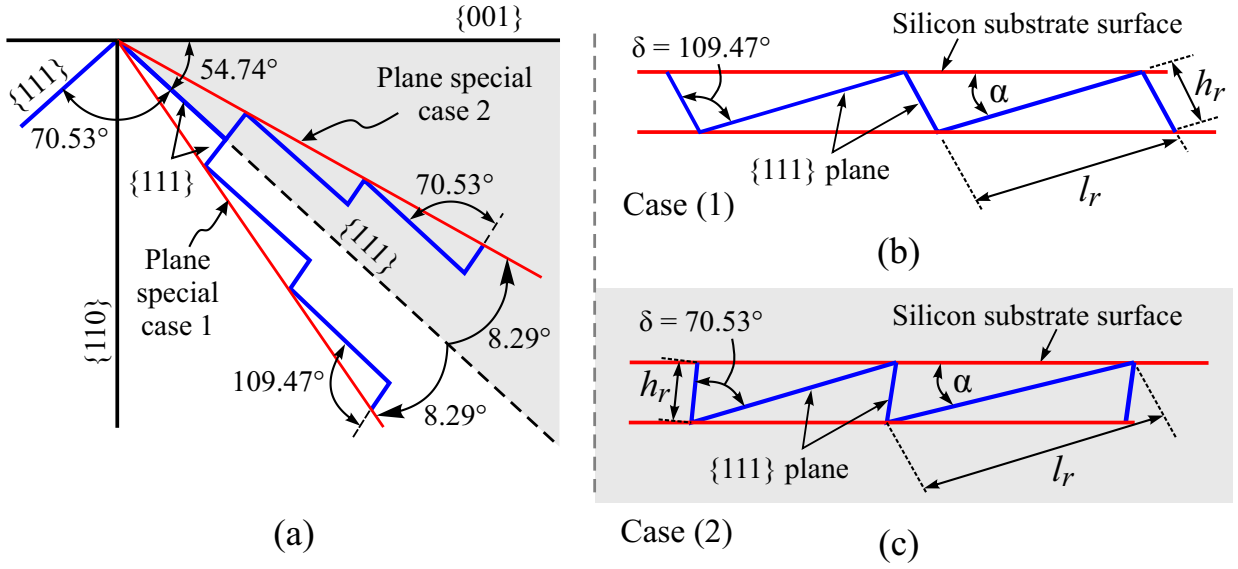

FIGURE 4.18: (a) Possible crystallographic configuration of the silicon wafer (b) Special case (1), α=8.29° and δ=109.47° (c) Special case (2), α=8.29° and δ=70.53°

Taking into account these configurations, we have selected the special case (2) in order to fabricate the silicon grating for the development of long range displacement sensor. So, based on this configuration {111} 8.30°-off, Ø100 mm, silicon wafers with both sides polished have been purchased form *Sil*chem[5] company in Germany. A thickness of 380 μm for the commercially purchased silicon wafers was selected from the perspective to integrate the planar grating into the MPS prototype (see next chapter for details).

4.4.2 Mask design and its fabrication

After selecting the silicon wafer, the design and fabrication of the mask have been carried out for the photolithography process. Based on the dimensions for the planar grating computed via Matlab® simulation, the 2D structures of the grating have been designed in the form of clear areas (w= 614.5 μm) and rectangular stripes[6](t=33 μm) as shown in figure 4.19. The value of the (w) parameter was computed using equation (4.7).

$$w = l \cdot [\cos(\alpha)]^{-1} \tag{4.7}$$

where, l is the useful length of the gratings step, α is the grating step angle.

The overall mask design has been optimized to achieve 32 planar grating specimens in single process during experimentation. In addition, a 14×14 mm^2 footprint dimensions

[5]http://www.silchem.de/
[6]The optimal value of the rectangular stripes width (t=33 μm) was selected after experimentation.

for each planar grating was selected in accordance with the mobile part dimensions of the MPS designed in the previous chapter.

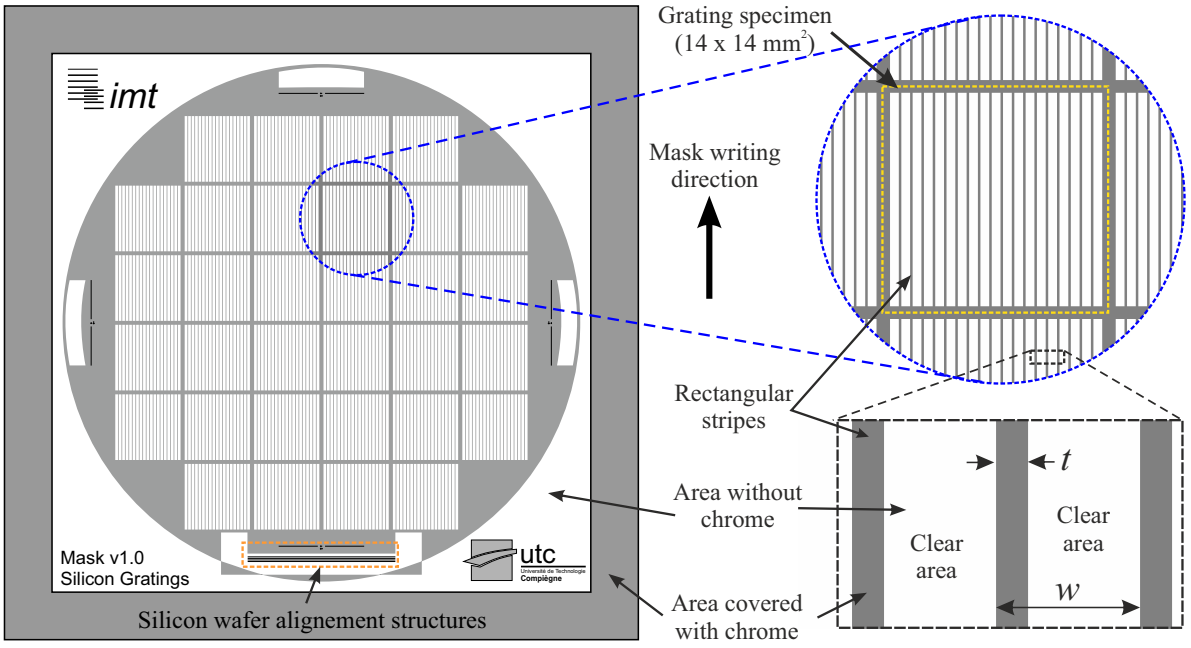

FIGURE 4.19: Layout of the mask with enhanced view of a single grating specimen

The design presented in figure 4.19 has been realized with AutoCAD and was written on a blank mask using a mask writer machine (see figure 4.20(a), step 1). The mask used in our study consists of a pre-coated square glass plate with a layer of chrome and photoresist on one side. So, during mask writing process, the mask writer transfer the design by exposing the photoresist with a laser spot. The mask writing direction was carefully selected to achieve smooth edges along the length of the stripes (see figure 4.19). In addition, some alignment structures have been designed in order to align the silicon wafer with respect to its crystallographic orientation during photolithography process.

Once the mask writing processing was completed, the exposed photoresist was developed using a chemical solution consists of a mixture of AZ 351B (50 ml) solution and water (250 ml) (see figure 4.20(a), step 2). After developing the photoresist, the chrome is etched using a chemical solution (composition: 51 g of Ceric ammonium nitrate $[(NH_4)_2Ce(NO_3)_6]$ + 324 ml of Perchloric acid $[HClO_4]$). This solution etched the chrome in the areas where it is not protected by the developed photoresist (see figure 4.20(a), step 3). After etching the chrome, the mask has been rinsed and inspected under microscope to verify the structures. After verification, the photoresist is removed with the help of acetone and ethanol (see figure 4.20(a), step 4). The finished mask consists of transparent and non-transparent (covered with chrome) areas as shown in the figure 4.20(b).

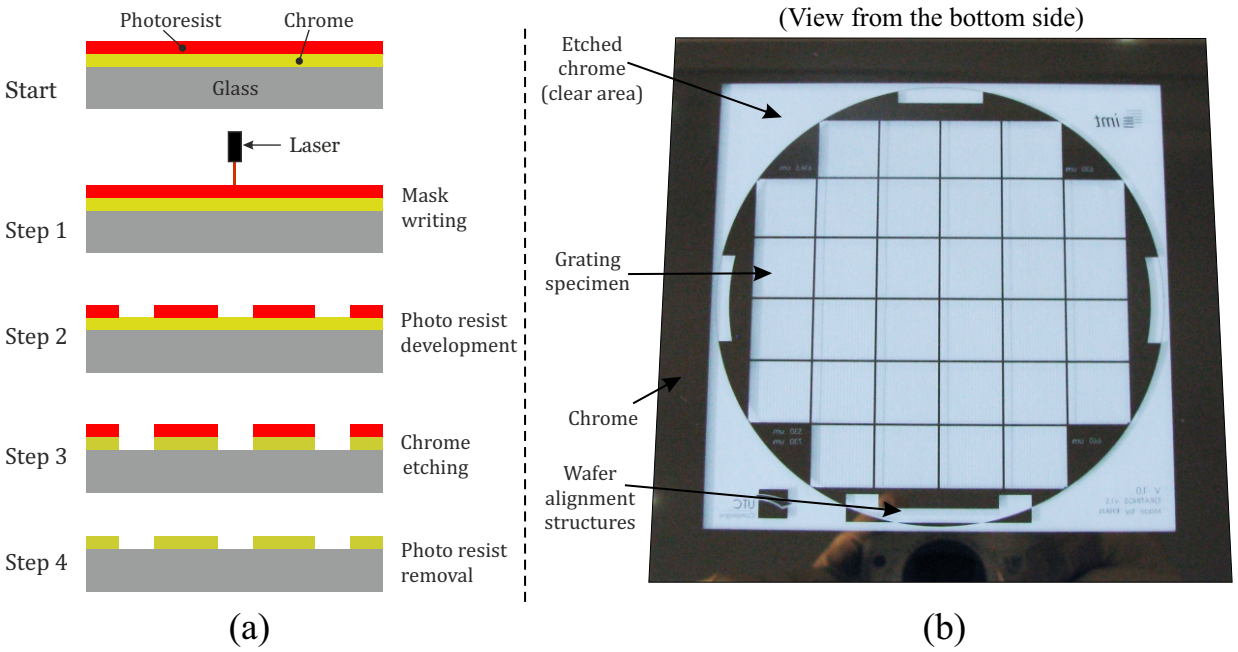

FIGURE 4.20: (a) Fabrication steps of the mask (b) Real view of the fabricated mask

4.4.3 Microfabrication of the silicon grating

After developing the mask, the micromachining of the silicon grating has been carried out. As described earlier, the main principle behind micromachining of silicon gratings is based on the deposition of inorganic layers which serves as masking layers during wet anisotropic etching process. In addition, chemical solutions such as Potassium Hydroxide (KOH) or TetraMethylAmmonium Hydroxide (TMAH) are used to remove the silicon material to form three dimensional structures. In this work, the overall process to realize silicon gratings for long range displacement sensor consists of 10 steps as shown in the figure 4.21. Initially the silicon substrate has been cleaned and inspected for any micro defects (e.g., pin holes, scratches, contamination, etc.) under microscope. In step 2, different masking layers have been realized on the silicon wafer. First, a 300 nm thick layer of silicon nitride (Si_3N_4) followed by a 300 nm thick layer of silicon dioxide (SiO_2) were realized using Plasma Enhanced Chemically Vapor Disposition (PECVD) machine on the both sides of the silicon wafer (see figure 4.21). After deposition of these layers, a layer of the positive photoresist (ma-P1215) was realized on both sides of the silicon wafer. For this process, 1 ml of the positive photoresist was spun on the top and bottom side of the substrate at 3000 rpm. The photoresist has been cured during each step by performing a soft baking for 1 min at 100°C . This soft baking is necessary in order to avoid any damage (i.e., scratching) to the photoresist layer in the following step.

In step 4, the photoresist on the top side of the substrate was exposed to the Ultra Violet (UV) light for 8 seconds using the mask shown in the figure 4.20(b). During this process, the pattern of the mask is aligned to the crystal orientation of the silicon

wafer. This is done by aligning the flat of the silicon wafer with respect to the alignment structures on the mask (see figure 4.20(b)). The wafer alignment process followed by photoresist exposure process has been carried out using a mask aligner/exposure machine (EV240). This machine is equipped with different systems such as optical alignment system, mask handling system, etc., in order to transfer the mask pattern on the wafer.

After exposing the photoresist to UV-light, it was then developed using ma-D331 developer solution (see step 4, figure 4.21). During this process, an exact image of the mask pattern forms on the silicon wafer as exposed photoresist dissolves in the developer solution. Moreover, the characteristics of the photoresist in the areas where it has been protected by the pattern of the mask (i.e., due to structured chrome layer) changes. The photoresist development time depends on several parameters such as saturation level of the ma-D331 solution, exposure time, structure dimensions, etc. In our case this time was found to be 25 seconds. After the development process, the structured photoresist was inspected under microscope for any irregularities such as improper transfer of the structure, over etching, etc. This inspection is necessary because if there is any problems regarding the development of the photoresist, it should be carried out again or else it can lead to improper etching in following steps and the silicon wafer may become unusable. After the inspection, the developed silicon wafer is hard baked at 110°C for 5 minutes.

After the development of the photoresist, Hydrofluoric acid (HF) solution (Concentration 40%, buffered 1:2) was used to etch the silicon dioxide layer (see step 5, figure 4.21). In this step, the photoresist acts as a masking layer, So the unprotected areas where SiO_2 layers is exposed to the HF solution undergoes chemical reaction. The etching of SiO_2 in HF solution is an isotropic process and the etch rate depends on the concentration of the etching solution as well as the etch depth (i.e., thickness of the SiO_2 layer). In our case, the etch rate of the SiO_2 in the buffered HF solution was found to be around 46 nm/min. So, in order to etch 300 nm thick layer of SiO_2 layer the Silicon wafer was placed in the HF solution for 6 minutes and 30 seconds. After etching the SiO_2 layer, the substrate is rinsed with deionized water in Quick Dump Rinser (QDR) machine to remove all the traces of the HF acid. After properly rinsing the wafer, the it was dried using a spin dryer machine and an inspection has been performed to validate the etching of the SiO_2 layer.

After etching the SiO_2 layer, the photoresist has been removed using acetone and ethanol (see step 6, figure 4.21). The removal of the photoresist was necessary in order to avoid any contamination in the Phosphoric acid (H_3PO_4) solution used for Si_3N_4 etching. In step 7, the Si_3N_4 layer has been etched using 100% concentrated H_3PO_4 solution at 180°C . During this process, the structured SiO_2 layer serves as masking layer. So, the areas where Si_3N_4 layers is not protected by SiO_2 are etched. The etching rate of the Si_3N_4 layer is very slow ($\approx$6 nm/min) in the H_3PO_4 solution. It takes around 45 minutes

to etch the 300 nm thick Si_3N_4 layer. After etching is finished, the wafer was rinsed, dried and an inspection under the microscope has been carried out to verify the structures etched in the Si_3N_4 layer. At this point the silicon surface of the wafer is exposed to realize grating (see step 7, figure 4.21).

In order to etch silicon, two alkaline solutions (i.e., KOH and TMAH) are mostly used in microfabrication field due to their lower environmental pollution and better surface smoothness [Bisw 06]. However, in the study conducted by Dr. Ali Khiat, it was concluded that silicon etching with TMAH solution leads to smaller values of surface roughness (19 ± 3 nm) and flatness (70 ± 13) as compared to silicon etching with KOH solution [Khia 07]. In this work, our main objective regarding the fabrication of silicon grating is to achieve further lower values for the described parameters. So, we have decided to realize silicon grating with 25% TMAH concentrated solution. During this process, the Si_3N_4 layer serves as masking layer. The silicon etching has been carried out for 4 hours with an average silicon etch rate of 0.37 μm/min.

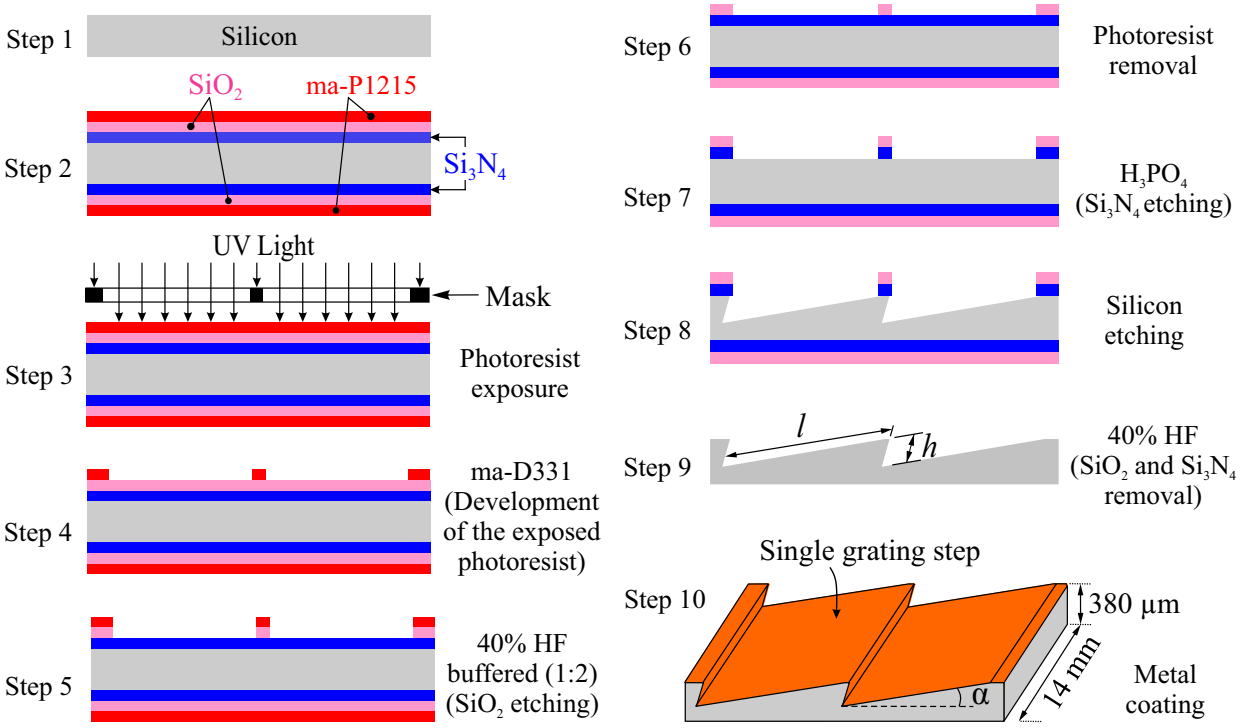

FIGURE 4.21: Micromachining process to realize three dimensional planar silicon gratings

During the etching process, the solution has been constantly stirred using a magnetic stirrer and the height of the silicon grating steps has been measured using a surface profilometer machine. In addition, the profile of the etched surface has been carefully inspected. Upon finishing the silicon etching process, the wafer was rinsed and dried in order to eliminate the traces of TMAH solution. Afterward, the layers of the Si_3N_4 and SiO_2 were removed using 40% concentrated HF solution (see step 9, figure 4.21). During this process, these layers dissolve into the HF solution thus leaving the etched silicon

substrate behind. After removing Si_3N_4 and SiO_2 layers, the silicon wafer was rinsed in QDR machine to eliminate the traces of HF solution using deionized water.

In step 10, the microfabricated silicon grating were coated with different metals (mostly gold, aluminum, chrome) to improve their surface characteristics such reflectivity index, roughness and flatness parameters [Khia 07]. This process was carried out using a Physical Vapor Deposition (PVD) machine. In this machine, the metal being deposited such as gold, aluminum, chrome, etc., on the silicon wafer is converted into vapor in a vacuumed chamber. The concept of the PVD sputtering (that has been carried out in IMT) is based on the ejecting the target material atoms (metal to be sputtered on silicon) with high-energy particles in vacuum environment. These atoms condensate on the surface of the wafer thus forms a fine layer of the metal. In MEMS, PVD sputtering is one of the most widely used techniques to deposit various metallic films on wafers such as platinum, tungsten, etc.

After metal sputtering process, the grating specimens from the wafer were cut using a diamond cutting machine. For this task, the final wafer was coated with 2 ml of the photoresist ma-1215 to protect the gratings from any particles or other contamination during cutting process. After cutting, the silicon grating specimens have been released from the silicon wafer and cleaned using Acetone and ethanol. Figure 4.22(a) represents three different planar gratings, each having dimensions $14\times14\times0.38$ mm^3 and coated with 300 nm thick chrome, aluminium and gold material, respectively. To provide a better view of the grating steps, figure 4.22(c) represents the Scanning Electron Microscope (SEM) image of the edge of the gold coated grating. In this figure the grating step (i.e., the slowest etch plane $\{111\}$) and different parameters such as height, angle and length can be clearly identified.

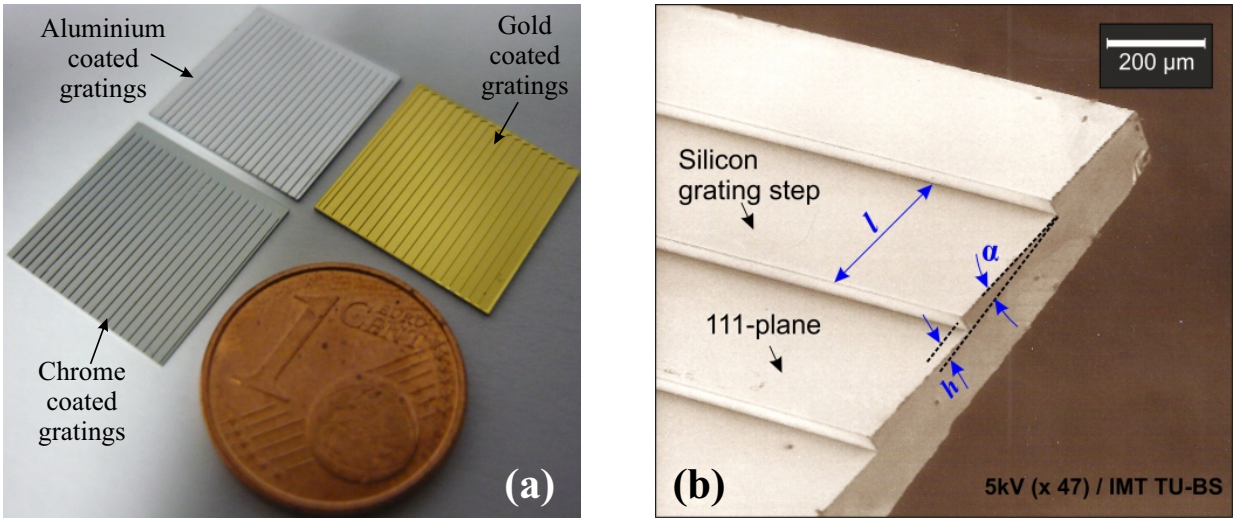

FIGURE 4.22: (a) Microfabricated silicon gratings (b) SEM image of the grating edge

After fabricating the silicon grating specimens, some analyses have been carried out in order to qualify it for the long range sensor application. In the following section, the descriptions regarding these analyses are presented.

4.5 Silicon grating analysis

The microfabricated silicon gratings have been examined using Zygo^{TM}(New view 200) white light interferometric microscope at Roberval laboratory at UTC, France. Our main objective behind this analysis is to extract good quality silicon gratings. The quality of these gratings has been characterized by measuring the values of their surface roughness (R_a) and Peak-Valley (PV) parameters over each grating step (for details, see Annex B). The PV parameter is the difference between the two extreme points of the surface which can also be interpreted as the flatness of the grating step. Furthermore, since the illuminated zone diameter (Φ_z) of the FODS probe (see figure 4.6) varies between 200 μm to 300 μm over a single grating step, these parameters have been analyzed for a length of 550 μm for each grating step.

Figure 4.23 represents an image of a single measurement zone via Zygo^{TM}(New view 200) microscope. The roughness and PV parameters in this zone were found to be 15 nm and 95 nm. From figure 4.23, it can be seen that the grating surface is not uniform which means that the values of these parameters will vary over each grating step. So, in order to estimate the average roughness and PV values of the complete planar grating, each grating step has been analyzed separately over its length by taking into account different measurement zones (see figure 4.24(a)).

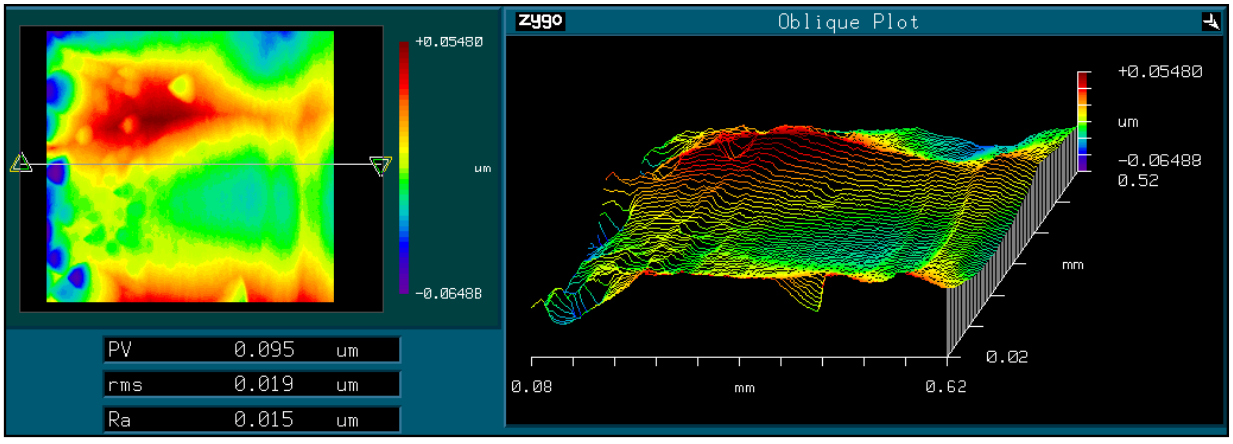

FIGURE 4.23: An image of a single measurement zone on the gold coated silicon grating step measured using Zygo^{TM}200 interferometer machine

The measured values of the R_a and flatness (i.e., PV value) are presented in figure 4.24(b). From the result the average values of the surface roughness and flatness were

found to be 14.9 and 72.8 with measurement uncertainty of type A[7] ± 4 nm and ± 12 nm, respectively. The variation in the R_a and PV values over each grating step depends on different silicon micromachining parameters such as temperature and concentration of the etching solution, residue of the Si_3N_4 or SiO_2, etc. In our case, the first set of the silicon grating have been fabricated with 25% concentrated TMAH solution at 80°C and from the result presented in the figure 4.24(b), it can be concluded that the variation in R_a and PV values remains very low for these etching parameters. However, the average values of the roughness and flatness of the silicon grating is very high as compared to our desired objectives that is to achieve these values in the order of few nanometers.

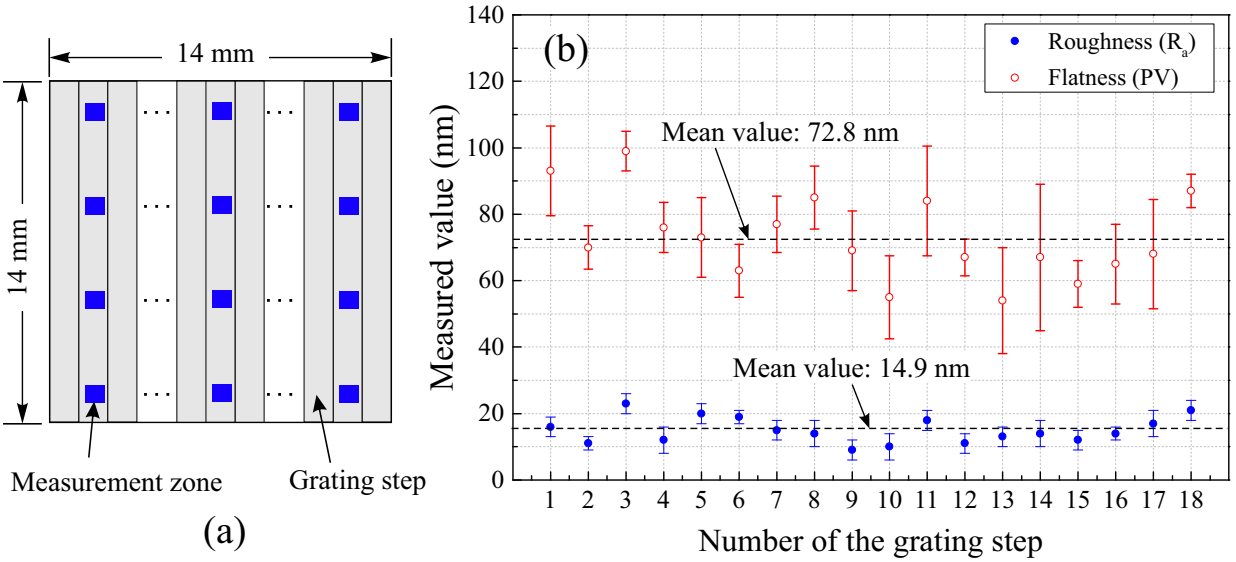

FIGURE 4.24: (a) Measurement zones (b) R_a and PV values over each grating step

In the following subsection, some studies have been conducted in order to first, identify the influence of main etching parameters and second, to improve the surface characteristics of the silicon gratings. These studies have been carried out for silicon grating machined with TMAH solution.

4.5.1 Improvement of the grating surface characteristics

In practice, the optimisation of the surface roughness and flatness parameters using wet anisotropic etching technique is not an easy task as it depends on several etching parameters. However, the temperature and concentration (expressed in "%wt") of the etching solution are the two main parameters that often lead to different silicon etching rates. This variation in the silicon etching rate results in different final surface quality [Marc 98]. According to the literature [Seid 90], high concentration of TMAH solution exhibit low silicon etch rate but around 2.5% TMAH concentration a higher silicon etch rate (≈0.65)

[7]Type A uncertainty is equal to the standard deviation divided by the square root of the number of measurement [Khia 07].

can be achieved (see figure 4.25(a)). However, Shikida *et al.*[Shik 01] have concluded in their study that despite high silicon etch rate at lower TMAH concentration, the final surface roughness value often deteriorates due to the appearance of hill locks[8] during wet etching of silicon (e.g., see figure 4.25(b)). On the other hand, the silicon etching with 25% TMAH solution leads to very smooth surface as shown in figure 4.25(c).

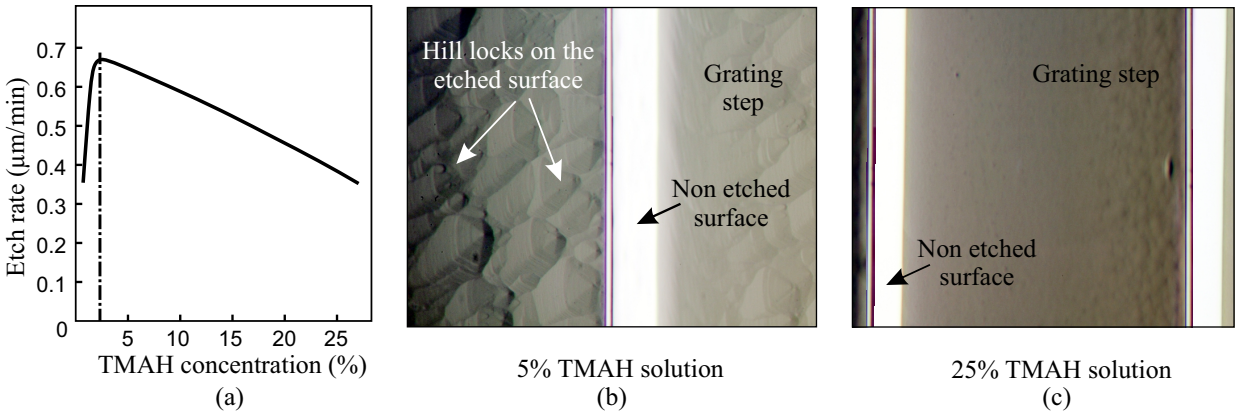

FIGURE 4.25: (a) Silicon etch rate at different TMAH concentration [Seid 90], Hill lock formation (b) with 5% TMAH solution (c) with 25% TMAH solution

As mentioned above, etching temperature is another main parameter that variates the etch rate. So, in order to study the influence of the temperature in our case, we have performed a set of experiments. The silicon gratings etched with 25% concentrated TMAH solution at different temperature has been examined with Zygo^{TM} microscope for surface roughness and flatness parameters. Figure 4.26(a) represents the variation of R_a and PV values. It can been seen that at lower etching temperature the etch rate of the silicon is very low (see figure 4.26(b)) which results in high roughness and flatness values. However, at higher temperature the silicon etch rate is very high and the resulting surface provides lower roughness and flatness values. In addition, the total etch time required to completely etch the silicon grating steps is decreased. From these measured results, we concluded that at 80°C , the average surface roughness and PV values always remain less than 20 nm and 90 nm, respectively (see figure 4.26(a)). At this concentration and temperature of the TMAH solution the average silicon etch rate and total etching time were found to be 0.37 μm/min and 3.5 hours, respectively.

***Chemical polishing*:** One of the techniques to achieve a flat surface is to perform chemical polishing after anisotropic etching. Since, the solutions used in the chemical polishing process exhibit isotropic etch characteristics (i.e., the solutions do not etch the silicon material with respect to its crystallographic orientation (see subsection 4.4.1.3)) they can be used to remove the sharp peaks on the final etched silicon surface [Boge 67]. Earlier,

[8]hill lock formation represents the appearance of small pyramids on the surface during anisotropic etching of silicon

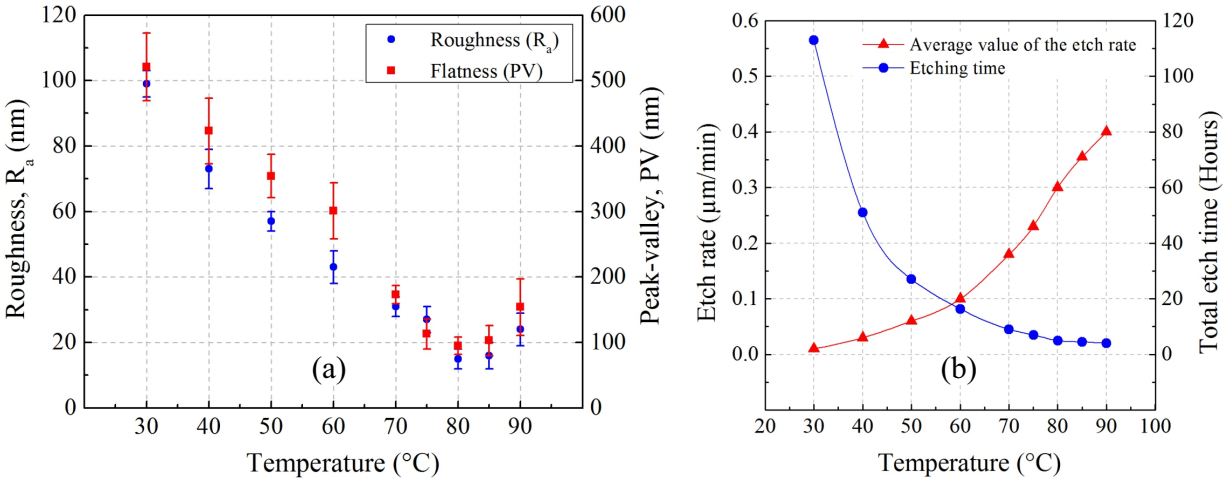

FIGURE 4.26: (a) R_a and PV values of silicon gratings at different temperature (b) Etch rate and total etch time

Dr. Ali Khiat, used a mixture of different acids to realize the isotropic etching solution in order to perform this process on the silicon grating fabricated with 40% KOH at 80°C . The solution was realized with following composition [Khia 07],

- 45.45% of Nitiric acid (HNO_3)
- 27.27% of Hydrofluoric acid (HF), Concentration 40%
- 27.27% of Acetic acid (CH_3COOH), Concentration 98%
- 0.5 ml Bromine (Br) for 100 ml of all three acids

This isotropic solution was used to treat the silicon grating at the silicon etch rate of 0.1 μm/min at 21°C . In his study, the surface treatment of silicon grating realized with KOH solution was carried out for three etch duration such as 5 min, 7.5 min and 10 min. From experiments, it was concluded that the isotropic polishing of the silicon grating lead to degradation of the surface (see figure 4.27(a)). In order to validate this effect at lower duration time (i.e.,< 5 min), we have used the same solution to treat the surface of the silicon grating fabricated with TMAH solution. Our objective was to polish the surface by removing few nanometers. So, four etch durations such as 0.5 min, 1 min, 2 min, 3 min were used to treat the silicon grating specimens (without metal coating) with average values of R_a= 27 nm and PV=114 nm. During experimentation, it was observed that the irregularities on the silicon grating steps were reduced (see figure 4.28(b)), however after analysis it was concluded that the final surface quality degraded even on lower etch durations as shown in the figure 4.27(b).

At high etch duration (i.e., 3 min), the surface irregularities completely diminishes but it leads to high roughness and flatness values. As a result, it was observed that the final grating surface becomes less reflective even when coated with a 300 nm thick gold layer. From our results, it was concluded that isotropic polishing is not suitable in our application so, further studies regarding the isotropic polishing were not conducted.

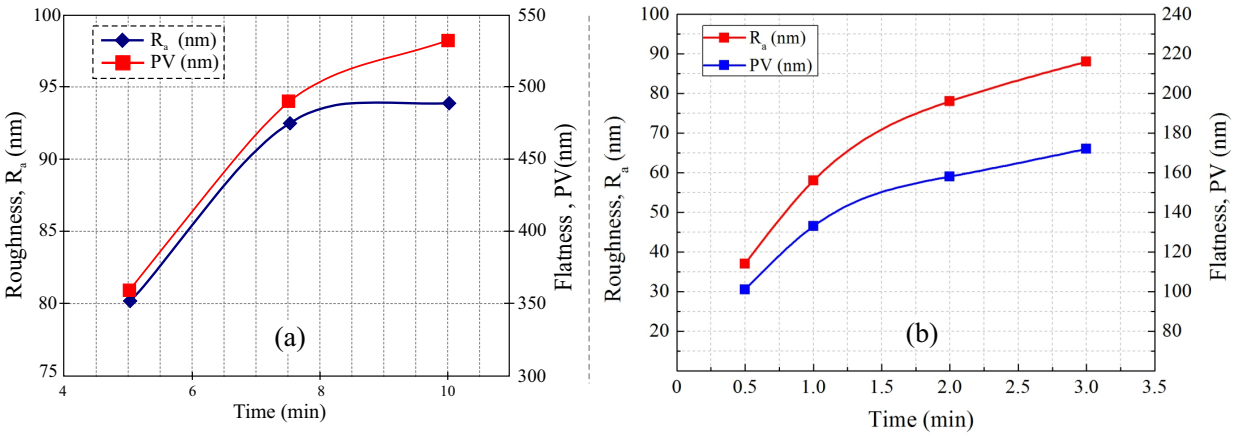

FIGURE 4.27: Isotropic polishing of silicon gratings etched with (a) 40% KOH solution at 80°C (b) 25% TMAH solution at 80°C

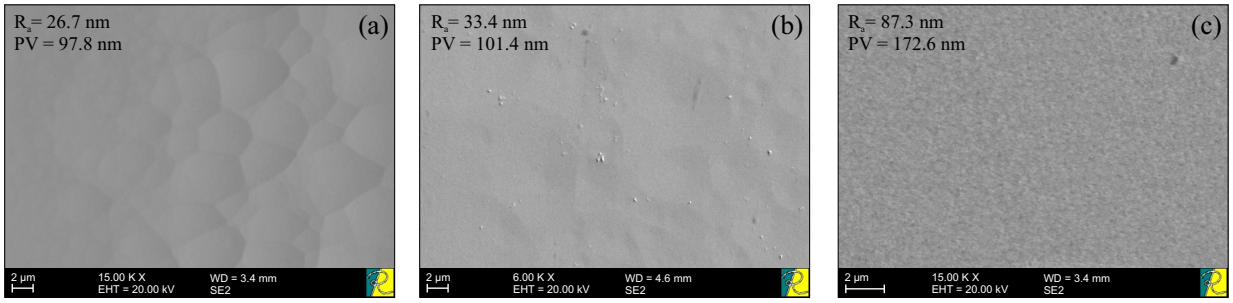

FIGURE 4.28: Silicon grating step surface quality (a) before treatment (b) after 0.5 min (c) after 3 min

***Addition of the Isopropyl alcohol*:** The addition of Isopropyl alcohol (IPA) during wet anisotropic etching of silicon, particularly with TMAH solution, is another approach to achieve final etched silicon surface with low roughness value. According to the literature, the exact role of the IPA during wet anisotropic etching of silicon has not yet been fully understood. However, as discussed earlier, one of the main reason of the surface deterioration is hill lock formation during wet etching [Zube 11, Sund 05]. Among many reasons for the appearance of hill locks is often linked to oxygen precipitates that results in small bubbles on the silicon surface during chemical reaction. These bubbles serve as temporary mask which leads to non homogenous etch rate of different crystallographic planes of the silicon [Shik 01].

In order to improve the final surface characteristics of the silicon grating in our study, we have performed several experiments by adding 250 ml of IPA solution to 1 litre of the 25% TMAH solution at 80°C . In figure 4.29 the comparison between the etched surface of the silicon grating obtained via 25% TMAH solution and that with the 25% TMAH+IPA solution can be clearly observed. With only 25% TMAH, the etched grating step often starts to deteriorate after 3 hours, which leads to appearance of small pits when all step in the planar grating are etched (see, SEM image, figure 4.29(a)). On the other hand, the addition of IPA solution leads to very smooth surface through out the etching process and

as a result the final surface quality remains very good (figure 4.29(b)).

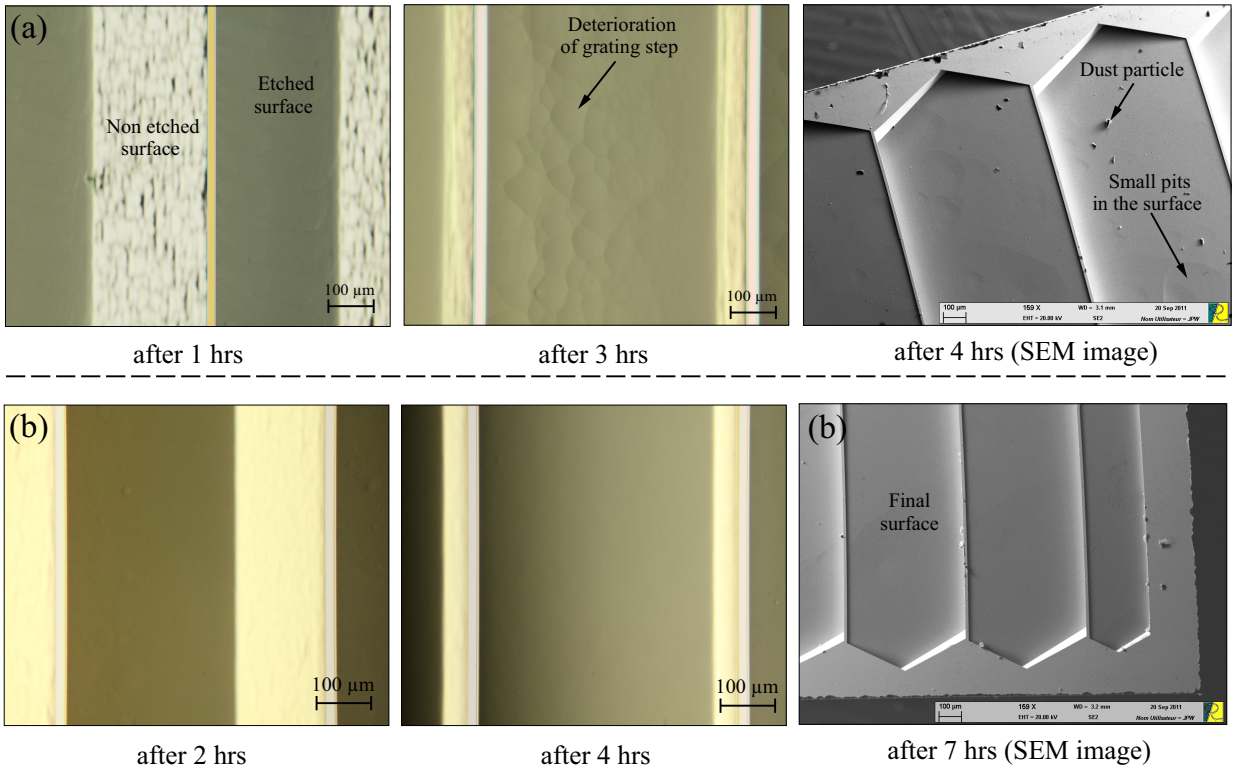

FIGURE 4.29: Silicon etched with 25% TMAH at 80°C (a) without IPA (b) with IPA

In addition, during fabrication it was observed that with IPA solution, the average silicon etch rate dropped to 0.1 μm/min as compared to the etch rate 3.7 μm/min when silicon grating is etched with 25% TMAH alone. According to the literature [Zube 01], this behaviour can be explained by the adsorption of IPA on the etched surface that restricts the TMAH attack and as result the silicon etch rate remarkably reduces [Zube 01]. However, our main objective was to achieve high quality surface for the silicon grating and the addition of IPA solution significantly improves the final quality of the silicon gratings in our application. To identify the final surface characteristics of the silicon grating obtained via two fabrication techniques, two specimens have been examined with Zygo^{TM} machine after coating with 300 nm thick gold. The average roughness and flatness parameters of the silicon grating fabricated with 25% TMAH solution at 80°C were found to be 14$\pm$4 nm and 73$\pm$12 nm (see figure 4.24), respectively. On the other hand, the addition of IPA solution leads to the average roughness and flatness values of 9$\pm$3 nm and 35$\pm$7 nm, respectively (see figure 4.30). Also, it has been observed that, with the addition of IPA solution, the variation in the described values are very low over each grating steps of the planar grating.

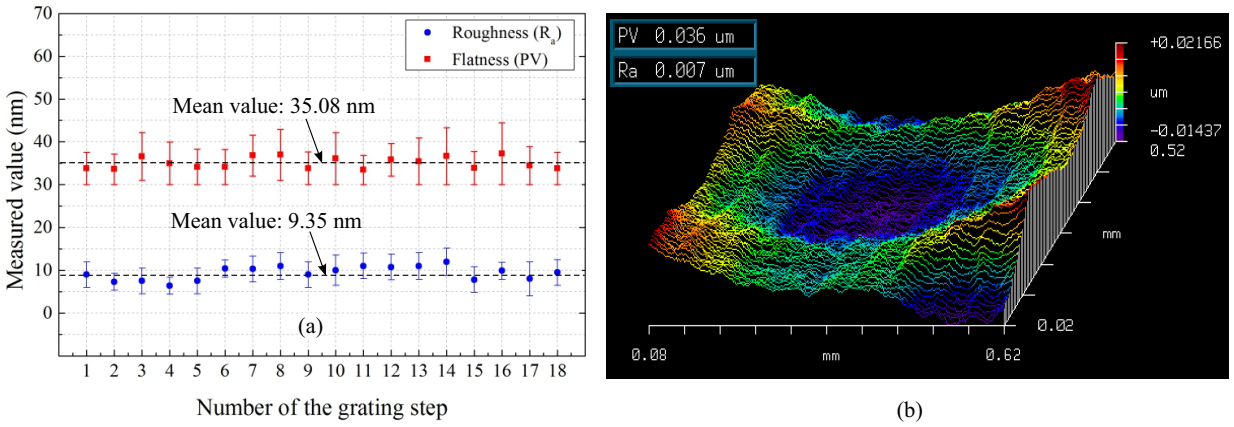

FIGURE 4.30: (a) R_a and PV values over each grating step (b) Image taken over a measurement zone with Zygo^{TM} interferometer machine

***Deposition of the metal on silicon grating*:** The deposition of metal on the final etched silicon grating serves two purposes. First, to improve the surface reflectivity and second, to improve the surface roughness and flatness parameters [Khia 07]. The metal deposition is mostly carried out in a vacuum chamber as shown in the block diagram in figure 4.31(a). This chamber is equipped with a pump mechanism to create a high vacuum ($<10^{-5}$ mbar). According to Hertz and Knudsen [Dani 04], when a pure substance is placed in a vacuum, it establishes its equilibrium state between solid or liquid phase and gaseous phase at pressure known as saturated vapor pressure. This characteristics is very important for evaporation process. At this pressure, the localized heating of the source metal (i.e., aluminium, gold, etc.), by focusing an electron beam on its surface, thermally releases the atoms from source metal which condensates on the substrate thus forming a metallic film. The thickness of this deposited film can be controlled by changing parameters such as temperature, heating time, etc.

For our application, we have deposited the silicon gratings that was etched with 25% TMAH+IPA solution at 80°C solution with three different metals, i.e., chrome (Cr), aluminium (Al) and gold (Au). In order to compare the surface quality, the thickness of these metal layers have been kept same (i.e., 300 nm). After examining with the Zygo^{TM} microscope, it has been observed that with the deposition of metallic layer, the silicon surface characteristics improves (see figure 4.22(b)). It can be seen that with 300 nm gold the grating surface roughness and flatness parameters are lower than with 300 nm coated layer of chrome or aluminium. So, on basis of these results and high coefficient of reflectivity (≈ 0.98), gold coating leads to further improvement of surface characteristics of the silicon grating.

Apart from the different surface improvement techniques, the final surface characteristics of the silicon grating also depends on the fabrication constraints such as temperature and concentration variation of the TMAH solution during etching process, presence

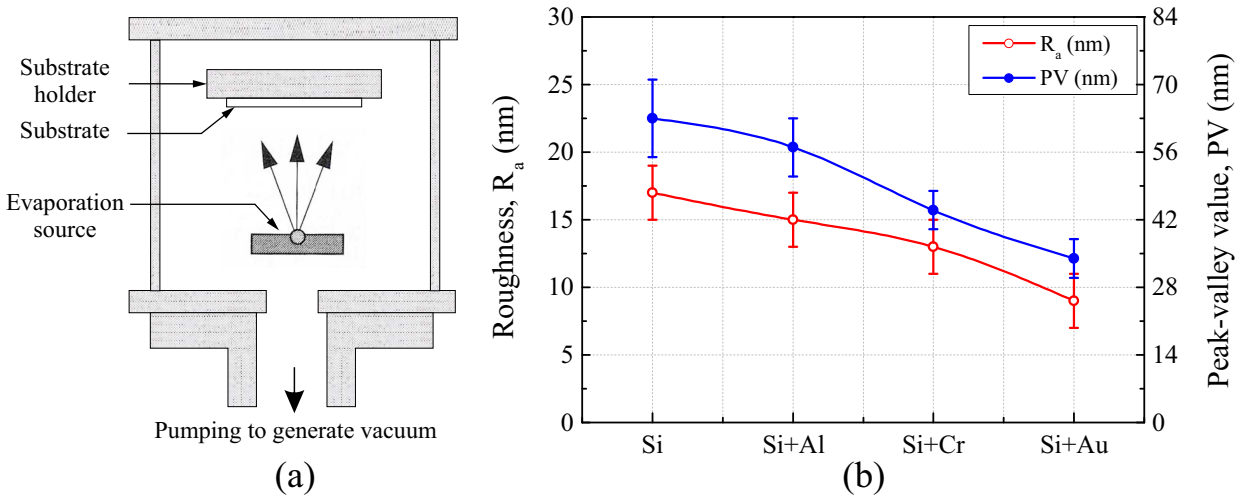

FIGURE 4.31: (a) Evaporation process in vacuum [Dani 04] (b) R_a and PV values with different metal coating

of dust particles and/or misalignment of silicon wafer flat with respect to mask during photolithography process, etc. In the literature [Khia 07], numerous solutions have been proposed regarding these constraints in order to acquire good quality gratings. However, in our study the microfabrication of the silicon grating have been conducted repeatedly in order to extract best silicon gratings per single silicon substrate in terms of their roughness and flatness values.

4.5.2 Conclusion regarding the silicon grating microfabrication

The microfabrication of the silicon grating for long range sensor application has been carried out in SCS material via wet anisotropic etching technique at IMT- TU Braunschweig. Furthermore, these silicon gratings have been realized with 25% TMAH solution at 80°C . The analysis of the best grating achieved via this process revealed an average surface roughness and flatness values of 14.9 $\pm$ 4 nm and 72.8 $\pm$ 12 nm, respectively. In order to improve these values different techniques have been studied and it was concluded that the addition of IPA to TMAH solution at 80°C leads to better surface quality. In addition, with the help of a 300 nm gold layer deposition, the average roughness and flatness values of the silicon gratings fabricated with 25% TMAH+IPA solution were found to be 9.35 $\pm$ 3 nm and 35.08 $\pm$ 7 nm, respectively.

4.6 Long range linear displacement sensor validation

After realizing the silicon gratings with microfabrication at IMT- TU Braunschweig, experiments have been carried out at Roberval laboratory at UTC Compiègne, to validate the long range displacement sensor. For this task, a 300 nm gold coated silicon grating with characteristics, R_a= 9.35 $\pm$ 3 nm and PV=35.08 $\pm$ 7 nm was used with two FODS probes.

In addition, an experimental setup has been realized by fixing the silicon grating on top of a Newport tilt platform which is driven by two motorized linear stages (Newport MFA 25CC) in *xy*-plane (see figure 4.32(a)). Moreover, a mechanical support in aluminium was realized to hold two FODS probes over the silicon grating. In order to position the FODS probes (e.g., rotation about its axis or height adjustment) with respect to silicon grating, additional devices such as tilt stages, manual linear stages, etc., (no shown in the figure) have been used.

At first, the axial calibration of both FODSs have been carried out in order to determine their typical characteristics such as sensitivity, measurement range, etc. In order to do so, the grating has been levelled in *xy*-plane using a levelling mirror and laser. Then, both of the FODS probes have been adjusted perpendicularly with respect to the flat grating steps. After adjustment, the axial calibration has been carried out by moving away both FODS probes along axial direction with respect to their facing grating steps (see figure 4.6(b)). The output voltages from both sensors have been plotted with respect to the axial displacement and linear fits have been applied as shown in the figure 4.33(a). From figure, with the help of linear fits, the sensitivities of the $FODS_1$ and $FODS_2$ were found to be 87.98 mV/μm and 82.85 mV/μm, respectively. The difference between the sensitives of both sensors is due to various factors such as deterioration of the PhD and its coupling with the reception fibers in the SPU, etc.

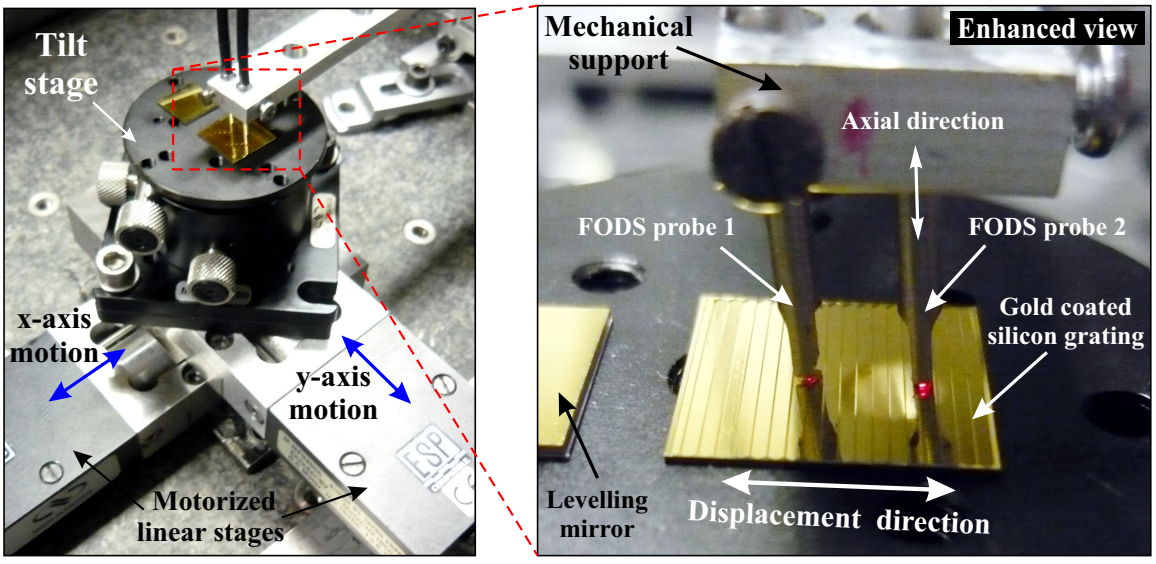

FIGURE 4.32: (a) Experimental setup of the long range displacement sensor (b) Enhanced view of the FODS probes and gold coated silicon grating

After axial calibration, the sensitivities of the both sensors have been measured in lateral direction (i.e., along the length of the planar grating). It is done by first placing the FODS probes near to the silicon gratings at the security distance 30 μm and then carefully moving the silicon grating along *y*-axis with the help of motorized linear stage.

Similar to the axial calibration, the lateral sensitivities of the both sensors have been measured over a single grating step located in front of each FODS probe. The output voltage values of the sensors have been stored using LabView® software and plotted with respect to the lateral displacement (i.e., 400 μm) as shown in the figure 4.33(a). After applying the linear fits, the lateral sensitives of the $FODS_1$ and $FODS_2$ were found to be 12.70 mV/μm and 11.96 mV/μm, respectively. The reduction in the sensitives is due to the fact that the grating steps are at 8.29° as discussed earlier in the section 4.2.

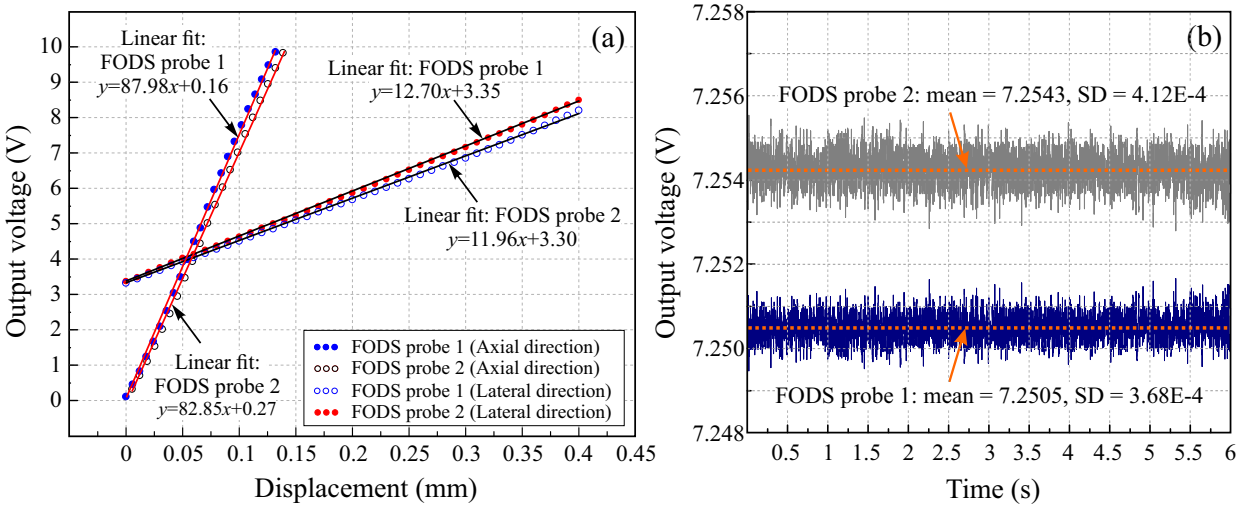

FIGURE 4.33: (a) Calibration curves of the two FODSs along axial and lateral directions with respect to silicon grating (b) Sensor noise

After determining the axial and lateral sensitivities, the RMS noise (in volts) of the both sensors has been measured without moving the grating and FODS probes (see figure 4.33(b)). The measured noise values of both sensors are due to the electronics of the SPU and deterioration of the electronic components such as PhD, coupling elements e.g., wires, connectors, etc. Taking into account all these parameters, the RMS noise of both sensors were found to be $\pm$0.368 mV and $\pm$0.412 mV as shown in the figure 4.33(b). Table 4.2 enlists different measured characteristics of both FODSs used with silicon grating.

		FODS probe 1	FODS probe 2	Units
Calibration results of the both sensors along axial direction, i.e., α = 90°				
Sensitivity	S_{axial}	87.98	82.85	mV/μm
Sensor noise (RMS)	N_{rms}	0.368	0.412	mV
Measurement range	d_{axial}	130	140	μm
Linearity error	LE_{axial}	0.86	0.73	%
Calibration results of the both sensors along lateral direction, i.e., α = 8.29°				
Sensitivity	S_α	12.7	11.95	mV/μm
Measurement range	d_y	400	400	μm
Linearity error	LE_α	0.67	0.73	%

TABLE 4.2: Characteristics of the two FODS probes used with silicon grating

After calibrating both FODSs, the silicon grating was displaced with the help of the motorized linear stage situated along y-axis (see figure 4.32(a)). In order to avoid any vibrations due to the motion of the linear stage, the translation speed was kept 1 μm/s. The experiment was carried out in open loop by measuring the output voltage response of both FODSs using a LabView® software.

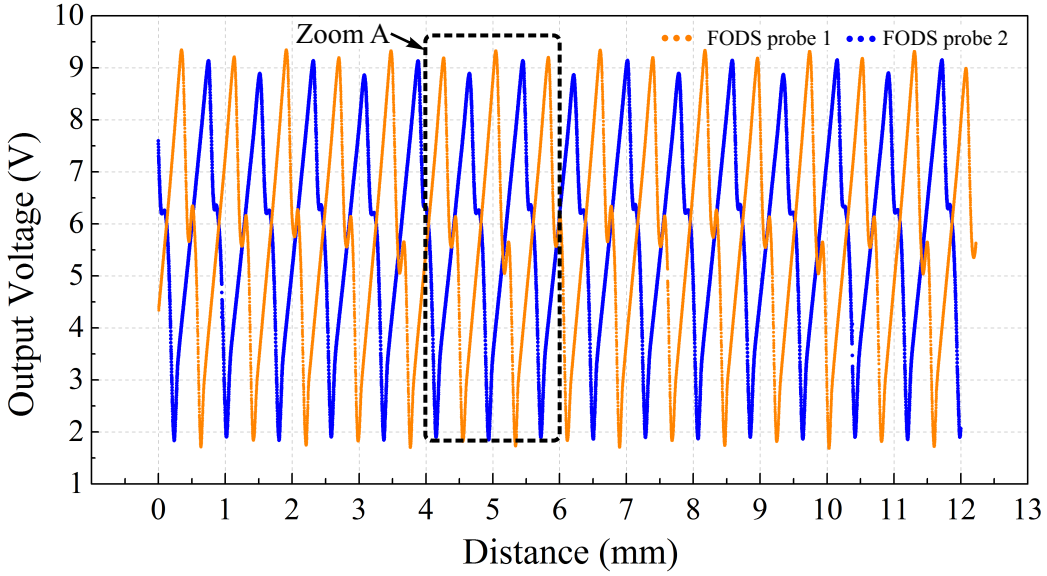

FIGURE 4.34: Output voltage response of the long range sensor

During experiment, the output voltages from both sensors have been recorded after each 1 μm displacement step over the range of 12.35 mm as shown in the figure 4.34. From the presented results it can be seen that both sensors exhibit a linear and a non linear zone. In the linear zone, the sensitivities of both sensors remain the same which means that the sensor probes are in front of the grating step. On the other hand, the non linear zone represents the output voltage due to the transition of the FODS probe between two adjacent grating steps. For better explanation, an enhanced view of the output voltage is presented in figure 4.35 in which the linear zones and non linear zones can easily be identified. In our study, the linear zones of the both sensors have been used to validate the working principle of the long range sensor. These linear zones have been filtered within an output voltage range of 3.25 V to 8.75 V which represents the start limit and end limits of the linear zone of both senors.

Moreover, in order to switch between both FODS probes for continuous measurement, the signal overlap (see figure 4.35) between the linear zone provided by both sensors was found to be 37 μm. This signal overlap value is higher than the one computed via simulation (i.e., 30 μm) in section 4.3.4. This increment can be explained by the slight orientation of the silicon gratings with respect to FODS probes axis in xy-plane (see sub figure 4.35) which results in motion of the silicon gratings along y_1-axis. In practice, this

problem arises due to the manual assembly of different component (e.g., linear stages, tilt stage, FODS handling mechanism, etc.) to realize the experimental setup. Despite these assembly errors, the increment in the signal overlap is very small as compared to the simulated results. So, in our calculations its effect has been neglected for the purpose of simplification.

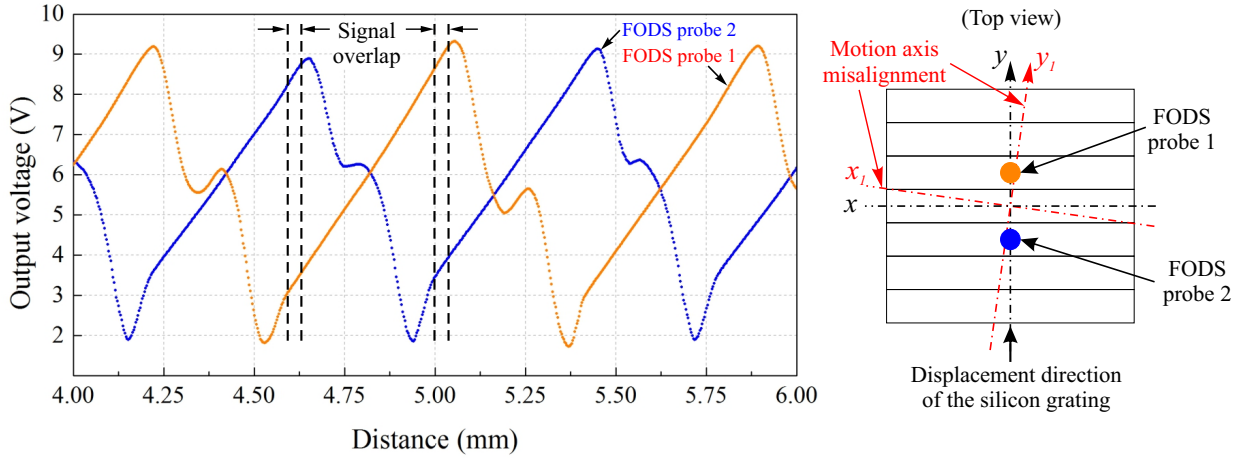

FIGURE 4.35: Zoom A: enhanced view of the output voltage signals

To measure the linear sensitivity of the long range sensor, the output voltages of the both FODSs have been accumulated as shown in the figure 4.36(a). From the presented result, the switching between the linear zones of FODSs can easily be observed. A linear fit was employed on the accumulated voltage curve to determine the average sensitivity of the long range linear displacement sensor. From the linear fit, the average sensitivity was found to be 12.63 $\pm$ 0.21 mV/μm with a linearity error less than 0.83%. Figure 4.36(b), represents the linearity error in the measurement over the long full length of the planar grating along y-axis. In figure 4.36(b), it can be observed that measurement error consists of periodic peaks. These peaks often appear due to the variation in the flatness of the grating steps as discussed previously in this chapter.

The accuracy of the long range sensor can be computed by the square root of the quadratic sum of different errors such as amplitude of the sensor noise ($\pm$ 0.20 mV_{rms}, see figure 4.33(b)), quantification noise ($\pm$ 5 V/2^{16} = $\pm$ 0.076 mV) and linearity error 0.83% (or $\pm$ 36.63 mV at full scale of 5.5 V, see figure 4.36(b)). After calculations, the RMS value of the uncertainty was found to be $\pm$ 36.63 mV. So, by taking into account the above mentioned average linear sensitivity (i.e., 12.63 mV/μm) for long range sensor, the uncertainty in the measurement was found to be $\pm$ 3 μm.

From the above text, the RMS noise value ($\pm$ 0.20 mV_{rms}) with average linear sensitivity (12.63 mV/μm) over complete length of grating, were used to compute theoretical limit of resolution, i.e., 30.8 nm. This resolution value is 4.4 times more than the simulation result (i.e., 7 nm) as discussed in section 4.3.4. This deterioration in the resolution

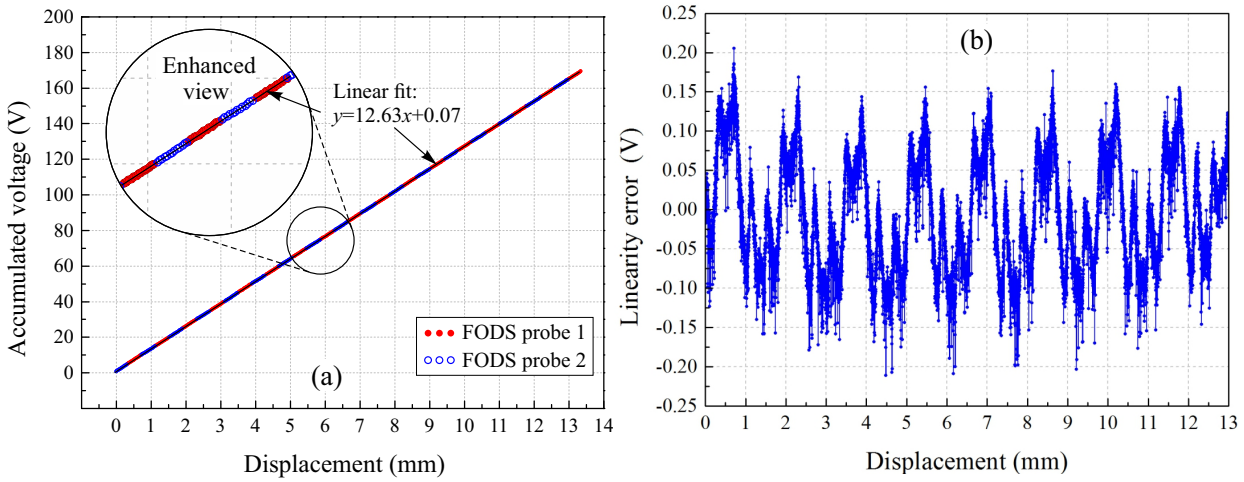

FIGURE 4.36: (a) Accumulated output voltage of both sensors probes (b) Linearity error

value can be explained by the low sensitivity and RMS noise values of the FODSs used with silicon grating due to the degradation of the electronics components with time. In order to verify the theoretical resolution value (i.e., 30.8 nm) an experimental setup has been realized as shown in the figure 4.37. The silicon grating was displaced beneath FODS probes using a piezo actuator (PI 845-10). The motion of the piezo actuator was controlled using a Labview® software. A continuous linear displacement step size of 30.8 nm was realized for 10 seconds and the output response of the long range sensor was measured in terms of displacement. Figure 4.37 (b), represents the measured displacement. From the result, it has been concluded the long range sensor is capable to provide a 30.8 nm resolution with a standard deviation of $\pm$ 0.27 nm.

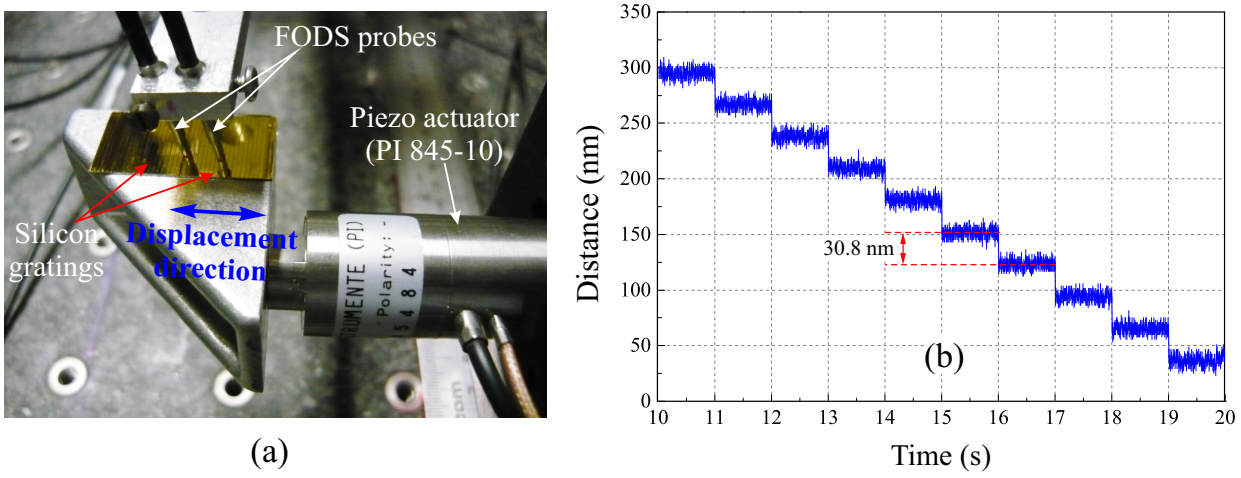

FIGURE 4.37: (a) Experimental setup (b) Limit of resolution, 30.8 $\pm$ 0.27 nm

Figure 4.38(a), shows the accumulated output voltage of the long range linear sensor, when the silicon grating is translated in *xy*-plane at an angle ψ=45°. This task was

achieved by using both motorized linear stages situated along *x*- and *y*-axis, simultaneously (see figure 4.32(a)). The output voltage acquired via both FODSs have been treated in similar fashion as described earlier in this section. From the result, it was concluded that the linear sensitivity of the long range sensor is reduced to 8.47 mV/μm (measured with a linear fit) in comparison to the linear sensitivity that was achieved in the case of translation only along *y*-axis (i.e., 12.63 mV/μm). As discussed earlier in this chapter, the sensitivity of the FODS used in our study depends on the motion direction of the silicon grating. So, in the planar motion case, when the silicon grating is moved at an angle ψ=45° in *xy*-plane, the theoretical linear sensitivity (S_ψ) of the long range sensor can be computed with the help of lateral sensitivity of the sensor, i.e., 12.63×cos ψ=8.93 mV/μm. The measured value of the sensitivity (8.47 mV/μm) is very close to the computed value. The small difference is due to the fact that the motion of the silicon grating have not been carried exactly at angle of 45° in *xy*-plane. So, in order to identify the real angle, the measured value of the sensitivity (8.47 mV/μm) was used to compute the real displacement angle (i.e., 47.88°).

Moreover, the linearity error has been measured as shown in the figure 4.38(b)). It was found to be ± 0.93% (or ± 47.35 mV) for a the full scale output of 5.5V over each grating step. In the planar motion case, the new RMS value of the uncertainty was found to be ± 47.36 mV. So, with the measured linear sensitivity (S_ψ=8.47 mV/μm) value in *xy*-plane, the uncertainty in the measurement was found to be ± 5.59 μm. In addition, by taking into account the RMS noise value (± 0.20 mV_{rms}) and the sensitivity of the sensor (S_ψ), the new limit of the resolution (R_ψ) of the long range sensor in *xy*-plane was found to be 47.22 nm. From these results, it has been concluded that in planar motion, the resolution of the long range sensor deteriorates with respect to displacement angle.

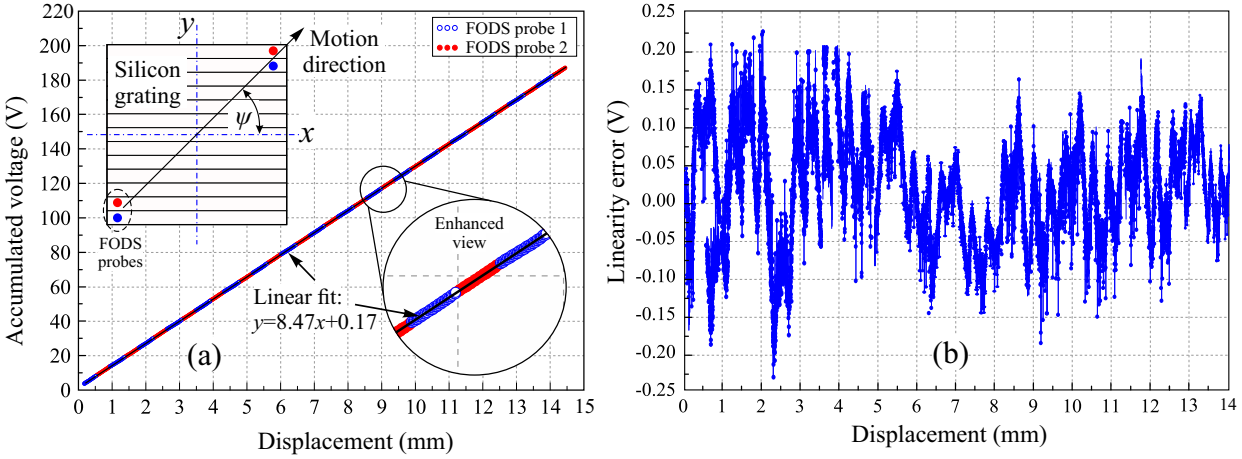

FIGURE 4.38: Linear motion in *xy*-plane (a) Accumulated output voltage of both sensors probes (b) Linearity error

4.7 Uncertainty in the displacement measurement

In practice, the developed long range displacement sensor is sensible to certain physical phenomenons such as vibrations, temperature variations, etc., which can lead to uncertainty in the measured displacement. For example, due to the temperature variation, the dimensions of the silicon grating can vary because of the thermal expansion coefficient of silicon material. This can result in variation in the measured lengths with respect to the temperature change. During our experiments, the silicon gratings have been used at ambient temperature which did not influence the measured displacement. However, steep change in the temperature can significantly deteriorate the output of the long range sensor.

Thermal noise of the SPU consists of different electronic components. It can increase the sensor noise which can reduce the limit of the resolution of the sensor. Moreover, in chapter 3, it has been deduced that the mobile part of the MPS undergoes small vibrations. From the perspective of integrated MPS design, the influence of these vibrations will also introduce uncertainty in the displacement measurement via long range optical sensor. In future, these uncertainty aspects of the long range optical sensor will be further investigated to ensure high quality measurement.

4.8 Conclusion

A high resolution non contact linear sensor for long range displacement measurement has been developed in this chapter. In the first part, the architecture and functioning of the long range linear displacement sensor has been discussed in detail. In order to achieve compact dimension for the long range linear sensor from the perspective to integrate it in the MPS prototype, the dimensions of different components of the sensor were optimized using a geometric model. In addition, the planar grating have been realized in silicon material using wet anisotropic etching technique with TMAH solution. To improve the surface roughness and flatness parameters of the silicon grating, different solutions have been discussed. However, it was concluded that a concentrated solution containing 25% TMAH and IPA at 80°C lead to better surface quality. Furthermore, the deposition of a 300 nm gold coating improved the surface roughness and flatness parameters. With this fabrication method, the best silicon grating obtained provided an average roughness and flatness values of R_a= 9.35 $\pm$ 3 nm and PV=35.08 $\pm$ 7 nm, respectively.

After realizing the silicon grating, the experimental validation of the long range linear displacement sensor was carried out. For this task, the silicon grating has been employed with two FODSs. From the experimental results, it was concluded that the sensor is capable to measure the displacement at a range of 12.5 mm with a high resolution of 30.8 nm in *xy*-plane.

Chapter 5

Microfabrication of novel cross structure and sensor integration

This chapter presents the integration of long range sensor into the MPS prototype. In order to facilitate the integration of silicon grating and PMAs into the mobile part of the MPS prototype, first, a novel cross structure has been designed to reduce assembly errors. This structure has been realized with microfabrication technology with the aim to achieve compact dimensions. Later, different components of the MPS prototype have been assembled together and experiments have been performed to validate the various motion characteristics such as displacement range, resolution, etc.

5.1 Final MPS design layout and sensor integration

In this section, some design modifications have been carried out regarding the MPS prototype. One of the main objectives behind these modifications is to reduce/eliminate the assembly errors such as alignment errors between the PMAs situated along single axis in the MPS, air gap variation between PMAs and PEDCs, etc. These errors appeared because of the difficulty in handling the miniature PMAs and hemispherical glass beads during their manual assembly with Zerodur® cross structure. As a consequence, these assembly errors often lead to deterioration in the mobile part displacement over the fixed part of the MPS due to the generation of the non homogenous electromagnetic forces along a single or both axes (see section 3.1.2).

Moreover, in order to integrate the long range sensor into the MPS, our aim was to fix a set of silicon gratings on top of the mobile part along each axis (i.e., x- and y-axis) to measure the long range displacement. Unfortunately, the addition of the silicon grating onto the Zerodur® cross structure will lead to an increase of 380 μm in the total height of the mobile part of the MPS. This additional height value represents the thickness of the silicon wafer in which silicon grating has been realized (see subsection 4.4.1.4). As a

result, an air gap value greater than 380 μm is needed between PEDC (placed on the top side) and PMAs to avoid any collision between silicon grating and PCB during functioning of the MPS.

Taking into account the design/assembly constraints of the initial prototype, a novel cross structure design has been proposed as shown in isometric view of the MPS in figure 5.1(a). The basic design of the new cross structure is similar to the Zerodur® cross structure. However, it consists of half depth cavities to place silicon gratings (each 14×14×0.38 mm^3), through cavities (each 6×15×0.38 mm^3) to fix PMAs of the LMs and through holes (Ø1 mm) to fix the spherical glass beads (see figure 5.1(a)). In addition, the centre of the new cross structure was designed to hold a miniature component with a footprint size of 12×12 mm^2. The overall dimensions of the new cross structure were kept 68×68 mm^2 as shown in the figure 5.1(b). These dimensions have been selected by taking into account the design parameters of the Zerodur® cross structure and the fixed part (i.e., PCB) of the MPS.

From the isometric view, it can be observed that the spherical glass beads have been used to support the mobile part over the fixed part. The PEDC of each LM is insulated with a 130 μm thick glass layer which also helps in providing a smooth motion surface for the mobile part. In addition, for displacement measurement, two sets of silicon gratings can be fixed inside the cavities as shown in the figure 5.1(b). The depth of these cavities are equal to the height of the silicon grating i.e., 380 μm.

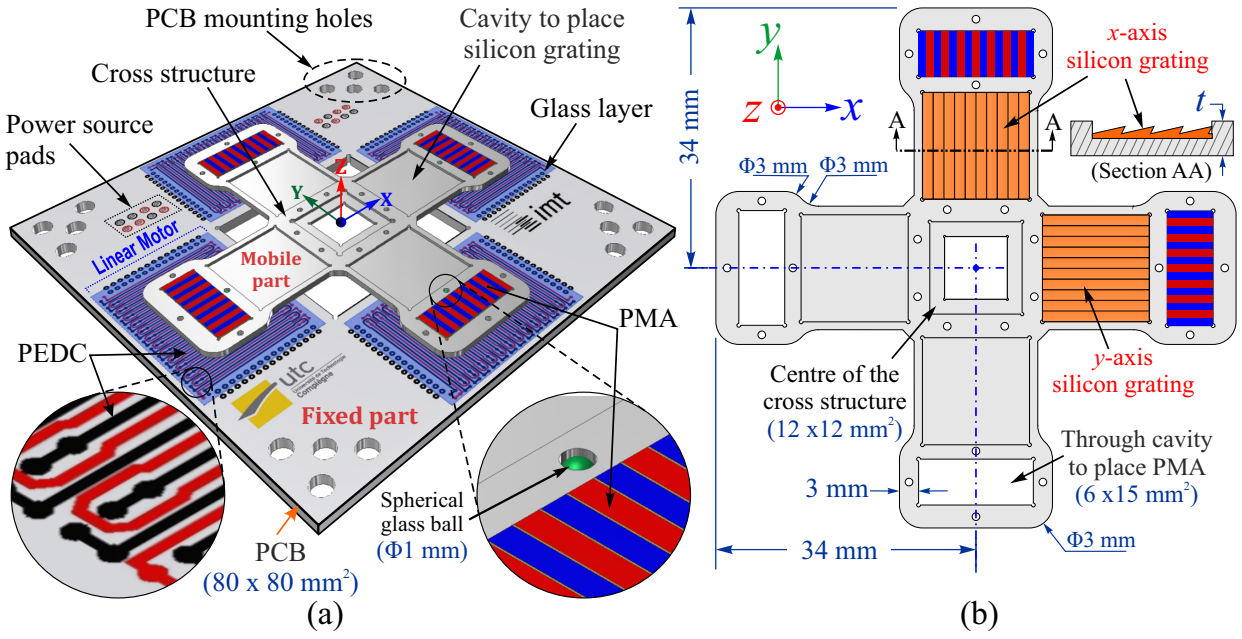

FIGURE 5.1: (a) Isometric view of the MPS prototype (b) Schematic layout of the new cross structure integrated with different components

The proposed cross structure design has been realized with microfabrication technology in silicon material. This fabrication approach was selected due to its simplicity and

ability to produce components with micro level fabrication tolerances. In our study, the cross structure has been realized with dry (or plasma) isotropic etching technique in silicon material. The description regarding the microfabrication of the silicon cross structure is presented in the following section.

5.2 Microfabrication of the novel cross structure

In this section, the microfabrication of the new cross structure in silicon material has been carried out. This material was selected due to its lower density (2329 kg·m^{-3}), high strength[1] (129.5 GPa) and low coefficient of thermal expansion (2.6$\times$10^{-6}/°C) [Mado 02]. The lower density of the silicon material leads a light weight cross structure design which interns results in increase in the load carrying capacity of the mobile part in our application. Moreover, the microfabrication approach was selected due to the complication in realizing the small dimensions of the proposed cross structure design such as cross structure thickness (<1 mm), depth of cavities (380 μm), etc., with conventional machining.

For microfabrication of the cross structure, the selection of the silicon wafer was carried out irrespective of the its crystallographic plane orientation. The choice was made due to the high silicon etch rate (≈1.5-1.8 μm/min) characteristics of the Inductively Coupled Plasma (ICP) etching process to achieve structure with vertical side walls (see figure 5.1). So, a Ø100 mm, standard {100} oriented silicon wafer with both side polished was selected to realize the cross structure. This wafer type was selected due to its three times lower cost as compared to the one used to realize silicon grating in our study. In addition, due to the height of the silicon grating, 0.8 mm thick silicon wafer was used to fabricate deep cavities. This thickness value was selected to avoid maximum height of the PMAs (i.e., 1 mm).

5.2.1 Design and development of the mask

After selecting the silicon wafer, the design and fabrication of the mask have been carried out for photolithography process. In our study, the silicon cross structure was realized in two steps to achieve cavities to hold the silicon grating. Initially the silicon wafer was etched from top side to reach desired etch depth and later it was etched from bottom side to realize through etched structures. For both of these steps, separate masks have been designed to transfer the desired cross structure pattern. Figure 5.2 represents the optimal designs for both masks used in top side and bottom side etching process. The designs of both masks are similar in shape with an exception that mask# 1 contains additional structures for cavities that will not be etched through during machining of silicon wafer.

[1]Silicon is an anisotropic material and its Young's modulus value varies along its different crystalline planes, i.e., 129.5 GPa (100 plane), 168 GPa (110 plane), 186.5 GPa (111 plane), [Mado 02].

In these mask designs, some additional supports have been included to support the etched cross structure in silicon wafer from falling during etching process (see 5.2).

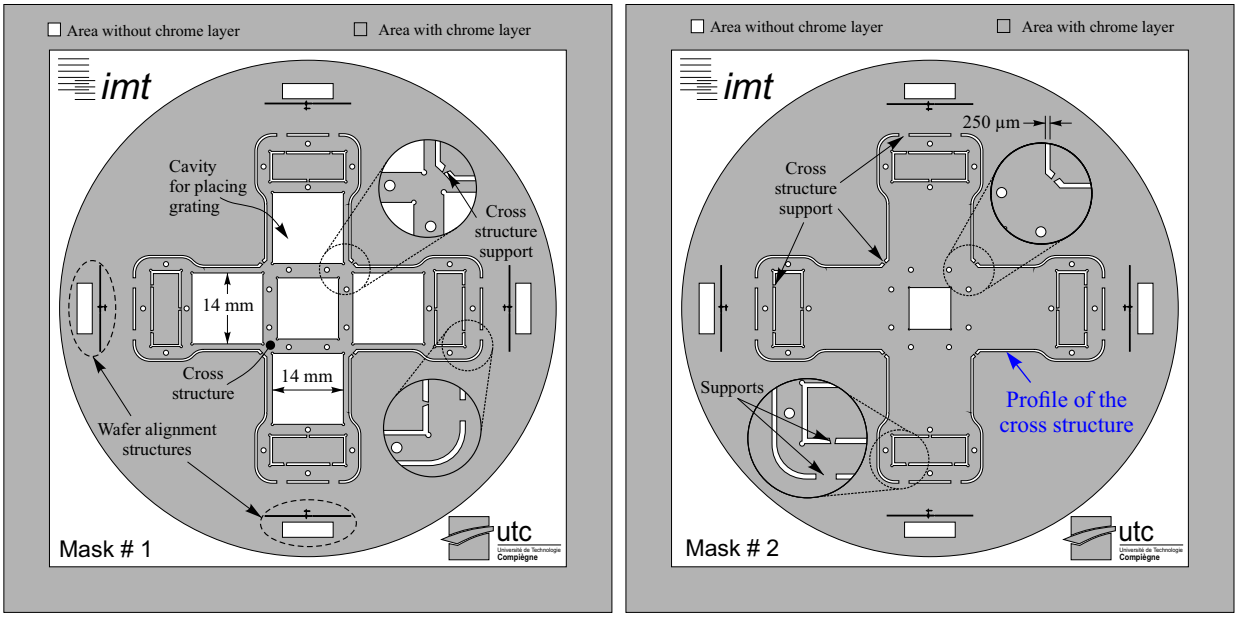

(a) (b)

FIGURE 5.2: Design layout of the (a) top side mask (b) bottom side mask

After designing both of the masks in AutoCAD® software, these two dimensional designs have been transferred on the blank masks that consist of a square glass plate which is pre-coated with chrome and photoresist layers on one side. This process was carried out with mask writing machine by exposing the photoresist layer with a laser spot. After writing process, the photoresist layer of the masks have been developed in similar fashion as described in section 4.4.2 in the previous chapter. The dimensions of the structures and profiles were verified under the microscope. After verification of the masks, the fabrication of the silicon cross structure has been carried out. The description regarding the microfabrication process is described in the following section.

5.2.2 Microfabrication process

The microfabrication of the cross structure in silicon material has been carried in 14 steps as shown in the figure 5.3. Initially, the silicon wafer was cleaned and coated with a 600 nm thick aluminum layer on one side. This process was carried out via metal sputtering process in PVD machine. This material serves as a protection mask during dry etching process that is carried out in an ICP machine. After the aluminium deposition, a layer of the photoresist was realized on top of it, by spinning 1 ml of positive photoresist (ma-P1215) at 3000 rpm in order to transfer the mask pattern via photolithography technique (see step 2, figure 5.3). A soft baking for 1 min at 100°C was carried out to avoid any kind of damage such as scratching during the mask alignment process in the next step.

In step 3, the mask presented in figure 5.2(a), was used to expose the photoresist layer to Ultra Violet (UV) light for 8 seconds. This process was realized with mask aligner/exposure machine. During this process, the wafer flat was first aligned with respect to the alignment structures on the mask. After exposure, the exposed photoresist was developed in ma-D331 developer solution for 25 seconds. After verifying the developed structures in the photoresist layer, the photoresist was cured for 5 min at 100°C . Then, aluminum etching was carried out with aluminium etching solution[2] at 35°C . After etching the aluminium layer, the wafer was rinsed with deionized water in Quick Dump Rinser (QDR) machine and dried with spin drying machine. Then, the photoresist layer was removed using acetone and ethanol and wafer was again washed (see figure 5.4(a)). After drying the wafer, a 2 μm copper layer was realized on the bottom side (the side without structured aluminium) of the wafer with PVD metal sputtering machine (see step 5, figure 5.3). This layer serves two purposes. First, it protects the bottom side from any contamination and second, due to high thermal conductively of the copper (401 W/(m·K)) it helps in cooling the wafer from the bottom side with liquid nitrogen, during ICP etching process.

In step 6, the silicon wafer is etched in ICP etching machine. During this process, the structured aluminium layer serves as mask and the plasma in the ICP machine reacts with the unprotected silicon material (on the top side on the silicon wafer). The silicon wafer was etched from the top side for 4 hrs at an average silicon etch rate of 1.6 μm/min (see figure 5.4(b)). After verification of the etch depth with Dektak profilometer, the aluminium and copper layers have been remove using aluminum etching solution in step 7. In the aluminum etching solution both copper and aluminum layers have been removed until no traces of these metals were observed via naked eye inspection. Then, the silicon wafer was rinsed with deionized water in QDR and dried. At this point, the top face of the silicon cross structure in the silicon wafer can be observed.

From step 8 to step 11, the process has been repeated in similar fashion as described in step 2 to step 5, however during the exposure, mask # 2 (see figure 5.2(b)) was used. During the alignment process, the etched alignment structures on the top face of the silicon wafer were used to align the mask and wafer. These etched alignment structures were used to achieve an overlap between the outer profile of the silicon cross structure between the bottom and top face to for through etching. Once the mask pattern is transferred into aluminum layer and a 2 μm copper layer is realize as shown in the figure 5.4(c) and (d), the dry isotropic etching was carried out on the bottom face of the silicon wafer in ICP etching machine (see step 12, figure 5.3). The silicon wafer was etched until the structures are through etched. Upon finishing, the aluminium and copper layers are removed with aluminium etching solution (see step 13, figure 5.3). At this point the silicon cross structure profile is through etched. After cleaning the wafer in QDR, the silicon cross

[2]100 ml of the aluminium etching solution consists of 73% Phosphoric acid (H_3PO_4), 3.1% Nitric acid (HNO_3), 3.3% Acetic acid (CH_3COOH) and 20.6% deionized water (H_2O)

structure has been released from the rest of the silicon wafer with diamond cutting machine. The inner parts of the cross structure have been removed by breaking the small cross structure supports with diamond pen as shown in the figure 5.4(e). Afterwards the cross structure is rinsed with ethanol and dried. The isometric view in step 13, figure 5.3 represents the final shape of the microfabricated silicon cross structure.

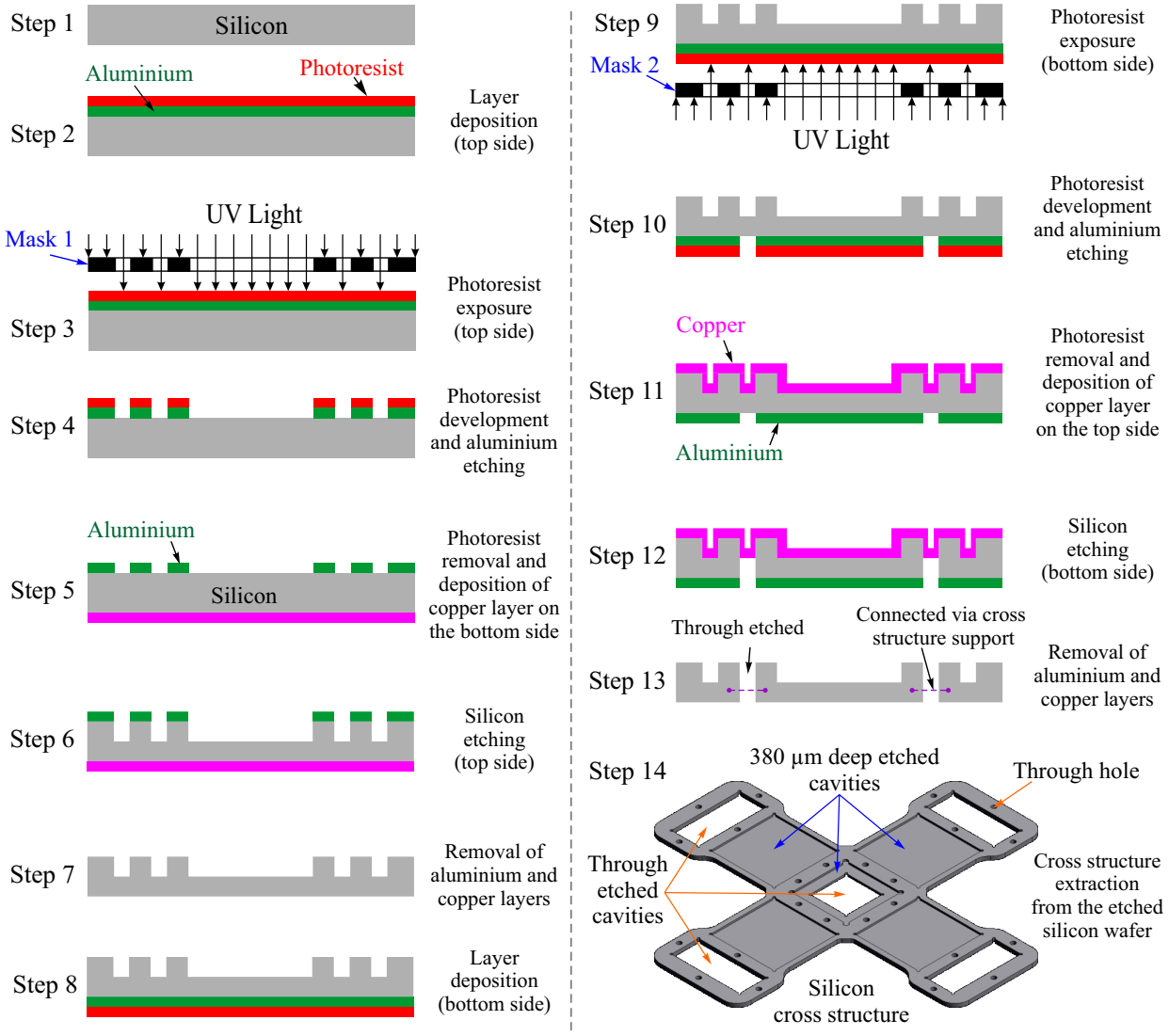

FIGURE 5.3: Microfabrication process of the silicon cross structure

Figure 5.4 represents, some of the silicon wafer status during the different microfabrication steps. The dicing of the silicon wafer was carried out along the silicon wafer cutting line (see figure 5.4(e)). The final 800 μm thick silicon cross structure with through and 380 μm deep etched cavities is shown in the figure 5.4(f). In addition, a series of Ø1 mm through holes can be seen in structure. These holes have been used to insert spherical glass beads to realize small separation between the mobile part and fixed part after complete assembly.

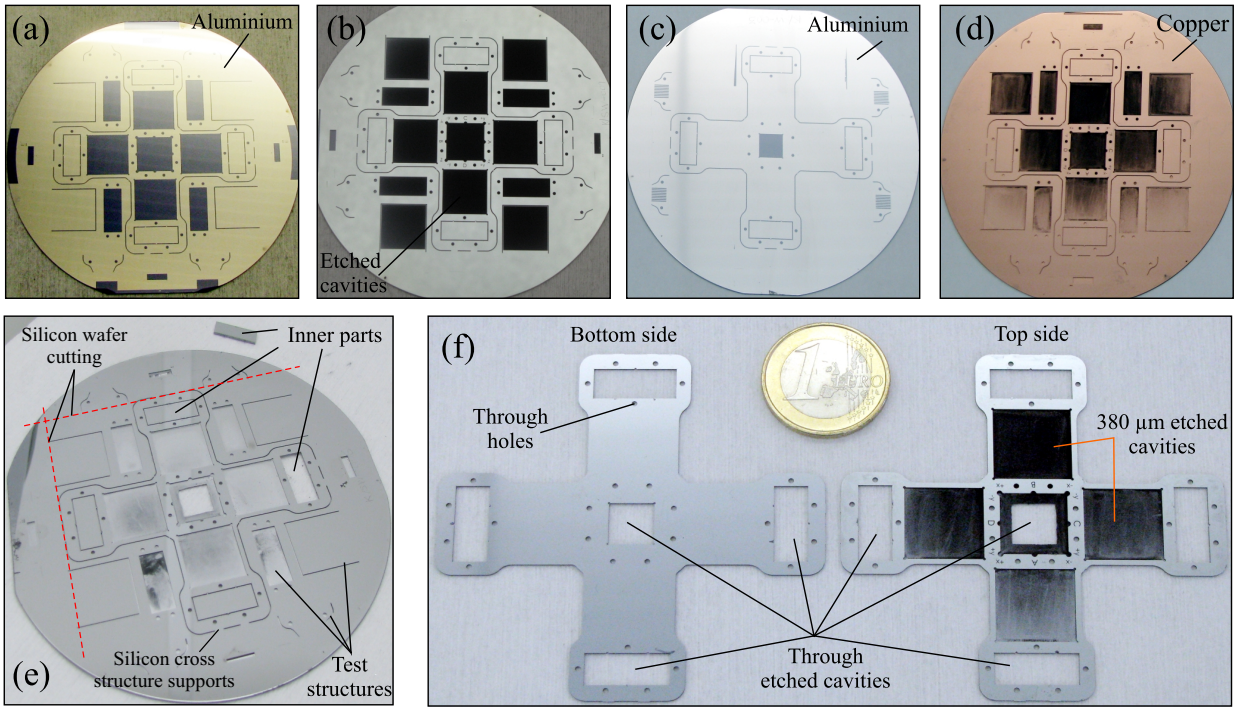

FIGURE 5.4: Different views of the silicon wafer during microfabrication process (a) Top side with structure aluminium (b) Top side etched (c) Bottom side with structure aluminium (d) Top side with 2 μm copper layer (e) Through etched wafer with removed inner part (f) Real view of the microfabricated silicon cross structure

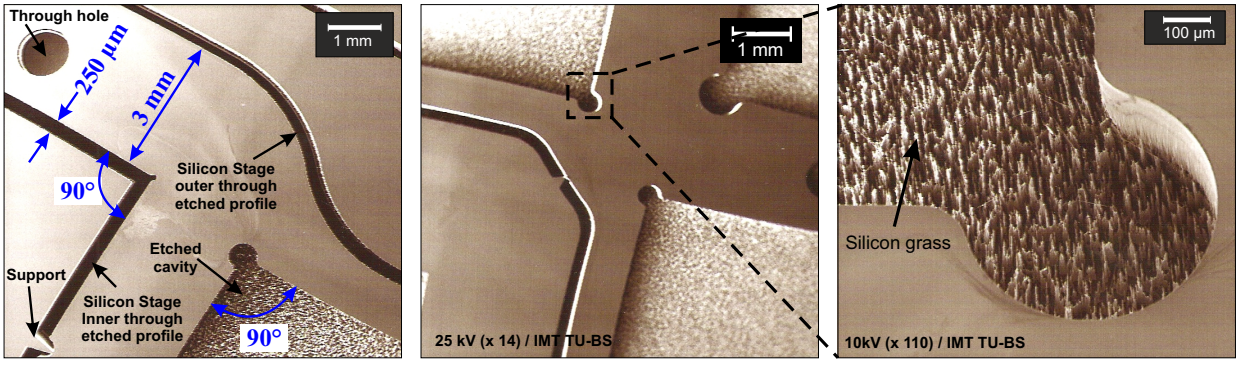

FIGURE 5.5: SEM images (a) Partial view of the etched cross structure (b) center view (c) Zoom view of silicon grass

Figure 5.5 presents the images of the silicon cross structure that have been taken with Scanning Electron Microscope (SEM). The inner and outer through etched silicon cross structure profiles can easily be seen. Often, after ICP etching process, black silicon appear can be seen on the deeply etched silicon surface. This black silicon is also referred as silicon grass as shown in the figure 5.5(c). According to literature, the appearance of silicon grass is often linked to the oxygen flow rate during the ICP etching process which can be controlled by changing different control parameter such as pressure, gas flow rate, etc.

In our study, the influence of this silicon grass has been neglected due to their small height. In addition, it has been observed that this black silicon often diminishes during cleaning process of the final etched silicon wafer as shown in the figure 5.4(e). From figure 5.5(a) and (b), the supports can be easily seen. After dicing the silicon wafer with diamond cutting machine these supports are scratched with a diamond tip pen.

5.3 Final assembly and experimentation

After realizing the silicon cross structure, different components such as PMAs, glass beads, and a mirror cube have been assembled together. An experimental setup has been realized to validate the new cross structure deigns as shown in the figure 5.6(a). To hold the fixed part of the MPS, an aluminum structure with dimensions 130×130×10 mm^3 has been fabricated. Two FODS probes have been installed to measure the displacement performed by the mobile part in *xy*-plane. Both of the FODSs (i.e., FODS$_x$ and FODS$_y$) have been calibrated in similar fashion as described in section 3.2.2.2. After calibration, the displacement measurement resolution of FODS$_x$and FODS$_y$ were found to be 15 nm and 12 nm, respectively.

Figure 5.6(b) represents the linear response of the silicon cross structure based MPS along y-axis in open loop control. An amplitude of 0.8 A for the injected currents were used in the PEDCs to generate electromagnetic forces. Figure 5.6(b) represents the simulated response (computed via model presented in section 2.5.2) and experimentally measured response of the MPS. For simulation results the new values of the total weight (i.e., 4.7 gms) of the mobile part have been used. In addition, since the glass beads are not the similar to the one used earlier with Zerodur® cross structure, the new friction values have been experimentally determines using inclined plane technique. The new values of the static friction coefficient (μ_{static}) and dynamic friction coefficient ($\mu_{dynamic}$) were found to be 0.21 and 0.18, respectively. For these parameters, the simulation result revealed a net displacement of 973 μm for a theoretically expected displacement of 1 mm along a single axis. Whereas from experimental results the displacement was found to be 978 μm. The small difference between the simulation and experimental results is mainly due to the dynamics of the MPS. From analysis it has been concluded that in comparison to our earlier prototype, the displacement loss due to friction is reduced by 11.78% in the new MPS prototype.

In order to evaluate the planar motion characteristics of the MPS. All four LMs have been injected with 0.8 A current. Figure 5.7(a) represents the linear profile in *xy*-plane. From the results it can be seen that, the trajectory of the profile is nearly repeatable. The small deviation between backward and forward motion is due to the characteristics of the the FODSs in their non linear zone. However, the maximum deviation in the trajectory was found to 7 μm. This less error indicates that the precise fabrication of the silicon

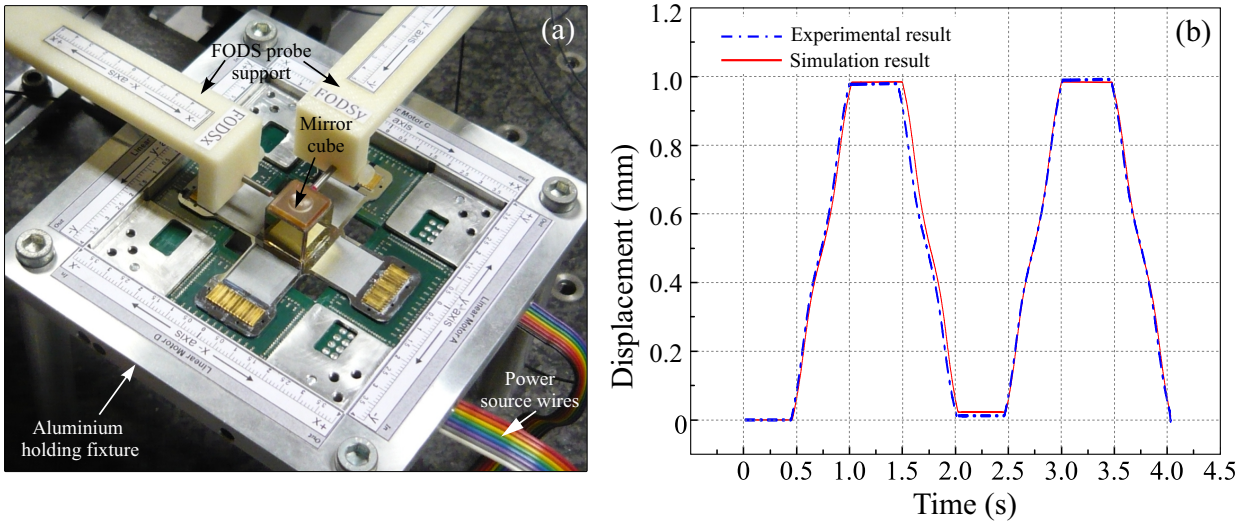

FIGURE 5.6: (a) Experimental setup (b) Translation along *y*-axis

cross structure has significantly improved the motion characteristics by reducing the PMA assembly errors. Another test concerning the planar motion has been carried out by injecting the currents in all of the four LMs in a fashion that only one axis should deliver motion at a time. This approach was adapted to realize 1 mm $\times$1 mm square motion profile. A 500 Hz sampling frequency of the injected current were used to realize the desired motion profile at 0.05 mm/s speed. Both of the FODS were used in their non linear zones.

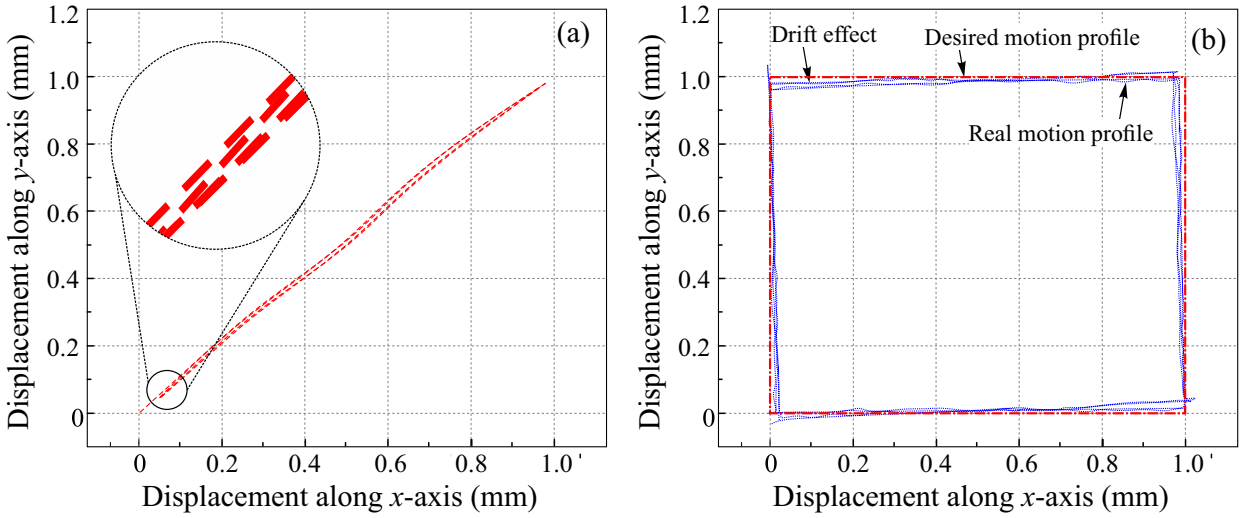

FIGURE 5.7: (a) Linear *xy*-profile (b) Square profile in *xy*-plane

Figure 5.7(b), represents the real motion profile. From the result it can be seen that, the measured profile contains a drift effect. The drift effect is because the platform is not perfectly leveled with respect to the horizontal plane. Nevertheless, the error in the measured profile is very small.

In addition, to validate the motion in closed loop control, all four LMs have been injected with 0.8 A sinusoidal currents and the frequency of the injected current has been adjusted via PI control as described in section 2.5.3. For desired displacement trajectory, a sinusoidal signal with amplitude ± 165 μm has been used to realize a circular profile of 330 μm. From the results presented in figure 5.8 the tracking error was found to be $\pm$ 2.8 μm.

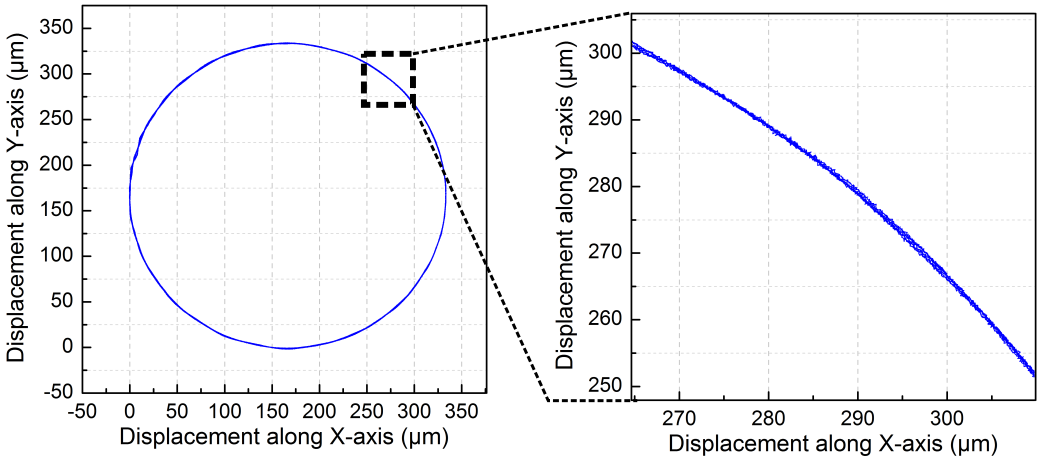

FIGURE 5.8: Circular motion profile

Figure 5.9, represents the integrated design. Four silicon gratings have been assembled into the etched cavities. In addition, four FODS probes (each with dimensions Ø1 mm) were used to measure the long range displacement. After the assembly, the sensor have been calibrated and average sensitives were found to be 11.37 mV/μm for x-axis sensor and 10.38 mV/μm for y-axis sensor with a linearity error less than 1% for both FODSs. Taking into the RMS noise values, the resolution of both sensor was found to be 43 nm and 69 nm, respectively. The degradation of the sensor resolution is mainly due to the difficulty of positioning the FODS probes in front of the silicon gratings in the cross structure.

In order to validate the concept, an experiment has been carried out in open loop control to measure long range displacement. This choice was made due to the difficulty in controller design. In future, the PI control will be modified to include the switching behaviour of the long range sensor. However, in this study we have decided to measure the output voltage with respect to the displacement performed by the mobile part. So, for this task along a single axis, PEDCs have been injected with 0.8 A currents with a sampling rate of 1 kHz. The objective was to realize the displacement at very slow speed (i.e., 10 μm/s) along both axis separately.

Figure 5.10(a), represents the accumulated voltage along x-axis. This measurement has been carried out over 7 mm displacement range. Theoretically, the travel range of the MPS prototype is 10 mm, but due to the relative distance between two FODS probes

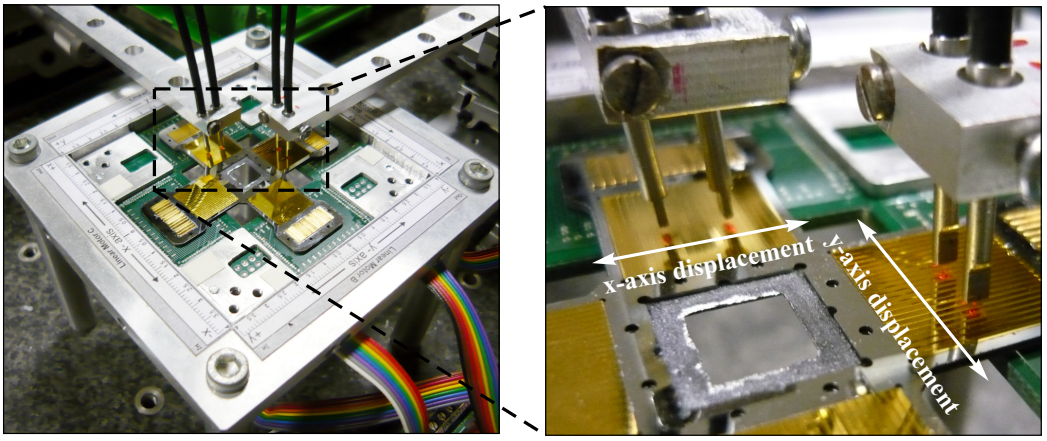

FIGURE 5.9: Integrated sensor and its enhanced view

over each grating, the measurement can only be performed for a range of 7 mm. In addition, another test has been carried out by driving the mobile platform along both axes (i.e., *x*- and *y*-axis). Figure 5.10(b) represents the *xy*-plot that has been realized with accumulated voltages achieved by both long range sensors. From the analysis, it has been concluded that the integrated MPS prototypes is able to provide a travel range of 7×7 mm^2 in *xy*-plane.

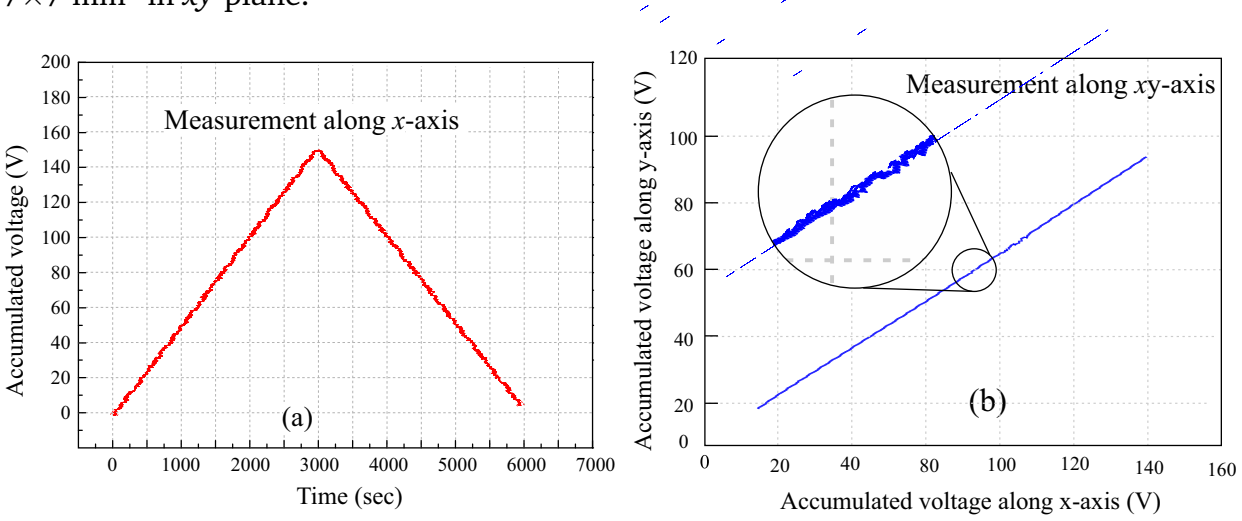

FIGURE 5.10: Open loop response along x-axis and y-axis

In order to estimate the motion resolution of the MPS prototype, the long range sensor can be used. Since, each grating step provides a measurable length of 621 μm. So, with the help of the PI control, a step response test was conducted without signal switching between two FODSs. For this task, the frequency of the currents in PEDCs have been controlled in similar fashion as described earlier. From the results presented in figure 5.11 it has been concluded that the motion resolution of the MPS prototype is 1.367 μm with a standard deviation of $\pm$ 0.285 μm.

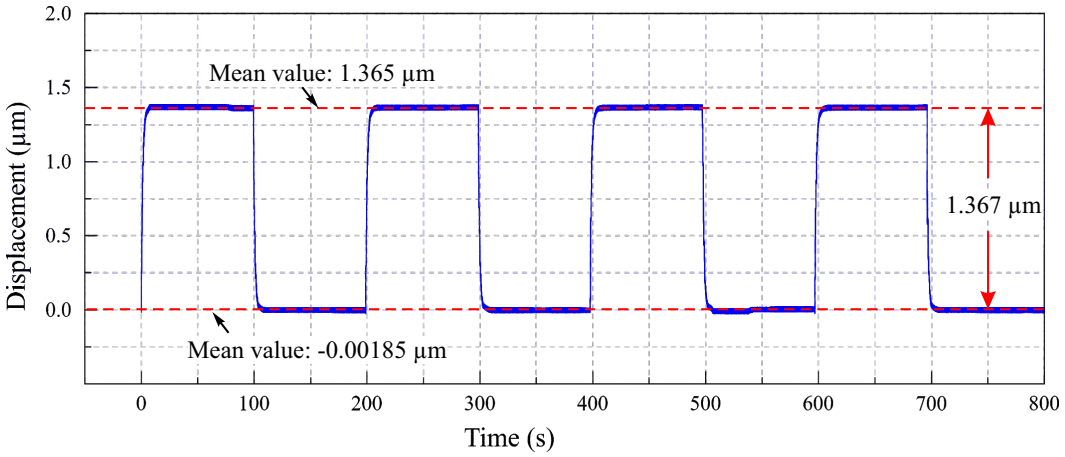

FIGURE 5.11: Step response realized with long range displacement measurement sensor

In the end, to investigate the rotation behaviour of the mobile part, image processing technique was used. A high resolution camera was fixed on top of the MPS prototype as shown in the figure 5.12. The camera was focused on a sticker fixed at the center of the stage. After calibrating the camera, four 1024 pixels×768 pixels (72 dpi of vertical and horizontal) images were taken to identify the position of the predefined markers (P1, P2, P3, P4, and P5) on the mobile part of the MPS. For one cycle by inverting the directions of the 0.8 A (peak to peak) currents (one period of 2 Hz with 200 Hz sampling frequency) were injected into PEDCs are along each axis thus creating a coupling effect which allows the mobile part to rotate about its centre point P5 to its maximum range. From captured images the calculated value for a single pixel is equal to 0.095 mm. By identifying the markers on the mobile part via image processing algorithm developed in Visual C++, the analysis of captured images revealed a maximum rotation angle between -11.13±0.91°and 10.97±0.69° about the centre point P5(319.97 pixels, 317.55 pixels). This rotation is limited because of geometrical limit of the PEDCs and that of aluminium structure. In future, advanced image processing algorithms along with control models will be developed in order to control the rotation motion in real time with high resolution.

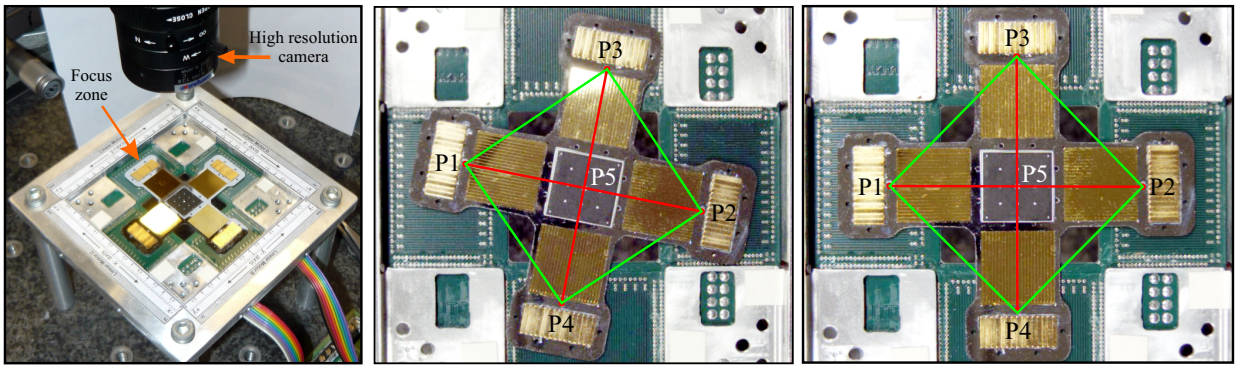

FIGURE 5.12: Experimental setup to measure the rotation

5.4 Conclusion

In this chapter, the design and development of a novel silicon cross structure has been presented. The integration concept of the sensor has been explained and the microfabrication of this cross structure has been carried out via ICP etching technology. For fabrication, two mask designs have been used to etch a standard silicon wafer in two steps, i.e., from top side and bottom side. The detail microfabrication layout has been realized and silicon cross structure has been fabricated. From the experimental results, it was concluded that the new cross structure eliminates the PMA assembly errors and reduce the displacement loss by 11.78% as compared to conventionally fabricated Zerodur® cross structure.

At the end some additional experiments have been carried out to evaluate the motion behaviour of the mobile part in *xy*-plane. In addition, open loop tests have been carried out to verify the functionality of the integrated long range sensor. With PI control, a displacement resolution of 1.37 μm has been achieved via measuring with integrated long range silicon sensor. At the end, a rotation test has been carried out to measure the maximum rotation range of the MPS. The rotation of the mobile part in our case is mainly limited due to the aluminum fixture that has been developed to mount the fixed part of the MPS. In our study, we used image processing technique to measure the maximum rotation that can be realized by the MPS. From the experiment, it was concluded that MPS is able to deliver a maximum rotation of $\pm$ 11° in *xy*-plane.

Chapter 6

Conclusion and perspective

This chapter presents the conclusion by summarizing the works presented in the previous chapters. In addition, a number of perspectives for future research on the basis of the study presented in this thesis will be discussed.

6.1 General conclusion

The objectives of the work presented in this thesis concern the development a compact miniature positioning system with integrated sensor that should be able to deliver millimeter level displacement strokes in *xy*-plane in micro applications. In order to reach our objective, first, a survey has been conducted to evaluate different existing technologies. Based on this survey, electromagnetic based direct drive actuation technology was selected due to its characteristics such as high speed, ability to realize wireless mobile part of the MPS, etc.

After selecting the drive technology, a long range MPS concept has been proposed in chapter 2. The uniqueness of the proposed design lies in its simple design and ability to perform millimeter level strokes in xy-plane with minimum possible overall dimensions of the whole system. The functioning of the MPS has been explained for a single LM due to its symmetrical design. Afterwards, different solutions have been discussed in order to realize the miniature drive components such as planar coils and permanent magnet arrays. Based on these solutions, a permanent magnet array with 14 Permanent Magnets Array (PMA) assembled in North-South configuration have been proposed to realize a compact long range LM. In order to achieve continuous motion of the mobile part, a design of two phase Planar Electric Drive Coils (PEDC) has been proposed. After the description of the long range motion concept for a single LM, the solution is then extended to realize a miniature positioning system with a cross structure design.

After the description of the miniature positioning system, its modelling has been carried out. For the purpose of simplification, models have been developed for a single LM

due to the symmetry of the MPS design. These models have been used to simulate the motion behaviour of the complete MPS prototype in open and closed loop control. From the simulation results, it has been concluded that the proposed MPS design can deliver millimeter level strokes in *xy*-plane.

In chapter 3, the proposed long range MPS design has been realized. In order to do so, the design layout and the description regarding the components used to realize the prototype have been discussed. Different solutions regarding the selection overall design parameters of the fixed and mobile part of the MPS have been carried out. In addition, analyses have been performed in order to qualify the MPS design for long range motion application by taking into account the influence of the magnetic field, vibration and the assembly errors generated over each LM. From these design and analysis, it was concluded that with an overall foot print size of 80×80 mm^2 of the fixed part, the prospered MPS is able to deliver a theoretical motion range of 10×10 mm^2 in *xy*-plane.

To verify the motion characteristics, experiments have been carried out in open loop control. Then, a PI control has been developed in order to control the motion of the mobile part by changing the frequency of the injected current in the PEDCs situated in the fixed part of the MPS. From these experiments, it has been concluded that the MPS is able to deliver variable stroke ranging from few micrometers to 2 mm with sub micrometer level accuracy. In addition, the MPS prototype can perform motion in xy-plane. It was also concluded that the maximum motion range of the MPS prototype was limited to 2 mm due to the fiber optic sensor used to measure the displacement range.

In order to solve the displacement measurement problem at long range (i.e., millimeter level), a high resolution non contact linear sensor has been realized in chapter 4. In the first part, the architecture and functioning of the long range linear displacement sensor has been discussed in detail. In order to achieve compact dimension for the long range linear sensor from the perspective to integrate it in the mobile part of the MPS prototype, the dimensions of the grating and sensor probe have been optimized using a geometric model.

To realize the long range sensor, its planar grating have been realized in silicon material by realizing a microfabrication process to etch the silicon gratings using wet anisotropic etching technique in TMAH solution. Furthermore, to improve the surface roughness and flatness parameters of the silicon grating, different solutions have been discussed and experimentally tested. From the results obtained after the analysis of the fabricated gratings, it was concluded that a concentrated solution containing 25% TMAH and IPA at 80°C lead to good surface quality. In addition, the deposition of a 300 nm gold coating improves the surface roughness and flatness parameters. With this fabrication method, the best silicon grating obtained provided an average roughness and flatness values of $R_a = 9.35\pm3$ nm and PV=35.08 ± 7 nm, respectively.

After realizing the silicon grating via microfabrication, experiments have been carried out in order to validate the long range linear displacement sensor. For this task, the silicon grating has been employed with two FODSs. From the experimental results, it was concluded that the sensor is capable to measure the displacement at a range of 12.5 mm with a high resolution of 30.8 nm in *xy*-plane.

In chapter 5, the integration of the long range sensor into the MPS prototype has been carried out. In order to facilitate and reduce assembly errors during manual assembly of the various components of the MPS, a novel cross structure in silicon material has been developed via ICP etching technology. For fabrication, two mask designs have been used to etch a standard silicon wafer in two steps, i.e., from top side and bottom side. The detail microfabrication layout has been realized and silicon cross structure has been fabricated. From the result, it has been concluded that the new cross structure eliminates the PMA assembly error thus reduce the displacement loss by 11.78% as compared to conventionally fabricated Zerodur® cross structure.

At the end some additional experiments have been carried out to evaluate the motion behaviour of the mobile part in *xy*-plane. In addition, open loop tests have been carried out to verify the functionality of the integrated long range sensor. With PI control, a displacement resolution of 1.37 μm has been achieved via measuring with long range silicon sensor. At the end, a rotation test has been carried out to measure the maximum rotation range of the MPS. The rotation of the mobile part in our case is mainly limited due to the aluminum fixture that has been developed to mount the fixed part of the MPS. In our study, we used image processing technique to measure the maximum rotation that can be realized by the MPS. From the experiment, it was concluded that MPS is able to deliver a maximum rotation angle of $\pm$ 11°.

6.2 Perspectives

The MPS design presented in this work has a fixed planar stroke (i.e., 10×10 mm^2). One of the perspective regarding the proposed MPS design is to further optimize its architecture to achieve larger strokes.

The rotation of the mobile is limited due to the length of the PEDCs. Based on the practical experience with the MPS prototype developed in this work, it was observed that the rotation of the mobile part in *xy*-plane does not entirely depend on the length of the PEDCs. So, in future it will be a good approach to redesign these coils and realize new models to simulate the rotation behaviour of the mobile part.

Concerning the payload capacity of the current MPS design which is limited to 11 grams, different solutions may be employed to increase its payload capacity. For example, by introducing another set of PEDC can increase the payload capacity due to the generation

of more electromagnetic force. Alternatively, this solution can also be employed to reduce the power consumption. In future, benefits of applying a second set of PEDCs on top of the mobile part need to be carried out. In addition, the sandwich structure based MPS design could help in levitation of the mobile part which can significantly improve the dynamics of the system due to elimination of the friction that appears because of the mechanical contact between the mobile and fixed parts.

The integration of the long range sensor has been manually carried out. Though, this solution seems suitable as silicon grating has been realized in a silicon wafer with special crystallographic orientation. However, the direct fabrication of the silicon gratings on the cross structure, is possible if the etching is preformed in silicon wafer with 111 crystallographic orientation at 45°. This approach will reduce the fabrication time and will eliminate manual assembly errors. The main complication that need to be assessed is to realize a hybrid microfabrication process that should integrate wet anisotropic etching followed by ICP etching process.

In future, the work presented in this thesis will be extended to realize compact smart actuation platform for micro factories. In addition, from the control aspect, a dedicated control will be developed in order to reduce the complexity of the displacement measurement with long range linear displacement sensor.

Appendix A

List of publications

The work presented in this thesis has been published and presented in the following international journals and international conferences.

- **Muneeb Ullah khan**, Nabil Bencheikh, Chritine prelle, Frédéric Lamarque, Tobias Beutel and Stephanus Büttgenbach, "A long stroke Electromagnetic *XY* positioning stage for micro applications, *IEEE Transaction on Mechatronics*, vol. 17, issue: 4, pp.866-897, 2012
- **Muneeb Ullah Khan**, Christine Prelle, Frédéric Lamarque, Tobias Beutel, Stephanus Büttgenbach, "A compact XYθ_z positioning stage", *International conference on Actuators (ACTUATOR 2012)*, 16 June, 2012, Bremen, Germany.
- **M.U.Khan**, C.Prelle, F.Lamarque, T.Beutel and S.Büttgenbach, "Silicon conveyor based planar electromagnetic device for linear displacement", *IEEE/ASME International conference on Advanced Intelligent Mechatronics (AIM 2010)*, 6-9 July 2010, Montreal, Canada.
- **Muneeb Ullah Khan**, N.Bencheikh, Christine Prelle, Frédéric Lamarque, Tobias Beutel and Stephanus Büttgenbach, "3DOF based electromagnetic planar stage", *International conference on Actuators (ACTUATOR 2010)*, 12 June 2010, Bremen Germany.
- N. Arora, L. Petit, **M.U.Khan**, F. Lamarque, C. Prelle, "Algorithm for signal processing of long-range fiber optic displacement sensor", 9th France-Japan & 7th Europe-Asia Congress on and Research and Education in Mechatronics (REM), pp.397-402, 21-23 Nov, 2012, Paris, France.
- N. Arora, L. Petit, **M.U.Khan**, F. Lamarque, C. Prelle, "Signal processing of a high resolution and long-range displacement sensor", pp. 1-4, 28-31 Oct. IEEE Sensors 2012.
- N. Arora, **M. U. Khan**, L. Petit, C. Prelle, "A planar electromagnetic actuator based on two layer coil assembly for micro applications", *IEEE/ASME International conference on Advanced Intelligent Mechatronics (AIM 2014)*, 8-11 July 2014, Besançon, France.

Appendix B

Measurement of the silicon grating surface characteristic

In chapter 4, section 4.5, the surface analysis of the micro fabricated silicon grating has been carried out using white light interferometer machine Zygo™ (New view 200) at Roberval laboratory UTC. The measurement principle this machine consists of passing a white light through optical system and create interference fringes on the surface of the specimen that is being analyzed. These fringes are recorded with a help of CCD sensor. The objective lens is mounted on a vertical piezoelectric actuator which saves the interferogram at each altitude. Based on the saved information, a three dimensional topography of the observed surface is realized and displayed. Similar to all optical measurement techniques, there is no contact between the surface of the sample which avoids the deterioration of the surface during measurement. Table B.1 represents the characteristics of this Zygo™ microscope.

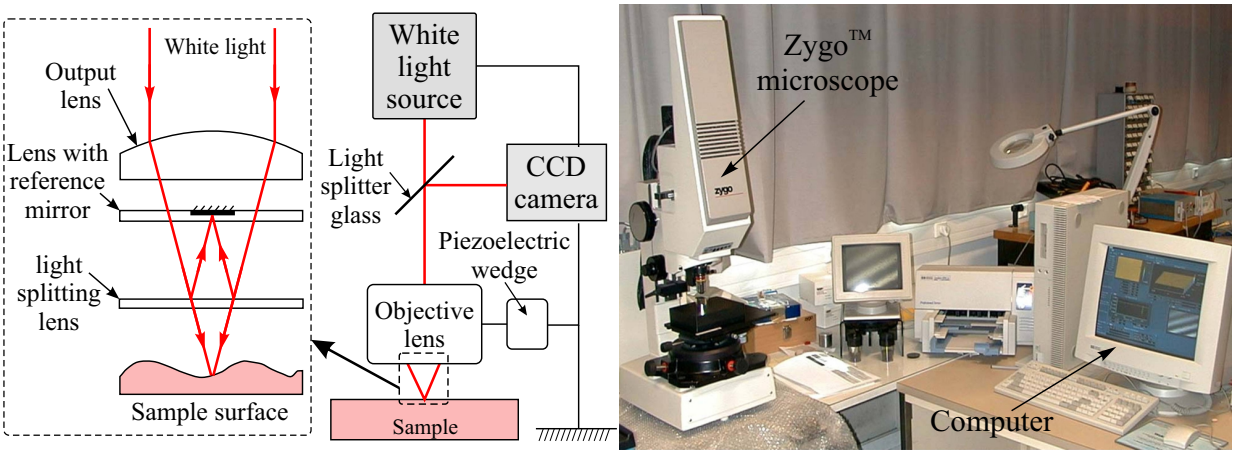

FIGURE B.1: Schematics of the working principle and real view of the Zygo™200 interferometer microscope

TABLE B.1: Typical characteristics of the Zygo™ 200 interferometer microscope

Vertical resolution	Spatial resolution	Vertical scan travel	Observable surface	Objective lens	Scan time	Obervable parameters
0.1 nm	0.44 μm to 8.8 μm	100 μm	140×110 μm^2 to 2.82×2.11 mm^2	x2.5, x10 and x50	55 sec (Max.)	Macro/micro roughness, waviness

In order to examine the microfabricated silicon gratings, it has been placed beneath the objective lens of the Zygo™200 machine. After leveling the grating steps with respect to the objective lens, the surface scan has been carried out. During analysis steps to examine the roughness and flatness parameters of the grating steps, the raw profile obtained via scanning the surface has been filtered using a plane form. This process is often carried out in order to remove any ambiguity concerning the leveling error of the grating step in horizontal plane. Different surface filtering options (e.g., plane form, cylindrical form, spherical form, etc.) can be carried out, however, since our grating steps are theoretically flat so we have selected the removal of a plane form for filtering process in order to remove the leveling error factor. The residual profile consists of roughness and waviness profiles as depicted in the figure B.2.

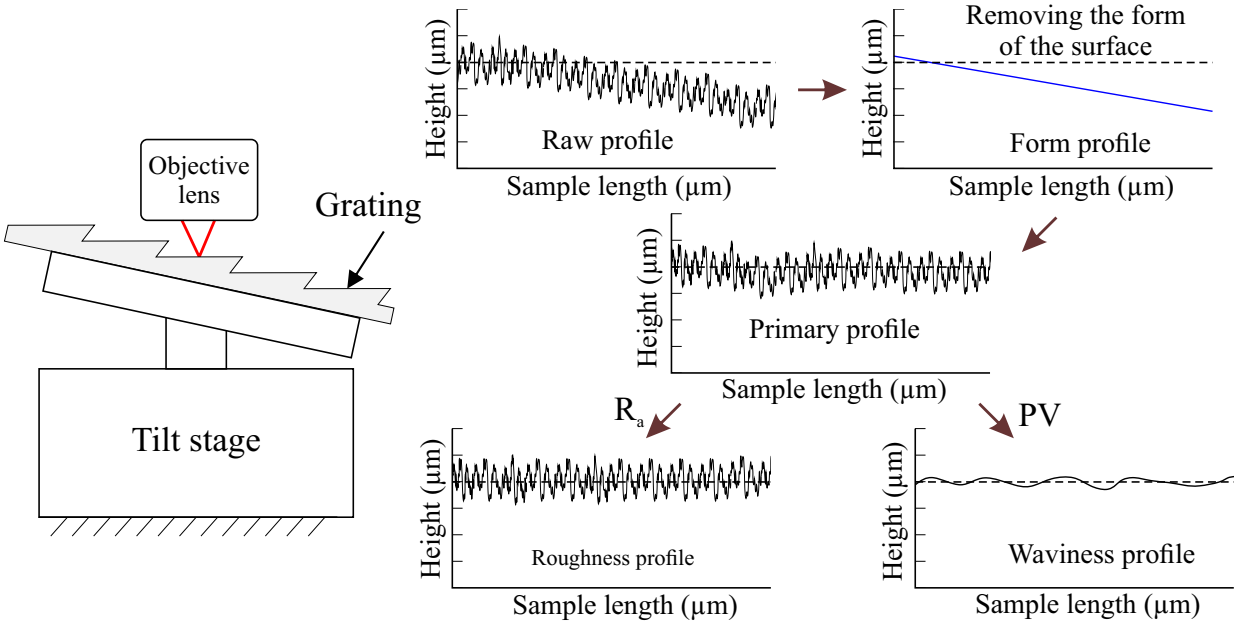

FIGURE B.2: Measurement of grating surface characteristics and analysis steps

The R_a value has been measured from roughness profile using equation (B.1). Furthermore, the PV value of the grating step surface has been measured from the waviness profile by taking into account the value of the maximum peak and valley values [Khia 07].

$$\begin{aligned} R_a &= \frac{1}{NM} \sum_{ij=(1,1)}^{ij=NM} |z_{ij} - \bar{z}| \\ PV &= |z_{\max} - z_{\min}| \end{aligned} \tag{B.1}$$

Where, n_x, n_y are the number of samples measured over a grating step and $\bar{z}$ is the mean value.

Appendix C

Description of the motorized linear stage

During experimentations, Motorized linear stages have been employed to calibrate fiber optic displacement sensors. These stages have been purchased from Newport[1] Corporation. Figure C.1 represents the schematic layout and the real view of the MFA-CC linear stage. It consists of a mobile part that is driven with a dc motor. The displacement of the mobile part is measured with a built in motor mounted rotary encoder. This encoder is able to deliver a resolution of 55 nm over a maximum linear displacement range of 25 mm. Further characteristics regarding the Newport motorized linear stage are presented in table C.1.

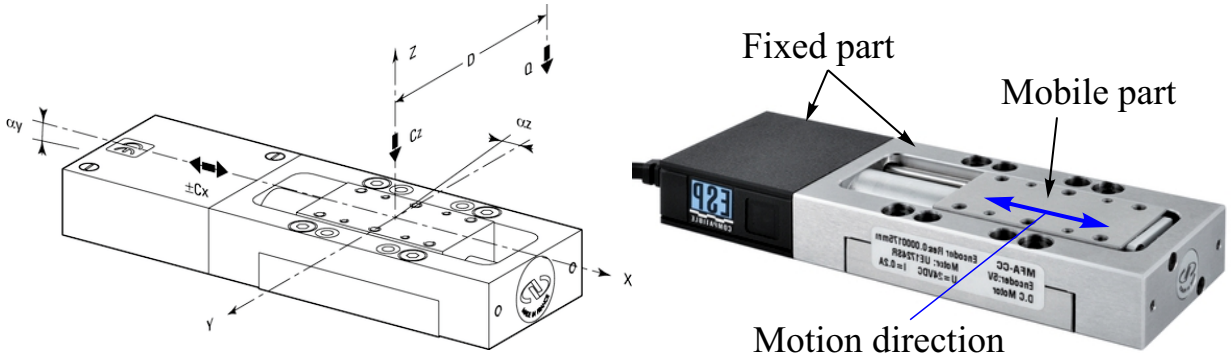

FIGURE C.1: Schematic layout and real view of the motorized linear stage

The linear stage was driven with a motion controlling unit ESP 100 that is coupled with a computer via serial port (RS232) as shown in the figure C.2. In addition, a program was developed in Labview® software to communicate and generate control signals for ESP controller in order to control/measure the position of the Newport linear stage.

[1] http://www.newport.com/

FIGURE C.2: Schematic layout of the linear stage control

TABLE C.1: Characteristics of the Newport motorized linear stage

1. Design Details		
Base material	Stainless steel	
Bearings	Double row linear ball bearings	
Drive Mechanism	Backlash compensated leadscrew	
Drive Screw Pitch (mm)	0.5	
Reduction Gear	MFA-CC: 1:14 and MFA-PP: 1:43	
Feedback	MFA-CC: Motor mounted rotary encoder; 2,048 cts/rev. MFA-PP: None	
Limit Switches	Mechanical switches	
Origin	Uses motor side limit for homing, typically < 4 μm repeatability	
Motor	MFA-CC: DC servo motor UE1724SR MFA-PP: 2-phase stepper motor UE16PP, 1 full step = 0.485 μm	
Cable Length (m)	1.5	
2. Specifications	**MFA-PP**	**MFA-CC**
Travel Range [in. (mm)]	**1(25)**	**1(25)**
Resolution (μm)**	0.00757	0.0175
Minimum Incremental Motion (μm)	0.1	0.1
Unidirectional Repeatability (μm) guaranteed	0.5	0.3
Bidirectional Repeatability (μm) guaranteed*	2.5	2
On Axis Accuracy (μm) guaranteed	8	8
Maximum Speed (mm/s)	0.3	2.5
Pitch / Yaw (μrad) guaranteed	200/100	200/100
* After backslash compensation **Equals 1/64 of a full step		
3. Load characteristics		
C_z (N)	Normal center load capacity on bearings	50
-C_x, +C_x (N)	Inverse/Direct load capacity on X axis	10
kax / kay (μrad/Nm)		100/120
Q Off-center load, Q$\leq C_z$ / (1 + D/20), D is Cantilever distance in mm		

Bibliography

[Ahme 05] H. B. Ahmed, B. Multon, and M. Ruellan. "Actionneurs linièaires directs et indirects". *La revue 3E.I*, Vol. 42, pp. 38–58, September 2005.

[Beeb 04] S. Beeby, G. Ensell, M. Kraft, and N. White. *MEMS Mechanical Sensors*, pp. 89–91. Art House Inc., United Kingdom, 2004.

[Benc 06] N. Bencheikh. *Conception et réalisation d'un conveyour électromagnétique planaire miniature*. PhD thesis, Université de Technologé de Compiègne, France, 2006.

[Berg 03] A. Bergander. *Control, wear testing and integration of stick-slip micropositioning*. PhD thesis, Department of Microtechnology, Ecole Polytechnique Fédérale de Lausanne, Laussanne, Suisse, 2003.

[Berl 00] A. Berlin, D. Biegelsen, P. Cheung, M. Fromherz, D. Goldberg, W. Jackson, B. Preas, J. Reich, and L. E. Swartz. "Motion control of planar objects using large-area arrays of MEMS-like distributed manipulators". *Micromechatronics*, Vol. XX, pp. 1–10, 2000.

[Bish 08] R. H. Bishop. *Mecatronics Systems, Sensors and Acuators*, Chap. 21, pp. 21–12. CRC Press, U.S, 2008.

[Bisw 06] K. Biswas and S. Kal. "Etch characteristics of KOH, TMAH and dual doped TMAH for bulk micromachining of silicon". *Microelectronics Journal*, Vol. 37, No. 6, pp. 519–525, 2006.

[Boge 67] F. Bogenschütz. *Ätzpraxis für Halbleiter*. Carl Hanser Verlag München, 1967.

[Breg 98] J. M. Breguet. *Actuionneurs stick and slip pour micro manipulateurs*. PhD thesis, École Polytechnique Fédérale de Lausanne, 1998.

[Butt 94] S. Büttgenbach. *Mikromechanik: Einführung in Technologie und Anwendungen*. Teubner B.G. GmbH, 1994.

[Cart 11] A. L. Cartal. "Mechancial amlification system for displacement produced by Piezoelectric actuators". *UPB Scientific Bulletin, Series D: Mechanical Engineering*, Vol. 73, No. 2, pp. 239–248, 2011.

[Cedr 11] Cedrat-Technologies. *Piezo product Catalog*. 2011.

[Chap 04] Y. A. Chapuis, Y. Fukuta, Y. Mita, and H. Fujita. "Autonomous decentralized systems based on distributed controlled mems actuator for micro conveyance application". *J-STAGE*, Vol. 56, No. 1, pp. 109–115, 2004.

[Chen 04] C. Chen, M. Jang, and K. Lin. "Modeling and high-precision control of a ball-screw-driven stage". *Precision Engineering*, Vol. 28, No. 4, pp. 483–495, 2004.

[Chen 10] M.-Y. Chen, H.-H. Huang, and S.-K. . Hung. "A New Design of a Submicropositioner Utilizing Electromagnetic Actuators and Flexure Mechanism". *IEEE Transactions on Industrial Electronics*, Vol. 57, No. 1, pp. 96–106, 2010.

[Culp 04] G. Culpepper Martin L. Anderson. "Design of a low-cost nano-manipulator which utilizes a monolithic, spatial compliant mechanism". *Precision Engineering*, Vol. 28, pp. 469–482, 2004.

[Culp 06] M. L. Culpepper and S. C. Chen. "Design of a six axis micro scale nanopositioner μHexFlex". *Precision Engineering*, Vol. 30, No. 3, pp. 314–324, 2006.

[Dani 04] W. Daniau and et al. *Chapter 3 - Les dépôts en couches minces in Technique de fabrication des microsystémes 1*. Hermes Science, Lavoisier ed, 2004.

[Dech 06] N. Dechev. "Basic Concepts: Semiconductors". University of Victoria, 2006. http://www.engr.uvic.ca/~mech466/MECH466-Lecture-3.pdf.

[Deji 05] S. Dejima, W. Gao, H. Shimizu, S. Kiyono, and Y. Tomita. "Precision positioning of a five degree-of-freedom planar motion stage". *Mechatronics*, Vol. 15, No. 8, pp. 969–987, 2005.

[Dele 11] G. J. Delettre, Anne. Laurent and N. Le Fort-Piat. "2-DOF Contactless Distributed Manipulation Using Superposition of Induced Air Flows". In: *IEEE/RSJ International Conference on Intelligent Robots and Systems, IROS'11.*, pp. 5121–5126, CA United States, 25-30 Sept 2011.

[Devo 04] S. Devos, W. Van de Vijver, K. Decoster, D. Reynaerts, and H. Van Brussel. "A planar piezoelectric drive with a stepping and a resonant operation mode". In: *4^{th} Euspen International Conference*, Glasgow, Scotland (UK), May-June 2004.

[Ditt 06] P. Dittrich and D. Radeck. “3 - DOF Planar Induction Motor”. In: *IEEE International Conference on Electro/information Technology*, pp. 81 – 86, 2006.

[Ebef 00] T. Ebefors, J. U. Mattsson, E. Kälvesten, and G. Stemme. “A robust micro conveyer realized by arrayed polyimide joint actuators”. *Journal of Micromechanics and Microengineering*, Vol. 10, No. 3, pp. 337–349, 2000.

[Furl 01] E. P. Furlani. *Permanent Magnet and Electromechanical Devices*, Chap. 4, pp. 110–111,211–216. Acedemic Press, 2001.

[Gao 04] W. Gao, S. Dejima, H. Yanai, K. Katakura, S. Kiyono, and Y. Tomita. “A surface motor-driven planar motion stage integrated with an XYZ surface encoder for precision positioning”. *Precision Engineering*, Vol. 28, No. 3, pp. 329–337, 2004.

[Gilb 96] R. G. Gilbertson and J. D. Busch. “A survey of micro-actuator technologies for future spacecraft missions”. *The Journal of The British Interplanetary Society*, Vol. 49, pp. 129–138, 1996.

[Gloe 12] R. Gloess, C. Mock, C. Rudolf, C. Walenda, C. Schaeffel, M. Katzschmann, and H.-U. Mohr. “Magnetic Levitation in 6-DOF with Halbach Array Configuration”. In: *13th International Conference on New Actuators (ACTUATOR 2012) , Bremen, Germany, 18-20 June 2012*, 2012.

[Heid] Heidenhain. “http://www.heidenhain.de/”.

[Hell 09] R. Hellinger and P. Mnich. “Linear Motor-Powered Transportation: History, Present Status, and Future Outlook”. *Proceedings of the IEEE*, Vol. 97, No. 11, p. 9, 2009.

[Holm 00] M. Holmes, R. , Hocken, and D. Trumper. “The long-stroke scanning stage: a novel platform for micro scanned probe microscopy”. *Precision Engineering*, Vol. 24, No. 3, pp. 191–209, 2000.

[Hu 06] T. Hu and W.-j. Kim. “Extended Range Six DOF High-Precision Positioner for Wafer Processing”. *IEEE/ASME Transactions on Mechatronics*, Vol. 11, No. 6, pp. 682–689, 2006.

[Ji 10] L. Ji, Y. Zhu, S. O. Reza Moheimani, and R. Yuce Mehmet. “A Micromachined 2DOF Nanopositioner with Integrated Capacitive Displacement Sensor”. 2010.

[Jong 06] B. d. Jong. *A Six Degrees of Freedom MEMS Manipulator*. PhD thesis, University of Twente, Enschede, The Netherlands, 2006.

[Joub 12] A. Joubair, M. Slamani, and I. A. Bonev. "A novel XY-Theta precision table and a geometric procedure for its kinematic calibration". *Robotics and Computer-Integrated Manufacturing*, Vol. 28, No. 1, pp. 57–65, 2012.

[Jung 05] K. Jung and Y. Baek. "Characteristics comparison of planar stages using repulsive and attractive type of surface actuator principle". *Sensors and Actuators A: Physical*, Vol. 117, pp. 173–182, 2005.

[Jung 10] K. S. Jung and S. H. Lee. "Contact-free planar stage using linear induction principle". *Mechatronics*, Vol. 20, No. 4, pp. 518–526, 2010.

[Karp 08] M. Karpelson., G.-Y. Wei., and R. J. Wood. "A Review of Actuation and Power Electronics Options for Flapping-Wing Robotic Insects". May 19-23 2008.

[Khia 07] A. Khiat. *Capteurs à fibres optiques pour la mesure à haute résolution de déplacements linéaires et angulaires sur une grande étendue. Application aux systèmes mécaniques de dimensions réduites.* PhD thesis, Université de Technologé de Compiègne, France, 2007.

[Khia 08] A. Khiat, F. Lamarque, C. Prelle, A. Phataralaoha, J. Dittmer, T. Krah, T. M. Leester-Schaedel, and S. Büttgenbach. "Silicon grating microfabrication for long range displacement sensor". *Journal of Micro/Nanolithography, MEMS, and MOEMS*, Vol. 7, No. 2, p. 8, 2008.

[Kim 03] C.-H. Kim, H.-M. Jeong, J.-U. Jeon, and Y.-K. Kim. "Silicon Micro XY-Stage With a Large Area Shuttle and No-Etching Holes for SPM-Based Data Storage". *Microelectromechanical Systems*, Vol. 12, No. 4, pp. 470–478, 2003.

[Kim 07] W.-j. Kim, S. Verma, and H. Shakir. "Design and precision construction of novel magnetic-levitation-based multi-axis nanoscale positioning systems". *Precision Engineering*, Vol. 31, No. 4, pp. 337–350, 2007.

[Kim 97] W. Kim. *High precision planar magnetic levitation*. PhD thesis, Department of Mechanical Engineering, MIT, Massachusetts, USA, 1997.

[Kiss 74] C. D. Kissinger. "Fiber optic displacement measuring apparatus". *US Patent*, 1974.

[Klum 95] A. Klumpp, K. Kaühl, U. Schaber, H. Käufl, and W. Lang. "Anisotropic etching for optical gratings". *Sensors and Actuators A: Physical*, Vol. 51, No. 1, pp. 77–80, Oct. 1995.

[Kuma 12] M. Kumagai and R. L. Hollis. "Development and Control of a Three DOF Planar Induction Motor". In: *IEEE International Conference on Robotics and Automation, RiverCentre, Saint Paul, Minnesota, USA*, May 2012.

[Lai 05] Y. Lai. *Eddy Current Displacement Sensor with LTCC Technology*. PhD thesis, University of Freiburg, Freiburg im Breisgau, Germany, 2005.

[Lee 00] S. Q. Lee and D. G. Gweon. "A new 3-DOF Z-tilts micropositioning system using electromagnetic actuators and air bearings". *Precision Engineering*, Vol. 24, pp. 24–31, 2000.

[Lee 09] J. Lee and D. Lee. "Fabrication of a micro XY-stage using SU-8 thermal actuators". *Microelectronic Engineering*, Vol. 86, No. 4-6, pp. 1267–1270, 2009.

[Lin 11] C. Y. Lin, T. Tsai, J. Chiou, and C. Chien. "Design, Fabrication and Actuation of 4-axis Thermal Actuating Image Stabilizer". February 20-23 2011.

[Liu 07] X. Liu, K. Kim, and Y. Sun. "A MEMS stage for 3-axis nanopositioning". *Journal of Micromechanics and Microengineering*, Vol. 17, No. 9, pp. 1796–1802, 2007.

[Lu 12] X. Lu and I.-u.-r. Usman. "6D direct-drive technology for planar motion stages". *CIRP Annals - Manufacturing Technology*, Vol. 61, pp. 359–362, 2012.

[Mado 02] M. J. Madou. *Fundamentals of microfabrication: The science of miniaturization*. CRC press, 2nd Ed., 2002.

[Malu 04] N. Maluf and K. Williams. *An Introduction to Microelectromechanical Systems Engineering*, pp. 82–83. Artech House,Inc., 2004.

[Marc 98] J. Marchetti, Y. He, O. Than, and S. Akkaraju. "Efficient process development for bulk silicon etching using cellular automata simulation techniques". pp. 287–295, 1998.

[Mino 96] P. Minotti and V. Nocton. "Etude Theorique d'Un Microtranslateur Piézoélectrique à ondes stationnaires: Une Introduction aux futurs micromoteurs multi-degrés de Liberté". *Mechanical Machine Theory*, Vol. 31, No. 1, pp. 91–108, 1996.

[Mole 00] L. Molenaar. *A noval planar magnetic bearing and motor configuration applied in positioning stage*. PhD thesis, Dept. of Mechanical engineering and marine technology, Delft university of technology, Delft, Netherlands, 2000.

[Mole 96] F. Molenaar, A. Auer and H. F. van Beek. "Application of Magnetic Bearing for Contactless Utlra High Precision Postioning". In: *5th International Symposium on Magnetic Bearings (5ISMB)*, pp. 441–445, Kanazawa, Japan, 1996.

[Nguy 12] V. H. Nguyen and W.-j. Kim. "Novel Electromagnetic Design for a Precision Planar Positioner Moving over a Superimposed Concentrated-Field Magnet Matrix". *IEEE Transactions on Energy Conversion*, Vol. 27, No. 1, pp. 52–62, March 2012.

[Nomu 07] Y. Nomura and H. Aoyama. "Development of inertia driven micro robot with nano tilting stage for SEM operation". *Microsystem Technologies*, Vol. 13, No. 8, pp. 1347–1352, 2007.

[Okaz 04] Y. Okazaki, N. Mishima, and K. Ashida. "Microfactory: Concept, History, and Developments". *Manufacturing Science and Engineering*, Vol. 126, No. 4, pp. 837–844, 2004.

[Pal 11] P. Pal, K. Sato, M. A. Gosalvez, B. Tang, H. Hida, and M. Shikida. "Fabrication of novel microstructures based on orientation-dependent adsorption of surfactant molecules in a TMAH solution". *Journal of Micromechanics and Microengineering*, Vol. 21, No. 1, p. 015008, 2011.

[Pan 11] J. F. Pan and N. C. Cheung. "An adaptive controller for the novel planar switched reluctance motor". *IET Electric Power Applications*, Vol. 5, No. 9, pp. 677–683, 2011.

[PI 12] PI. *Piezo Mechanism, Piezo Mechanics: Catalog,*. Physik Instrumente, 2012.

[Pons 05] J. L. Pons. *Emerging Actuator Technologies*, Chap. 2, p. 47. John Wiley & Sons, Ltd., 2005.

[Prel 06] C. Prelle, F. Lamarque, and P. Revel. "Reflective optical sensor for long range and high resolution displacements". *Sensors and Actuators A*, Vol. 127, pp. 139–146, 2006.

[Ratc 06] S. Ratchev. *Precision Assembly Technologies For Mini and Micro Products*. Springer, 2006.

[Rive 04] W. Rivera. "Minimization of distortion and increasing resolution in wide angle viewing by means of actuated micro-mirrors". NSF Summer Undergraduate Fellowship in Sensor Technologies, University of Pennsylvania, 2004.

[Sabr 09] M. F. M. Sabri, O. Takahito, and M. Esashi. "A large displacement piezodriven silicon xy-microstage". June 21-25 2009.

[Scho 10] Schott. *ZERODUR-Product Information, SCHOTT Catalog*. 2010.

[Seid 90] H. Seidel, L. Csepregi, A. Heuberger, and H. Baumgärtel. "Anisotropic Etching of Crystalline Silicon in Alkaline Solutions". *Journal of the Electrochemical Society*, Vol. 11, pp. 3626–3632, 1990.

[Shik 01] M. Shikida, T. Masuda, D. Uchikawa, and K. Sato. "Surface roughness of single-crystal silicon etched by TMAH solution". *Sensors and Actuators A: Physical*, Vol. 90, No. 3, pp. 223–231, 2001.

[Smar 11] SmarAct. *SmarAct Product Catalogue*. SmarAct, 2011.

[Sun 08] L. Sun, J. Wang, W. Rong, X. Li, and H. Bao. "A silicon integrated micro nano-positioning XY-stage for nano-manipulation". *Journal of Micromechanics and Microengineering*, Vol. 18, No. 12, pp. 125004–125014, 2008.

[Sund 05] K. B. Sundaram, A. Vijayakumar, and G. Subramanian. "Smooth etching of silicon using TMAH and isopropyl alcohol for MEMS applications". *Microelectronic Engineering*, Vol. 77, No. 3-4, pp. 230–241, 2005.

[Taka 07] K. Takahashi, H. N. Kwon, M. Mita, K. Saruta, H. Lee, Jong Hyun. Fujita, and H. Toshiyoshi. "A Silicon Micromachined f-θ Microlens Scanner Array by Double-Deck Device Design Technique". *IEEE Journal of Selected Topics in Quantum Electronics*, Vol. 13, No. 2, pp. 227–282, 2007.

[Trum 98] D. L. Trumper and W. J. Kim. "High-precision magnetic levitation stage for photolithography". *Precision Engineering*, Vol. 22, pp. 66–77, 1998.

[Voll 10] S. Vollach and D. Shilo. "The Mechanical Response of Shape Memory Alloys Under a Rapid Heating Pulse". *Experimental Mechanics*, Vol. 55, pp. 803–811, 2010.

[Wang 99] D. Wang. *Conception et réalisation d'un minicapteur de déplacement à fibres optiques à résolution nanométrique*. PhD thesis, Laboratoire Roberval, Université de Technologie de Compiègne, Compiègne, France, 1999.

[Wils 05] J. S. Wilson. *Sensor Technology Handbook*, pp. 400–410. Elsevier Inc., 2005.

[Wim 06] V. d. V. Wim, V. B. Hendrik, and R. Dominiek. "A Multi-DOF Positioning Stage based on Novel Piezoelectric Resonant Drive Modules". 2006.

[Wu 04] Y. Wu and Z. Zhou. "An XY mechanism actuated by one actuator". *Mechanism and Machine Theory*, Vol. 39, No. 10, pp. 1101–1110, 2004.

[Yu 10] H. Yu and W.-j. Kim. "A compact Hall-Effect sensing 6-DOF precision positioner". *IEEE/ASME Transactions on Mechatronics*, Vol. 15, No. 6, pp. 982–985, December 2010.

[Zesc 95] W. Zesch, R. Buechi, A. Codourey, and R. Y. Siegwart. "Inertial drives for micro- and nanorobots: two novel mechanisms". In: *Int.Symp.on Microrobotics and Micromechanical Systems*, pp. 80–88, Philadelphia, Pennsylvania, 1995.

[Zhao 11] C. Zhao. *Ultrasonic Motors: Technologies and Applications*. Springer, 2011.

[Zube 01] I. Zubel and M. Kramkowska. "The effect of isopropyl alcohol on etching rate and roughness of (1 0 0) Si surface etched in KOH and TMAH solutions". *Sensors and Actuators A: Physical*, Vol. 93, No. 2, pp. 138–147, 2001.

[Zube 11] I. Zubel, K. Rola, and M. Kramkowska. "The effect of isopropyl alcohol concentration on the etching process of Si-substrates in KOH solutions". *Sensors and Actuators A: Physical*, Vol. 171, No. 2, pp. 436–445, 2011.